POLITECNICO DI MILANO
DEPARTMENT OF ENERGY
DOCTORAL PROGRAM IN ENERGY AND NUCLEAR SCIENCE AND TECHNOLOGY

IMPROVEMENT OF THE CONTROL-ORIENTED MODELLING OF THE GEN-IV LEAD-COOLED FAST REACTOR: DEVELOPMENT OF REDUCED ORDER METHODS

Doctoral Dissertation of
Stefano Lorenzi

Supervisors:
Prof. Antonio Cammi
Prof. Lelio Luzzi
Prof. Gianluigi Rozza

Tutor:
Prof. Marco Enrico Ricotti

The chair of the Doctoral Program:
Prof. Carlo Enrico Bottani

28th Cycle

November 2015 – Milano, Italy

(this page is intentionally left blank)

Acknowledgements

The thesis has been carried out in the framework of a collaboration between Politecnico di Milano and the SISSA (International School for Advanced Studies) on the development of reduced order methods for control applications. Activities in this framework included a detachment (February 1 – June 31, 2015) at the SISSA – mathLab Department, under the supervision of Prof. Gianluigi Rozza.

The work has been supported by CINECA supercomputing center under Sis14_COGESTA Project and PoliM_EneDAF Project.

The author acknowledges the European Commission for funding the LEADER (Lead-cooled European Advanced DEmonstration Reactor) Project, a medium-scale LFR-focused Project developed within the 7th Framework Programme "Fission 2009 – Advanced Nuclear Systems for Increased Sustainability". Acknowledgement is also due to all the colleagues of the participant organizations for their contributions in many different topics, in particular to Dr. Alessandro Alemberti and Dr. Luigi Mansani (Ansaldo Nucleare, Italy) for their valuable support and fruitful criticism.

(this page is intentionally left blank)

Abstract

The context of the present Ph.D. thesis is the domain of research oriented toward the improvement of the control-oriented modelling of Generation IV Lead-cooled Fast Reactors (LFRs) through the development of reduced order methods. The Reduced Order Modelling (ROM) approach is aimed at combining the high-detail modelling usually adopted for design purposes with the requirements demanded for a control-oriented tool, firstly the computational efficiency. The practical application of this study is the improvement of a control-oriented simulator of an LFR plant, i.e., substituting some components based on zero-dimensional approach with ROM-based models ensuring a high level of accuracy and a better physical description without increasing the computational burden. The plant simulator is based on the object-oriented modelling, is developed with Modelica language and implemented in the Dymola simulation environment. In the first part of the thesis, an introduction on the current approach of the control-oriented modelling and its impact on the control scheme design are presented. The second part is focused on the development of a spatial neutronics model for the reactor core, highlighting the differences in terms of modelling and assumptions. A simple 3D test case is analysed in order to demonstrate the feasibility of the spatial neutronics approach, to assess its better performance with respect to the classic Point Kinetics, and to show how it can be implemented in an object-oriented simulator, as well. Moreover, the full core model of the Advanced Lead Fast Reactor European Demonstrator (ALFRED) is set up in order to evaluate the performance of the different modelling choices in reproducing the reactivity insertion following a temperature change or a CR movement. In the third part of the thesis, the development of a spatial model of the ALFRED reactor pool is described. This model is based on the POD (Proper Orthogonal Decomposition)-FV-ROM procedure, developed on purpose for extending the literature approach based on Finite Element to the Finite Volume (FV) approximation of the Navier-Stokes equations. Moreover, the proposed procedure allows building a reduced order model that is capable to handle turbulent flows modelled through the Reynold-Averaged Navier Stokes equations. The POD-FV-ROM is tested in the classic benchmark of numerical simulations for the 2D lid-driven cavity. In particular, two simulations at Re = 1.000 and Re = 100.000 are considered in order to assess both a laminar and turbulent case. As final step, the developed approach is employed to build a ROM-based component of the coolant pool of the ALFRED reactor.

(this page is intentionally left blank)

Estratto

Questa tesi di dottorato si inserisce nel contesto della ricerca rivolta al miglioramento della modellazione orientata al controllo di reattori nucleari di quarta generazione, ed in particolare del reattore raffreddato a piombo (LFR – *Lead-cooled Fast Reactor*), attraverso lo sviluppo e l'implementazione di metodi di riduzione d'ordine. Questo approccio si prefigge di unire la modellazione ad elevato grado di dettaglio utilizzata a fini della progettazione con i requisiti che vengono solitamente richiesti ad uno strumento di simulazione orientato al controllo, *in primis* l'efficienza computazionale. L'applicazione pratica di questo studio è il miglioramento di un simulatore d'impianto orientato al controllo del reattore a piombo ALFRED (*Advanced Lead Fast Reactor European Demonstrator*) attraverso la sostituzione di alcuni componenti basati su un approccio puntiforme con componenti basati su modelli di riduzione d'ordine. Quest'ultimi possono garantire un elevato grado di accuratezza e una migliore modellazione fisica senza aumentare il carico computazionale. Il simulatore d'impianto è basato su una modellazione orientata agli oggetti, è sviluppato con il linguaggio Modelica ed implementato nell'ambiente di simulazione Dymola. Nella prima parte della tesi viene fornita un'introduzione sull'attuale approccio impiegato nella modellazione orientata al controllo e il suo impatto sulla progettazione dello schema di controllo. La seconda parte riguarda lo sviluppo di un modello di neutronica spaziale per il nocciolo di ALFRED, ponendo l'accento sui differenti metodi di riduzione d'ordine e le relative assunzioni modellistiche. Un semplice caso tridimensionale viene analizzato sia per dimostrare la fattibilità del modello di neutronica spaziale, sia per valutarne le migliori prestazioni rispetto al classico metodo della cinetica puntiforme, sia per dimostrare come tale approccio possa essere inserito all'interno di un simulatore d'impianto orientato al controllo. Inoltre, si è sviluppato un modello completo (3D) del nocciolo di ALFRED per valutare le prestazione dei metodi di riduzione d'ordine nel riprodurre l'inserzione di reattività a seguito di un cambiamento di temperatura o di movimento di un organo di controllo. Nella terza e ultima parte della tesi viene descritto lo sviluppo di un modello spaziale per la piscina del reattore ALFRED. Quest'ultimo è basato su una procedura POD-FV-ROM (*Proper Orthogonal Decomposition – Finite Volume – Reduced Order Modelling*), appositamente sviluppata per estendere l'approccio a elementi finiti (solitamente usato in letteratura) all'approssimazione a volumi finiti dell'equazione di Navier-Stokes. In aggiunta, la procedura proposta permette di costruire un modello d'ordine ridotto capace di gestire fluidi in regime turbolento attraverso l'utilizzo delle equazioni di Navier-Stokes mediate (RANS). Il metodo POD-FV-ROM è testato con riferimento al classico confronto numerico della cavità bidimensionale. Sono stati considerati due casi principali, con numeri di Reynolds pari a 1000 e 100000, per valutarne l'efficacia sia in caso laminare che turbolento. Come stadio finale, il metodo POD-FV-ROM è stato utilizzato per mettere a punto un componente basato sul modello d'ordine ridotto della piscina del reattore ALFRED.

(this page is intentionally left blank)

Contents

Acronyms

ALFRED	Advanced Lead Fast Reactor European Demonstrator
APOD	Adjoint Proper Orthogonal Decomposition
BC	Boundary Condition
BDF	Backward Differentation Formula
CANDU	CANada Deuterium Uranium
CFD	Computational Fluid Dynamics
CR	Control Rod
CRT	Computational Reduction Techniques
CSG	Combinatorial Solid Geometry
DAE	Differential Algebraic Equation
DNS	Direct Numerical Simulation
ELSY	European Lead-cooled System
FA	Fuel Assembly
FE	Finite Elements
FOM	Full Order Model
FP7	7th Framework Programme
FV	Finite Volume
HLM	Heavy Liquid Metal
I&C	Instrumentation and Control
IAEA	International Atomic Energy Agency
ICN	Istitute de Cercetari Nucleare
LEADER	Lead-cooled European Advanced DEmonstrator Reactor
LES	Large Eddy Simulation
LFR	Lead-cooled Fast Reactor
LTI	Linear Time Invariant
MC	Monte Carlo
MIMO	Multiple Input Multiple Output
MM	Modal Method
MOX	Mixed-Oxide
MSR	Molten Salt Reactor
NPP	Nuclear Power Plant
NRG	Non-square Relative Gain array
NRG	Nuclear Reactor Group
NSE	Navier-Stokes Equation
O&M	Operation and Maintenance
ODE	Ordinary Differential Equation
PDE	Partial Differential Equation
PID	Proportional-Integral-Derivative controllers
PK	Point Kinetics
POD	Proper Orthogonal Decomposition

POLIMI	Politecnico di Milano
RANS	Reynolds Averaged Navier-Stokes
RB	Reduced Basis
RGA	Relative Gain Array
ROM	Reduced Order Modelling
RS	Row Sum
SISO	Single Input Single Output
SISSA	Scuola Internazionale Studi Superiori Avanzati
SN	Spatial Neutronics
SR	Safety Rod
SRS	Surrogate Response Surfaces
SST	Shear Stress Transport
SVD	Singular Value Decomposition
UQ	Uncertainty Quantification

Introduction

In the last years, the research in the nuclear field has focused on the Generation-IV reactors to reach high standard in the areas of sustainability, economics, safety and reliability, proliferation resistance and physical protection. Among these reactor concepts, the Lead-cooled Fast Reactor (LFR) seems promising due to the excellent material management capabilities since it operates in the fast-neutron spectrum and uses a closed fuel cycle for efficient conversion of fertile uranium, allowing also the possibility to use the reactor as a burner of minor actinides. Advanced reactor concepts cooled by Heavy Liquid Metal (HLM) coolants ensure a great potential for plant simplifications and higher operating efficiencies compared to other coolants, introducing however some safety concerns and design challenges.

The need to investigate the control strategy for this innovative system arises from two main reasons:

- the new technological issues brought by the use of lead as coolant (Tucek et al., 2006) do not make possible the adoption of the classic approaches retrieved from Light Water and Sodium Fast Reactor concepts since the different features result in different constraints on control and controlled variables. In particular, the spatial dependence plays a relevant role in the dynamics evolution, both in neutronics and in thermal-hydraulics environment.
- the need of improving the plant availability and the present energy production situation require constantly enhanced performance for Nuclear Power Plants (NPPs), along with a more and more ability to follow grid demands (IAEA, 1999).

In the development of the control system, it is of primary importance to rely on simulation tools for its realization, testing and validation by means of an accurate description of the reactor-controlled response. The modelling approach used to represent the system plays a relevant role. A poor detailed modelling precludes the possibility to exploit all the potentialities of the advanced control schemes and techniques. In particular, these techniques should adopt a detailed modelling in order to provide the control system design with spatial information regarding neutron flux, temperature, pressure, and mass flow rate. Besides control purpose, the latter can be useful for diagnostics and fault detection during operational transients (IAEA, 2009) and safety insights as well. At the same time, a simulation tool for control purposes has to fulfil some requirements. In particular, (*i*) fast-running simulations, (*ii*) a comprehensive representation of the entire plant behaviour, (*iii*) the possibility to couple the plant dynamics simulator with the control system are the main requests in this sense. The control system usually adopted in nuclear reactors is based on Proportional-Integral-Derivative controllers (PID) in decentralized control scheme, which ensure simplicity in the implementation and robustness towards malfunctioning of single control loops, favoring the Operation and Maintenance (O&M) (Levine, 1996). The choice of simple Single Input Single Output (SISO) control laws has brought to the development of simulators that implement simple models (zero-dimensional) for the description of the main physics of a nuclear

reactor (e.g., the point kinetics for the neutronics). The classic control-oriented approach based on 0D/1D modelling is appropriate whether the spatial effects are not relevant and only the estimation of integral quantities is required as for the SISO control laws. On the opposite side, the 3D modelling is usually devoted to design purposes having a high level of detail but extremely expensive from a computational point of view (Figure 1).

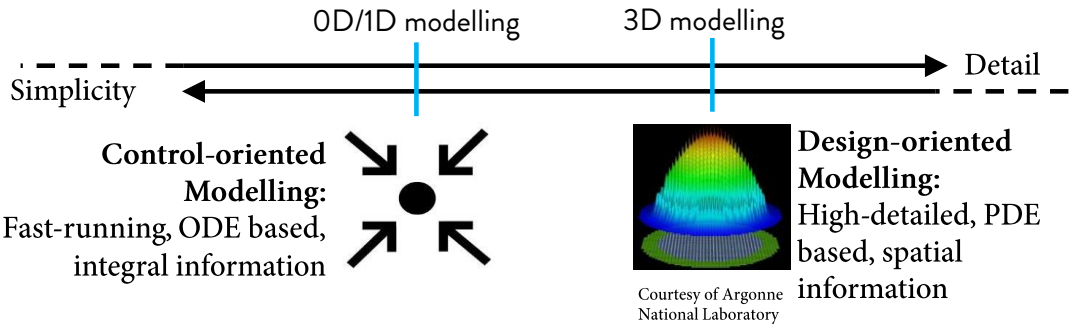

Figure 1. Different approaches in modelling, 0D/1D modelling (control-oriented) vs 3D modelling (design-oriented).

In the light of the previous considerations, the research efforts should be devoted to combine a high-detail modelling featuring spatial capabilities (e.g., 3D modelling) with the requirements demanded for a control-oriented tool, firstly the computational efficiency. A viable solution is to employ Reduced Order Modelling (ROM) techniques, such as Proper Orthogonal Decomposition (POD) and Reduced Basis (RB) (Rozza et al., 2008; Hesthaven et al., 2016). The aim of a computational reduction technique is to retain the governing dynamics of a system in rapid and reliable way (Rozza et al., 2009; Manzoni et al., 2012). The main assumption of ROM is that the behaviour of the system with respect to a parameter (physical, geometrical) or the time can be represented by a small number of dominant modes. In this way, the system evolution is compared by a reduced set of Ordinary Differential Equations (ODEs). The latter can be employed, for instance, as the basis for the synthesis and the verification of controllers (Barbagallo et al., 2011). A suitable computational offline/online procedure is usually employed in order to efficiently decouple the generation of the basis (made only once – offline phase), which involves the resolution of a Full Order Model (FOM), and the simulation of the reduced order model that can be run many times as required (online phase).

The subject of the thesis is the improvement of the control-oriented modelling by means of reduced order methods. Though the focus is kept more on the modelling aspects rather than control ones, this effort is a necessary step in the progress of the current approach employed in the control system design. The high accuracy guaranteed by the adoption of reduced order models allows solving some control issues related to modelling aspects, in particular the spatial ones, which otherwise could not be managed by means of the classic control-oriented approach.

Reduced order modelling approach

Reduced-order modelling (also model order reduction or reduced order methods) is a generic expression to identify any approach aimed at replacing a high-fidelity problem, i.e., the Full Order Model (FOM), by one featuring a much lower computational complexity, i.e, the reduced order model (Quarteroni et al., 2016 – Figure 2).

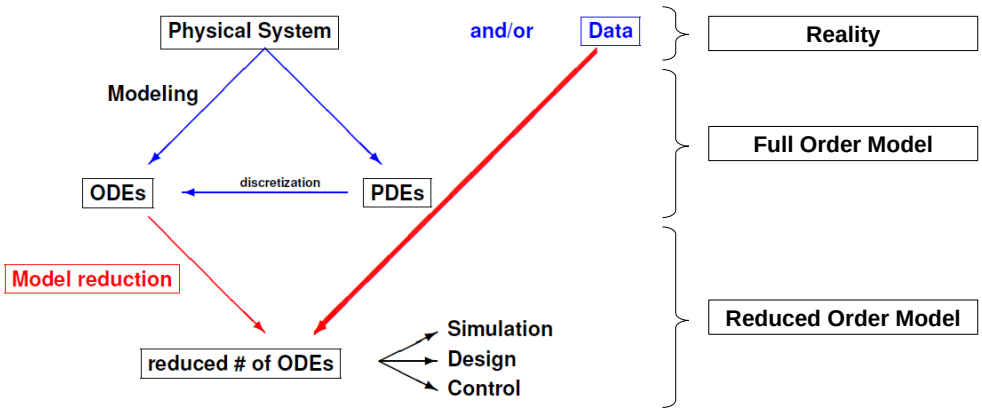

Figure 2. Scheme of the reduced order modelling approach underling the several phases (courtesy of Antoulas, 2010).

As said, the purpose of a computational reduction technique is to retain the governing dynamics of a system in a rapid and reliable way. In particular, the reduced order modelling is aimed at approximating a Partial Differential Equation (PDE) solution (or a set of Ordinary Differential Equations (ODEs)) with a reduced number of degrees of freedom. The common procedure is to solve the full-order problem only for a properly selected number of instances of the input parameter (through a demanding Offline computational step), in order to be able to perform many low-cost real-time simulations (inexpensive Online computational step) for new instances of the parameter (Manzoni et al., 2012).

One of the main challenge of the reduced order modelling is to find the desired compromise between accuracy and the size of the model, i.e., the computational cost (Quarteroni et al., 2011 – Figure 3). It is worthwhile to remind that reduced order modelling do not replace high-fidelity discretization technique but they are linked in a kind of algorithmic collaboration since the reduced order model are usually built upon and compared (as regards accuracy) to the FOM.

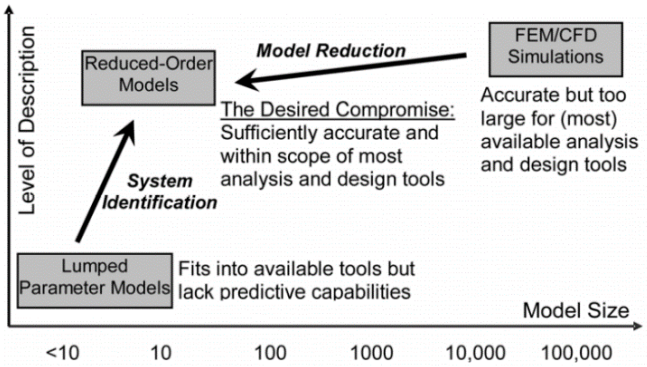

Figure 3. Scheme of the reduced order modelling approach underling the compromise between the level of accuracy and the model size (courtesy of Shapiro, 2003).

There are two main paradigms usually adopted in the reduced order modelling, mainly based on projection or interpolation (Manzoni et al., 2012). To the first family belongs all the *Computational Reduction Techniques* (CRT), which aim at reducing the dimension of the algebraic system through the projection onto a small subspace made by global basis functions. On the other hand, the *Surrogate Response Surfaces* (SRS) family provides an approximation of the dynamics of the system by fitting a set of data obtained through numerical simulations. The main difference between the two approaches is that the CRT are problem-dependent methods whereas the SRS are problem-transparent. This means that in the first approach the reduced order model is built upon physical modelling, which can be more reliable in situations far from which the reduced order model has been developed. In this thesis, considering the control-oriented purpose applied to an innovative nuclear system for which there is no operational experience, the focus is kept on the CRT approach rather than the SRS one.

The most common CRT options are the Proper Orthogonal Decomposition (POD) and the Reduced Basis (RB) methods (Rozza et al., 2008; Chinesta et al., 2015). They seek for a reduced solution through a projection onto suitable low dimensional subspaces. In particular, the essential components of a CRT can be summarized as follows (Manzoni et al., 2012):

- a high-fidelity discretization technique aimed at calculating some high-fidelity PDE solutions (called snapshots) which are needed to build the reduced basis.
- a (Galerkin) projection. The reduced solution is usually expressed as a linear combination of the basis functions. The coefficients of this combination are calculated by means of Galerkin-like projection of the equations onto the reduced space.
- an offline/online procedures. The expensive computation of the snapshot and the basis calculation can be performed just once (offline phase) and totally decoupled from the fast-running ROM simulation.
- an error estimation procedure both to assess the accuracy of the ROM and to construct a reliable, certified, and suited reduced basis[1].

In Table 1, the model reduction approaches and the method for the basis function calculation used in this Ph.D. thesis are listed.

Table 1. Model reduction approaches and the method for the basis function calculation used in this Ph.D. thesis.

	General approach	Basis function calculation	References
Neutronics	Modal Method	Eigenvalue calculation	(Stacey, 1969)
	POD	Singular Value Decomposition	(Holmes et al., 1996; Sirovich, 1987; Volkwein, 1999)
Thermal-hydraulics		Correlation Matrix	

[1] The development of an error estimation procedure is out of the scope of this thesis.

Objective and outline of the thesis

This Ph.D. thesis seeks to improve the control-oriented modelling of Generation IV Lead-cooled Fast Reactors (LFRs) (GIF, 2013) through the development of reduced order methods. In this thesis, the reference reactor is ALFRED (Advanced Lead Fast Reactor European Demonstrator) (Alemberti et al., 2013b), a pool-type reactor whose conceptual design has been developed within the Euratom LEADER Project (htp://www.leader-fp7.eu, 2012, for further details on the reactor design, please refer to Appendix A.1), even if the proposed approach and modelling techniques can be applied to any reactor concept. The reduced order models are aimed at being assessed and implemented in an Object-Oriented simulator developed with the Modelica language (The Modelica association, 2014), in the Dymola environment (DYMOLA, 2015). In particular, the attention is focused on the component (object) representing the neutronics and the component (object) representing the reactor pool of the reactor. The rest of the plant simulator will be not affected by the implementation of the ROM-based components.

Throughout the thesis, a special attention is paid to the modelling aspects, highlighting the differences between the approaches and the assumptions (e.g., the choice of the spatial basis). The results point out both the accuracy of the proposed models (with respect to high fidelity outcomes) as well as the reduced computational times. Whether possible, a benchmark or test case is set up in order to evaluate the approach in simple or well-known conditions. Finally, the object-oriented component retrieved from the reduced order model is described. In Figure 4, the outline of the Ph.D. thesis is depicted.

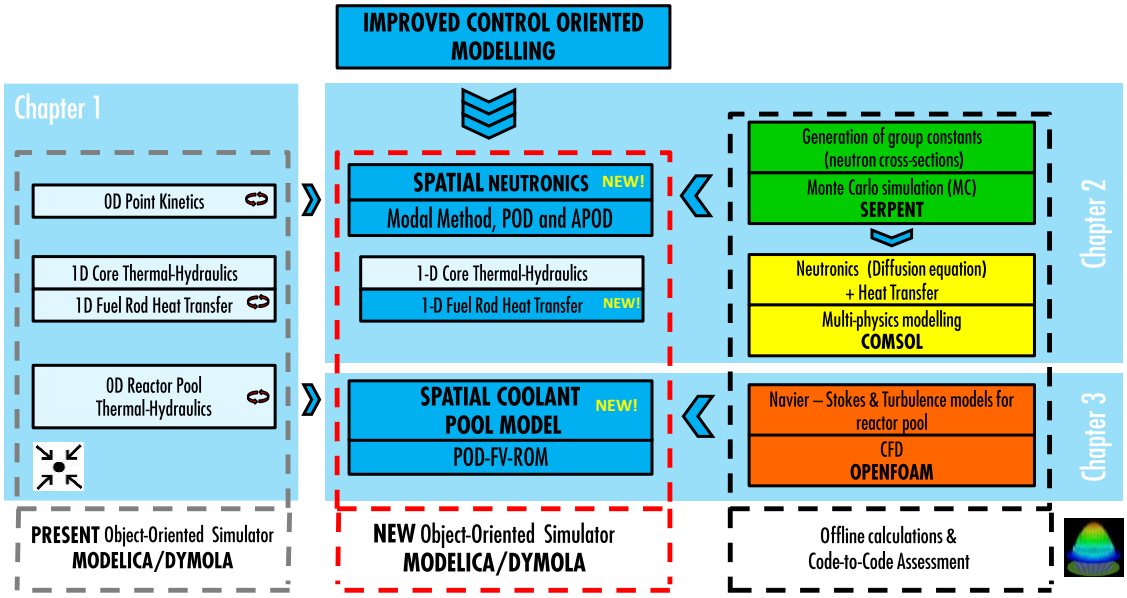

Figure 4. Outline of the Ph.D. thesis.

In Chapter 1, the review of the state of the art concerning the control-oriented modelling of LFR systems and the related PID-based control scheme developed at PoliMi – Nuclear Reactor

Group (NRG) is presented[2]. This part is meant to provide an insight into the current approach of the control-oriented modelling, and its impact on the control scheme design as well. In this way, the reader can appreciate the weak points of the zero-dimensional modelling of some relevant physics and the need to improve these models with ROM-based components ensuring a high level of accuracy without increasing the computational burden. Improved modelling tools will allow developing innovative control techniques, which require not only integral information but also spatial data.

In Chapter 2, the development of a spatial neutronics model for the reactor core is described. This approach is meant to replace the Point Kinetics currently used in control-oriented simulators. Such simple approach may prevent the use of advanced techniques made available thanks to the significant developments of digital Instrumentation & Control (I&C) technology in recent decades. On the other hand, this modelling improvement may allow adopting innovative control strategies, whose feasibility in the nuclear field cannot be adequately studied with a zero-dimensional model. The focus of this Chapter is more applicative than methodological since a theoretical background is already present in literature (Stacey, 1969). Notwithstanding, some new insights from the methodological point of view are addressed.

In Chapter 3, the development of a spatial model of the reactor pool is described. This approach is directed to overcome the 0D/1D modelling usually employed in control-oriented models for the fluid dynamics. In particular, this kind of approach allows the simulation tool to take into account the spatial features of the fluid flow, which can be relevant for certain reactor systems. The focus of this Chapter, differently from the previous one, is more methodological than applicative since no previous theoretical background is present in literature. Notwithstanding, an application has been developed even if it is not intended to be the definitive one.

[2] The simulator was developed in the framework of the LEADER Project as part of the Ph.D. work of Roberto Ponciroli (2014) and of the research assistant activity of the author.

Chapter 1

State of the art of the control-oriented modelling

In this Chapter, the state of the art concerning the control-oriented modelling of LFR systems and the related PID-based control scheme developed at PoliMi – Nuclear Reactor Group (NRG) is presented. This introduction is meant to provide an insight into the current approach of the control-oriented modelling and its impact on the control scheme design as well. In this way, the reader can appreciate the weak points of the zero-dimensional modelling of some relevant physics and the need to improve these models with ROM-based components ensuring a high level of accuracy without increasing the computational burden. Improved modelling tools will allow developing innovative control techniques, which require not only integral information but also spatial data.

In the development of nuclear reactor control design, a relevant role plays the plant simulator whose purpose is to obtain detailed information on the dynamic behaviour and to help the control system implementation for both its realization and its validation (Section 1.1). During the LEADER Project, a dynamic simulator of the ALFRED reactor was realized by adopting the Modelica object-oriented language in the Dymola software environment (Section 1.2). The object-oriented approach was selected among the modelling options due to its features in terms of hierarchical structure, abstraction and encapsulation, which allow developing a model that satisfies the requirements of modularity, openness and efficiency. The primary and secondary systems are modelled and implemented in Modelica by assembling conventional component models and specifically developed nuclear component models. Starting from the outcomes made available by the simulator and thanks to the possibility to easily linearize the object-oriented model, a decentralized control scheme was investigated based on SISO PID controller (Section 1.3).

The main results of this Chapter have been published in:

- Ponciroli, R., Bigoni, A., Cammi, A., Lorenzi, S., Luzzi, L., 2014a. Object-oriented modelling and simulation for the ALFRED dynamics. *Progress in Nuclear Energy*, **71**, 15–29.
- Ponciroli, R., Cammi, A., Lorenzi, S., Luzzi, L., 2014b. A preliminary approach to the ALFRED reactor control strategy. *Progress in Nuclear Energy*, **73**, 113–128.

1.1 Introduction

The definition of the control strategy for a nuclear reactor is a multi-phase and multidisciplinary process whose final result is the implementation of dedicated controllers (Figure 1.1). During the development of nuclear reactor control design, a relevant role is played by the plant simulator whose purpose is: (*i*) to obtain detailed information on the dynamic behaviour; and (*ii*) to help the control system implementation for both its realization and its validation. In particular, due to the innovative features of the LFR reactor concept, some analyses should be performed to properly characterize the system governing dynamics. For instance, it is necessary to prove the intrinsic system stability and to assess the control system robustness at different operational conditions. Several aspects (e.g., the investigation of the reactor dynamics, the study of the interactions among input and output variables, the verification of the effectiveness and feasibility of the control strategy,…) are usually studied thanks to a plant simulator specifically developed for control purposes. Different from a system code for safety study, a simulation tool for control purposes has to fulfill some typical requirements. In particular, fast-running simulations, a comprehensive representation of the entire plant behaviour, and the possibility to couple the plant dynamics simulator with the control system model are the main requests.

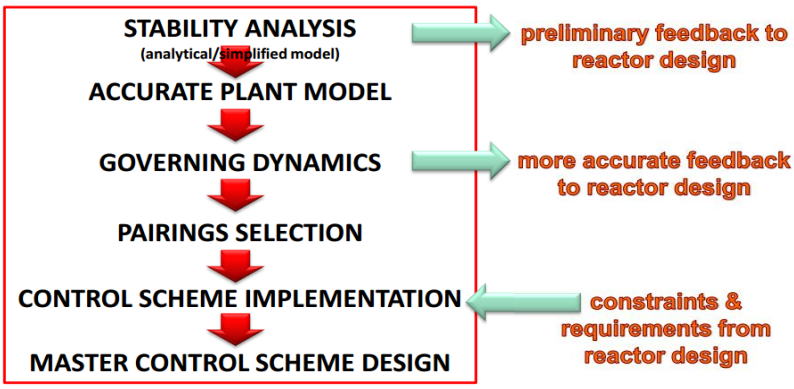

Figure 1.1. Schematic view of the control strategy procedure.

In order to accomplish these goals, among the several modelling options, the Object-Oriented approach constitutes a suitable choice for the model-based control design since its features in terms of hierarchical structure, abstraction and encapsulation allow developing a model that satisfies the requirements of modularity, openness and efficiency (Fritzson, 2004). A viable path to achieve the above-mentioned goals is constituted by the adoption of the Modelica language (The Modelica Association, 2014). Introduced in 1997, Modelica is "a language for modelling and simulation of complex cyber-physical systems" (Fritzson, 2004). In particular, it is an object-oriented modelling approach specifically designed for the study of engineering system dynamics. In this perspective, Modelica facilitates the system description in terms of physical and engineering principles (i.e., mass, energy and momentum balance equations). Modelica is employed for the modelling of general physical phenomena described by sets of differential algebraic and discrete equations, supporting a declarative language. The different components (i.e., objects described by equations) are connected through rigorously defined interfaces corresponding to the physical interactions occurring with the external environment or other

objects. These features allow acausal modelling, i.e., the direct use of equations without imposing the classic input/output declaration, enabling a more flexible and efficient data flow (Fritzson, 2011). Finally, Modelica is open-source and it has already been successfully adopted in different fields, such as automotive, robotics, thermo-hydraulic and mechatronic systems, but also in nuclear simulation field (Cammi et al., 2005; Souyri et al., 2006).

One of the main advantages of employing the Modelica language is the possibility of adopting acausal modelling approach. The system dynamics is described in terms of conservation laws that, combined with the constitutive equations of the components, determine the overall set of equations to be solved. Thanks to the acausal modelling, the equations of each component model can be written independently from the definitions of input/output variables. Thus, the causality of equation-based models is unspecified and becomes fixed only when the corresponding equation systems have to be solved (Fritzson, 2004). In this way, models are much easier to write and reuse, while the burden of determining the actual sequence of computations required for the simulation is entirely left to the compiler. In the common practice, most of the present simulators are based on causal modelling, e.g., MATLAB® and SIMULINK® (The MathWorks, 2015), whose main features are reported in Table 1.1.

Table 1.1. Main features and differences between causal and acausal approach.

Causal approach	Acausal approach
System input and output variables have to be established at the beginning	It is not necessary to establish *a priori* input and output variables
Equations have to be rewritten for each specific application in state space representation	Causality remains unspecified as long as equations are solved
Low flexibility in changing the model configuration	More realistic description of components and modularity
Low reusability of previous work. Problem formulation in a series of operations must be performed by the user, according to the particular applicative context	Possibility of easily reusing previously developed models. Models of components are defined independently of their potential connections
Block diagram representation (physics-oriented)	Plant representation (component-oriented)
Integration algorithm for ordinary differential equations (lower computational cost)	Integration algorithm for differential algebraic equations (higher computational cost)
Low order modelling, easy to linearize (stability analyses)	Potentially high number of equations involved

In addition, the multi-physics approach of the Modelica language must be mentioned. General in scope, it provides modelling primitives such as generic algebraic, differential and difference equations, and it is not tied to any specific physical or engineering domain (i.e., mechanics, electrical engineering, or thermodynamics). Thus, it is quite straightforward to describe multi-disciplinary systems, e.g. the reactor core, where several physics (e.g., neutronics, heat transfer and fluid dynamics) interact with each other. Furthermore, a more realistic plant representation is made possible by the component-based description. As simulation environment, Dymola (Dynamic Modelling Laboratory) (Elmqvist et al., 1993) has been adopted, as dedicated libraries of validated models for power plant components are available. As to the efficiency of the simulation code, Modelica compilers incorporate sophisticated symbolic manipulation algorithms, which allow obtaining index-1 systems of Differential Algebraic Equations (DAEs) from higher-index ones, to symbolically solve both linear and nonlinear model equations

(Fritzson, 2004). The resulting code is then linked to state-of-the-art numerical integration codes such as DASSL (Brenan et al., 1989).

In the past years, a dynamic simulator of the ALFRED reactor (Ponciroli et al., 2014a) was realized in the framework of the LEADER Project by adopting the Modelica object-oriented language in the Dymola software environment (DYMOLA, 2015). The resulting overall plant simulator consists of the following essential parts: core, steam generator, primary and secondary pumps, cold and hot legs, cold pool, turbine, and condenser. In particular, point reactor kinetics and one-dimensional heat transfer models are implemented for the core. The coolant hot and cold pool models are represented by a component describing a free-surface lead tank on which mass and energy balances are taken (0D approach). Starting from the outcomes made available by the simulator and thanks to the possibility to easily linearize the object-oriented model, a decentralized control scheme was investigated based on SISO PID controller (Ponciroli et al., 2014b, Ponciroli et al., 2015a). Moreover, thanks to the simulator, a model-based assessment of the reactor startup and the load-following capabilities of the ALFRED reactor was carried out (Ponciroli et al., 2015b, Ponciroli et al., 2015c).

As pointed out in the Introduction, the practical application of this thesis is the improvement of the mentioned object-oriented simulator, i.e., substituting some components based on zero-dimensional approach with ROM-based components ensuring a high level of accuracy without increasing the computational burden. In order to provide an insight into the object-oriented modelling employed in the simulator, the description of the main component models is presented in Section 1.2. An example of control scheme based on the simulator is described in Section 1.3. A few concluding remarks are drawn in Section 1.4.

1.2. Object-oriented model of the ALFRED reactor

In this section, the non-linear one-dimensional object-oriented model of the ALFRED reactor developed by means of the Modelica language is presented. The overall system model was built by connecting the different components (objects) through rigorously defined interfaces (connectors) corresponding to specific physical interactions occurring with the external environment or other objects. The overall plant simulator, incorporating also the BoP, consists of the following essential parts: core, steam generator, primary and secondary pumps, cold and hot legs, cold pool, turbine, and condenser (Figure 1.2). The primary and secondary systems were modelled and implemented in Modelica by assembling conventional component models already available in a specific thermal-hydraulic library, named Thermopower (Casella et al., 2006), and specifically developed nuclear component models, taken from the NuKomp library (Cammi et al., 2005), modified in order to provide the required capabilities for the analysis.

1.2.1. Core

As far as the ALFRED core is concerned (Figure 1.3), point reactor kinetics and one-dimensional heat transfer models are implemented, coherently with the plant specifications, by incorporating suitable geometry, material properties and correlations, neutronic feedback coefficients and kinetic parameters (see Appendix A.1).

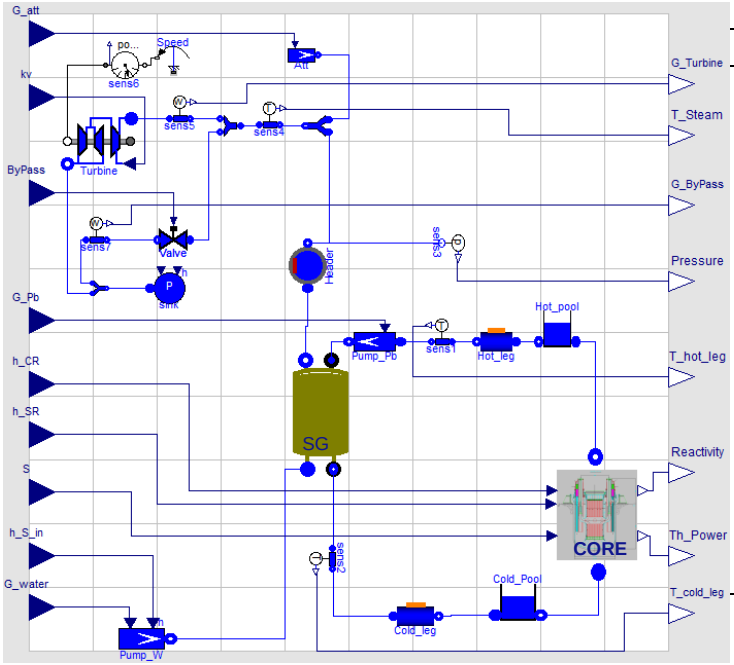

Component	Description
Core	Reactor core
Cold_pool	Pool collecting the lead coming from the SG outlet
Cold_leg	Collector between the SG outlet and the core inlet
Hot_pool	Pool collecting the lead coming from the core outlet
Hot_leg	Collector between the core outlet and the SG inlet
sens	Temperature and pressure sensor placed in the plant
Pump_Pb	Lead axial pump
SG	Steam generator
Header	Volume collecting the produced steam
Pump_W	Water pump
Turbine	Steam turbine unit
Sink	Condenser
Att	Attemperator that regulates the steam temperature

Figure 1.2. ALFRED object-oriented model.

The component-based core model is constituted by four sub-systems, each one dedicated to a particular physics. The component *Kinetics* employs a point reactor kinetics model with one neutron energy group and eight delayed precursor groups. Therefore, the neutron density evolution is described by the following equation:

$$\frac{dn}{dt} = \frac{\rho - \beta}{\Lambda} n + \sum_{i=1}^{8} \lambda_i c_i + q \tag{1.1}$$

and the corresponding concentration of precursors being expressed as:

$$\frac{dc_i}{dt} = \frac{\beta_i}{\Lambda} n - \lambda_i c_i \qquad i = 1, \dots, 8 \tag{1.2}$$

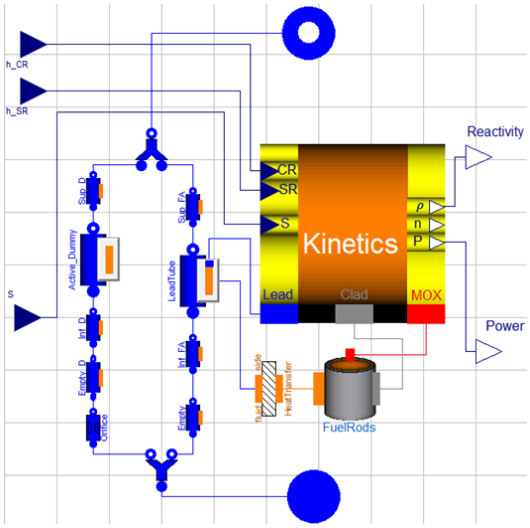

Figure 1.3. ALFRED core object-oriented model.

In the model, two different definitions are implemented to describe the effective fuel temperatures, and namely: ${T_f}^D$, which expresses the effective temperature to allow for the Doppler effect, and ${T_f}^{eff}$, which represents the average temperature that allows to evaluate quantitatively the reactivity feedback due to the pellet deformation caused by thermal stresses. Therefore, as far as the Doppler reactivity contribution is concerned, an effective fuel temperature allowing for resonances broadening (Kozlowski and Downar, 2007) is considered:

$$ {T_f}^D = 0.3 \cdot {T_f}^1 + 0.7 \cdot {T_f}^3 \tag{1.3} $$

In Equation (1.3), ${T_f}^1$ and ${T_f}^3$ represent the average temperatures in the central region and in the external one of the fuel pin, respectively (see Figure 1.4). In Equation (1.4) the weights provide an estimate of the volume-weighted average behaviour, and are used to reproduce the parabolic trend of the temperature field within the fuel pellets:

$$ T_f^{eff} = (1/2) \cdot {T_f}^1 + (1/2) \cdot {T_f}^3 \tag{1.4} $$

The reactivity variation from a generic fuel temperature distribution T_{f1} (with effective average ${T_{f1}}^D$) to a fuel temperature distribution T_{f2} (with effective average ${T_{f2}}^D$), due to the Doppler effect, is evaluated as follows (Waltar et al., 2012):

$$ \Delta\rho \left[T_{f1} \rightarrow T_{f2}\right] \approx 1.1 \cdot K_D \left(ln \frac{{T_{f2}}^D}{{T_{f1}}^D} \right) \tag{1.5} $$

Reactivity effects due to the coolant density variations, as well as to the axial and radial expansions, are taken into account by adopting linear equations with constant coefficients. In particular, axial and radial cladding expansions are related to the average cladding thermal conditions, while axial and radial wrapper expansions are considered governed by the lead temperature. On the other hand, the grid expansion effect concerns the increase of the core radius due to the incoming coolant temperature enhancement. Therefore, the coolant volume inside core increases as well as the core volume and, in turn, the leakages. These combined effects determine an overall negative contribution. The pad effect is determined by the radial expansion difference between the bottom of the subassemblies at the incoming coolant temperature and their top at the outlet coolant temperature. However, this reactivity contribution is quite reduced (Grasso et al., 2014).

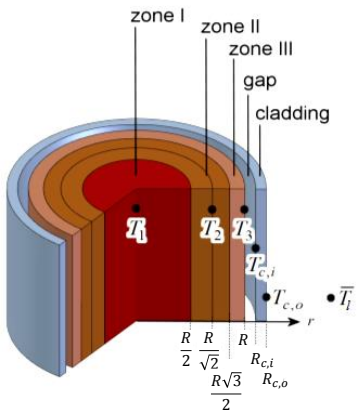

Figure 1.4. Fuel pin radial scheme for heat transfer modelling.

As far as the CRs are concerned, a reactivity differential curve is adopted based on the reactivity worth of the 12 rods at different insertion lengths (Figure 1.5).

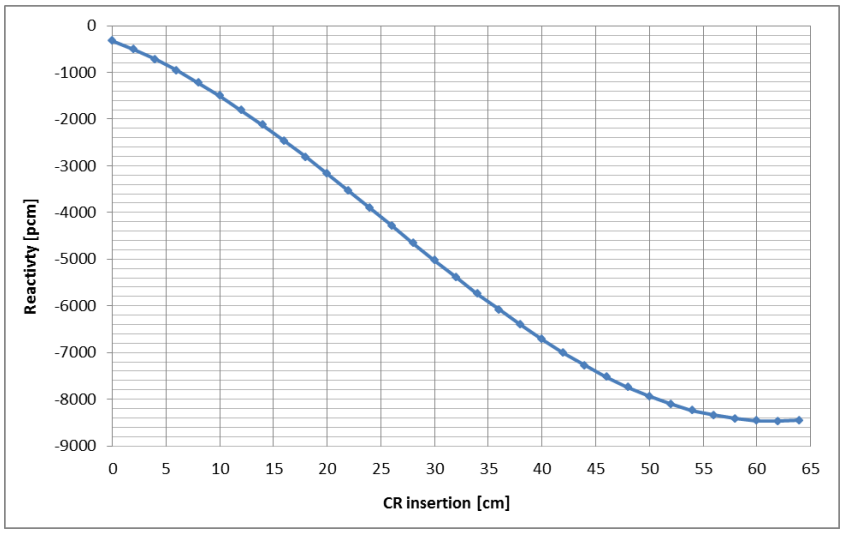

Figure 1.5. Calibration curve of control rods and safety rods.

On the other hand, the worth characterization of SRs does not require such an accuracy, because these rods are extracted during start-up phase and then they are kept out of the core while the reactor is operating at full power conditions. Consequently, a linear dependence of the reactivity as function of axial position is sufficient to describe the SR reactivity contribution.

The overall system reactivity is given by the sum of the various contributes, as follows:

$$\rho(t) = \alpha_L \cdot (T_l - T_{l,0}) + 1.1 \cdot K_D \left(ln \frac{{T_f}^D}{{T_{f,0}}^D} \right) + \alpha_{CZ} \cdot (T_c - T_{c,0}) + \alpha_{WZ} \cdot (T_l - T_{l,0})$$
$$+ \alpha_{CR} \cdot (T_c - T_{c,0}) + \alpha_{WR} \cdot (T_l - T_{l,0}) + \alpha_{FZ} \cdot (T_c - T_{c,0}) + \alpha_{Dia} \cdot (T_{l,in} - T_{l,in,0}) + \tag{1.6}$$
$$A_{CR} \cdot sen(B_{CR} \cdot h_{CR} + C_{CR}) + D_{CR} + A_{SR} \cdot \frac{(h_{SR} - x_{SR})}{L_{SR}} + \rho_0$$

The terms in Equation (1.6) represent the effect due to lead density, Doppler effect, axial cladding expansion, axial wrapper expansion, radial cladding expansion, radial wrapper expansion, axial fuel expansion, diagrid expansion, control rod contribution, safety rod contribution, and the initial reactivity margin, respectively.

The component *FuelRods* describes the thermal behaviour of the fuel pins by adopting five radial regions within the element (i.e., cladding, gaseous gap and three concentric zones of equal volume within the pellet). The time-dependent Fourier equation is applied considering only the radial heat transfer, thus disregarding both the axial and the circumferential thermal diffusion. Fourier equation is discretized radially in five zones and longitudinally in a user-defined number (*N*) of nodes.

$$d_f c_f \frac{\partial T_f}{\partial t} = \frac{1}{r} \frac{\partial}{\partial r} \left(r k_f \frac{\partial T_f}{\partial r} \right) + q''' \tag{1.7}$$

$$\frac{\partial}{\partial r} \left(r k_g \frac{\partial T_g}{\partial r} \right) = 0 \tag{1.8}$$

$$d_c c_c \frac{\partial T_c}{\partial t} = \frac{1}{r}\frac{\partial}{\partial r}\left(r k_c \frac{\partial T_c}{\partial r}\right) \tag{1.9}$$

The component *LeadTube* models the coolant flowing through the core channels represented as cylindrical conduits. It simulates a one-dimensional single-phase fluid flow with heat transfer from the fuel pin boundary and with temperature-dependent physical properties (OECD-NEA, 2007). This approach is based on distributed-parameter mass, momentum and energy conservation equations discretized by employing a finite volume method.

$$A\frac{\partial d}{\partial t} + \frac{\partial w}{\partial x} = 0 \tag{1.10}$$

$$\frac{\partial w}{\partial t} + A\frac{\partial p}{\partial x} + dgA\frac{\partial z}{\partial x} + \frac{C_f \omega}{2dA^2} w|w| = 0 \tag{1.11}$$

$$dA\frac{\partial h}{\partial t} + dAu\frac{\partial h}{\partial x} - A\frac{\partial p}{\partial t} = \omega\varphi \tag{1.12}$$

Equations (1.10) and (1.11) describe the pressure and mass flow rate dynamics, while Equation (1.12) describes the slower dynamics of heat transport with the fluid velocity.

The component *HeatTransfer* allows evaluating the heat flux exchanged between two one-dimensional interacting objects (e.g., the fluid flow and metal wall) as a function of the corresponding surface temperatures. Since the fuel pins are arranged on a triangular lattice, the Ibragimov-Subbotin-Ushakov correlation (Cheng and Tak, 2006) is adopted to properly estimate the convective heat transfer coefficient. Moreover, among the possible correlations, it is the most conservative one since gives the lowest value of the Nusselt number.

$$Nu = 4.5 + 0.014 \cdot Pe^{0.8} \tag{1.13}$$

In the ALFRED core, the presence of a *bypass mass flow rate* is foreseen since it has a fundamental role in certain plant operational modes, such as the start-up phase. In the proposed configuration, the main part of the coolant passes through the fuel elements, while a reduced fraction passes through the interstices between the wrappers, and through the dummy elements and the cases of the CRs and the SRs. Indeed, the power is deposited not only in the fuel, but also in the other materials, mainly due to the γ emission. For these reasons, the lead mass flow rate devoted to the bypass is fixed at the 3% of the one that circulates in the primary circuit. In a preliminary description, in order to represent the evolution of the temperature fields of the main components of the core, the presence of the bypass mass flow rate can be neglected. This approach can be suitable if the system is studied only in nominal operating conditions. Nevertheless, in accidental scenarios or in operating conditions in which the lead mass flow rate is not kept constant at the nominal value (e.g., during the reactor start-up), a more accurate characterization of the pressure field is essential. In particular, in the core thermal-hydraulics description, two types of channels, which represent the fuel elements and the dummy elements, were allowed for.

In the modelling of the channels, in order to reproduce the actual layout of the assemblies (Figure 1.6), different types of components (Figure 1.7) are employed. Furthermore, a component that allows imposing additional pressure losses is added to the dummy elements description. Since the channels are subjected to the same inlet and the outlet pressure field, hydraulic resistance at the entrance of dummy elements is suitably tuned to achieve the desired pressure field.

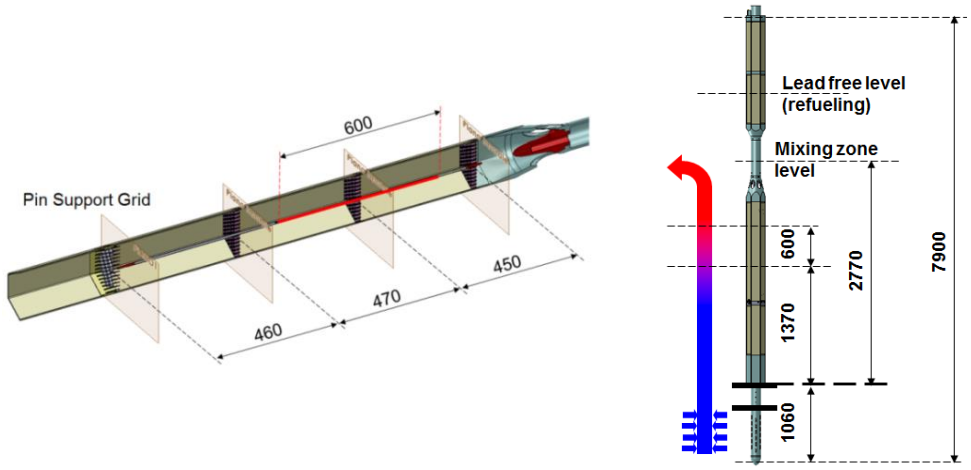

Figure 1.6. Fuel assembly geometry (lengths are expressed in mm).

As for the distributed losses within the coolant channels, they are preliminarily estimated adopting the McAdams correlation (Todreas and Kazimi, 2012) for the Fanning friction factor. On the other hand, the modelling of the form losses is quite difficult since the dimensional specifications concerning the spacers are not assessed yet. At this point, since the total pressure losses are specified in the core design and the distributed ones are evaluated, the contribution of the form losses is obtained representing the influence of the spacers in the core thermal-hydraulics by using the dedicated component Orifice, which allows implementing a suitable hydraulic resistance.

All the several core subsystems are eventually connected. In particular, the mutual influences between neutronics and thermal-hydraulics are taken into account by means of the above-mentioned feedback reactivity coefficients represented in the Modelica language through dedicated connectors. As shown in Figure 1.3, blue, grey and red connectors allow carrying the information about lead, cladding and fuel thermal behaviour in order to consider their influence on the neutronics.

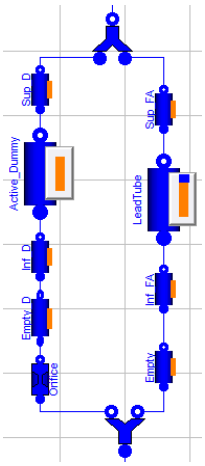

Component	Description
Sup D	Upper region of dummy elements
Active_Dummy	Region of dummy elements corresponding to the active zone of fuel assemblies
Inf D	Lower region of dummy elements
Empty D	Empty region of dummy elements
Orifice	Form pressure drop which allow to achieve the real pressure field
Sup FA	Upper region of fuel assemblies
LeadTube	Active region of fuel assemblies
Inf FA	Lower region of fuel assemblies
Empty	Empty region of fuel assemblies

Figure 1.7. Detailed view of ALFRED core: representation of coolant channels.

1.2.2. Hot and cold pool

The coolant hot and cold pool models (named *Hot_pool* and *Cold_pool*) are implemented by employing a component describing a free-surface cylindrical lead tank (responsible for most of the large thermal inertia characterizing the overall system), on which mass and energy balances are taken, assuming that no heat transfer occurs, except through the inlet and outlet boundaries.

1.2.3. Hot and cold legs

In order to represent transport phenomena, simple one-phase *LeadTube* components are employed (named *Hot_leg* and *Cold_leg*). One-dimensional flow models are implemented, neglecting thermal dispersion, to properly consider the time delays due to transport phenomena between the core and the SG, and between the SG and the cold pool.

1.2.4. Pumps

As far as the primary and secondary pumps are concerned, ideal flow rate regulators are employed.

1.2.5. Steam generator

Due to its non-conventional bayonet-tube design, an effort is spent to set up a specific component representing the ALFRED SG (Figure 1.8). A simplified description is adopted, based on a one-dimensional description of the actual geometry, which is reproduced by means of different tube models connected together. In this way, the advantage of reusability of the Modelica models is exploited. Indeed, the same tube, based on a certain set of equations, can be employed in different contexts and then extended through *inheritance* by adding further equations. After entering the SG, water flows down in the slave tube (see Appendix A.1) and there is no heat exchange neither thermal dispersion, thanks to the effective insulation provided. Thus, water conditions at the SG inlet and at the bottom of the tube are the same. For this reason, this first part is neglected and the feedwater is simulated to flow directly in a counter-current configuration, exchanging thermal power with the external lead. The component geometry is substituted with concentric tube bundles in a counter-current flow configuration where the pressure drops are concentrated at the bayonet bottom (i.e., where the fluid flow reverses). A turbulent, lumped pressure drop model is assumed, proportional to the kinetic pressure.

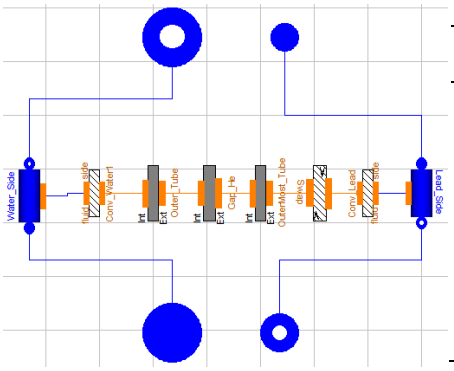

Component	Description
Water_Side	Tube model that describes the water flowing.
Conv_Water	Component that describes the convective heat transfer on water side.
Outer_tube, Gap_He, Outermost_tube	Components that allows for the conduction phenomena within the different interfaces.
Swap	Component that allows to reproduce the counter-current configuration.
Conv_Lead	Component that describes the convective heat transfer on lead side.
Lead_Side	Tube model that describes the lead flowing.

Figure 1.8. ALFRED SG object-oriented model.

As far as the water side is concerned, a tube allowing to describe a two-phase fluid is selected, adopting averaged densities in the neighbourhood of phase changes so as to avoid non-physical

simulation artefacts due to phase change discontinuities at the model nodes. A two-phase homogeneous model (i.e., with the same velocity for the liquid and vapour phases) is adopted. Water-side convective heat transfer coefficients are evaluated by implementing the Dittus-Boelter correlation for one-phase regions, and the Kandlikar correlation for the boiling region (Todreas and Kazimi, 2012). According to the latter correlation, the two-phase heat transfer coefficient, h_{TP}, is equal to the larger of $h_{TP,NBD}$ and $h_{TP,CBD}$, i.e., the two-phase heat transfer coefficients in the nucleate boiling dominant and convective boiling dominant regions, respectively. These coefficients are given by the following equations:

$$h_{TP,NBD} = 0.6683Co^{-0.2}(1-x_v)^{0.8}f(Fr_{LO})h_{LO} + 1058.0Bo^{0.7}(1-x_v)^{0.8}F_{Fl}h_{LO} \tag{1.14}$$

$$h_{TP,CBD} = 1.136Co^{-0.2}(1-x_v)^{0.8}f(Fr_{LO})h_{LO} + 667.2Bo^{0.7}(1-x_v)^{0.8}F_{Fl}h_{LO} \tag{1.15}$$

where

$$Co = \left(\frac{d_L}{d_v}\right)^{0.5}\left(\frac{1-x_v}{x_v}\right)^{0.8} \tag{1.16}$$

$$Bo = \frac{q''}{w \cdot i_{LG}} \tag{1.17}$$

are the convection and boiling numbers, respectively. F_{Fl} is the fluid-surface parameter that incorporates the effect of surface and fluid properties, and allows to take into account differences in nucleating characteristics. h_{LO} is the single-phase heat transfer coefficient with all flow as liquid. The function $f(Fr_{LO})$ is a Froude number with all flow as liquid. This parameter addresses the stratified flow region.

On the lead side, the component describing the behaviour of a single-phase fluid, previously used for the core model, is adopted. Convective heat transfer coefficients are evaluated by implementing the Ibragimov-Subbotin-Ushakov correlation as well. The multiple wall interfaces are modelled by adopting different conductive-exchange elements, in which thermal resistance is computed according to the formulation of Fourier equation in cylindrical coordinates, while the heat capacity is lumped in the middle of the tube thickness. Dedicated components are implemented to represent each interface constitutive layer (i.e., insulating layer, outer tube, helium gap, outermost tube). Besides, the *HeatTransfer* component is used to evaluate the convective heat exchange on both water and lead sides, a *Swap* component is adopted to allow for the counter-current configuration. In this way, temperature and flux vectors on one side are swapped with respect to the ones on the other side. Furthermore, only one SG with a suitably rescaled number of tubes guaranteeing a thermal power of 300 MW_{th} (instead of the actual eight 37.5 MW_{th} SGs) is considered.

1.2.6. Outlet header

The steam coming out from the SG is suitably collected in a *header*, i.e., a well-mixed chamber having no pressure drop and no energy exchange with the environment that allows dampening any pressure transient, limiting the impact on the conditions of the steam that flows into the turbine.

1.2.7. Attemperator

An attemperator is foreseen between the outlet header and turbine, i.e., a reduced water mass flow rate at saturation conditions that is added to the steam flow. In this way, it is possible to

promptly limit the steam temperature at the turbine inlet keeping this variable of interest as close as possible to its nominal value (450°C).

1.2.8. Turbine unit

Particular attention is paid to this component, which is fundamental to properly take into account the electrical power provided to the grid, and constitutes a crucial parameter in a control perspective. The component selected for the turbine model describes a simplified steam turbine unit in which a fraction of the available enthalpy drop is disposed by the High Pressure (HP) stage, whereas the remaining part by the Low Pressure (LP) one, with different time constants. A valve governs the overheated steam mass flow rate passing through the turbine. By adopting a simplified approach, choke flow conditions are imposed. If the ratio of upstream pressure to downstream pressure is higher than the critical ratio ($x_c \approx 0.5$), in the section of maximum damping of the fluid vein a sonic shock wave is produced (Dolezal and Varcop, 1970). In this way, the inlet steam mass flow rate does not depend on the downstream pressure, namely:

$$\frac{p_{\text{up}} - p_{\text{down}}}{P_{\text{up}}} > x_c \quad \Longrightarrow \quad w_v = A_v \lambda_c \sqrt{d_v(p) p} \tag{1.18}$$

Given that, it is possible to adopt the following approximation for the superheated steam:

$$d_v(p) p \propto p^2 \tag{1.19}$$

It follows that:

$$w_v \cong k_v p \tag{1.20}$$

Accordingly, the steam mass flow rate is regarded proportional to the inlet pressure and governed by operating the turbine admission valve (system input), not by throttling (i.e., no loss of thermodynamic efficiency occurs).

1.2.9. Bypass

After having passed through the SG, downstream of the temperature sensor, the steam mass flow rate can be subdivided into two ways (Figure 1.9). The former is a pipe that leads to the turbine, whereas the latter constitutes a bypass that directly leads to the condenser.

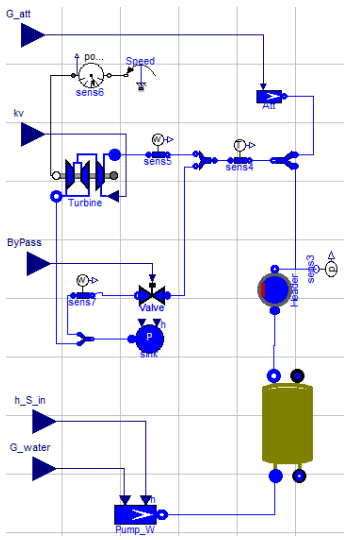

Figure 1.9. ALFRED reactor secondary side.

This "alternative way" performs a very important function in particular operative conditions of the secondary side, when the reactor is operating at very low power levels, such as during the start-up phase. Indeed, when the thermal power from the primary circuit is not sufficient to ensure the steam nominal conditions, the flow is directly disposed to the condenser to avoid jeopardizing the integrity of the turbine, which cannot process an incoming fluid in such conditions. On the other hand, when the power level allows obtaining overheated steam, it is possible to let it flow to the turbine, while the bypass way is progressively closed.

1.2.10 Free dynamics simulations

As for the dynamics simulation, the object-oriented model presented in this Section allows simulating a transient of 2500 s requiring a computational time of less than 30 seconds (2.20 GHz with 8 GB memory), hence turning out to be suitable for control-oriented purposes.

For the sake of brevity, in this thesis only the Unprotected Transient of OverPower (UTOP) simulation, starting from nominal full power steady-state operating conditions, is shown[3]. In particular, an extraction of control rods corresponding to a 20 pcm step reactivity variation (Figure 1.10a) is considered. This is an interesting operational transient to be evaluated since it involves the dynamics associated to the handling of the control rods, and how this kind of perturbation has effect on the rest of the plant. This core-driven simulation determines an immediate feedback to the SG due to the coolant core outlet temperature enhancement. Thanks to the presence of the pool, the action of the SG on the core, consisting in an increase of the coolant core inlet temperature, is delayed and softened.

For the first part of transient, the behaviour of the system is the same as if a stand-alone core simulation were performed. Indeed, after the step-wise insertion of reactivity given by control rods the power suddenly increases exhibiting the typical prompt jump behaviour and, after a small decrease, starts reaching the steady-state (Figure 1.10b). The reactivity insertion in the core affects the SG as a temperature enhancement of the lead coming from the core (Figure 1.10c). As a direct consequence of the improved heat exchange conditions due to the hotter primary fluid, the steam temperature increases (Figure 1.10d). The abrupt change of the steam density determines a perturbation in the SG pressure (Figure 1.10e), which ends when the primary circuit reaches a new equilibrium condition. The higher thermal power level promotes an enhancement of the lead SG outlet temperature (Figure 1.10f). As for the core behaviour, the MOX-based fuel elements, because of the low thermal conductivity, cause a stepwise increase of fuel temperature and, consequently, of the coolant average temperatures (Figure 1.10g-h), after the reactivity insertion. This response produces an immediate feedback on the system due to the Doppler effect and to lead density contribution, which cause an abrupt inversion of the reactivity evolution that quickly gets back to zero.

[3] For the additional free-dynamics simulations, the reader may refer to Ponciroli et al. (2014a).

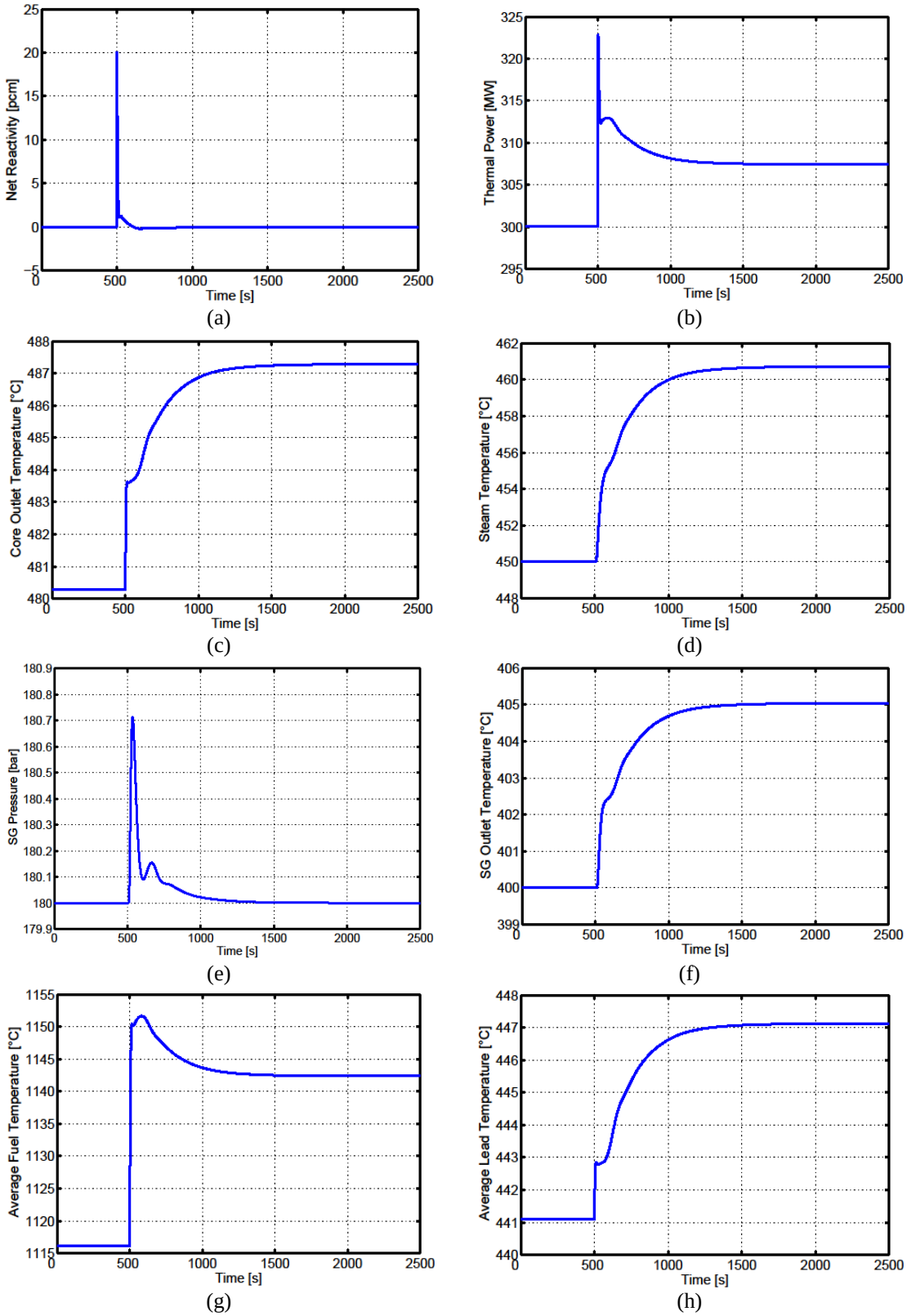

Figure 1.10. Variables evolution after a step reactivity variation: (a) net reactivity variation; (b) core thermal power variation; (c) core outlet temperature variation; (d) steam temperature variation; (e) SG pressure variation; (f) lead SG outlet temperature variation; (g) average fuel temperature variation; (h) average lead temperature variation.

1.3 PID-based control scheme of the ALFRED reactor

In order to give an example of the relevance of the system simulation tool in the development of the control system design, a brief summary of the PID-base control scheme developed for the ALFRED reactor during the LEADER Project is presented in this Section.

In an NPP, the main system output to be controlled is the thermal power produced within the core. As far as the conventional part of the plant is concerned, the other controlled variables are the SG pressure and the steam temperature at the turbine inlet, which should be kept as close as possible to their respective nominal values. As for the ALFRED primary loop, the most constrained output that must be efficiently controlled is the SG outlet lead temperature, called also cold leg temperature which is representative of the temperature of the cold pool. The nominal value of 400 °C represents the optimum working condition for the cold pool. Temperatures below this limit would lead to a degradation of structural steels due to the embrittlement enhanced by neutron irradiation. On the other hand, if the inlet lead temperature rises beyond this value, the reactor vessel may overcome the design limit concerning thermal creep.

One of the major efforts in the development of LFR concept is the design of pumps which operate in the highly aggressive lead environment. In the reactor layout, the coolant is currently envisaged to be driven by an axial pump requiring a constant number of revolutions per minute. Moreover, working at nominal mass flow rate also for power levels lower than the nominal one brings benefits as far as structural materials are concerned since they would operate at reduced temperatures with consequent positive effects on corrosion. Despite these considerations, it may be worthwhile considering the possibility to adopt the lead mass flow rate in the primary loop as a control variable to ensure a more flexible control action on the coolant pool temperature. Accordingly, a control strategy was proposed considering the lead mass flow rate as a possible input variable.

Starting from the outcomes made available by the dynamics simulations and thanks to the possibility to easily linearize the object-oriented model, a decentralized control scheme for the ALFRED reactor was investigated based on SISO PID controllers. To this aim, given that for the LFR systems neither prior experience nor operational data are available, a quantitative well proven investigation tool was adopted in order to choose the pairing between input and output variables (see Table 1.2), i.e. the selection of control and controlled variables, respectively. In particular, the *Relative Gain Array* (RGA) method (Bristol, 1966) and its *Non-square Relative Gain array* (NRG) (Chang and Yu, 1990) variant were considered (for further information about the RGA and NRG methods, the reader may refer to Appendix A.2). These tools allow developing the most efficient control strategy starting from the constitutive equations that describe the physical system taken into account. These methods have been widely used in several industrial fields including chemical processes and power production (Papadourakis et al., 1987), and recently adopted in nuclear applications as well (Guerrieri et al., 2014). In exploiting this technique, the object-oriented model turned out to be of fundamental importance, since it allows applying the RGA method on a reliable model of the system to be studied.

Table 1.2. Possible input and output variables of the ALFRED reactor (see Figure 1.2).

Input variable	Definition	Output variable	Definition
G_att	Attemperator mass flow rate	*G_turbine*	Turbine admitted mass flow rate
h_CR	Control rod height	*T_steam*	Turbine inlet steam temperature
Bypass	Bypass valve coefficient	*G_bypass*	Bypass discharged mass flow rate
S	Neutron source	*Pressure*	SG pressure
kv	Turbine admission valve coefficient	*T_hot_leg*	Temperature of lead flowing out of the core
h_SR	Safety rod height	*Reactivity*	System reactivity
G_Pb	Primary circuit lead mass flow rate	*Th_power*	Thermal power produced within the core
T_feed	Feedwater inlet temperature	*T_cold_leg*	Temperature of lead flowing into the core
G_water	Feedwater mass flow rate		

1.3.1. Control system implementation

In order to develop the control system for the ALFRED reactor, the object-oriented simulator of the entire plant described in Section 1.2 was first employed with the main purpose of studying the system free dynamics to understand the basic relationships between input and output variables. Afterward, the object-oriented model was linearized in the neighbourhood of the nominal power conditions by means of a useful feature of the Dymola simulation environment. As a result of this operation, the resulting model was expressed by adopting the matrix-based form of the Linear Time-Invariant (LTI) systems

$$\begin{cases} \delta\dot{x}(t) = A\delta x(t) + B\delta u(y) \\ \delta y(t) = C\delta x(t) + D\delta u(y) \end{cases} \tag{1.21}$$

A 194th order system was obtained and it was necessary to reduce the system to a more suitable and manageable size. There are several procedures that can be implemented to get a satisfactory order reduction and there are several examples in literature (Moore, 1981; Van Dooren, 2000). Hereafter, the methodology adopted by MATLAB® will be referred, which provides precompiled functions to reduce LTI models. It consists in an appropriate coordinate transformation, which allows obtaining a balanced and equivalent representation, in terms of system state variables, so that observability and reachability Gramians result to be equal and diagonal (Moore, 1981). The balanced model that is obtained is then defined by

$$\begin{cases} \delta\dot{\tilde{x}}(t) = \tilde{A}\delta\tilde{x}(t) + \tilde{B}\delta\tilde{u}(y) \\ \delta\tilde{y}(t) = \tilde{C}\delta\tilde{x}(t) + \tilde{D}\delta\tilde{u}(y) \end{cases} \tag{1.22}$$

where

$$\begin{aligned} \tilde{A} &= T_L^{-1}AT_L \\ \widetilde{B} &= T_L^{-1}B \\ \tilde{C} &= CT_L \\ \widetilde{D} &= D \end{aligned} \tag{1.23}$$

The matrix that realizes the change of coordinates is indicated with T_L and it can be obtained according to the procedure indicated by Laub (Laub et al., 1987). At this point, the order of the balanced system was reduced by removing the undesired states, obtaining a 43th order system.

The NRG method was applied to the linearized and balanced model. The outcomes achieved by means of the NRG method, shown in Table 1.3, suggest to use the lead mass flow rate (*G_Pb*) to maintain the lead temperature in the cold leg (*T_cold_leg*) close to its nominal value. In

addition, the values representing the interactions between lead mass flow rate and other outputs are sufficiently low to allow the closure of a feedback control loop without problematic interactions with other output variables. As far as the remaining control loops are concerned, it appears clear that the steam temperature (*T_steam*) and mass flow rate (*G_turbine*) can be governed by the feedwater temperature (*T_feed*) and mass flow rate (*G_water*), respectively. On the other hand, the core power (*Th_Power*) and the SG pressure (*Pressure*) can be regulated by adjusting the CR position (*h_CR*) and the turbine admission valve opening (*kv*), respectively. Finally, two outputs out of seven were necessarily excluded in order to control the remaining five with the available five inputs. In particular, the fuel (*T_fuel*) and the hot leg (*T_hot_leg*) temperatures were left out since they are of secondary importance compared to the other output variables in the perspective of controlling the power plant. Moreover, the poor value of the feasible pairings induces to eliminate them since their control would not be very effective in any case.

Table 1.3. Pairing selection performed by means of the NRG method. The rows in grey represent the outputs that were discarded for control purposes, whereas red values represent the elements that correspond to the chosen input/output pairs.

OUTPUTS	INPUTS				
	T_feed	***G_water***	***h_CR***	***G_Pb***	***kv***
T_steam	**0.4169**	0.0082	0.1729	0.0274	-0.0006
T_fuel	0.0478	0.0003	0.2683	-0.0008	-0.0002
Pressure	0.0000	-0.0021	-0.0000	-0.0000	**0.9989**
G_turbine	-0.0000	**0.9986**	-0.0000	-0.0000	-0.0000
T_cold_leg	0.1597	-0.0019	0.0741	**0.5911**	0.0007
Th_power	0.2757	-0.0007	**0.4267**	-0.0018	0.0004
T_hot_leg	0.1000	-0.0024	0.0581	0.3841	0.0009

The implemented control system is made up of a battery of feedback loops in which PI[4] controllers are adopted. The corresponding control law is given by:

$$u(t) = K_p e(t) + K_i \int_0^t e(t)dt \tag{1.24}$$

where *u(t)* represents the value assumed by the control variable, *e(t)* is the difference between the set-point signal and the instantaneous value of the output variable, K_p is the gain of the proportional controller, and K_i is the integrator gain. The controller parameters, K_p and K_i, were tuned on the linearized system. These PI regulators are used when the integral action is essential to provide good static performance, but, at the same time, the presence of a zero in the corresponding transfer function is necessary to guarantee a wider bandwidth compared with the one obtainable by adopting a simple integral action. Moreover, it is important that the error between the set-point signal (e.g., the power requested) and the instantaneous value of the output (e.g., the power produced within the core) vanishes at the end of the transients (Åström and Hägglund, 1995). The PI controllers gains were tuned in order to achieve a large phase margin so as to get good performance even in operational conditions quite different from the nominal one. In addition, because of the tight connection between the phase margin and the damping, the choice

[4] A derivative (D) controller turns out to be useful when the reference signal varies with a high frequency and it is necessary that the system quickly follows it. In a nuclear power plant, the reference signals always have characteristic time constants of the order of seconds, and thus the proportional (P) controller and the integrator (I) are sufficient.

of adopting a considerable phase margin permits to avoid excessive overshooting during transients which may jeopardize the integrity of some components (e.g., the pressure in the SGs). Finally, considering the previous constraints, the cut-off frequencies were optimized so as to reduce the transient time of the controlled transients. The characteristic times of the PIs were considered less relevant in the tuning process since the stability, the robustness, and the absence of oscillations in the controlled transient were favoured in the control design. As far as the control of inlet lead temperature (*T_cold_leg*) and steam temperature (*T_steam*) is concerned, an anti-windup was necessarily inserted in the respective control loop to limit overshooting[5] (Figure 1.11). The gains and parameters of the adopted controllers are listed in Table 1.4. Among the several figures of merit of the SISO controllers, the settling time and the maximum delay were selected for the different control loops (Table 1.5). The former is defined as "the time required for the response curve to reach and stay within a 2% of the final value" (Ogata, 2009). This value constitutes an indication of the time required to consider a controlled transient finished. In particular, the proposed scheme allows obtaining more rapid controlled transients with acceptable robustness features.

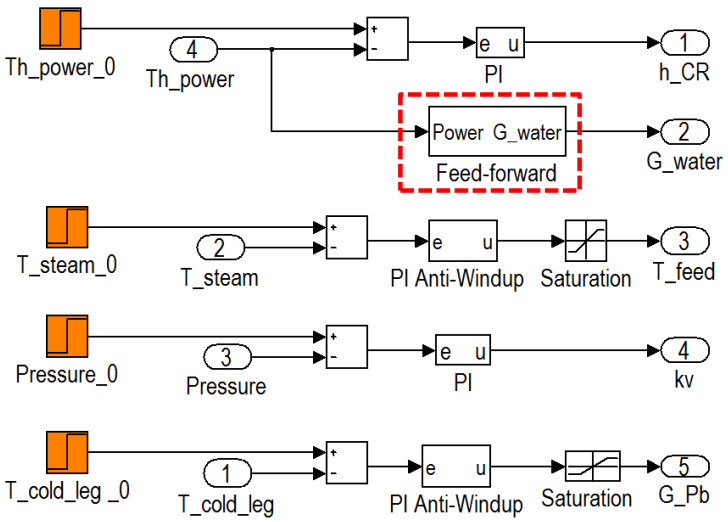

Figure 1.11. Feedback loops of the control strategy.

Table 1.4. Parameters of the PI controllers (5-input scheme). In the table, the parameters of the four feedback control loops are reported, since the feedwater mass flow rate (G_water) performs a feedforward control action.

Control loop		Controller gain		Controller performance	
Controlled variable	*Control variable*	K_p	K_i	*Phase margin* (°)	*Cut-off frequency* (rad s^{-1})
T_cold_leg (°C)	G_Pb (kg s^{-1})	250	20	116	$2\cdot10^{-2}$
T_steam (°C)	T_feed (°C)	1	$6\cdot10^{-4}$	142	$1.6\cdot10^{-3}$
Th_power (W)	h_CR (cm)	$-2\cdot10^{-11}$	$-4\cdot10^{-11}$	109	$3.2\cdot10^{-3}$
Pressure (Pa)	kv (-)	$-3\cdot10^{-7}$	$-1\cdot10^{-8}$	104	$5.4\cdot10^{-1}$

The second figure of merit is represented by the maximum admissible time delay for the considered control loop beyond which it loses its asymptotic stability properties. Besides taking into account the uncertainties in the estimation of the time lag between the SG outlet and the core inlet, this aspect has to be considered for the feedback loop dedicated to the lead temperature

[5] Such a situation occurs when large changes in set-points take place and the integral term accumulates a significant error, which causes overshooting to be kept increasing.

control. The time delays due to the transport phenomena in the hot and cold collectors depend on the coolant mass flow rate in the primary circuit. Therefore, in the proposed strategy, if the lead mass flow rate is reduced, the lead speed in the collectors drops and the time delay between core and SG increases. Performing the same operational transient in nominal conditions and in partial load conditions (in which the lead mass flow rate is reduced), the system stability turns out to be quite different. Indeed, in partial load conditions, the allowable delay tends to decrease, thus making the system less robust against any uncertainties related to the timing involved in the controlled process.

Table 1.5. PI figures of merit.

Control loop		Figures of merit	
Controlled variable	*Control variable*	*Settling time* (s)	*Maximum delay* (s)
T_cold_leg (°C)	G_Pb (kg s^{-1})	200	100
T_steam (°C)	T_feed (°C)	2025	1550
Th_power (W)	h_CR (cm)	1315	595
Pressure (Pa)	kv (-)	10	5

The control scheme was coupled and tested on the nonlinear object-oriented model, realized by employing the Modelica language and exported in the SIMULINK® environment, as shown in Figure 1.12.

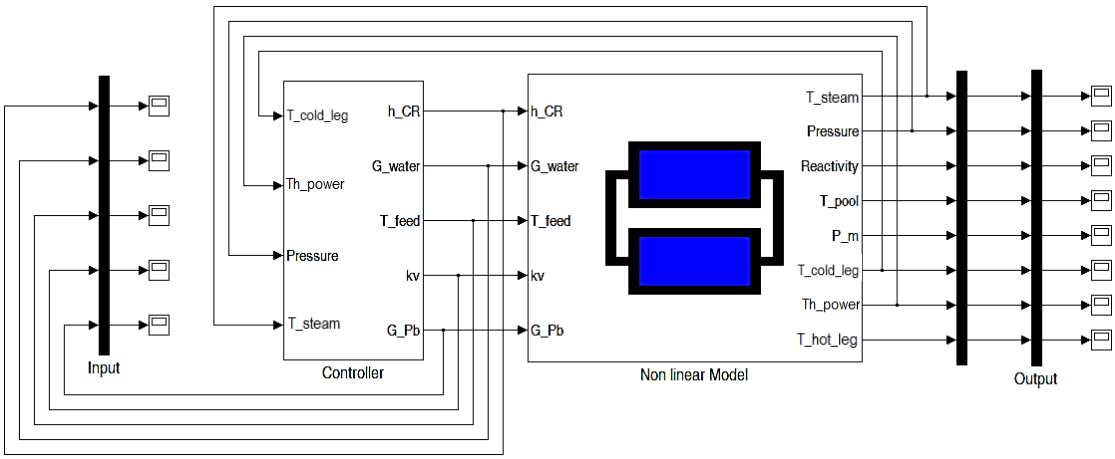

Figure 1.12. Decentralized control scheme adopted for ALFRED reactor control.

In order to test its performance, a reduction of the reactor power from 300 MWth to 250 MWth was performed. In Figure 1.13a, the power transient is represented showing a settling time of 600 s, indicating the absence of coupling between this loop and the other ones and confirming the validity of the adopted decentralized control scheme. The relevant slowness of the dynamic response is partially due to the choice of reducing the control system performance in order to guarantee control system robustness, but it is mainly ascribed to a structural feature of the controlled physical system. In virtue of the coupling between the primary and the secondary circuit of the plant, the SG is characterized by a very slow dynamic response as well. Nevertheless, the pressure in the SG shows a good behaviour (Figure 1.13b). After having reached a maximum difference from the nominal value of 0.5 bar, the controlled variable settles on its nominal value of 180 bar in 1200 s (time to reach the 2% of the maximum variation). This time constant would have been reduced by simply increasing the gain parameters of PI controllers, but relevant

overshooting would have occurred. Indeed, such a pressure response may constitute a concern because of the induced mechanical stresses.

The CRs insertion value and the turbine admission valve coefficient (i.e., the two control variables that regulate the reactor thermal power and the SG pressure, respectively) are shown in Figure 1.14a and Figure 1.14b, respectively. Observing the SG outlet temperature evolution (Figure 1.13c), a time constants of 4000 s is found. It is worth observing that the lead mass flow rate variation (Figure 1.14c) necessary to control the lead temperature is not demanding (the maximum requested variation is slightly more than the 3% of the nominal value). On the other hand, the narrow operational range of the feedwater temperature constitutes a relevant concern in the use of this variable (Figure 1.14d) since the steady state value is very close to the lead freezing point (327°C).

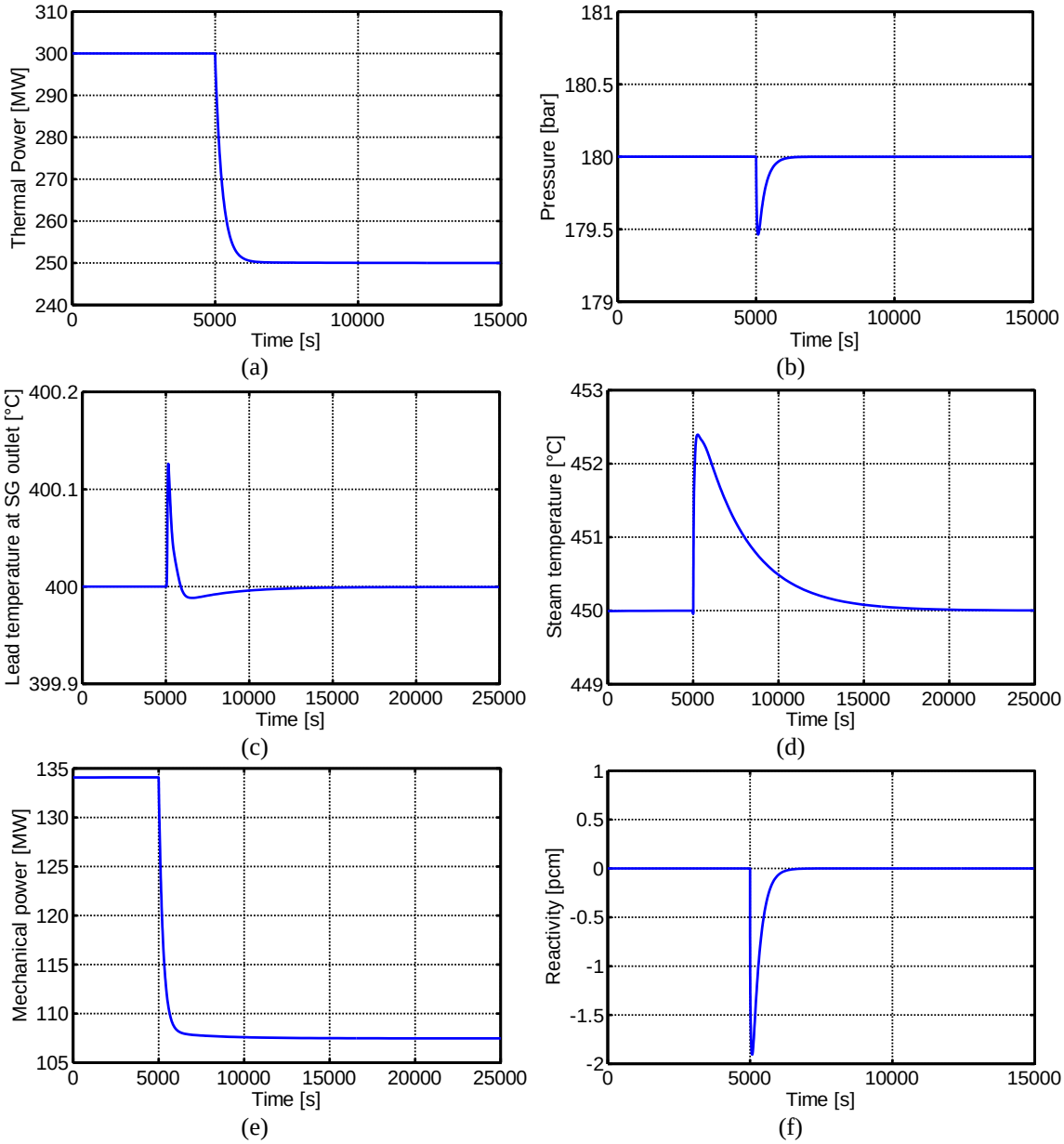

Figure 1.13. Evolution of the output variables in the power level reduction case: (a) reactor thermal power, (b) pressure, (c) lead temperature at the SG outlet, (d) steam temperature, (e) mechanical power, (f) reactivity.

As far as the steam temperature evolution is concerned (Figure 1.13d), the settling time is 12000 s. As for the control variable, the feedwater temperature don't exhibit any particular issue. For the sake of completeness, the responses of other output variables of interest are presented in Figure 1.13e (mechanical power) and Figure 1.13f (system reactivity). Since the entire steam mass flow rate is sent to the turbine and the turbine admission coefficient is devoted to the pressure control, the mechanical power evolution is characterized by the same time constant of the thermal power produced in the core. Finally, it is worth noting that the overall performed control actions limit the variation of the system reactivity (less than 2 pcm).

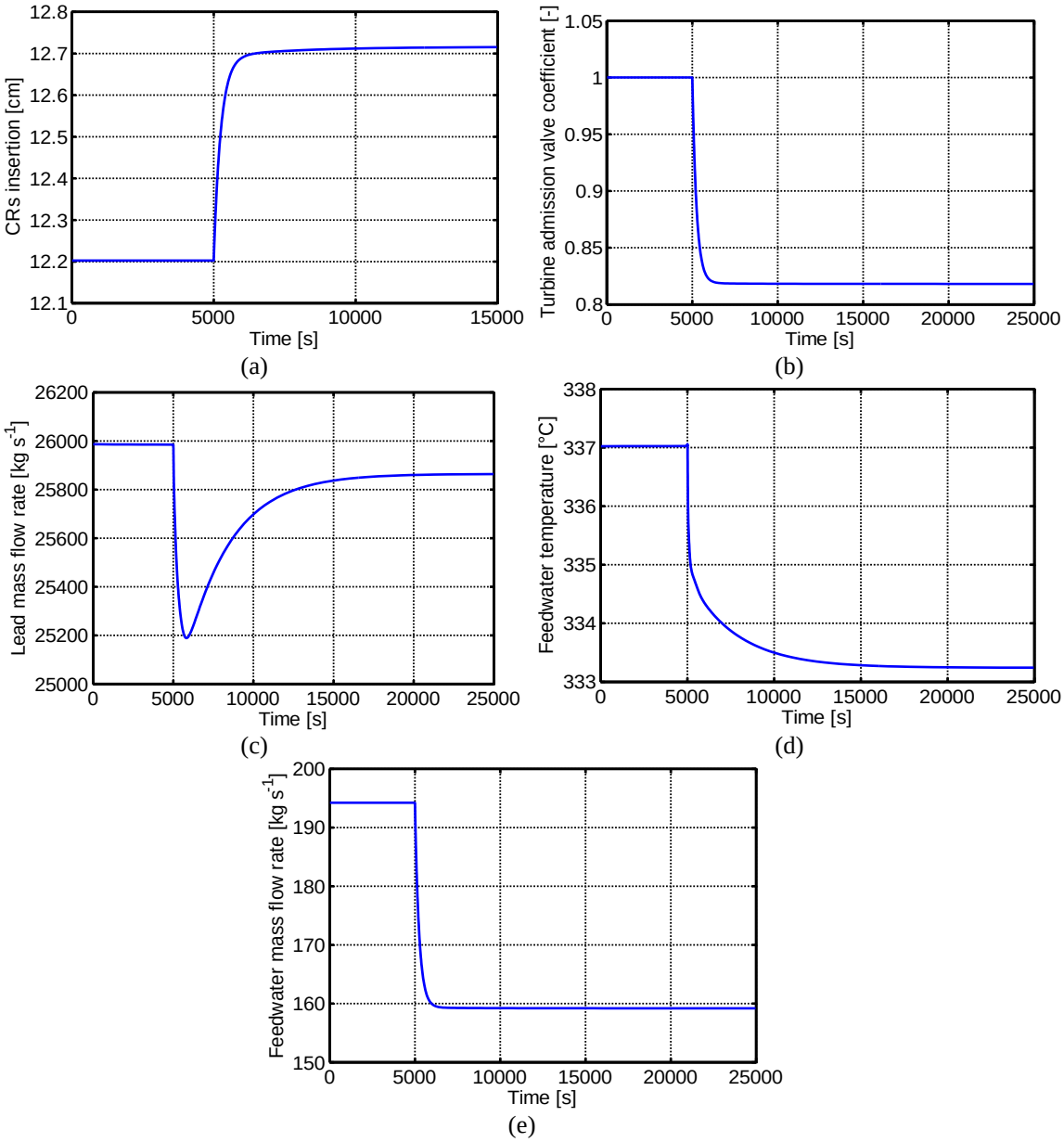

Figure 1.14. Evolution of the control variables in the power level reduction case: (a) CRs insertion, (b) turbine admission valve coefficient, (c) lead mass flow rate, (d) feedwater temperature, (e) feedwater mass flow rate.

1.4 Concluding remarks

In this Chapter, the state of the art concerning the control-oriented modelling of LFR systems and the related PID-based control scheme developed at PoliMi – Nuclear Reactor Group (NRG) have been presented. An object-oriented model of the ALFRED reactor has been described. It is aimed at pointing out the weak points of the current control-oriented approach. In particular, the two main concerns are the modelling of the neutronics and the cold pool. As for the former, the neutronics is represented by a zero-dimensional model, i.e., the point kinetics. This lumped parameter approach describes the time dependence of the neutron population in the reactor relating it to the flux by a constant of proportionality (single-energy group approximation). The system reactivity feedback is expressed as a linear function of the mean values of characteristic temperatures with constant coefficients. The approach neglects the spatial dependence of the variables, and consequently the control system based on a simulator that relies on this assumption is not capable to discriminate the spatial effects of the CR movement. This represents a limit whether, for instance, a proper coordination of the CRs is needed to limit the flux distortion. On the other hand, the simple mass and the energy balances (i.e., lumped parameter approach) for the cold pool modelling is inadequate to allow conceiving a proper oxygen control strategy for the LFR systems.

In conclusion, as shown in the description of the PID-based control system of ALFRED reactor, the control strategy is influenced by the modelling assumption of the simulator used to realize and validate it. In order to overcome these limitations, some ROM approaches are proposed in the next Chapters aimed at being used in the mentioned ALFRED simulator. In this framework, Modelica with its component approach represents a powerful tool since it makes possible to update or substitute a component without modifying the rest of the simulator. In particular, the effort is focused on two sides: the neutronics and the thermal-hydraulics. The former is improved introducing a spatial neutronics model for the reactor core (Chapter 2) whereas the latter is enhanced developing a spatial model for the reactor pool (Chapter 3). The models are implemented in the corresponding components (objects) representing the core neutronics and the reactor pool. The rest of the plant simulator is not affected by the implementation of the ROM-based components. These improvements may allow adopting innovative control strategies[6], whose feasibility in the nuclear field cannot be adequately studied by means of zero dimensional models.

[6] The development and the implementation of innovative control strategies are out of the scope of this work.

List of symbols

Latin Symbols

A	single channel coolant flow area, m^2
A_{CR}	coefficient for the calibration of CRs, pcm
A_{SR}	coefficient for the calibration of SRs, pcm
A_v	flow area, m^2
B_{CR}	coefficient for the calibration of CRs, m^{-1}
Bo	boiling number, -
c	average specific heat capacity, $J\ kg^{-1}\ K^{-1}$
C_{CR}	coefficient for the calibration of CRs, -
C_f	Fanning friction coefficient, -
c_i	density of the ith precursor group, cm^{-3}
Co	Convection number, -
d	density, $kg\ m^{-3}$
D_{CR}	coefficient for calibration of CRs, pcm
F_{Fl}	fluid-surface parameter
Fr_{LO}	Froude number with all flow as liquid
g	gravitational acceleration, $m\ s^{-2}$
h	specific enthalpy, $J\ kg^{-1}$
h_{CR}	height of control rods, m
h_{LO}	single-phase heat transfer coefficient with all flow as liquid, $W\ m^{-2}\ K^{-1}$
h_{SR}	height of safety rods, m
h_{TP}	two phase heat transfer coefficient, $W\ m^{-2}\ K^{-1}$
i_{LG}	latent heat of vaporization, $J\ kg^{-1}$
k	thermal conductivity, $W\ m^{-1}\ K^{-1}$
K_D	Doppler constant, pcm
k_v	turbine admission valve coefficient, m s
L_{SR}	total length of SRs, m
n	neutron density, cm^{-3}
N	number of axial nodes, -
Nu	Nusselt number, -
p	pressure, Pa
Pe	Peclet number, -
q	neutron source, $cm^{-3}\ s^{-1}$
q''	heat flux, $W\ m^{-2}$
q'''	thermal power density, $W\ m^{-3}$
r	radial coordinate, m
t	time, s
T	average temperature, K
u	fluid velocity, $m\ s^{-1}$
w	mass flow rate, $kg\ s^{-1}$
x	axial coordinate, m
x_c	critical ratio, -
x_v	vapour quality, -
x_{SR}	height of SRs at full power, m
z	elevation, m

Greek Symbols

α_{CR}	radial cladding expansion reactivity coefficient, pcm K^{-1}
α_{CZ}	axial cladding expansion reactivity coefficient, pcm K^{-1}
α_{Dia}	diagrid expansion reactivity coefficient, pcm K^{-1}
α_{FZ}	axial fuel expansion reactivity coefficient, pcm K^{-1}
α_L	coolant density reactivity coefficient, pcm K^{-1}
α_{WR}	radial wrapper expansion reactivity coefficient, pcm K^{-1}
α_{WZ}	axial wrapper expansion reactivity coefficient, pcm K^{-1}
β	DNP total fraction, pcm
β_i	DNP fraction of the ith precursor group, pcm
Λ	neutron generation time, s
λ_i	decay constant of the ith precursor, s^{-1}
ρ	reactivity, pcm
ρ_0	reactivity margin stored in the core, pcm
φ	heat flux entering the tube (lateral surface), $W\ m^{-2}$
ω	tube perimeter, m

Superscripts

D	Doppler
eff	effective
1,3	fuel internal and external regions

Subscripts

0	steady-state
c	cladding
CBD	convective boiling dominant
down	downstream
f	fuel
g	gap
in	inlet

l	lead coolant	out	outlet
L	liquid	up	upstream
NBD	nucleate boiling dominant	v	vapour

Chapter 2

Spatial neutronics modelling

In this Chapter, the development of a spatial neutronics model for the reactor core is presented. This approach is meant to replace the Point Kinetics currently used in control-oriented simulators. Such simple approach may prevent the use of advanced techniques made available thanks to the significant developments of digital Instrumentation & Control (I&C) technology in recent decades. On the other hand, this modelling improvement may allow adopting innovative control strategies, whose feasibility in the nuclear field cannot be adequately studied with a zero-dimensional model.

The spatial neutronics is based on the paradigm of the ROM, formulated on purpose for the neutronics, separating the spatial and time dependence of the neutron flux, which can be represented as a linear combination of spatial basis functions. The aim of this Chapter is describing the modelling approach (Section 2.2), which can be divided in an offline and an online phase. The former is devoted to the generation of the cross sections and the spatial basis/test functions pairs, whereas the latter is the reduced order model itself. A simple 3D test case is analysed (Section 2.3) in order (i) to demonstrate the feasibility of the proposed approach, (ii) to assess the better performance of the spatial neutronics model with respect to the classic Point Kinetics, and (iii) to show how the spatial neutronics model can be implemented in an object-oriented simulator. The full core model of the ALFRED reactor is set up (Section 2.4) in order to assess the performance of the different choice of spatial basis/test functions in reproducing the reactivity insertion following a temperature change or a CR movement.

The main results of this Chapter have been published in:

- Lorenzi, S., Cammi, A., Luzzi, L., Ponciroli, R., 2014. Development of a Spatial Neutronics Model for Control-Oriented Dynamics Simulation. In *Proceeding of the 22nd International Conference On Nuclear Engineering*, Prague, July 7–11, 2014, Paper 30818.
- Lorenzi, S., Cammi, A., Luzzi, L., Ponciroli, R., 2015. A control-oriented modeling approach to spatial neutronics simulation of a Lead-cooled Fast Reactor. *Journal of Nuclear Engineering and Radiation Science*, **1**, 031007, 1–10.
- Lorenzi, S., Cammi, A., Luzzi, L., 2015. Spatial neutronics modelling to evaluate the temperature reactivity feedbacks in a Lead-cooled Fast Reactor. In *Proceedings of the International Congress on Advances in Nuclear Power Plants*, Nice, May 3–6, 2015.
- Lorenzi, S., Cammi, A., Luzzi, L. Optimized reduced order approach for the spatial neutronics modelling of the Lead-cooled Fast Reactor. In preparation *for Annals of Nuclear Energy*.

2.1. Introduction

The zero-dimensional Point Kinetics model (Schultz, 1961) is commonly employed in control-oriented tools for the neutronics description. This lumped parameter approach describes the time dependence of the neutron population in the reactor and relates it to the flux by a constant of proportionality (single energy group approximation). The approach neglects the spatial dependence of the variables, such an assumption being valid if the system is reaching the critical state and if there are no large localized perturbations (Hetrick, 1993). The system reactivity feedback is usually expressed as a linear function of the mean values of characteristic temperatures with constant coefficients. The resulting model is represented by a set of Ordinary Differential Equations (ODEs), which are suitable for control purposes since they usually fulfill the mentioned requirements, and they can be easily linearized to study the system with linear analysis tools. On the other hand, the solution of the time-dependent Partial Differential Equations (PDEs) related to the neutron diffusion cannot be directly exploited for control system studies. Indeed, besides the high computational burden, it does not allow immediately to get the system governing dynamics without a proper post-processing. Notwithstanding, the adoption of the PK description precludes the possibility of exploiting all the capabilities of advanced control schemes, limiting the achievable control performance. In particular, two modelling limitation should be pointed out. The first one is that the PK neglects the spatial dependence of the flux and consequently it cannot allow for the flux distortion due to the CR insertion. This prevents the use of advanced modelling-based control schemes to minimize the effect of the CR, for instance. The second weak point is that the PK does not allow considering the different contributes of each zone to the reactivity. This is related to the estimation of thermal reactivity feedbacks occurring in a nuclear reactor. Since these effects have a great impact on the dynamics of the core, they have to be fully characterized. In particular, in a LFR, the impact of the coolant density variation may act in different directions (i.e., with a positive or negative local coefficient) according both to the core zone involved and to the size of the reactor, leading to a different dynamics response and, in turn, to a different control strategy to consider (Lorenzi et al., 2012).

In order to overcome these limitations and to develop a sufficiently accurate description of the reactor core spatial dynamics, preferably based on a set of ODEs, a ROM approach can be adopted. In particular, the paradigm of the ROM can be transferred into neutronics separating the spatial and time dependence of the neutron flux, which can be represented as a linear combination of spatial basis functions calculated from the neutron diffusion PDEs weighted by time-dependent coefficients. The spatial basis calculation is performed only once as part of the offline phase of the entire procedure. The dynamic behaviour of the flux is reduced to the study of these time-dependent coefficients, and can be represented by a set of ODEs. This set is obtained multiplying the PDEs with suitable test functions, as in a Petrov-Galerkin projection.

The selection of the spatial basis and test functions is a crucial issue in the development of the control-oriented spatial neutronics modelling. In particular, the aim is selecting the optimal pair of spatial basis/test functions that maximizes the accuracy of the model and minimizes the computational cost. In this work, two possible approaches in the calculation of the spatial basis are undertaken. The classic one is the Modal Method (MM) that employs as spatial basis the eigenfunctions of the neutron diffusion PDEs calculated in a reference configuration (Stacey,

1969). The Modal Method, which is proved to give better results than a multi-point kinetics approach (Dulla et al., 2009), was theorized in the sixties but it was not systematically employed for dynamics simulations because of the high computational burden for the determination of the higher order eigenfunctions. The Modal Method provides a "general" spatial basis since it is related to the eigenvalue equation of the system. An alternative option can be constituted by the adoption of the POD with the snapshot technique (Holmes et al., 1996; Sirovich, 1987), which is a reduction order technique aimed at using low dimensional approximations of a high dimensional system according to a "maximum energy/info" criterion. The Proper Orthogonal Decomposition is able to provide "ad hoc" spatial basis tailored on the specific simulation case, thanks to its optimality properties (for further information about the POD technique, the reader may refer to Appendix A.3). In this case, instead of calculating the eigenfunctions of the neutron diffusion PDEs, some proper solutions have to be calculated (i.e., "snapshots") and the most energetic modes are selected. As for the test functions, they usually are the same functions that constitute the spatial basis as in a Galerkin projection. Nevertheless, the test functions can be different as in a Petrov-Galerkin projection. In this sense, a possible option is to employ the adjoint functions related to the spatial basis thanks to the property of bi-orthogonality. This choice assumes a particular meaning in the neutronics field since it is related to the neutron importance.

As pointed out in the Introduction, the practical application of this thesis is the improvement of the mentioned object-oriented simulator, i.e., substituting some components based on zero-dimensional approach with ROM-based components ensuring a high level of accuracy without increasing the computational burden. In particular, in this Chapter, the effort is focused on the improvement of the neutronics introducing a spatial neutronics modelling. In Section 2.2, the modelling approach employed for the spatial neutronics model is presented with the description of the several phases involved in the procedure, with a particular attention to the spatial basis and test functions selection. In Section 2.3, the implementation of the spatial neutronics modelling for an LFR pin test case is described. In particular, the aims of this test case are (i) to demonstrate the feasibility of the approach proposed in the Section 2.2, (ii) to assess the better performance of the spatial neutronics model with respect to the classic Point Kinetics approach, and (iii) to show how the spatial neutronics model can be implemented in an object-oriented simulator and, also adopting a new heat transfer pin model suitable for the purpose. The ALFRED full core modelling is presented in Section 2.4, analysing the optimal spatial basis/test functions pair and the performance of the several method in assessing the reactivity following a temperature change and a CR movement. A few concluding remarks are drawn in Section 2.5.

2.2. Modelling approach

In this Section, the procedure employed to obtain the spatial neutronics model is described. As shown in Figure 2.1, in order to set up the spatial neutronics model (i.e., an online calculation that can be run several times without expensive computational cost), an offline procedure has to be arranged in order to solve the neutron diffusion PDEs and to calculate the spatial basis. In the following, the general modelling framework along with the description of the possible choice in terms of spatial basis and test functions are presented.

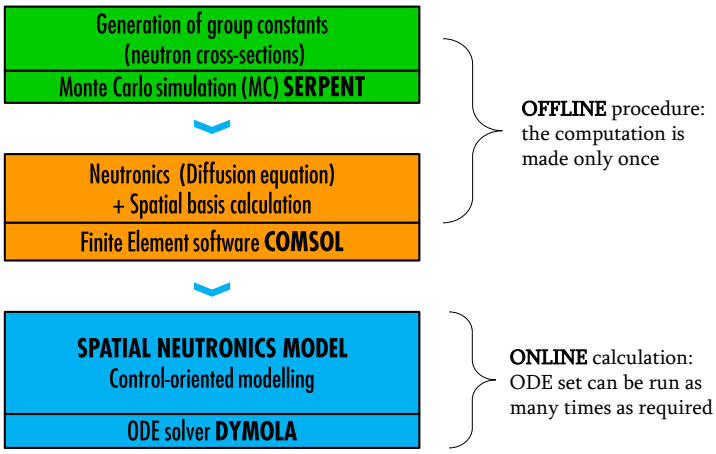

Figure 2.1. Derivation of the spatial neutronics model: offline procedure and online calculation.

2.2.1 General Modelling Framework

In order to describe the neutron kinetics, the multi-group diffusion theory (Duderstadt and Hamilton, 1976), with a generic number G of energy groups and eight groups of precursors are considered. In equations, it reads:

$$\underline{\underline{V}}^{-1}\frac{\partial \underline{\phi}}{\partial t} = \nabla\cdot\left(\underline{\underline{D}}\nabla\underline{\phi}\right) - \underline{\underline{\Sigma_a}}\,\underline{\phi} - \underline{\underline{\Sigma_s}}\,\underline{\phi} + (1-\beta)\underline{\chi_p}\underline{F}^T\underline{\phi} + \sum_j \lambda_j \underline{\chi_d} C_j \tag{2.1}$$

$$\frac{\partial C_j}{\partial t} = -\lambda_j C_j + \beta_j \underline{F}^T\underline{\phi} \qquad j = 1 \div 8 \tag{2.2}$$

where

$$\underline{\phi}(\boldsymbol{r},t) = \begin{bmatrix}\phi_1(\boldsymbol{r},t)\\ \vdots \\ \phi_G(\boldsymbol{r},t)\end{bmatrix} \qquad \phi_g(\boldsymbol{r},t) = \int_{E_g}^{E_{g-1}} dE\,\phi(\boldsymbol{r},E,t)$$

$$\underline{\underline{V}}^{-1} = diag\left(\frac{1}{v_g}(\boldsymbol{r})\right) \qquad \underline{\underline{D}} = diag\left(D_g(\boldsymbol{r})\right) \qquad \underline{\underline{\Sigma_a}} = diag\left(\Sigma_a^g(\boldsymbol{r})\right)$$

$$\underline{\underline{\Sigma_s}} = \begin{bmatrix}\Sigma_s^{1\to}(\boldsymbol{r}) & -\Sigma_s^{2\to1}(\boldsymbol{r}) & \cdots & -\Sigma_s^{G\to1}(\boldsymbol{r})\\ -\Sigma_s^{1\to2}(\boldsymbol{r}) & \Sigma_s^{2\to}(\boldsymbol{r}) & \cdots & -\Sigma_s^{G\to2}(\boldsymbol{r})\\ \vdots & \vdots & \ddots & \vdots\\ -\Sigma_s^{1\to G}(\boldsymbol{r}) & -\Sigma_s^{2\to G}(\boldsymbol{r}) & \cdots & \Sigma_s^{G\to}(\boldsymbol{r})\end{bmatrix} \tag{2.3}$$

$$\underline{\chi_p} = \begin{bmatrix}\chi_p^1\\ \vdots \\ \chi_p^G\end{bmatrix} \qquad \underline{\chi_d} = \begin{bmatrix}\chi_d^1\\ \vdots \\ \chi_d^G\end{bmatrix} \qquad \underline{F}^T = \begin{bmatrix}\nu\Sigma_f^1(\boldsymbol{r}) & \cdots & \nu\Sigma_f^G(\boldsymbol{r})\end{bmatrix}$$

The neutron flux can be expressed as

$$\underline{\phi}(\boldsymbol{r},t) \cong \sum_{i=1}^{N} \underline{\underline{\psi_i}}(\boldsymbol{r})\cdot\underline{n_i}(t) \tag{2.4}$$

$$\underline{\underline{\psi_i}}(\boldsymbol{r}) = \begin{bmatrix}\psi_i^1(\boldsymbol{r}) & 0 & 0\\ 0 & \ddots & 0\\ 0 & 0 & \psi_i^G(\boldsymbol{r})\end{bmatrix} = diag\left(\underline{\psi_i}(\boldsymbol{r})\right) \tag{2.5}$$

$$\underline{n}_i(t) = \begin{bmatrix} n_i^1(t) \\ \vdots \\ n_i^G(t) \end{bmatrix} \tag{2.6}$$

where $\underline{\underline{\psi}}_i(\boldsymbol{r})$ is a spatial basis where the flux is projected and $\underline{n}_i(t)$ are the time-dependent coefficients.

In order to transform the multi-group diffusion PDEs into a set of ODEs involving only the time-dependent coefficient $\underline{n}_i(t)$, the expression of Equation (2.4) has to be substituted into Equations (2.1) and (2.2), the latter have to be multiplied by test functions $\underline{\underline{\xi}}_i = diag(\underline{\underline{\xi}}^g_i(\boldsymbol{r}))$ and integrated over the computational domain. This procedure can be related to a Petrov-Galerkin projection. Finally, the ODE system for the time-dependent coefficients can be expressed, for each basis function, as

$$\sum_{m=1}^{N} \underline{\underline{RV}}_{im} \cdot \dot{\underline{n}}_m = \sum_{m=1}^{N} \left(-\underline{\underline{L}}_{im} - \underline{\underline{\delta L}}_{im} + (1-\beta) \cdot \left(\underline{\underline{M}}_{im} + \underline{\underline{\delta M}}_{im} \right) \right) \cdot \underline{n}_m + \sum_{j=1}^{8} \lambda_j \underline{c}_{ij} \tag{2.7}$$

$$\dot{\underline{c}}_{ij} = \beta_j \underline{\underline{X}} \left[\sum_{m=1}^{N} \left(\underline{\underline{M}}_{im} + \underline{\underline{\delta M}}_{im} \right) \cdot \underline{n}_m \right] - \lambda_j \underline{c}_{ij} \quad j = 1 \div 8 \tag{2.8}$$

where

$$\begin{aligned}
\underline{\underline{RV}}_{im} &= \int \underline{\underline{\xi}}_i \cdot \underline{\underline{V}}^{-1} \cdot \underline{\underline{\psi}}_m d\Omega \\
\underline{\underline{L}}_{im} &= \int \underline{\underline{\xi}}_i \cdot \left(-\nabla \cdot \underline{\underline{D}} \nabla + \underline{\underline{\Sigma}}_a + \underline{\underline{\Sigma}}_s \right) \underline{\underline{\psi}}_m d\Omega \\
\underline{\underline{\delta L}}_{im} &= \int \underline{\underline{\xi}}_i \cdot \delta \left(-\nabla \cdot \underline{\underline{D}} \nabla + \underline{\underline{\Sigma}}_a + \underline{\underline{\Sigma}}_s \right) \underline{\underline{\psi}}_m d\Omega \\
\underline{\underline{M}}_{im} &= \int \underline{\underline{\xi}}_i \cdot \left(\underline{\chi}_p \underline{F}^T \right) \underline{\underline{\psi}}_m d\Omega \\
\underline{\underline{\delta M}}_{im} &= \int \underline{\underline{\xi}}_i \cdot \delta \left(\underline{\chi}_p \underline{F}^T \right) \underline{\underline{\psi}}_m d\Omega \\
\underline{c}_{ij} &= \int \underline{\underline{\xi}}_i \cdot \underline{\chi}_d \cdot C_j \, d\Omega \qquad \underline{\underline{X}} = \begin{bmatrix} \chi_d^1/\chi_p^1 & 0 & 0 \\ 0 & \ddots & 0 \\ 0 & 0 & \chi_d^G/\chi_p^G \end{bmatrix}
\end{aligned} \tag{2.9}$$

$\underline{\underline{L}}_{im}$ and $\underline{\underline{M}}_{im}$ represent the contribution to the removal and production operator calculated in the unperturbed system. These quantities are calculated once in the "offline" process, and are kept constant during the transient simulation. $\underline{\underline{\delta L}}_{im}$ and $\underline{\underline{\delta M}}_{im}$ represent the variation of the removal and the production operators during the transients. On one hand, the variation is due to the temperature change of the cross-sections, i.e. the reactivity thermal feedbacks. On the other hand, the removal and production operator can change due to the CR movement. Both of them assume a particular relevance in the control-oriented perspective affecting the system dynamics. According to this procedure, the variation is weighted on the spatial basis and test functions, allowing for the spatial characteristics of the perturbation and obtaining an accurate estimation of the reactivity evolution. This goal cannot be achieved with a PK approach since the reactivity variations are uniformly evaluated through the system.

2.2.2 Generation of Group Constants

In order to solve the neutron diffusion PDEs, the neutronic parameters (V^{-1}, D, Σ_a, Σ_s, χ_p, χ_d, F^T) should be calculated. In the thesis, the continuous energy Monte Carlo neutron transport code SERPENT (Serpent, 2011), featuring group constant generation capabilities and using the nuclear data library JEFF 3.1 (Koning et al., 2006) is exploited.

2.2.3 Spatial basis calculation

The choice of the spatial basis $\underline{\psi}_i(\boldsymbol{r})$ (i.e., the selection of the functions used to expand the neutron flux) is crucial for the spatial neutronics model. An optimized spatial basis ensures faster simulation and improved accuracy. Another degree of freedom is the choice of the test functions $\underline{\xi}_i$. Typically, they are the same functions, which constitute the spatial basis as in a Galerkin projection. Nevertheless, the test functions can be different as in a Petrov-Galerkin projection. In this sense, a possible option is to employ the adjoint functions related to the spatial basis due to the property of bi-orthogonally. This choice assumes a particular meaning in the neutronics field since it is related to the neutron importance. Accordingly, two methods for the spatial basis selection are undertaken, namely the Modal Method and the Proper Orthogonal Decomposition, and two possible test functions (i.e., the same functions of the spatial basis and the adjoint ones). In Table 2.1, the four cases studied in this thesis, spanning the possible combination of spatial basis/test functions, are summarized.

Table 2.1. Spatial basis and test function pairs studied in this work.

		Test function	
		Function of spatial basis	*Adjoint functions*
Method for the spatial basis	*MM*	Case A	Case B
	POD	Case C	Case D

Modal Method

In the MM, the spatial basis is constituted of the eigenfunctions associated to the neutron diffusion equation. The eigenvalue problem associated is

$$\left(-\nabla \cdot \underline{\underline{D}}\nabla + \underline{\underline{\Sigma_a}} + \underline{\underline{\Sigma_s}}\right)\underline{\psi}_i = \lambda_i^* \underline{\chi_t}\underline{F}^T \underline{\psi}_i \tag{2.10}$$

where the first eigenfunction $\underline{\psi}_1$ gives the fundamental flux distribution. The core criticality condition is determined by the inverse of the first eigenvalue, λ^*_1. As suitable test functions, both the same eigenfunctions (Case A) or the adjoint eigenfunctions of the Equation (2.10) (Case B) have been evaluated.

Proper Orthogonal Decomposition

Another possible option for the spatial basis $\underline{\psi}_i(\boldsymbol{r})$ is the Proper Orthogonal Decomposition (POD) combined with the snapshot method (Holmes et al., 1996; Sirovich, 1987). This approach is a reduction order technique aimed at using low dimensional approximations of high dimensional system according to a maximum energy (or info) criterion in the least square sense. Starting from proper numerical solutions (the snapshots) of the Full Order Model, i.e., the neutron diffusion PDEs, an orthonormal POD basis maximizing the energy content in the starting ensemble data (i.e., the optimal basis) can be used as spatial basis for the Reduced Order Model

(i.e., the spatial neutronics model). Moreover, the first modes have the property to retain the most of the information present in the original solutions (Berkooz et al., 1993). It is worthwhile to mention that the more the snapshots include information about the behaviour of the system, the better the Reduced Order Model based on POD is accurate.

In order to obtain the POD basis, two main procedure are usually adopted, namely the Singular Value Decomposition (SVD) and the Correlation Matrix methods (Volkwein, 1999). As for the spatial neutronics modelling, the SVD method is selected. The offline spatial basis calculation is the following:

1. Compute the N_s snapshots $\underline{\phi}^1, \underline{\phi}^2, \ldots, \underline{\phi}^{N}s$
2. Build the matrix of the snapshots $\underline{\underline{Y}} = [\underline{\phi}^1, \underline{\phi}^2, \ldots, \underline{\phi}^{N}s]$
3. Perform the SVD on $\underline{\underline{Y}}$ in order to obtain:

$$\underline{\underline{Y}} = \underline{\underline{U}}\,\underline{\underline{S}}\,\underline{\underline{G}}^T \tag{2.11}$$

where $\underline{\underline{U}}=[\underline{\psi}_1^{POD}, \underline{\psi}_2^{POD}, \ldots, \underline{\psi}_{Np}^{POD}]$ is the matrix containing the POD modes $\underline{\psi}_i^{POD}$, $\underline{\underline{S}}=diag(\sigma_i)$ is the matrix containing the singular values σ_i associated to each mode and sorted in descending order of relevance. A high value of the singular value indicates that the related mode contributes in a significant way to the reconstruction of information contained in the snapshots. The snapshot are collected form the eigenfunctions related to different configuration of the ALFRED reactor in terms of temperature and CR position. As suitable test functions, the same POD modes are usually employed (Sartori et al., 2013) (Case C). Nevertheless, the use of adjoint functions (Case D) is envisaged for the reasons already mentioned. To this aim, the following procedure is proposed to obtain a kind of "*Adjoint Proper Orthogonal Decomposition*" (APOD):

1. Compute the N_s adjoint snapshots $\underline{\phi}^{\dagger,1}, \underline{\phi}^{\dagger,2}, \ldots, \underline{\phi}^{\dagger,Ns}$ related to the same configuration of the snapshot calculated for the POD modes
2. Build the matrix of the adjoint snapshots $\underline{\underline{A}}=[\underline{\phi}^{\dagger,1}, \underline{\phi}^{\dagger,2}, \ldots, \underline{\phi}^{\dagger,N}s]$
3. Compute the matrix of test functions $\underline{\underline{E}}$ starting from

$$\underline{\underline{A}} = \underline{\underline{E}}\,\underline{\underline{S}}\,\underline{\underline{G}}^T \tag{2.12}$$

where $\underline{\underline{E}}=[\underline{\xi}_1^{APOD}, \underline{\xi}_2^{APOD}, \ldots, \underline{\xi}_{Np}^{APOD}]$ is the matrix containing the test function modes $\underline{\xi}_i^{APOD}$, $\underline{\underline{S}}$ and $\underline{\underline{G}}$ are the matrices obtained from the SVD of the spatial basis (see Equation (2.11)). In this way, the test functions are obtained according to the same "decomposition" of the spatial basis, i.e., the linear combination to obtain the test functions starting from the snapshots is the same of the POD modes.

In this work, the spatial basis for the MM method and the snapshots for the POD (see Table 2.1) are calculated solving the eigenvalue problem of the Equation (2.10), adopting the Finite Element COMSOL Multiphysics software (Comsol, 2011). As for the test functions, the adjoint problem of the Equation (2.10) is considered. The cross-sections calculated by means of SERPENT are homogenized in the coarse zones. In order to derive the reactivity effects due to the temperature and the CR movement of the ALFRED reactor, the results of the simulations at different temperature and CR conditions are converted to a COMSOL readable format by

adopting a dedicated procedure, which allows obtaining a set of temperature dependent cross-sections as:

$$\Sigma(T) = \left[\Sigma_0 + A \cdot log\left(\frac{T}{T_0}\right)\right] \tag{2.13}$$

As far as the boundary conditions are concerned, the albedo boundary conditions, previously calculated in the SERPENT model, are imposed at the axial and radial boundaries of the COMSOL model domain, namely:

$$\boldsymbol{n} \cdot \left(D_g \nabla \phi_g\right) = -\gamma_a \phi_g \qquad \boldsymbol{n} \cdot \left(D_g \nabla \phi_g\right) = -\gamma_r \phi_g \tag{2.14}$$

2.2.4 Spatial Neutronics Model and output evaluation

The spatial neutronics model can be implemented in any control oriented environment, as in the MATLAB software or in the DYMOLA simulator since the set of Equations (2.7) and (2.8) can be expressed in a general, compact and matrix form as:

$$\underline{\dot{n}} = \underline{\underline{iRV}} \cdot \left[\left(\underline{\underline{A}}_{1,np} + \underline{\underline{A}}_{1,p}\right)\underline{n} + \underline{\underline{A}}_2\,\underline{c}\right] \tag{2.15}$$

$$\underline{\dot{c}} = \left(\underline{\underline{A}}_{3,np} + \underline{\underline{A}}_{3,p}\right)\underline{n} - \underline{\underline{A}}_4\,\underline{c} \tag{2.16}$$

where

$$\underline{n} = \left[\underline{n}_1; \underline{n}_2; \dots; \underline{n}_N\right]^T \qquad \underline{c} = \left[\underline{c}_{11}; \underline{c}_{12}; \dots; \underline{c}_{1P}; \underline{c}_{21}; \dots; \underline{c}_{NP}\right]^T$$

$$\underline{\underline{i\mathrm{RV}}} = \begin{bmatrix} \underline{\underline{RV}}_{11} & \cdots & \underline{\underline{RV}}_{1N} \\ \vdots & \ddots & \vdots \\ \underline{\underline{RV}}_{N1} & \cdots & \underline{\underline{RV}}_{NN} \end{bmatrix}^{-1}$$

$$\underline{\underline{A}}_{1,np} = \begin{bmatrix} -\underline{\underline{L}}_{11} + (1-\beta)\underline{\underline{M}}_{11} & \cdots & -\underline{\underline{L}}_{1N} + (1-\beta)\underline{\underline{M}}_{1N} \\ \vdots & \ddots & \vdots \\ -\underline{\underline{L}}_{N1} + (1-\beta)\underline{\underline{M}}_{N1} & \cdots & -\underline{\underline{L}}_{NN} + (1-\beta)\underline{\underline{M}}_{NN} \end{bmatrix}$$

$$\underline{\underline{A}}_{1,p} = \begin{bmatrix} -\underline{\underline{\delta L}}_{11} + (1-\beta)\underline{\underline{\delta M}}_{11} & \cdots & -\underline{\underline{\delta L}}_{1N} + (1-\beta)\underline{\underline{\delta M}}_{1N} \\ \vdots & \ddots & \vdots \\ -\underline{\underline{\delta L}}_{N1} + (1-\beta)\underline{\underline{\delta M}}_{N1} & \cdots & -\underline{\underline{\delta L}}_{N} + (1-\beta)\underline{\underline{\delta M}}_{N} \end{bmatrix} \tag{2.17}$$

$$\underline{\underline{\lambda}}_j = \lambda_j \underline{\underline{I}} \qquad j = 1 \div 8 \qquad \underline{\underline{A}}_2 = \begin{bmatrix} \underline{\underline{\lambda}}_1 \cdots \underline{\underline{\lambda}}_P & \underline{\underline{0}} & \underline{\underline{0}} & \underline{\underline{0}} & \underline{\underline{0}} \\ \underline{\underline{0}} & \underline{\underline{0}} & \underline{\underline{0}} & \ddots & \underline{\underline{0}} & \underline{\underline{0}} & \underline{\underline{0}} \\ \underline{\underline{0}} & \underline{\underline{0}} & \underline{\underline{0}} & \underline{\underline{0}} & \underline{\underline{\lambda}}_1 \cdots \underline{\underline{\lambda}}_P \end{bmatrix}$$

$$\underline{\underline{A}}_{3,np} = \begin{bmatrix} \beta_1 \underline{\underline{X}} \cdot \underline{\underline{M}}_{11} & \cdots & \beta_1 \underline{\underline{X}} \cdot \underline{\underline{M}}_{1N} \\ \vdots & \cdots & \vdots \\ \beta_P \underline{\underline{X}} \cdot \underline{\underline{M}}_{11} & \cdots & \beta_P \underline{\underline{X}} \cdot \underline{\underline{M}}_{1N} \\ \vdots & \ddots & \vdots \\ \beta_1 \underline{\underline{X}} \cdot \underline{\underline{M}}_{N1} & \cdots & \beta_1 \underline{\underline{X}} \cdot \underline{\underline{M}}_{NN} \\ \vdots & \cdots & \vdots \\ \beta_P \underline{\underline{X}} \cdot \underline{\underline{M}}_{N1} & \cdots & \beta_P \underline{\underline{X}} \cdot \underline{\underline{M}}_{NN} \end{bmatrix} \quad \underline{\underline{A}}_{3,p} = \begin{bmatrix} \beta_1 \underline{\underline{X}} \cdot \underline{\underline{\delta M}}_{11} & \cdots & \beta_1 \underline{\underline{X}} \cdot \underline{\underline{\delta M}}_{1N} \\ \vdots & \cdots & \vdots \\ \beta_P \underline{\underline{X}} \cdot \underline{\underline{\delta M}}_{11} & \cdots & \beta_P \underline{\underline{X}} \cdot \underline{\underline{\delta M}}_{1N} \\ \vdots & \ddots & \vdots \\ \beta_1 \underline{\underline{X}} \cdot \underline{\underline{\delta M}}_{N1} & \cdots & \beta_1 \underline{\underline{X}} \cdot \underline{\underline{\delta M}}_{NN} \\ \vdots & \cdots & \vdots \\ \beta_P \underline{\underline{X}} \cdot \underline{\underline{\delta M}}_{N1} & \cdots & \beta_P \underline{\underline{X}} \cdot \underline{\underline{\delta M}}_{NN} \end{bmatrix}$$

$$\underline{\underline{A}}_4 = \begin{bmatrix} \underline{\underline{\lambda}}_1 & \underline{\underline{0}} & \underline{\underline{0}} & \underline{\underline{0}} & \underline{\underline{0}} & \underline{\underline{0}} & \underline{\underline{0}} \\ \underline{\underline{0}} & \ddots & \underline{\underline{0}} & \underline{\underline{0}} & \underline{\underline{0}} & \underline{\underline{0}} & \underline{\underline{0}} \\ \underline{\underline{0}} & \underline{\underline{0}} & \underline{\underline{\lambda}}_P & \underline{\underline{0}} & \underline{\underline{0}} & \underline{\underline{0}} & \underline{\underline{0}} \\ \underline{\underline{0}} & \underline{\underline{0}} & \underline{\underline{0}} & \ddots & \underline{\underline{0}} & \underline{\underline{0}} & \underline{\underline{0}} \\ \underline{\underline{0}} & \underline{\underline{0}} & \underline{\underline{0}} & \underline{\underline{0}} & \underline{\underline{\lambda}}_1 & \underline{\underline{0}} & \underline{\underline{0}} \\ \underline{\underline{0}} & \underline{\underline{0}} & \underline{\underline{0}} & \underline{\underline{0}} & \underline{\underline{0}} & \ddots & \underline{\underline{0}} \\ \underline{\underline{0}} & \underline{\underline{0}} & \underline{\underline{0}} & \underline{\underline{0}} & \underline{\underline{0}} & \underline{\underline{0}} & \underline{\underline{\lambda}}_P \end{bmatrix}$$

The variation of removal and production operators is usually due to temperature change of material (i.e., the reactivity thermal feedbacks) or due to the CR movement. For the neutronics calculation, the geometry is divided in coarse zones. For each region, the reactivity insertion is weighted on the spatial basis functions and the test functions integrated over the zone (not over all the system as happens for $\underline{\underline{L}}_{im}$ and $\underline{\underline{M}}_{im}$), considering the operator variation constant. The latter assumption consist in considering the temperature constant inside the coarse zone and consequently the reactivity variation, in case of the reactivity feedback. On the other hand, in case of CR movement, this entails that an effective variation of removal or production over the coarse zone following the CR movement is considered. In this way, the calculation of the integral between the spatial basis and the test functions over the zone can be performed once during the offline process, and it is kept constant during the transient simulation. Indeed, this quantity is multiplied by the removal (or production) variation, which is temperature or CR position dependent (and therefore also time-dependent). According to this procedure, $\underline{\underline{\delta L}}_{im}$ can be expressed as follows:

$$\begin{aligned}
&\underline{\underline{\delta L}}_{im}(h_{CR},T) = \int \underline{\underline{\xi}}_i \cdot \delta L(h_{CR},T)\underline{\underline{\psi}}_m d\Omega = \\
&= \sum_{gz} \int \underline{\underline{\xi}}_i \cdot \left[-\nabla \cdot \left(\underline{\underline{D}}(h_{CR,gz},T_{gz})\nabla\right) + \underline{\underline{\Sigma}}_a(h_{CR,gz},T_{gz}) + \underline{\underline{\Sigma}}_s(h_{CR,gz},T_{gz})\right] \underline{\underline{\psi}}_m d\Omega_{gz} = \\
&= \sum_{gz} \left[\int \nabla\underline{\underline{\xi}}_i \cdot \underline{\underline{D}}(h_{CR,gz},T_{gz})\nabla\underline{\underline{\psi}}_m d\Omega_{gz} - \int_{\partial\Omega_{gz}} \underline{\underline{\xi}}_i \cdot \left(\boldsymbol{n} \cdot \underline{\underline{D}}(h_{CR,gz},T_{gz})\nabla\underline{\underline{\psi}}_m\right) dS_{gz} + \right. \\
&\quad \left. + \int \underline{\underline{\xi}}_i \cdot \underline{\underline{\Sigma}}_a(h_{CR,gz},T_{gz}) \cdot \underline{\underline{\psi}}_m d\Omega_{gz} + \int \underline{\underline{\xi}}_i \cdot \underline{\underline{\Sigma}}_s(h_{CR,gz},T_{gz}) \cdot \underline{\underline{\psi}}_m d\Omega_{gz} \right] = \\
&= \sum_{gz} \left[\underline{\underline{D}}(h_{CR,gz},T_{gz}) \int \nabla\underline{\underline{\xi}}_i \cdot \nabla\underline{\underline{\psi}}_m \, d\Omega_{gz} + \underline{\underline{\Sigma}}_a(h_{CR,gz},T_{gz}) \int \underline{\underline{\xi}}_i \cdot \underline{\underline{\psi}}_m \, d\Omega_{gz} + \right. \\
&\quad \left. + \underline{\underline{\Sigma}}_s(h_{CR,gz},T_{gz}) \int \underline{\underline{\xi}}_i \cdot \underline{\underline{\psi}}_m \, d\Omega_{gz} \right] + \gamma_r \int_{\partial\Omega_r} \underline{\underline{\xi}}_i \cdot \underline{\underline{\psi}}_m dS_r + \gamma_a \int_{\partial\Omega_a} \underline{\underline{\xi}}_i \cdot \underline{\underline{\psi}}_m dS_a
\end{aligned} \tag{2.18}$$

where the Green's first identity is applied to the diffusion operator and, in the final form, the corresponding surface integrals can be computed only on the radial $\partial\Omega_r$ and axial boundary $\partial\Omega_a$ of the domain. Moreover, the summation is carried out over the zones which the domain is divided in.

In a control-oriented perspective, it is fundamental that the model provides three integral quantities of interest, i.e., the neutron flux, the fission power and the reactivity. These quantities

are not directly available from the Equations (2.15) and (2.16) and additional calculations are needed.

The neutron flux can be evaluated through the integrals of the spatial basis function suitably normalized. Indeed, the spatial basis function does not report any information about the actual value, the neutron flux being normalized during the offline computation. The information can be retrieved by calculating a reference flux ϕ^{ref}, i.e., referred to the unperturbed initial condition. In this way, the neutron flux reads as

$$\underline{\phi}(t) = K\,\phi^{ref} \sum_{j=1}^{N} \left[\left(\int \underline{\underline{\psi}}_j d\Omega \right) \cdot \underline{n}_j(t) \right] \tag{2.19}$$

where the constant K is computed so as to respect the initial condition $\Phi(0) = \phi^{\mathrm{ref}}$.

As far as the fission power is concerned, this value can be retrieved from the neutron flux in the fuel zone, previously calculated for the reactivity feedback assessment.

$$q(t) = K\,\phi^{ref} V \sum_{z=fuel} \sum_{j=1}^{N} \left[\left(\int E_f \underline{\underline{\Sigma}}_f \cdot \underline{\underline{\psi}}_j d\Omega_z \right) \cdot \underline{n}_j(t) \right] \tag{2.20}$$

Finally, the reactivity can be monitored both to assess the capabilities of the spatial neutronics model compared with other approaches, and to monitor this relevant quantity during the simulated transients. The system reactivity can be estimated via the Inverse Method (Duderstadt and Hamilton, 1976). Nevertheless, this method is not particularly suitable in case of sharp time-dependent variation of the reactivity since it exploits the concept of "stable period". A formulation similar to the reactivity assessment in transport theory can be proposed (Henry, 1975), exploiting the choice of the adjoint as test functions.

$$\rho(t) = \frac{\int d\Omega \phi^{\dagger} \left[\mathcal{L}\phi + \left[(1-\beta)\chi_p + \beta\chi_d \right] \mathcal{F}\phi \right]}{\int d\Omega \phi^{\dagger} \left[\left[(1-\beta)\chi_p + \beta\chi_d \right] \mathcal{F}\phi \right]} \tag{2.21}$$

According to the spatial neutronics model, Equation (2.21) can be formulated as follows:

$$\rho(t) = \frac{\underline{n}^T \cdot \left[\underline{\underline{A}}_{1,np} + \underline{\underline{A}}_{1,p} + \beta \underline{\underline{A}}_{md} \right] \cdot \underline{n}}{\underline{n}^T \cdot \left[(1-\beta) \underline{\underline{A}}_{mp} + \beta \underline{\underline{A}}_{md} \right] \cdot \underline{n}}$$

$$\underline{\underline{A}}_{md} = \begin{bmatrix} \underline{\underline{X}} \cdot \left(\underline{\underline{M}}_{11} + \underline{\underline{\delta M}}_{11} \right) & \cdots & \underline{\underline{X}} \cdot \left(\underline{\underline{M}}_{1N} + \underline{\underline{\delta M}}_{1N} \right) \\ \vdots & \ddots & \vdots \\ \underline{\underline{X}} \cdot \left(\underline{\underline{M}}_{N1} + \underline{\underline{\delta M}}_{N1} \right) & \cdots & \underline{\underline{X}} \cdot \left(\underline{\underline{M}}_{NN} + \underline{\underline{\delta M}}_{NN} \right) \end{bmatrix} \tag{2.22}$$

$$\underline{\underline{A}}_{mp} = \begin{bmatrix} \underline{\underline{M}}_{11} + \underline{\underline{\delta M}}_{11} & \cdots & \underline{\underline{M}}_{1N} + \underline{\underline{\delta M}}_{1N} \\ \vdots & \ddots & \vdots \\ \underline{\underline{M}}_{N1} + \underline{\underline{\delta M}}_{N1} & \cdots & \underline{\underline{M}}_{NN} + \underline{\underline{\delta M}}_{NN} \end{bmatrix}$$

2.3. ALFRED pin test case

Initially, the spatial neutronics model is tested on a test case involving three fuel pins of the ALFRED reactor (Figure 2.2). The main fuel pin data are reported in Table A.1.The focus of this test case is:

- to demonstrate the feasibility of the approach proposed in the Section 2.2;
- to assess the better performance of the spatial neutronics model with respect to the classic Point Kinetics approach;
- to show how the spatial neutronics model can be implemented in an object-oriented simulator and to implement a new heat transfer pin model suitable for the purpose.

Accordingly, for this simple case, only the Case B is studied[7] considering as spatial basis functions the eigenfunctions associated with the neutron diffusion equation calculated in a reference configuration. As suitable test functions, the eigenfunctions of the adjoint generalized problem associated to Equation (2.10) are employed as they are related to the neutron importance.

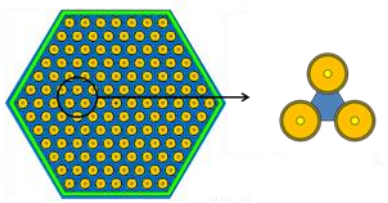

Figure 2.2. The ALFRED sub-channel adopted as a case study.

2.3.1 The offline procedure

In order to solve the eigenvalue problem and its adjoint, the neutronic parameters of the six energy groups (see Table 2.2 for the energy group boundaries) are assessed by means of SERPENT, using the nuclear data library JEFF 3.1. The isotopic composition of the input materials related to the ALFRED fuel pin is shown in Table 2.3.

Table 2.2. Energy group boundaries adopted in multi-group diffusion equations.

Group	Upper boundary	Lower boundary
1	20 MeV	2.23 MeV
2	2.23 MeV	0.82 MeV
3	0.82 MeV	67.38 keV
4	67.38 keV	15.03 keV
5	15.03 keV	0.75 keV
6	0.75 keV	0 keV

The group constants are obtained after runs of 10 million active neutron histories. Simulations consist of 500 active cycles of $2 \cdot 10^4$ neutrons, leading to a standard deviation lower than 3% for all the computed parameters. Fifty inactive cycles are adopted to ensure the convergence of the fission source distribution employed for the active cycles. As far as the SERPENT model is concerned, an infinite lattice of pins is simulated on the transversal xy plane (Figure 2.3a). In particular, periodic boundary conditions in radial direction are set, i.e. neutron escaping from the

[7] The choice of the spatial basis and the test function is evaluated in the next Section.

domain is moved to the opposite side of the geometry. Above and below the active region (Figure 2.3b,c), lead reflectors are adopted. Several SERPENT simulations have been carried out at different fuel and lead temperatures to derive the trend of the temperature and density dependent cross-sections and diffusion coefficients.

Table 2.3. Isotopic composition of the serpent input materials.

Fuel (Sobolev et al., 2009)		Cladding (Gavoille et al., 2013)		Lead (NIST)	
Isotope	wt%	Isotope	wt%	Isotope	wt%
U-234	0.0019	C-nat	0.09	Pb-204	1.40
U-235	0.2643	Mn-55	1.5	Pb-206	24.1
U-236	0.0065	Si-nat	0.8	Pb-207	22.1
U-238	65.1782	Cr-nat	15	Pb-208	52.4
Pu-238	0.5335	Ni-nat	15		
Pu-239	13.0079	Mo-nat	1.5		
Pu-240	6.1746	P-31	0.04		
Pu-241	1.3962	Ti-nat	0.4		
Pu-242	1.7594	B-nat	0.006		
O-16	11.6775	Fe-nat	65.67		

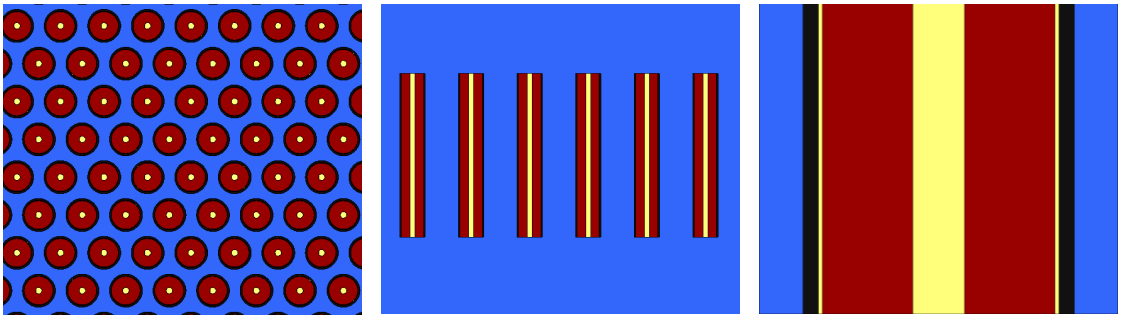

(a) (b) (c)

Figure 2.3. xy view (a), yz view (b) and its zoom (c) of the SERPENT model of the ALFRED pin test case.

The calculation of the eigenfunctions and adjoint eigenfunctions of the neutron diffusion equation with six energy groups are performed through the Finite Element COMSOL Multiphysics software (Figure 2.4a). The mesh employed (Figure 2.4b) features a 3D geometry using Lagrangian and linear-order triangular prism and hexahedral elements. In this way, a good compromise between numerical accuracy and computational requirements is achieved, confirmed by a mesh sensitivity test as well. The outcomes of the SERPENT simulations are converted to a COMSOL readable format by adopting a dedicated procedure, which allows obtaining a set of temperature dependent cross-sections and diffusion coefficients. Once the cross-sections set is introduced in COMSOL as input, the γ_a coefficient of Equation (2.14) is calculated to have the same effective multiplication factor in both COMSOL and SERPENT models at nominal conditions. Conversely, the γ_r coefficient of Equation (2.14) is set to allow for the radial leakage term and calculated to bring the system critical.

A “reference model” implementing the multi-group diffusion equations, Equations (2.1) and (2.2), has been developed in COMSOL and coupled with a heat transfer model in order to obtain a reference solution for the assessment of the spatial neutronics model both in static and dynamic conditions. The heat transfer model can be described in a general form as follows:

$$dc_p \frac{\partial T}{\partial t} + dc_p \boldsymbol{v} \cdot \nabla T = \nabla \cdot (k \nabla T) + Q''' \tag{2.23}$$

where the second term in the left side is present only in the lead zone with a constant velocity and the source term Q''' is present only in the fuel zone.

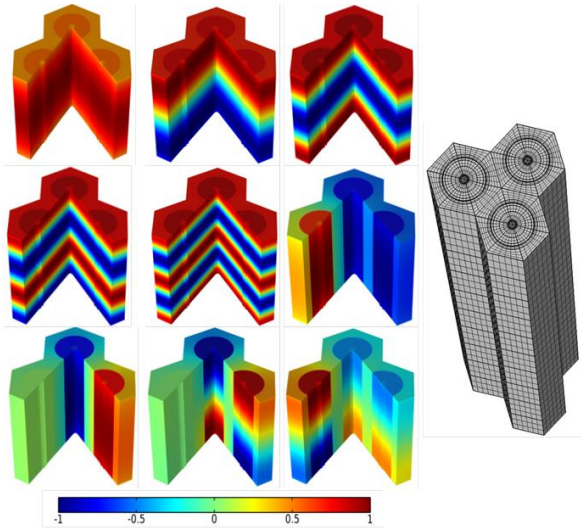

(a) (b)

Figure 2.4. (a) The first nine neutronics spatial modes (normalized flux) and (b) computational mesh of the test case.

2.3.2. The object-oriented modelling

The control-oriented tool of the ALFRED test case has been developed adopting the object-oriented modelling, based on the Modelica language. The overall model (Figure 2.5) is built by connecting different components.

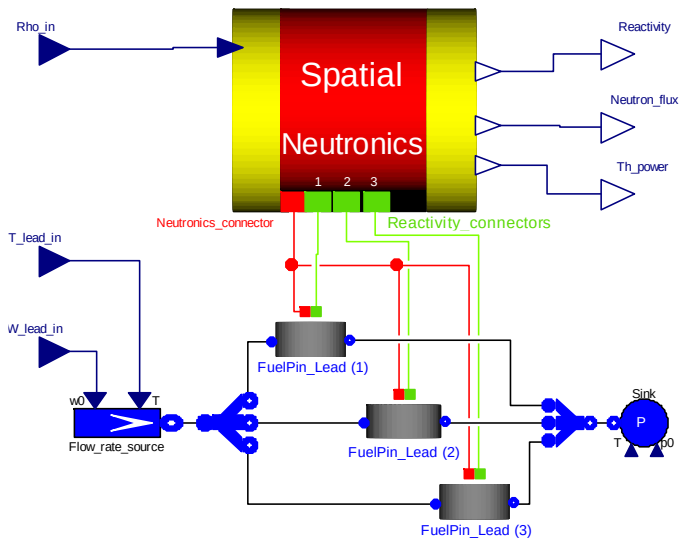

Input variables	Definition
T_Lead_in	Lead inlet temperature
W_Lead_in	Lead mass flow rate
Rho_in	External reactivity
Output variables	**Definition**
Reactivity	Total reactivity system
Neutron_flux	Neutron flux
Th_Power	Thermal power

Figure 2.5. Object-oriented model of the test case.

In particular, the two main components are the *Spatial Neutronics* (SN) and the *FuelPin_Lead*, the latter being the component describing the heat transfer inside a fuel pin and the surrounding

lead. For the most conventional components (i.e., the mass flow rate source, the sink, …) the *ThermoPower* library is employed (Casella et al., 2006).*Spatial Neutronics component*

The Spatial Neutronics component employs a kinetics model based on the approach described in Section 2.2. In particular, the set of Equations (2.16) and (2.17) are implemented with the Modelica language (Figure 2.6).

```
Model Spatial Neutronics
    import Neutronica_Spaziale.Models_Base.Funzioni.MM_reactivity;
    constantNeutronica_Spaziale.Interfaces.KineticParameters_red KP1=Neutronica_Spaziale.GroupKinetics_
    red.EightGroupKinetics_red;
    parameter Modelica.SIunits.Energy E_f=3.2e-11
    parameter Real Flux_0=1.2290e19;
    parameter Integer N_eigen=10;
    parameter Real N_0[N_eigen*KP1.N_groups,1]=[1;1;1;1;1;1];
    parameter Real C_0[N_eigen*KP1.N_groups*KP1.NPG,1]=[3.994738e-008;…;2.150385e-011];
    parameter Real A1NP[N_eigen*KP1.N_groups,N_eigen*KP1.N_groups]=[-1.385680e+008,…,-3.248002e+006];
    parameter Real A1NP_rho[N_eigen*KP1.N_groups,N_eigen*KP1.N_groups]=[-1.655627e+008,…,-
    3.248026e+006];
    parameter Real
    A2NP[N_eigen*KP1.N_groups,N_eigen*KP1.N_groups*KP1.NPG]=[3.625754e+009,0…,3.809446e+012];
    parameter Real A3NP[N_eigen*KP1.N_groups*KP1.NPG,N_eigen*KP1.N_groups]=[8.141488e-011,…,1.713675e-
    013];
    parameter Real A4NP[N_eigen*KP1.N_groups*KP1.NPG, N_eigen*KP1.N_groups*KP1.NPG]=[-1.246670e-
    002,…,-3.5546];
    parameter Real npsi[N_eigen*KP1.N_groups,1]=[5.422535e-002;…;2.361061e-003];
    parameter Real npsi_energy[N_eigen*KP1.N_groups,N_eigen*KP1.N_groups]=[1,…,1];
Real C[N_eigen*KP1.N_groups*KP1.NPG,1];
Real npsi_n[N_eigen*KP1.N_groups,1];
Modelica.Blocks.Interfaces.RealOutput n_norm;
Modelica.Blocks.Interfaces.RealOutput rho;
Modelica.Blocks.Interfaces.RealOutput flux;
Neutronica_Spaziale.Interfaces.Neutronics n_i(N=10, N_eigen=N_eigen)
Modelica.Blocks.Interfaces.RealInput rho_in;
Interfaces.Reactivity React_Pin_1;
Interfaces.Reactivity React_Pin_2;
Interfaces.Reactivity React_Pin_3;
equation
    der(n_i.n) = ((A1NP-A1NP_rho*rho_in)/(1-rho_in))*n_i.n+
    + React_Pin_1.Pert_L+ React_Pin_2.Pert_L+ React_Pin_3.Pert_L + A2NP*C;
    der(C) = (A3NP/(1-rho_in))*n_i.n+ React_Pin_1.Pert_M+ React_Pin_2.Pert_M+
    React_Pin_3.Pert_M+A4NP*C;
    for i in 1:N_eigen*KP1.N_groups loop
        npsi_n[i,1] = n_i.n[i,1]*npsi[i,1];
    end for;
    n_norm = sum(npsi_energy*npsi_n);
    rho=SN_reactivity(n_i.n, Pert_L_tot, Pert_M_tot, rho_in, N_eigen);
    flux=n_norm*Flux_0;
initial equation
    n_i.n=N_0;
    C=C_0;
End Spatial Neutronics;
```

Figure 2.6. Modelica code of the *Spatial Neutronics* component.

The temperatures are calculated in the *FuelPin_Lead* component and the reactivity feedback information shared with the *Spatial Neutronics* component by means of the green connectors (see Figure 2.5). On the other hand, the information about the evolution of the time-dependent coefficient n_i of the neutronics model is shared thanks to the red connector (see Figure 2.5). For

the neutronics calculation, the geometry is divided in 4 radial coarse zones (three for the fuel, inner, central and outer, and one for the lead) and in 10 evenly spaced axial coarse zones.

FuelPin_Lead component

The *FuelPin_Lead* component, divided in the *FuelPinHT* and the *LeadTube* sub-components, is devoted to the evaluation of the dynamic behaviour of the fuel pin and lead temperatures (Figure 2.7). The modelling of the heat transfer is of paramount importance since the temperature field appears in the reactivity assessment (see Equation (2.18)).

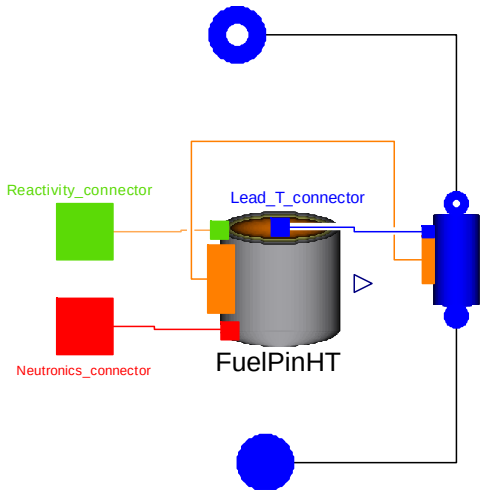

Figure 2.7. Object-oriented model of the *FuelPin_Lead* component.

The *FuelPinHT* component is dedicated to the heat transfer in the fuel rods, adopting radial regions within the element. This component has been conceived *ad-hoc* in order to obtain some advisable features (i.e., modularity, reusability and efficiency) in an object-oriented perspective. Differently from the heat transfer model described in Section 1.2.1, it allows selecting the number of the fuel, cladding and gap zone which the pin is divided in. In this way, the reusability of the model is enhanced and the heat transfer modelling can employ a geometrical division coherent with the neutronics model. In addition, a better accuracy during the transient behaviour is envisaged.

In the component, the reactivity feedback is calculated and shared with the *Spatial Neutronics* by means of a proper connector. As for the power, it is calculated thanks to the information of the evolution of the n_i coefficient (Equation (2.20)). The *LeadTube* is made by a standard component of the *ThermoPower* library modelling the coolant flowing through the core channels (represented as cylindrical conduits). Hereinafter, the attention is focused on the *FuelPinHT* modelling, whereas for the *LeadTube* component, the reader can refer to the Section 1.2.1.

As far as the *FuelPinHT* modelling is concerned, the time-dependent Fourier equation (Equation (2.24)) is applied considering only the radial heat transfer, thus disregarding both the axial and the circumferential thermal diffusion. The equation is discretized radially in different cylindrical zones and longitudinally in a user-defined number of nodes (Figure 2.8).

$$dc_p \frac{\partial T}{\partial t} = \nabla \cdot (k \nabla T) + Q''' \tag{2.24}$$

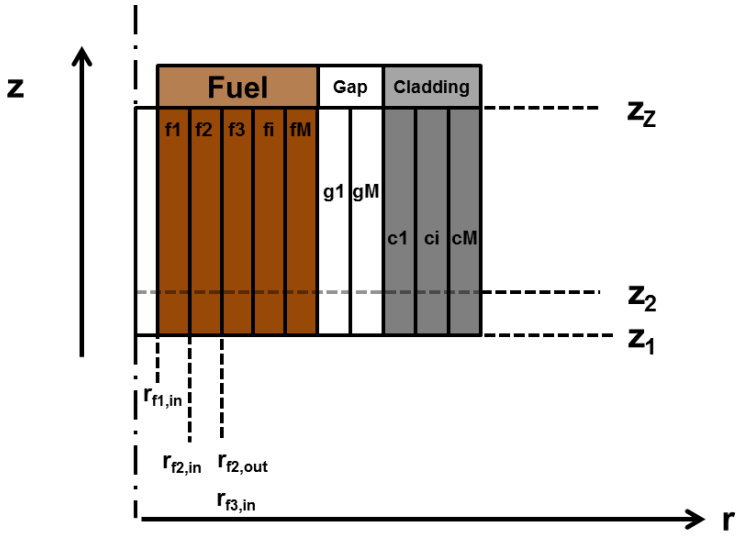

Figure 2.8. Axial and radial discretization of the fuel pin.

The common discretization procedure (Todreas and Kazimi, 2012) is to integrate twice, first performing an indefinite integration and then integrating from r_{in} to r_{out} and T_{in} to T_{out}, which are the inner and the outer radius and temperature of the considered cylindrical zone, respectively. After the first integration, the equation reads:

$$dc_p \frac{dT}{dt}\frac{r}{2} = k\frac{dT}{dr} + Q'''\frac{r}{2} + \frac{C}{r} \tag{2.25}$$

where C represents the constant of the indefinite integration. In order to set a value for the constant, a boundary condition is applied on the heat flux at r_{in} or r_{out}. In particular, for the inner zone, the vanishing of the flux at r_{in} is set:

$$q''_{f1}\Big|_{r=r_{f1,in}} = -k\frac{dT_{f1}}{dr}\Big|_{r=r_{f1,in}} = 0 \tag{2.26}$$

On the other hand, for the other zones, the continuity of the heat flux between adjacent zones is used for determining the constant. For example, between two generic adjacent zones *f2* and *f3*:

$$q''_{f2}\Big|_{r=r_{f2,out}} = q''_{f3}\Big|_{r=r_{f3,in}} \rightarrow -k\frac{dT_{f2}}{dr}\Big|_{r=r_{f2,in}} = -k\frac{dT_{f3}}{dr}\Big|_{r=r_{f3,out}} \tag{2.27}$$

Usually, in the determination of the C constant, the term in Equation (2.25) involving the time derivative is neglected since this procedure is normally applied for stationary calculation. Notwithstanding, as far as dynamics simulation is concerned, the time-dependent behaviour is relevant and this aspect cannot be left apart. For example, for the inner zone *f1*, the constant C reads:

$$C_{f1} = -Q'''\frac{r_{f1,in}^2}{2} + dc_p\frac{dT}{dt}\frac{r_{f1,in}^2}{2} \tag{2.28}$$

where the second right term allows for the transient behaviour of the temperature. For the other zones, it is possible to express the constant in a recursive way, starting from the C of the inner adjacent zone:

$$C_{f3} = C_{f2} + \left[\left(Q'''_{f2} - Q'''_{f3}\right) - \left(d_{f2}c_{p,f2}\frac{dT_{f2}}{dt} - d_{f3}c_{p,f3}\frac{dT_{f3}}{dt}\right)\right] \cdot \frac{r_{f3,in}^2}{2} \tag{2.29}$$

The heat equation, after the final integration, reads:

$$dc_p\frac{dT}{dt}\frac{r_{out}^2 - r_{in}^2}{4} = k(T_{out} - T_{in}) + Q'''\frac{r_{out}^2 - r_{in}^2}{4} + C \cdot log\left(\frac{r_{out}}{r_{in}}\right) \tag{2.30}$$

As closure equation for the temperature T, a volume averaged expression is adopted:

$$T = T_{in} - \frac{r_{out}^2 - r_{in}^2}{8k}\left(Q''' + dc_p\frac{dT}{dt}\right) - \frac{C}{k}\left(\frac{r_{out}^2}{r_{out}^2 - r_{in}^2}log\left(\frac{r_{out}}{r_{in}}\right) - \frac{1}{2}\right) \tag{2.31}$$

The presented procedure allows an extremely high degree of flexibility since the user can select the number of the radial and axial zones of the fuel pin discretization, optimizing the balance between model accuracy and time simulation cost. For the present case, in order to be coherent with the neutronics modelling, three zones for the fuel are selected, one for gap and cladding. For each radial zone, Equation (2.30) is implemented and discretized in Z nodes, specifying the material properties (Luzzi et al., 2014) and whether it is a fuel zone or not (Figure 2.10). Once established the number and the type of the zones, the modelling is completed specifying in a recursive way the integration constant (see Equations (2.28) and (2.29)). The stand-alone *FuelPinHT* component has been tested by means of a comparison with the heat transfer model developed in COMSOL (Equation (2.23)). The results are very satisfactory, especially considering the good agreement reached during the transient (Figure 2.9).

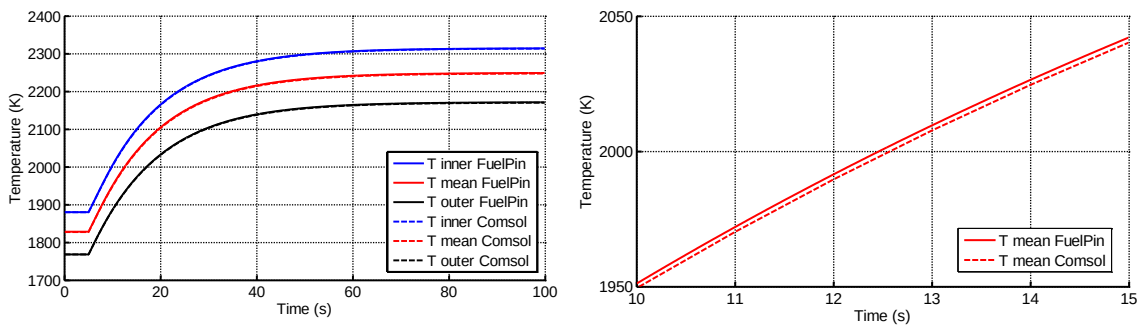

(a) (b)

Figure 2.9. Comparison between the COMSOL heat transfer model and the *FuelPinHT* component results.

```
partial model FuelPinHT
    import Modelica.Math; import Spatial_Neutronics;
    replaceable package Prop_F = Material_Model.ALFRED_MOX;
    replaceable package Prop_C = Material_Model.ALFRED_Ti1515;
    replaceable package Prop_G = Material_Model.ALFRED_Gap;
    model Fuel = Spatial_Neutronics.NuKomp.Thermal.Components.Fuel_zone;
    model Non_Fuel = Spatial_Neutronics.NuKomp.Thermal.Components.Non_Fuel_zone;
    parameter Integer N=11; parameter Integer M=3; parameter Integer M_gap=1;
    parameter Integer M_clad=1; parameter Length R_hole; parameter Length Rin_fuel[M];
    parameter Length Rout_fuel[M]; parameter Length Rin_gap[M_gap]; parameter Length Rout_gap[M_gap];
    parameter Length Rin_clad[M_clad]; parameter Length Rout_clad[M_clad];
    parameter Boolean steadyStateInit=true; parameter Temperature T_fuel_start[M];
    parameter Temperature T_gap_start[M_gap]; parameter Temperature T_clad_start[M_clad];
    Fuel Pin[M]; Non_Fuel Gap[M_gap]; Non_Fuel Clad[M_clad];
equation
for j in 1:N loop
    Pin[1].Cost[j]=(Pin[1].qvol[j]-
    Prop_F.rho(Pin[1].T[j])*Prop_F.cp(Pin[1].T[j])*der(Pin[1].T[j]))*Pin[1].r_in^2/2;
    Gap[1].Cost[j]=Pin[M].Cost[j]+(Prop_F.rho(Pin[M].T[j])*Prop_F.cp(Pin[M].T[j])*der(Pin[M].T[j])-
    Prop_G.rho(Gap[1].T[j])*Prop_G.cp(Gap[1].T[j])*der(Gap[1].T[j])-Pin[M].qvol[j])*Gap[1].r_in^2/2;
    Clad[1].Cost[j]=Gap[M_gap].Cost[j]+(Prop_G.rho(Gap[M_gap].T[j])*Prop_G.cp(Gap[M_gap].T[j])*der(Gap[
    M_gap].T[j])-Prop_C.rho(Clad[1].T[j])*Prop_C.cp(Clad[1].T[j])*der(Clad[1].T[j]))*Clad[1].r_in^2/2;
    Pin[M].T_out[j]=Gap[1].T_in[j];
    Gap[M_gap].T_out[j]=Clad[1].T_in[j];
end for;
for i in 2:M loop
    for j in 1:N loop
        Pin[i].Cost[j]=Pin[i-1].Cost[j]+(Prop_F.rho(Pin[i-1].T[j])*Prop_F.cp(Pin[i-1].T[j])*der(Pin[i-
        1].T[j])-Prop_F.rho(Pin[i].T[j])*Prop_F.cp(Pin[i].T[j])*der(Pin[i].T[j])-(Pin[i-1].qvol[j]-
        Pin[i].qvol[j]))*Pin[i].r_in^2/2;
        Pin[i].T_in[j]=Pin[i-1].T_out[j];
    end for;
end for;
for i in 2:M_gap loop
    for j in 1:N loop
        Gap[i].Cost[j]=Gap[i-1].Cost[j]+(Prop_G.rho(Gap[i-1].T[j])*Prop_G.cp(Gap[i-1].T[j])*der(Gap[i-
        1].T[j])-Prop_G.rho(Gap[i].T[j])*Prop_G.cp(Gap[i].T[j])*der(Gap[i].T[j]))*Gap[i].r_in^2/2;
        Gap[i].T_in[j]=Gap[i-1].T_out[j];
    end for;
end for;
for i in 2:M_clad loop
    for j in 1:N loop
        Clad[i].Cost[j]=Clad[i-1].Cost[j]+(Prop_C.rho(Clad[i-1].T[j])*Prop_C.cp(Clad[i-
        1].T[j])*der(Clad[i-1].T[j])-
        Prop_C.rho(Clad[i].T[j])*Prop_C.cp(Clad[i].T[j])*der(Clad[i].T[j]))*Clad[i].r_in^2/2;
        Clad[i].T_in[j]=Clad[i-1].T_out[j];
    end for;
end for;
for j in 1:N loop
    Clad[M_clad].r_out*RodWall.phi[j]=Clad[M_clad].Cost[j]+Prop_C.rho(Clad[M_clad].T[j])*Prop_C.cp(Clad
    [M_clad].T[j])*der(Clad[M_clad].T[j])*Clad[M_clad].r_out^2/2;
    RodWall.T[j]=Clad[M_clad].T_out[j];
end for;
end FuelPinHT;
```

Figure 2.10. Modelica code of the *FuelPinHT* component.

2.3.3. Simulation results

The capabilities of the proposed object-oriented tool is evaluated in two different kinds of simulation. The first is devoted to the reactivity evaluation to assess how the *Spatial Neutronics* component can predict the reactivity variation. The model performance is evaluated against the reference model (i.e., the multi-group diffusion equations) and the classic Point Kinetics. The second type of simulation concerns the dynamic behaviour of the system. In particular, the object-oriented model is compared to the reference model during some typical transients, i.e., an enhancement of the lead inlet temperature and an externally imposed reactivity insertion.

Reactivity comparison

One of the main requirements of a control-oriented simulator is to accurately evaluate the reactivity variation following a temperature change. Accordingly, the capability of the SN component to correctly reproduce this trend is assessed in several cases imposing an arbitrary temperature variation and reporting the reactivity insertion (or extraction) due to the resulting cross-section variation (see Equation (2.18)). Since the main purpose is to assess only the reactivity change, the *FuelPin_Lead* is not taken into account, considering the temperature variation as an input for the SN component.

As far as the reference model is concerned, the reactivity variation is evaluated as difference of the first eigenvalues between the unperturbed case and the perturbed one. As far as the SN component is concerned, the reactivity is evaluated according to Equation (2.21). Eventually, the reactivity value related to the PK is assessed in the classic way:

$$\rho_{PK} = \alpha_f \cdot \left(\bar{T}_f - \bar{T}_{f,0}\right) + \alpha_l \cdot \left(\bar{T}_l - \bar{T}_{l,0}\right) \tag{2.32}$$

The fuel and lead reactivity coefficients of Equation (2.32) are obtained from the SERPENT calculation, and the fuel and lead temperature are evaluated as weighted average of the temperature profile of the fuel and lead. Three different temperature profiles are studied as test cases in order to underline the PK limits and the MM potentiality:

(1) Uniform temperature decrease, ΔT_{f1}=-50 K, ΔT_{f2}=-50 K, ΔT_{f3}=-50 K, ΔT_l=-50 K;

(2) Temperature enhancement in a single pin and in the 5th axial slice, i.e., ΔT_{f1}=+400 K, ΔT_{f2}=+300 K, ΔT_{f3}=+200 K, ΔT_l=+100 K;

(3) Shutdown scenario: all the temperature are set equal to the inlet lead temperature (i.e., T=673.15 K).

In Table 2.4, the reactivity inserted in the system for each case and for the three neutronics modelling approaches, (i.e., Point Kinetics, Spatial Neutronics component and the multi-group diffusion PDEs) are shown. For the SN component, seven eigenfunctions are employed as spatial basis. The results show a very good agreement between the value obtained from the reference model and the SN component, assessing the desired capabilities of the proposed model. On the other hand, especially in the test cases 2 and 3, the reactivity assessed by the PK is far away from the other values. In particular, the case 1 shows that the PK is able to properly predict the reactivity inserted in the system whether the perturbation (i.e., the temperature variation) is uniform. Nevertheless, the temperature evolution in operational transient is not uniform. The case 2, representing the extreme opposite case of a strong localized perturbation, is useful to assess the

SN capabilities and the PK limit. The case 3 is relevant since represents an operational situation, i.e., all the temperature are brought to 400°C as in shutdown condition. In this case, the perturbation is neither localized nor uniform. The PK overestimates the reactivity insertion of almost 8%, whereas the SN value has a very good agreement with the reference one.

Table 2.4. Reactivity comparison results for the three cases studied.

Neutronics modelling approach	Reactivity inserted (pcm)		
	Case 1	Case 2	Case 3
Multi-group diffusion PDEs (reference)	78.4	-25.5	1267.6
Spatial Neutronics component (SN)	78.8	-25.6	1268.9
Point Kinetics (PK)	81	-18.9	1363.8

Transient comparison

Another requirement demanded for a control-oriented simulator is the capability to reproduce the transient behaviour of the main variables of interest (firstly the power, but also the system temperatures and reactivity). For this purpose, in the object-oriented model, the SN component is linked with the *FuelPin_Lead* component so as to provide the dynamic model for the temperature evolution. Two typical transient scenarios are simulated, namely: a 20°C enhancement of the inlet lead temperature and a 100 pcm reactivity insertion. The outcomes of the object-oriented model are compared to the reference time-dependent solution of the multi-group diffusion PDEs (Equations (2.1) and (2.2)). As already mentioned in the Introduction, the computational time of the object-oriented model should fulfil the fast-running request for control-oriented purposes. In Table 2.5, the computational time[8] of the object-oriented model and the reference one for the simulation concerning the enhancement of the inlet lead temperature (simulated time of 50 s) is provided. The following simulations are with five eigenfunctions, achieving a good compromise between accuracy and computational cost.

Table 2.5. Computational time of the object-oriented model compared with the reference model.

Neutronics modelling approach	Computational time			
Multi-group diffusion PDEs (reference)	40 h			
Object-oriented model	*N=1*	*N=3*	*N=5*	*N=10*
	10 s	23 s	45 s	143 s

Enhancement of the inlet lead temperature. The simulation is performed by rising the inlet lead temperature by 20°C. The system response is well represented by the total pin power shown in Figure 2.11, where the outcomes of the object-oriented model (solid line) and the reference model developed in COMSOL (dashed line) are presented. The satisfactory agreement confirms the capabilities of the developed tool also in transient simulation. Due to the increase in the lead temperature entering the channel (Figure 2.12), a positive reactivity is inserted in the system (Figure 2.13). After 1-2 seconds, the negative reactivity insertion, mainly due to the Doppler effect caused by the increase of the fuel temperature, sets the power to a lower level (Figure 2.11).

[8] The object-oriented model has been run with a laptop (2.20 GHz, 8 GB RAM). The multi-group diffusion PDEs have been solved with a workstation (8 x 2.8 GHz, 64 GB RAM).

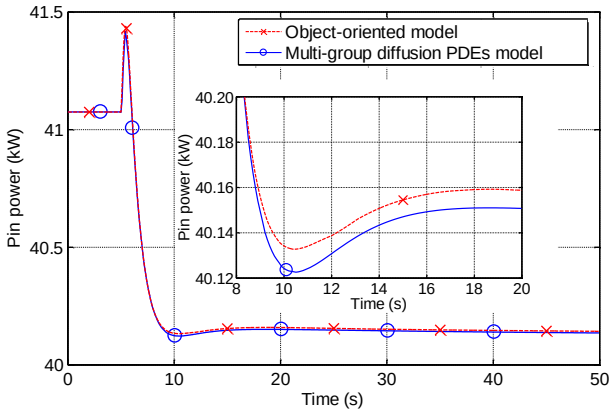

Figure 2.11. Pin power variation following a lead inlet temperature enhancement.

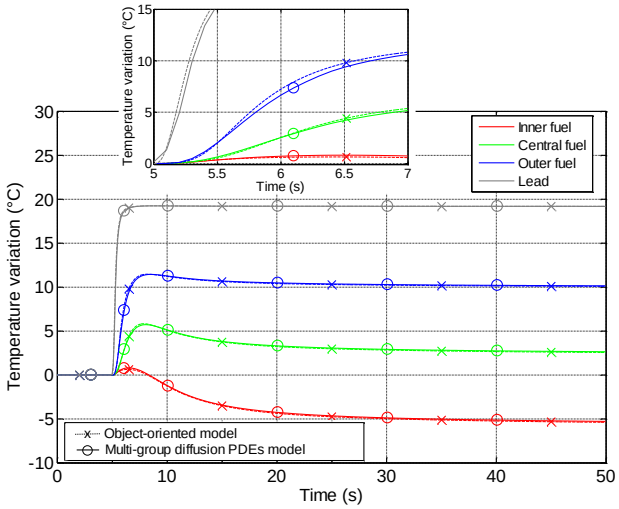

Figure 2.12. Fuel and lead temperature variations following a lead inlet temperature enhancement.

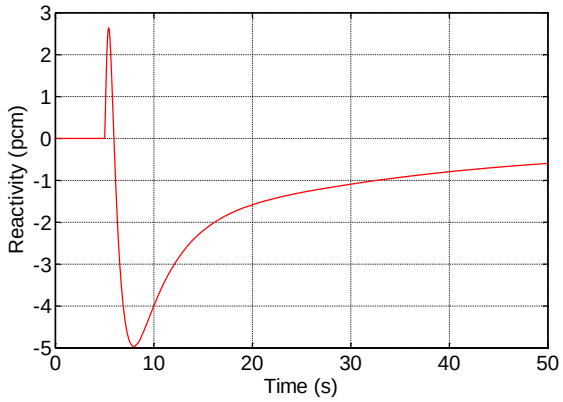

Figure 2.13. Reactivity variation following a lead inlet temperature enhancement.

Reactivity insertion. A reactivity insertion of 100 pcm is simulated. As in the previous case, the figure of merit for the comparison between the object-oriented model (dashed line) and the reference model (solid line) is the pin power (Figure 2.14). A good agreement between the object-oriented model and the reference model also for this simulation is achieved. After the prompt

power increase, the corresponding enhancement of the fuel temperature (Figure 2.15) introduces a negative reactivity limiting the power and restoring the criticality (Figure 2.16).

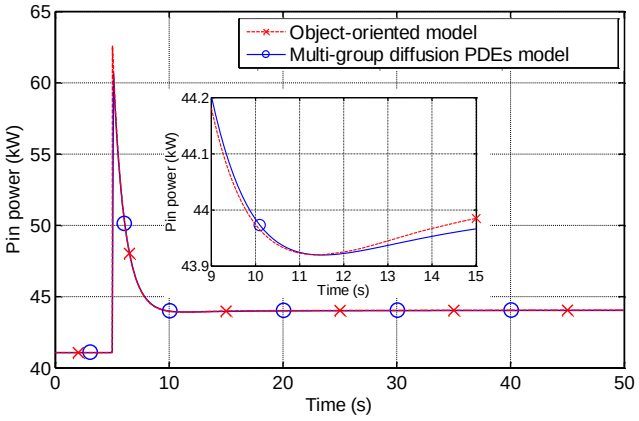

Figure 2.14. Pin power variation following a reactivity insertion.

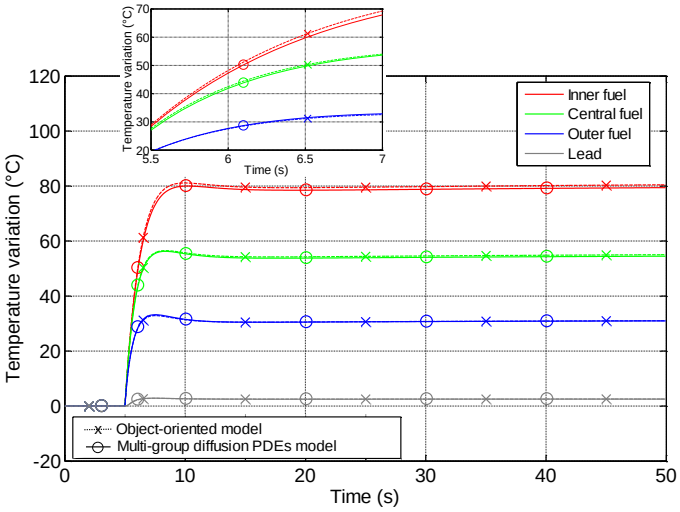

Figure 2.15. Fuel and lead temperature variation following a reactivity insertion.

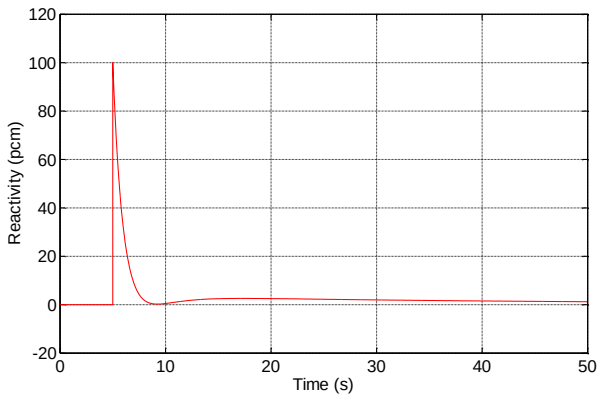

Figure 2.16. Reactivity variation following a reactivity insertion.

2.4. ALFRED full core model

Once having evaluated the capabilities of the spatial neutronics modelling in a simple case, the attention is focused on the modelling of the entire core of the ALFRED reactor at Fuel Assembly (FA) level (Figure 2.17). In particular, the focus is kept on the capability of the different pairs spatial basis/test function (see Figure 2.1) to correctly reproduce the reactivity due to the thermal feedback and the CR movements.

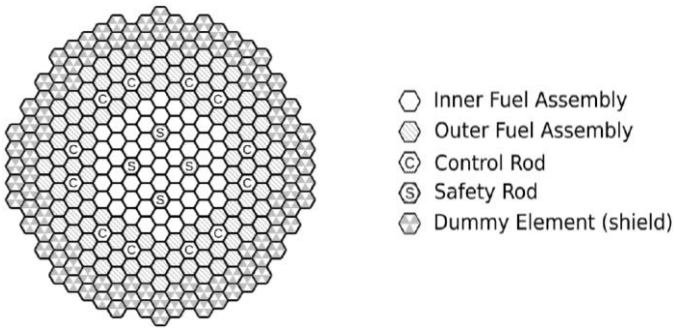

Figure 2.17. The ALFRED core configuration.

2.4.1. The offline procedure

A detailed model of ALFRED is set up with a heterogeneous description of the reactor. The SERPENT model represents the 171 FAs, 110 dummy elements, 12 CRs and 4 SRs, the inner vessel and the surrounding lead (Figure 2.18a). The zones above and below the active zone are also modelled (Figure 2.18b) in order to take into account the CRs and SRs position as well as the contribution of these zones to the reactivity effect (i.e., in particular for the lead density). For the isotopic composition of the input materials concerning ALFRED (fuel, cladding, coolant, control rods), the reader may refer to Table 2.3 and to (Grasso et al., 2014). The group constants of the seven energy group (Table 2.6) are obtained after runs of 150 million active neutron histories. Such a computational effort allows obtaining also information about the flux distribution useful for the comparison with the diffusion model results (Figure 2.19). For further information about the SERPENT model of the ALFRED reactor, the reader may refer to Appendix A.4.

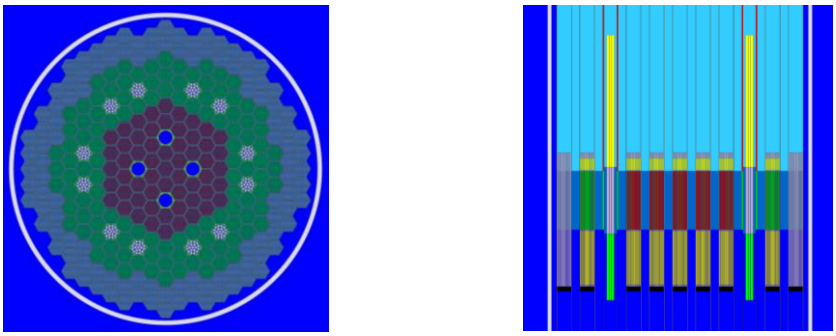

(a) (b)

Figure 2.18. Radial view (a) and longitudinal view (b) of the SERPENT model of the ALFRED reactor.

Several simulations have been carried out at different conditions so as to derive the main reactivity feedback effects of the ALFRED reactor and the CR insertion curve. The results of the

thermal reactivity coefficients are summarized in Table 2.7, and compared to the outcomes of the LEADER Project calculated by means of the deterministic transport code ERANOS (Grasso et al., 2014).

Table 2.6. Energy group boundaries for the generation of the group constant (ALFRED core model).

Group	Upper boundary	Lower boundary
1	20 MeV	2.23 MeV
2	2.23 MeV	0.82 MeV
3	0.82 MeV	0.30 MeV
4	0.30 MeV	67.38 keV
5	67.38 keV	15.03 keV
6	15.03 keV	0.75 keV
7	0.75 keV	0 keV

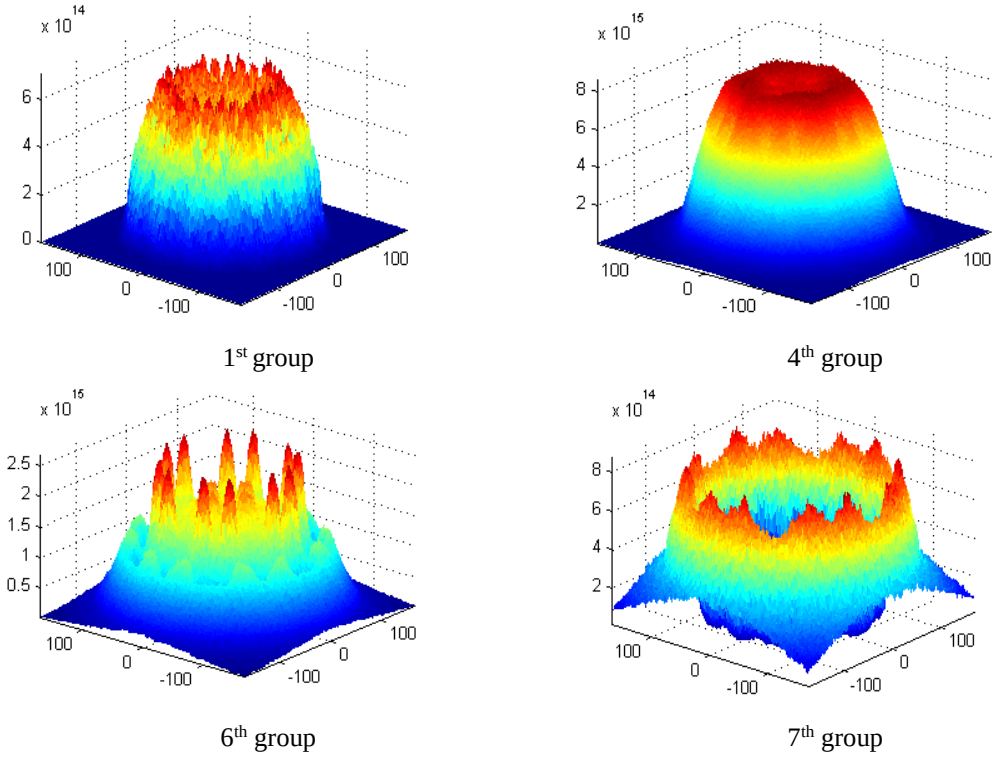

Figure 2.19. Flux distribution in different energy group calculated by means of SERPENT.

Table 2.7. Comparison of the reactivity coefficients, EoC.

	SERPENT	Reference
Doppler constant (pcm)	-549 ± 18	-566
Lead expansion coefficient (pcm/K) Case A[9]	-0.327 ± 0.019	-0.268[10]
Lead expansion coefficient (pcm/K) Case B[4]	-0.268 ± 0.019	-0.268[4]
Axial fuel expansion (pcm/K)	-0.152 ± 0.006	-0.155
Axial cladding expansion (pcm/K)	+0.044± 0.006	+0.037
Axial wrapper expansion (pcm/K)	+0.036± 0.006	+0.022
Radial grid expansion (pcm/K)	-0.780 ± 0.007	-0.789

[9] Calculated considering all the lead inside the inner vessel.
[10] Calculated for the whole height of the fissile subassemblies.

The Doppler effect is calculated decreasing the fuel temperature of 600 K, starting from an unperturbed situation of 1500 K for the inner fuel zone and 1200 K for the outer fuel zone. The lead density effect is computed increasing the lead temperature of 800 K, starting from a unperturbed situation of 673 K (lead below the active core and in dummy elements), 713 K (lead in active core) and 753 K (lead above the active core). An increase of the active length of 2% is considered in order to derive the axial fuel expansion coefficient. Finally, an increase of the FA pitch of 0.5% is employed to calculate the radial grid expansion coefficient. The axial cladding and wrapper expansion are not taken into account in the analysis due to the negligible effect.

As for the CR insertion, SERPENT simulation at different CR height have been performed. The results are shown in Figure 2.20 along with the outcomes of the LEADER Project (obtained by means of the MCNP MonteCarlo code).

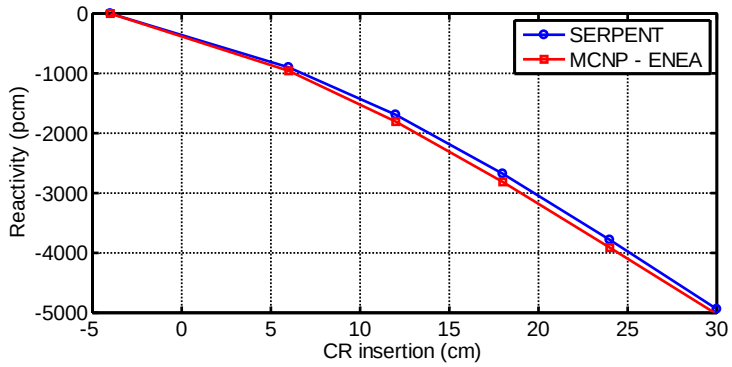

Figure 2.20. Reactivity curve of the control rods, comparison between SERPENT and MCNP result.

In order to obtain the spatial basis and the test functions for the different case (MM with and without adjoint, POD and APOD), the eigenvalue problem of the neutron diffusion PDEs equation and its adjoint are solved adopting the Finite Element COMSOL Multiphysics software. The mesh of the ALFRED core model (Figure 2.21) features a 3D geometry using Lagrangian and linear-order hexahedral elements. The cross-sections calculated by means of SERPENT are homogenized in different zones (Figure 2.22), i.e., 5 for the inner fuel, 5 for the outer fuel, 4 for the SRs, 5 for the CRs and 3 for the dummy elements. As far as the boundary conditions are concerned, the albedo boundary conditions, previously calculated in the SERPENT model, are imposed at the axial and radial boundaries of the COMSOL model domain.

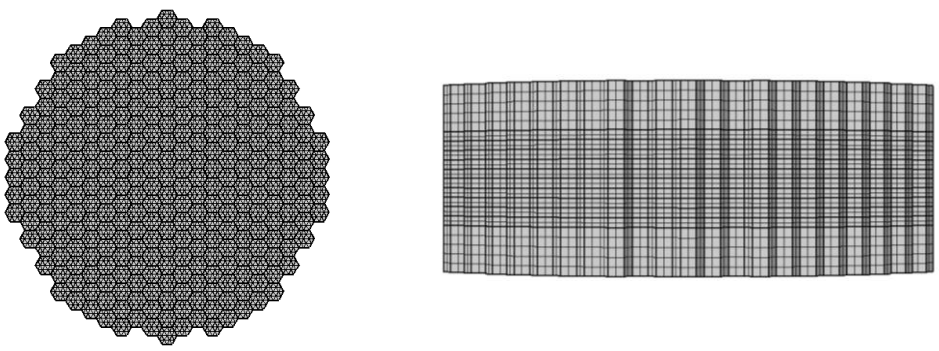

(a) (b)

Figure 2.21. Radial view (a) and longitudinal view (b) of the COMSOL model mesh of the ALFRED reactor.

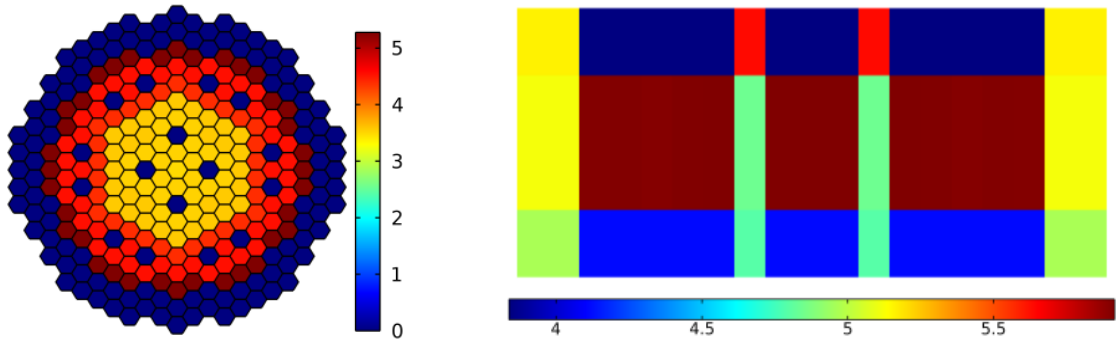

(a) (b)

Figure 2.22. Homogenized production cross-section (m^{-1}) for the 7th energy group (a) and removal cross-section (m^{-1}) for the 1st energy group (b) employed in the COMSOL model.

Eventually, the eigenfunctions (Figure 2.23) and the adjoint eigenfunction are calculated in different configuration of the ALFRED core (different temperature configurations and different CR position) and the procedures described in Section 2.2.2 are applied in order to derive the spatial basis and the test functions for the different case (Table 2.1).

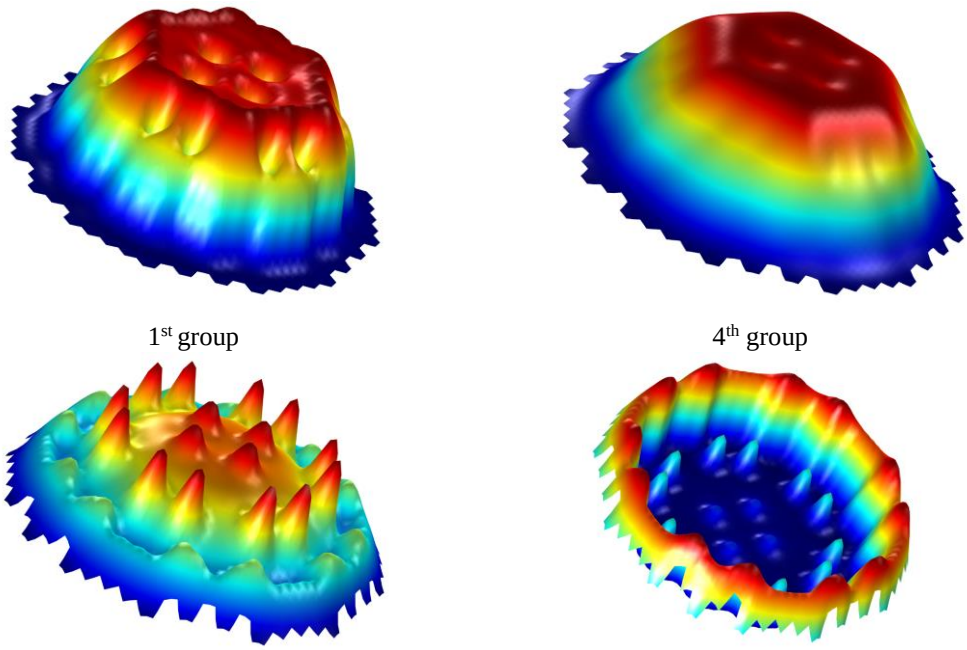

1st group 4th group

6th group 7th group

Figure 2.23. Eigenfunction of different energy group, CR extracted.

2.4.2. Thermal feedback results

In order to assess the temperature reactivity feedbacks by means of the spatial neutronics model, seven simulation cases have been carried out at the conditions described in Section 2.3.2 and summarized in Table 2.8. For each case, SERPENT and COMSOL simulations have been performed in order to obtain the cross-sections and to calculate the spatial basis and the test functions (see Table 2.9).

Table 2.8. Simulation cases carried out to reproduce the reactivity feedbacks.

	Fuel temp. (K) (inner/outer)	Lead temp. (K) (below active zone & dummy/active zone/above active zone)	Active length (cm) (inner/outer)	Fuel density (g/cm^3) (inner/outer)	FA pitch (cm)
Unperturbed	1500 / 1200	673 / 713 / 753	60 / 60	10.443 / 10.47	17.1
Doppler (inner)	900 / 1200	673 / 713 / 753	60 / 60	10.443 / 10.47	17.1
Doppler (outer)	1500 / 600	673 / 713 / 753	60 / 60	10.443 / 10.47	17.1
Lead density	1500 / 1200	1473 / 1513 / 1573	60 / 60	10.443 / 10.47	17.1
Axial fuel expansion (inner)	1500 / 1200	673 / 713 / 753	61.2245 / 60	10.234 / 10.47	17.1
Axial fuel expansion (outer)	1500 / 1200	673 / 713 / 753	60 / 61.2245	10.443 / 10.261	17.1
Radial grid expansion	1500 / 1200	673 / 713 / 753	60 / 60	10.443 / 10.47	17.1855

Table 2.9. First three functions of the spatial bases and test functions for the thermal reactivity effects (in normalized unit).

#	$\underline{\psi}_i$ for Case A,B $\underline{\xi}_i$ for Case A	$\underline{\xi}_i$ for Case B	$\underline{\psi}_i$ for Case C,D $\underline{\xi}_i$ for Case C	$\underline{\xi}_i$ for Case D
1	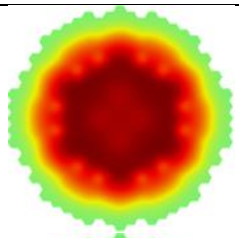	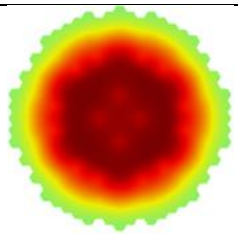	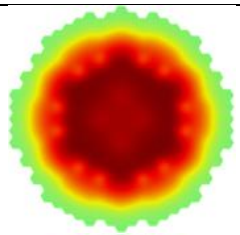	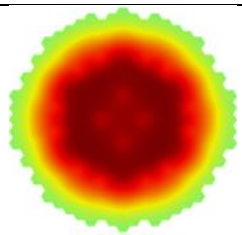
2	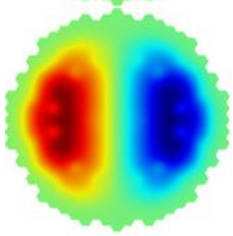	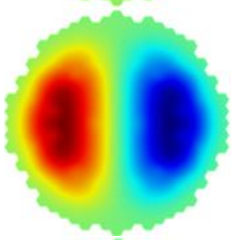	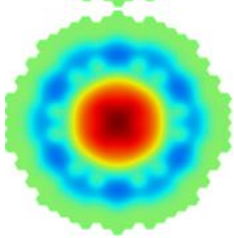	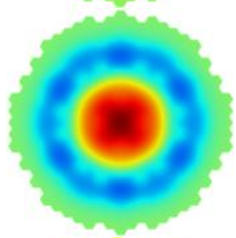
3	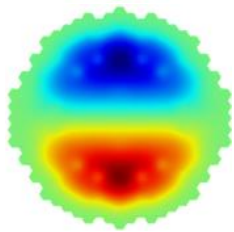	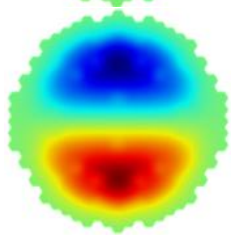	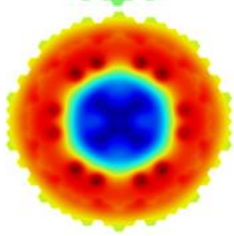	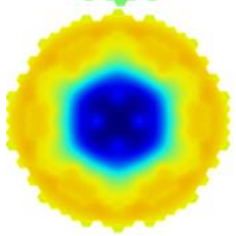

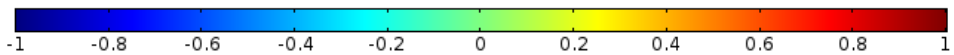

The four pairs of spatial basis/test functions reported in Table 2.1 are implemented and their capability to reproduce the reactivity feedbacks is verified. The reactivity variation between the unperturbed case and the representative simulation of the temperature effect is assessed in terms of global features and spatial distribution in the reactor. For the sake of brevity, only the results regarding the Doppler and the lead density effects are reported in the next subsections. Nevertheless, the other three simulations, regarding the axial and radial expansion, show similar results and lead to the same conclusions. In Table 2.10, the results of the SERPENT and

COMSOL simulations are reported. The discrepancies between the two simulations are acceptable considering the different neutronics approach (i.e., transport for SERPENT and diffusion for COMSOL).

Table 2.10. Simulation cases carried out to reproduce the reactivity feedbacks.

	SERPENT (transport)	COMSOL (diffusion)	Error (%)
Doppler (inner)	128.1±7.5	121.1	5.5
Doppler (outer)	206.7±7.5	224.3	8.5
Lead density	-261.7±7.5	-275.3	5.21
Axial fuel expansion (inner)	-101.5±7.5	-105.6	4
Axial fuel expansion (outer)	-154.6±7.5	-139.1	10
Radial grid expansion	-206.8±7.5	-207	0.11

Doppler effect

Two separate simulations have been performed in order to take into account the different impact of a fuel temperature decrease in different zones of the core (and different enrichments). Since the spatial neutronics model relies on the spatial basis calculated according to the COMSOL outcomes, the result of the diffusion model should be taken as reference. The results of the spatial neutronics model for the different cases are reported in Table 2.11. Five functions for the flux expansion are considered for the Case A, B, C, D. In addition, the result employing seven functions for the Case C is given. The results indicate that the best performance is obtained in Case D (APOD method) and also in Case C (classic POD method) with seven expansion functions. Nevertheless, Case D reaches the same performance of Case C (i.e., exactly reproducing the insertion in the reference) with less functions. This means that, if employed in the spatial neutronics model, the set of ODE based on APOD requires less computational time than the POD one. As far as the Modal Method is concerned, acceptable results are reached only if the adjoint eigenfunctions are employed as test functions (Case B).

Table 2.11. Doppler effect. Reactivity variation (pcm), spatial neutronics model results.

	Case A (N=5)	Case B (N=5)	Case C (N=5)	Case C (N=7)	Case D (N=5)	COMSOL (reference)
Inner zone	46.7	119.1	98.6	121.1	121.1	**121.1**
Outer zone	73.8	221.7	212.0	224.3	224.3	**224.3**

The evolution of the reactivity versus the number of the functions employed[11] is described in Figure 2.24a and Figure 2.24b for the Doppler effect in inner and outer fuel zone, respectively. This analysis is useful to understand how many functions should be included for the flux expansion, giving a figure of merit for the employed methods. In particular, as far as the Modal Method is concerned (Case B), it is clear that no information is brought by the functions upper the first one, i.e., the dominant eigenfunction of the reference configuration. As to the POD and APOD methods, the convergence to the “exact” result is reached using 4 functions for the Case D, conversely for the Case C until the seventh function the behaviour is not satisfactory.

[11] The Case A has been excluded from this analysis since it is not suitable to reproduce the reactivity.

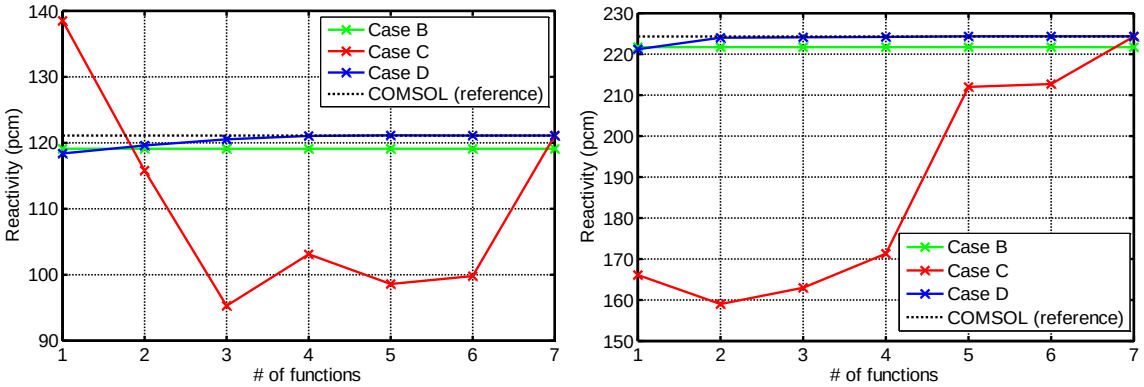

Figure 2.24. Doppler effect in inner fuel zone (a) and outer fuel zone (b). Evolution of the reactivity variation versus the number of functions employed in the model.

One of the major advantage of employing the spatial neutronics model is the possibility to take into account the reactivity spatial distribution, i.e., the temperature feedbacks are locally calculated, improving the model accuracy compared to the classic Point Kinetics. In Figure 2.25a the contribution of each assembly in active zone to the reactivity following a decrease of 600 K in the inner zone is shown. In Figure 2.25b, for the same simulation, a longitudinal view of the reactivity in the ALFRED core is given, highlighting the reactivity axial distribution.

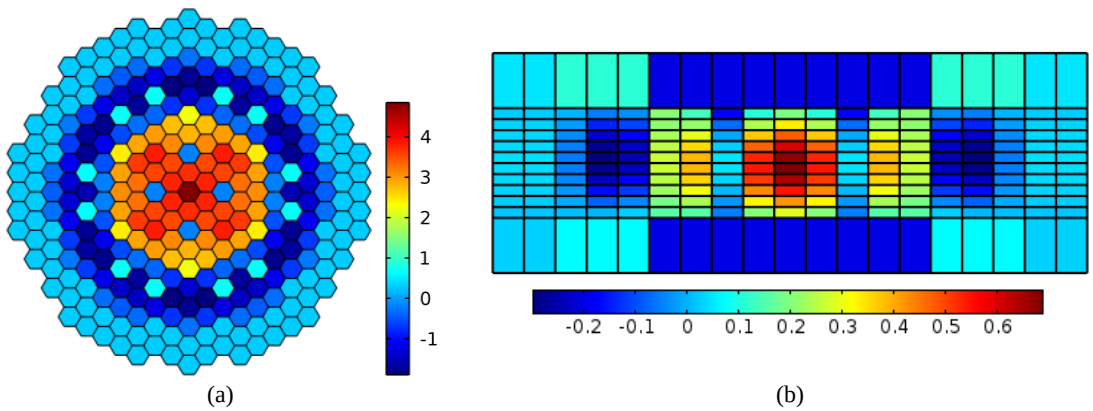

Figure 2.25. Doppler effect. Spatial reactivity (pcm) variation in each assembly in the active zone (a) and along the axial direction (b) calculated with APOD method (Case D).

Lead density effect

The results of the spatial neutronics model in the different cases are reported in Table 2.12. Five functions for the flux expansion have been considered for the Cases A, B, C, D. In addition, the result employing seven functions for the Case C is given. The results are similar to the Doppler simulation. Once again, they indicate that the best performance is obtained in Case D and also in Case C with seven expansion functions, even if Case D obtains the same accuracy with less function. As to the Modal Method, acceptable results are reach only if the adjoint eigenfunctions are employed as test functions (Case B).

Table 2.12. Lead density effect. Reactivity variation (pcm), spatial neutronics model results.

Case A (N=5)	Case B (N=5)	Case C (N=5)	Case C (N=7)	Case D (N=5)	COMSOL (reference)
-559.1	-286.2	-277.4	-275.3	-275.3	-275.3

The evolution of the reactivity versus the number of the functions employed is described in Figure 2.26. Even in this case, the convergence to the reference result is reached by the APOD method (Case D) with less functions compared to the POD method (Case C). It is interesting to notice that for the lead density effect, an acceptable result for the Case C is obtained with three functions. On the other hand, for the Doppler effect relevant discrepancies are observed until the 7th mode is added. Conversely, the APOD method is not affected by this dependence on the convergence to the reference value.

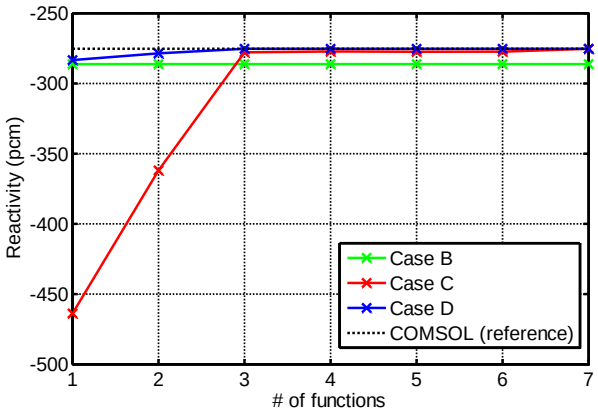

Figure 2.26. Lead density effect. Evolution of the inserted reactivity versus the number of functions employed in the model.

As already mentioned in the Introduction, the lead density effect may be positive or negative according to the zone involved. This spatial effect is taken into account in the spatial neutronics model as represented in Figure 2.27a and Figure 2.27b. In particular, the lead density effect is positive in the centre of the core where the effect of absorption reduction is predominant on the effect of the increase of leakage. On the other hand, the contribution is negative in the periphery of the active zone, i.e, in some FAs of the outer zone, in the dummy elements and in the upper and lower reflector. The possibility to take into account these effects in the dynamics modelling is definitely a major outcome of the spatial neutronics model.

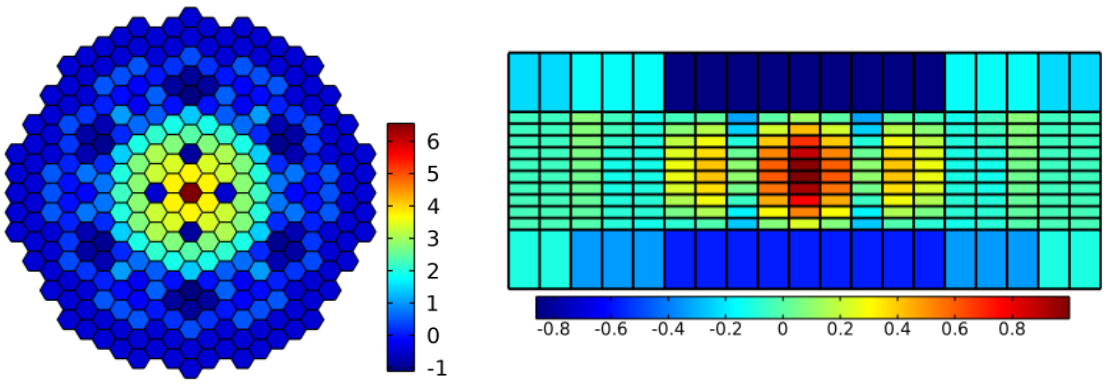

(a) (b)

Figure 2.27. Lead density effect. Spatial reactivity (pcm) variation in each assembly in the active zone (a) along the axial direction (b) calculated with APOD method (Case D).

The capability to reproduce different situations from what included in the snapshots has been assessed. Even if the *optimum* is to calculate as much as possible snapshots related to the system behaviour in order to "train" the spatial basis, it is not possible to include every possible situation

that may happen in the core and therefore it is important to ensure acceptable results if the simulation is run outside the range delimited by the calculated snapshots. In this work, as far as the lead density is concerned, only one case has been included in the snapshots, representing an increase of 800 K of the lead temperature in the entire system. For this reason, a simulation involving a 800 K lead temperature increase only in the fuel region has been carried out. The reactivity results for the different cases are reported in Table 2.13.

Table 2.13. Lead density effect in the fuel region. Reactivity variation (pcm), spatial neutronics model results.

Case A (N=5)	Case B (N=5)	Case C (N=5)	Case C (N=7)	Case D (N=5)	COMSOL (reference)
-56.2	3.9	54.9	31.8	7.8	8.7

The results show that, for a situation which is not directly contemplated in the set of snapshots, the APOD method provides better results than POD due to the reduced error compared to the reference result of COMSOL.

2.4.3. CR movement results

In order to assess the capability of the different approaches to correctly reproduce the reactivity insertion following a CR insertion, different simulation cases at different CR position have been carried out (see Table 2.14). For each case, SERPENT and COMSOL simulations have been performed (Figure 2.28) in order to obtain the cross-sections and to calculate the spatial basis and the test functions (see Table 2.15). It is worthwhile mentioning that, due to the Modal Method approach, the spatial basis for the Case A and B are the same of the thermal feedback study.

Table 2.14. Simulation cases carried out to reproduce the CR insertion.

CR insertion (relative height in cm)	Multiplication factor			Reactivity insertion		
	SERPENT (transport)	COMSOL (diffusion)	Error (%)	SERPENT (transport)	COMSOL (diffusion)	Error (%)
-4 (extracted)	$1.07391 \pm 6 \cdot 10^{-5}$	1.07387	7.4	0	0	
6	$1.06362 \pm 6 \cdot 10^{-5}$	1.06409	6.4	-901±7.5	-855.8	-5
12	$1.05474 \pm 6 \cdot 10^{-5}$	1.05405	5.4	-1692±7.5	-1751.7	3.5
18	$1.0439 \pm 6 \cdot 10^{-5}$	1.04201	4.2	-2677±7.5	-2847.5	6.4
24	$1.03201 \pm 6 \cdot 10^{-5}$	1.02911	2.9	-3781±7.5	-4050	7.1
30	$1.01982 \pm 6 \cdot 10^{-5}$	1.01584	1.6	-4939±7.5	-5320.1	7.7

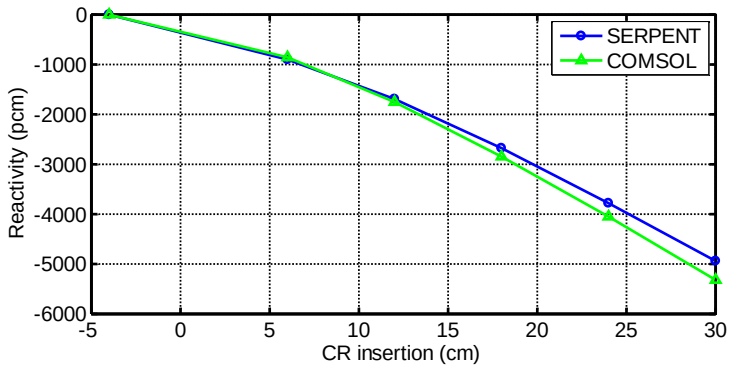

Figure 2.28. Reactivity curve of the control rods, comparison between SERPENT and COMSOL result.

Table 2.15. First three functions of the spatial bases and test functions for the CR insertion (in normalized unit).

#	$\underline{\psi}_i$ for Case A,B $\underline{\xi}_i$ for Case A	$\underline{\xi}_i$ for Case B	$\underline{\psi}_i$ for Case C,D $\underline{\xi}_i$ for Case C	$\underline{\xi}_i$ for Case D
1	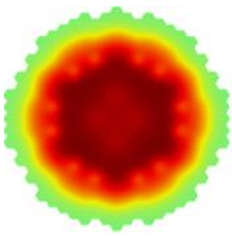	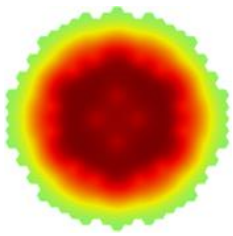	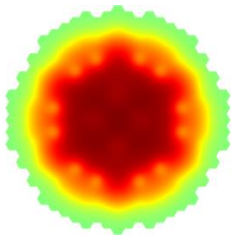	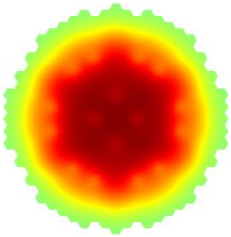
2	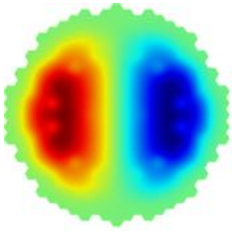	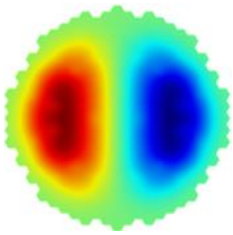	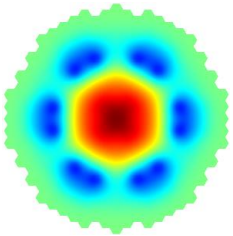	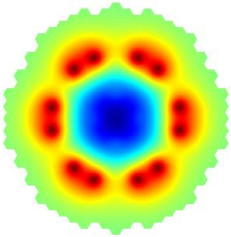
3	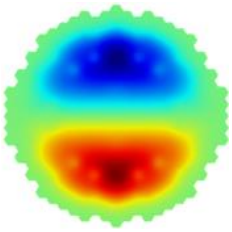	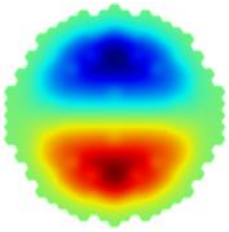	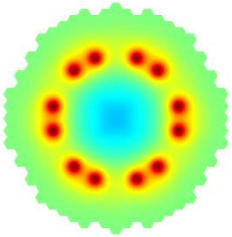	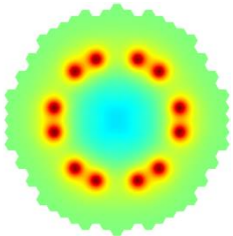

The multiplication factor calculated with the spatial neutronics model in the different cases are reported in Table 2.16 and in Table 2.17. Seven functions for the flux expansion are considered for the Cases A, B, C, D. The results give two indications. The first one is that the best performance is obtained in Case D (APOD method). The second one is that the Modal Method, both Case A and B, are totally inadequate to reproduce the effect of the CR movement. This can be explained considering that the MM employs the spatial basis calculated in a unique reference solution. This means that it is suitable only if the flux is not strongly perturbed, which is not the case of the CR movement.

Table 2.16. CR insertion. Multiplication factor, spatial neutronics model results.

CR insertion (relative height in cm)	Multiplication factor (N=7)						
	CaseA	Case B	Case C		Case D		COMSOL (reference)
			Value	Diff. (pcm)	Value	Diff. (pcm)	
-4 (extracted)	1.075426	1.073484	1.07458	-65.80	1.073864	0.82	1.073873
6	1.052188	1.049962	1.06447	-34.93	1.064055	3.63	1.064094
12	1.018336	1.015744	1.05485	-76.10	1.053916	12.29	1.054045
18	0.976147	0.973072	1.04207	-6.00	1.041890	11.52	1.042010
24	0.931826	0.928297	1.02980	-66.11	1.029048	6.52	1.029115
30	0.889722	0.885887	1.01624	-39.35	1.015817	1.93	1.015837

Table 2.17. CR insertion. Reactivity variation (pcm), spatial neutronics model results.

CR insertion (relative height in cm)	Reactivity insertion (N=7) (pcm)						
	CaseA	Case B	Case C		Case D		COMSOL (reference)
			Value	Diff. (pcm)	Value	Diff. (pcm)	
6	-2053.7	-2086.9	-884.2	28.4	-858.4	2.64	-855.8
12	-5213.0	-5295.4	-1740.8	-10.9	-1762.6	10.90	-1751.7
18	-9457.2	-9612.7	-2903.0	55.5	-2857.8	10.29	-2847.5
24	-14329.8	-14569.6	-4047.0	-3.0	-4055.6	5.57	-4050
30	-19408.3	-19726.6	-5342.6	22.5	-5321.2	1.14	-5320.1

The evolution of the multiplication factor versus the number of the functions employed is described in Figure 2.29a (CR extracted) and in Figure 2.29b (CR height 18 cm). Even in this case, the convergence to the reference result is reached by the APOD method (Case D) with less functions compared to the POD method (Case C). It is interesting to notice that in the APOD case the addition of a spatial basis function turn results in an improvement of the model performance (i.e., the error decreases monotonously with the number of the functions). This is not true for the Case C.

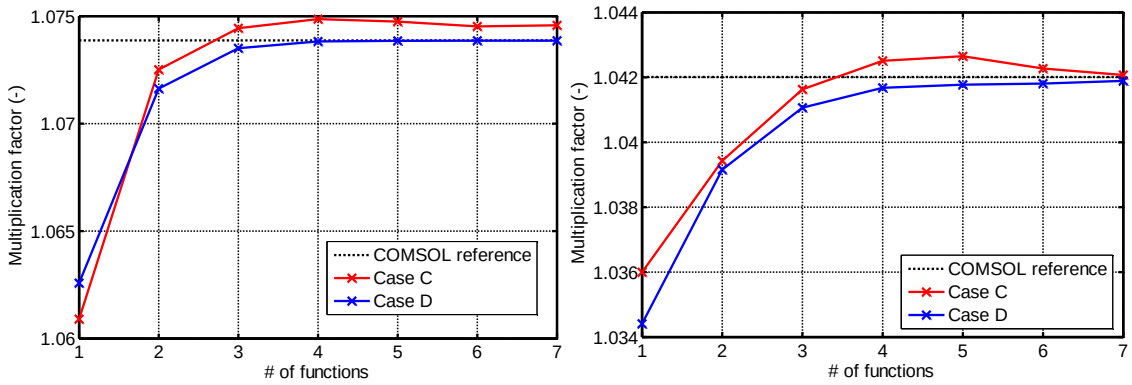

(a) (b)

Figure 2.29. CR extracted (a) and CR height 18 cm (b). Evolution of the multiplication factor versus the number of functions employed in the model.

2.4.4. Discussion of results

As far as the Modal Method is concerned, the results of the previous sections state that only in the case of the thermal reactivity effect, the approach gives acceptable results and in particular only if the adjoint eigenvectors are employed (Case B). If the eigenvectors of the flux are employed as test functions (Case A), the spatial neutronics model is not able at all to reproduce the reactivity. The Modal Method, both Case A and B, is totally inappropriate for considering strong perturbation of the flux as happens during the control rod movements. Therefore, it is not the ideal candidate to be employed in the spatial neutronics model.

The problem of strong perturbation can be overcome employing the POD method for the selection of the spatial basis. The results show very good results for Case C (the test functions are the same POD modes) and Case D (the test functions take into account the adjoint flux). In particular, both for the thermal reactivity effects and the CR movement, the APOD method (Case D) shows better outcomes compared to the classic POD method for several reasons. Firstly, it reaches the best accuracy with less functions employed, meaning that the computational cost to run the model is reduced. Secondly, the APOD method is less affected by the dependence of the

functions number on the convergence to the reference value, compared to the POD method. Thirdly, it obtains good results also in situations which are not included in the snapshots set.

Finally, the best performance of the APOD method can be explained considering the role that the adjoint flux takes on in the perturbation theory. In this context, it is used as weighting function for the evaluation of the reactivity variation (Henry, 1975). Similarly, in our context, the test functions are used to "evaluate" the residual introduced with the approximation of Equation (2.4) and constraining it to zero (Amsallem and Farhat, 2012).

2.5. Concluding remarks

In this Chapter, the development of a spatial neutronics model for the reactor core is described. This approach is directed to go beyond the classic Point Kinetics (PK) currently used in control-oriented models due to the inability of such zero-dimensional method to allow for the spatial dependence of the flux. To this aim, the paradigm of the ROM is transferred into neutronics separating the spatial and time dependence of the neutron flux, which can be represented as a linear combination of spatial basis functions. The spatial neutronics modelling has been developed considering different choices of spatial basis and test functions, based on the Modal Method and the Proper Orthogonal Decomposition. The proposed approach is easy to implement in any control simulator environment, thanks to its matrix formulation and the derivation of the main variables of interest (power, flux, reactivity).

The spatial neutronics approach has been tested in a simple 3D case. The results show that the proposed approach improves the modelling accuracy with respect to the classic Point Kinetics, being the model capable to predict the reactivity evolution also in strong localized transients or relevant operational scenarios (e.g., shutdown). In addition, an object-oriented model of the 3D test case has been settled in order to prove the feasibility of employing ROM-based components in control-oriented simulators. The component (object) can replace the 0D model described in Section 1.2.1 without affecting the rest of the simulator. The developed model performs simulations in real time, being satisfactory from a computational point of view. In addition to the spatial neutronics, a new pin heat transfer model has been conceived ad-hoc in order to obtain some advisable features (i.e., modularity, reusability and efficiency) in an object-oriented perspective. Differently from the heat transfer model described in Section 1.2.1, it allows selecting the number of the fuel, cladding and gap zone which the pin is divided in. In this way, the reusability of the model is enhanced and the heat transfer modelling can employ a geometrical division coherent with the neutronics model along with a better accuracy during the transient behaviour.

As for the entire reactor core, a detailed model of the ALFRED reactor has been set up by means of the continuous energy MC neutron transport code SERPENT with a heterogeneous description of the active zone. The average cross-sections for each assembly, calculated by means of the MC model, have been used to solve the neutron diffusion PDEs exploiting the capabilities of the COMSOL software. Starting from the spatial basis and the test functions calculated by means of the neutron diffusion equations, the MM has proved not to be suitable in case of CR movement even if it works for thermal feedback effects. On the other hand, an Adjoint Proper

Orthogonal Decomposition approach is proposed to merge the benefit of the POD spatial basis and the relevance of the adjoint flux as test function. This new approach has been tested in case of both thermal reactivity effects and CR movement, giving better results with respect to the classic POD approach. These results can be explained considering the role that the adjoint flux takes on in the perturbation theory as weighting function for the neutron importance.

In conclusion, a spatial neutronics modelling approach has been proposed aimed at being used in a control-oriented simulator. The adopted description allows for the spatial heterogeneity of the system, in particular as far as the thermal reactivity feedbacks are concerned, providing a spatial representation of the neutron flux. On the other hand, it turns out to be employed in control-oriented applications, being accurate in both the reactivity and transient representation without an excessive computational cost. This modelling improvement may allow adopting innovative control strategies, whose feasibility in the nuclear field cannot be adequately studied with the Point Kinetics approach. For instance, with a spatial neutronics model, an optimal control of the Control Rods movement that minimizes the perturbation on the neutron flux can be assessed, since the model allows for the flux distortion due to the CR insertion.

List of symbols

Latin Symbols

A	coefficient used in Eq. (2.13), cm^{-1}
c	generic cladding zone
c_p	heat capacity, J kg^{-1} K^{-1}
C_j	concentration of the jth precursor group, cm^{-3}
D_g	neutron diffusion coefficient of the gth energy group, cm
d	density, g cm^{-3}
E	energy, MeV
E_f	average energy released per fission event, J
E_g	energy group threshold, eV
f	generic fuel zone
$\mathcal{F}$	fission operator of transport theory
G	number of energy group, -
g	generic gap zone
h_{CR}	height of control rods, m
$\underline{\underline{I}}$	identity matrix of G x G size, -
k	thermal conductivity, W cm^{-1} K^{-1}
$\mathcal{L}$	removal operator of transport theory
M	number of radial nodes, -
N	number of employed functions in the spatial basis, -
N_s	number of snapshots in the POD method, -
N_p	number of employed POD for the spatial basis, -
$\boldsymbol{n}$	surface normal unit vector, -
n_i^g	time-dependent coefficient of the ith spatial function of the neutron flux of the gth energy group, -
P	number of precursor groups employed, -
Q'''	volumetric heat source, W cm^{-3}
q	power, W
q''	heat flux, W cm^{-2}
r	radius, cm
r_{in}	inner radius of generic cylindrical zone, cm
r_{out}	outer radius of generic cylindrical zone, cm
$\boldsymbol{r}$	spatial coordinate, cm
S	surface of the spatial domain, cm^2
T	temperature, K
$\bar{T}$	mean temperature, K
t	time, s
V	fuel volume, cm^3
$\boldsymbol{v}$	lead velocity vector, cm s^{-1}
v_g	neutron speed of the gth energy group, cm s^{-1}
z	axial coordinate, cm
Z	number of axial nodes, -
$\underline{\underline{0}}$	zero matrix of G x G size, -

Greek Symbols

α	reactivity coefficient used in Eq. (2.32), pcm K^{-1}
β	total delayed neutron fraction, pcm
β_j	delayed neutron fraction of the jth precursor group, pcm
γ	albedo coefficient used in Eq. (2.14), -
λ_j	decay constant of the jth precursor group, s^{-1}
λ_i^*	i^{th} eigenvalue, -
ν	average number of neutrons emitted per fission event, -
ξ_i^g	i^{th} test function of the gth energy group, cm^{-2} s^{-1}
ρ	reactivity, pcm
Σ	generic macroscopic cross-section, cm^{-1}
Σ_a^g	macroscopic absorption cross-section of the gth energy group, cm^{-1}
Σ_f^g	macroscopic fission cross-section of the gth energy group, cm^{-1}
$\Sigma_s^{g\rightarrow}$	macroscopic cross-section including scattering out of the energy group g, cm^{-1}
$\Sigma_s^{g\rightarrow g'}$	macroscopic group transfer cross-section from energy group g to g´, cm^{-1}
ϕ_g	neutron flux of the gth energy group, cm^{-2} s^{-1}
χ_d^g	fraction of delayed neutrons generated in the gth energy group, -
χ_p^g	fraction of prompt neutrons generated in the gth energy group, -
χ_t^g	fraction of total neutrons generated in the gth energy group, -

ψ_i^g	i^{th} spatial eigenfunction of the neutron flux of the gth energy group, $cm^{-2}\ s^{-1}$
Ω	spatial domain, cm^3

Subscripts

0	reference value
a	axial
f	fuel
f1	inner fuel zone
f2	central fuel zone
f3	outer fuel zone
g	energy group number
gz	generic zone
in	inner
l	lead
out	outer
PK	Point Kinetics
r	radial

(this page is intentionally left blank)

Chapter 3

Spatial modelling of the reactor pool

In this Chapter, the development of a spatial model of the reactor pool is described. This approach is directed to overcome the 0D/1D modelling usually employed in control-oriented models for the fluid dynamics physics. In particular, this kind of approach allows the simulation tool to take into account the spatial features of the fluid flows, which can be relevant for certain reactor systems.

Spatial modelling of the reactor pool is based on the POD-FV-ROM procedure, developed on purpose for extending the literature approach based on Finite Element to the Finite Volume approximation of the Navier-Stokes equations. In addition, the proposed procedure allows building a reduced order model that is capable to handle turbulent flows modelled through the Reynold-Averaged Navier Stokes equations. The aim of this Chapter is describing the POD-FV-ROM approach (Section 3.2), pointing out the modifications implemented with respect to the literature approach. The different treatment of the turbulence issues originating from the use of RANS simulations as snapshots is also presented (Section 3.3). In Section 3.4, the POD-FV-ROM is tested in the classic benchmark of the numerical simulations for the 2D lid-driven cavity. In particular, two simulations at Re=1.000 and Re=100.000 are considered in order to assess both a laminar and turbulent case. In Section 3.5, the developed approach is employed to build a ROM-based component of the coolant pool of the ALFRED reactor. Finally, a few concluding remarks are drawn in Section 3.6.

The main results of this Chapter are to be published in:

- Lorenzi, S., Cammi, A., Luzzi, L., Rozza, G., 2015. POD-Galerkin Method for Finite Volume Approximation of Navier-Stokes and RANS equations. Submitted to Computer Methods in Applied Mechanics and Engineering.
- Lorenzi, S., Cammi, A., Luzzi, L., Rozza, G., 2015. A reduced order model for the spatial description of the Gen-IV LFR coolant pool. In preparation for Nuclear Engineering and Design.

3.1. Introduction

In the present simulators for control purposes, the modelling of the coolant pool is usually based on zero-dimensional or one-dimensional models. This kind of approaches prevents the simulation tool from taking into account turbulence mixing and 3D effects. These phenomena assume great relevance in a pool-type reactor, which is the typical configuration for LFRs. Moreover, due to the lead corrosion issues on structural materials, an oxygen control in the reactor pool is advisable and the design of the control system should properly take into account these spatial issues.

To this aim, a viable solution is to employ ROM techniques especially focused on the fluid dynamics field (Lassila et al., 2013). Numerical simulation of fluid flows requires a strong computational effort but it is essential in engineering applications. Even if the computational power is becoming more and more available, the need of finding a trade-off between computational cost and solution accuracy is a preeminent issue not only in the control field but also in process optimization and in general in any real time or many query context (Gunzburger, 2003; Rozza, et al., 2008; Quarteroni et al., 2011; Chinesta et al., 2015; Hesthaven et al., 2016). ROM can be employed for instance as the basis for the synthesis and the verification of controllers (El-Farra and Christofides, 2002; Bergmann et al., 2005; Barbagallo et al., 2011) or used in some optimization algorithms (Oliveira and Patera, 2007; Carlberg and Farhat, 2008; Lassila and Rozza, 2010). Among the several reduced order techniques, the Proper Orthogonal Decomposition (POD) with the snapshot technique (Sirovich, 1987; Holmes et al., 1996) is probably the most widespread in the complex fluid flow computation. POD technique was first introduced to study the coherent structures in experimental turbulent flows (Lumley, 1967; Aubry et al., 1988; Berkooz et al., 1993) but it has recently become a valuable option in the ROM framework (Cazemier et al., 1998; Kunisc and Volkwein, 2003; Weller et al., 2010; Wang et al., 2012) due to the capability to select the most energetic modes representing the most significant features of the system. Starting from proper numerical solutions of the system, i.e., the so called “snapshots”, a POD basis maximizing the energy content in the starting ensemble data is created. By applying the Galerkin projection of the original system into the space spanned by the POD basis, a low-order model can be obtained (POD-G-ROM) (Wang et al., 2012; Iliescu and Wang, 2014).

Even if in principle the several ROM techniques can be applied to different approximation schemes (i.e., finite difference, Finite Volume (FV), Finite Elements (FE), spectral methods), the most widespread method used is the FE method. This entails that the several reduced-order techniques are usually optimized for this discretization method. On the other hand, the fluid-dynamics approach consolidated in the industrial field, and especially in nuclear engineering, is usually based on FV approximation of the Navier-Stokes Equations (NSEs). In particular, the latter is considered (a) robust, (b) computationally inexpensive, and (c) suitable when the conservativity of the numerical flux is a relevant issue, like in the fluid-dynamics application (Eymard et al., 2000). Even if the FE can be more accurate, the FV is usually chosen for industrial applications in fluid dynamics since it does not require any particular functional framework as FE and it preserves locally the conservation laws (Fletcher, 1996; Versteeg and Malalasekera, 2007). Nowadays, the most widespread computational codes used in the industry, both commercial

(CFX, FLUENT, STARCD) (Iaccarino, 2001) and open-source (OpenFOAM) (Weller et al., 1998), are based on FV discretization. In literature, the general application of ROM technique using FV approximation has been investigated in the works of Haasdonk and Ohlberger (Drohmann et al., 2009; Haasdonk and Ohlberger, 2008a; Haasdonk and Ohlberger, 2008b; Hasssdonk et al., 2008; Haasdonk and Ohlberger, 2009;) extending the Reduced Basis (RB) approach to general linear evolution schemes such as finite volume schemes. Notwithstanding, there is a lack of literature regarding POD-G-ROM with FV approximation of the Navier-Stokes equations. At the best of the author knowledge, only Östh et al. (2014) used a commercial FV code to solve the LES equation in the offline procedure without specifying if a special procedure was used. On the other hand, a flux matching procedure (instead of Galerkin projection) based on Reynold-Averaged Navier Stokes (RANS) equations is proposed by Rambo et al. (Rambo and Yoshi, 2005; Rambo, 2006; Rambo and Yoshi, 2007).

Another remarkable issue is that the fluid flow usually considered in the nuclear engineering field is turbulent, as in the coolant pool of the ALFRED reactor. The eddies created by the turbulence span a large range of length and time scales. Accordingly, they can be modelled with several degrees of accuracy according to the resolution needed for the engineering application (Versteeg and Malalasekera, 2007). Even if Large Eddy Simulation (LES) and Direct Numerical Simulation (DNS) are very accurate (but computational expensive), for most engineering applications the RANS equations are sufficient to describe the main time-averaged properties of the flow (velocity, pressures, and stresses). To this end, suitable turbulence models are taken into account such as the eddy viscosity models (e,g, Spalart-Allmaras, $k-\varepsilon$, $k-\omega$) (Pope, 200; Versteeg and Malalasekera, 2007). A lot of papers are present in the literature dealing with POD-ROM models for High Reynolds number starting from snapshots collected by LES and DNS simulations (Aubry et al., 1988; Bergmann and Bruneau, 2009; Wang et al., 2011; Balajewicz and Dowell, 2012; Wang et al., 2012; Balajewicz et al., 2013; Cordier et al., 2013; San and Iliescu, 2013; Iliescu and Wang, 2014; Osth et al., 2014; Protas et al., 2015). As stated in these works, the main problem is the occurrence of unstable time behaviour in the reduced order model. This can be explained, as it has been confirmed in (Couplet et al., 2003), considering the concept of the energy cascade, firstly proposed by Richardson (1922) and then confirmed by the Kolmogorov's theory (Kolmogorov, 1941). A turbulent flow is composed by different size eddies. The large eddies carry most of the energy, extracting the energy from the mean flow. These eddies are unstable and break up into smaller eddies. In this way, the energy is transferred from the large scale to the smaller one. At a certain point, the eddies reach a sufficiently small length and energy scale that the viscosity can dissipate the kinetic energy into internal energy. Since the POD basis is built considering a maximum energy criterion, the POD truncation error leaves out the higher order modes, which are the less energetic but the most dissipative ones. Accordingly, the truncated POD-ROM model can blow up. In literature, this issue has been fixed introducing proper closure modelling. Among the possible solutions, the introduction of a fictitious eddy viscosity, modelling a stabilizing dissipative term, was considered in several ways (Aubry et al., 1988; Wang et al., 2011).

As pointed out in the Introduction, the practical application of this thesis is the improvement of the mentioned object-oriented plant simulator of ALFRED, i.e., substituting some components based on zero-dimensional model with ROM-based ones ensuring a high level of accuracy without increasing the computational burden. In particular, in this Chapter, the effort is focused

on the improvement of the fluid dynamics introducing a spatial modelling of the coolant pool. In Section 3.2, the modifications needed to the classic POD-G-ROM to be adopted in a FV framework are highlighted, i.e., a ROM for Computational Fluid Dynamics (CFD) application based on FV approximation (POD-FV-ROM) is developed. In this way, starting from the results available in RANS simulations, the application field of POD-ROM technique can be enlarged to the industrial world of the nuclear engineering. In this light, it is important to adopt the consolidated tools employed for the resolution of NSEs in nuclear field and to modify as less as possible the turbulent models usually employed. To this end, for the offline calculation, i.e., the resolution of the Full Order Model and the basis calculation, the open-source OpenFOAM software is adopted (Weller et al., 1998; OpenFOAM, 2014) as a reliable, tested and flexible tool for CFD application also in the nuclear field (Cai and Wanabe, 2011; Gandhir and Yassan, 2011; Clifford et al., 2013; Aufiero et al., 2014; Fiorina et al., 2015; Jareg et al., 2015). As a favourable feature, the POD-FV-ROM should be implemented just introducing some post-processing utilities, avoiding the need to modify the already tested solvers. In Section 3.3, the approach adopted for the turbulence, starting from RANS simulations, is presented in order to handle turbulent flows. The adoption of RANS with eddy viscosity models (necessary for the creation of the snapshots) allows avoiding the incorporation of the fictitious eddy viscosity since this quantity is already calculated in the Full Order Model (FOM). In Section 3.4, the POD-FV-ROM is tested in the classic benchmark of the numerical simulations for the 2D lid-driven cavity (Ghia et al., 1982; Botella and Peyret, 1998; Bruneau and Saad, 2006). In particular, two simulations at Re=1.000 and Re=100.000 are considered in order to assess both a laminar and turbulent case. In Section 3.5, the developed approach is employed to build a ROM-based component of the coolant pool of the ALFRED reactor. Finally, a few concluding remarks are drawn in Section 3.6.

3.2. POD-Galerkin projection with Finite Volume

In this section, the attention is paid to define a procedure for obtaining a POD-ROM of the Navier-Stokes equations considering the Finite Volume approximation (POD-FV-ROM). For the moment, we consider the incompressible Navier-Stokes equations without any turbulence treatment (this aspect will be introduced in Section 3.3). In equations, it reads:

$$\begin{cases} \boldsymbol{u}_t + (\boldsymbol{u} \cdot \nabla)\boldsymbol{u} - \upsilon \Delta \boldsymbol{u} + \nabla p = 0 \\ \nabla \cdot \boldsymbol{u} = 0 \end{cases} \tag{3.1}$$

where $\mathbf{u}$ is the velocity, p is a normalized pressure[12] and υ is the kinematic viscosity. The equations are given in a domain Ω with proper boundary and initial conditions.

3.2.1 The classic POD-Galerkin Reduced Order Modelling

In literature, there are several papers about POD-Galerkin ROM for Navier-Stokes equations. In this subsection, the classic POD-G-ROM methodology is briefly summarized according to (Lassila et al., 2010; Wang et al., 2012; Kunisch and Volkwein, 2013; Wang and Iliescu, 2014). For more details about the POD theory, the reader may refer to (Sirovich, 1987; Holmes et al., 1996).

[12] p is the thermodynamic pressure divided by the fluid density.

The main assumption in the reduced order techniques based on projection method is that the approximated solution of the problem $\boldsymbol{u}_r(\boldsymbol{x},t)$ can be expressed as linear combination of spatial modes $\boldsymbol{\varphi}_i(\boldsymbol{x})$ multiplied by temporal coefficients $a_i(t)$. If we consider the velocity, this assumption reads[13]

$$\boldsymbol{u}(\boldsymbol{x},t) \approx \boldsymbol{u}_r(\boldsymbol{x},t) = \sum_{i=1}^{N_r} a_i(t)\boldsymbol{\varphi}_i(\boldsymbol{x}) \tag{3.2}$$

The selection of the spatial modes is one of the crucial point in the reduced order modelling. A correct choice of these functions leads to an efficient ROM, reducing the online simulation time and/or increasing the accuracy with respect to the Full Order Model (FOM). The POD basis

$$X_{N_r}^{POD} \coloneqq span\{\boldsymbol{\varphi}_i\}_{i=1,..,N_r} \tag{3.3}$$

can be build starting from a set of velocity solutions sampled at different and evenly spaced times (i.e., the snapshots)

$$\boldsymbol{u}_n(\boldsymbol{x}) \coloneqq \boldsymbol{u}(\boldsymbol{x},t_n) \qquad n = 1,\dots,N_s \tag{3.4}$$

The snapshot can be numerical solutions of the NSEs (typical from LES and DNS simulations or even by the RANS equations considered in this paper) or they are obtained from experimental results. The POD basis minimizes the difference between the snapshots and the spatial modes in the X-norm, given the orthonormality of the modes. If the L^2-norm is chosen, the POD basis is optimal considering the energy contained in the snapshots.

$$X_{N_r}^{POD} = \arg min \frac{1}{N_s}\sum_{n=1}^{N_s}\left\|\boldsymbol{u}_n(\boldsymbol{x}) - \sum_{i=1}^{N_r}\langle \boldsymbol{u}_n(\boldsymbol{x}),\boldsymbol{\varphi}_i(\boldsymbol{x})\rangle_{L^2}\boldsymbol{\varphi}_i(\boldsymbol{x})\right\|_{L^2}^2 \quad \langle \boldsymbol{\varphi}_i(\boldsymbol{x}),\boldsymbol{\varphi}_j(\boldsymbol{x})\rangle_{L^2} = \delta_{ij} \tag{3.5}$$

In order to solve Equation (3.5), the following eigenvalue problem is considered

$$C\xi_i = \lambda_i\xi_i \qquad i = 1,\dots,N_s \tag{3.6}$$

where $C \in \mathbb{R}^{N_s \times N_s}$ is the correlation matrix whose components are calculated as follows

$$[C]_{kl} = \frac{1}{N_r}\langle \boldsymbol{u}_k(\boldsymbol{x}),\boldsymbol{u}_l(\boldsymbol{x})\rangle_{L^2} \tag{3.7}$$

The (λ_i,ξ_i) eigenvalue – eigenvector pair is used to construct the functions of the POD basis

$$\boldsymbol{\varphi}_i(\boldsymbol{x}) = \frac{1}{\sqrt{\lambda_i}}\sum_{n=1}^{N_s}\xi_{i,n}\boldsymbol{u}_n(\boldsymbol{x}) \qquad i = 1,\dots,N_r \tag{3.8}$$

It is worthwhile to remind that, since the eigenvalues are sorted in descending order, the first modes have the property to retain the most of the energy present in the original solutions (Berkooz et al., 1993) This is an important feature when considering the turbulence effects. In addition, the functions are orthogonal and they can be suitable normalized in order to obtain $\langle \boldsymbol{\varphi}_i(\boldsymbol{x}),\boldsymbol{\varphi}_j(\boldsymbol{x})\rangle_{L^2} = \delta_{ij}$.

[13] Generally, the velocity field is decomposed in a mean time-independent flow and a linear combination of time-dependent fluctuations. Hereinafter, we consider a general formulation with no base flow.

Replacing the velocity $\boldsymbol{u}$ with $\boldsymbol{u_r}$ in the Equation (3.1) and applying a Galerkin projection of the resulted system on the functions of the POD basis, the following POD-Galerkin ROM (POD-G-ROM) is obtained

$$\frac{da_j(t)}{dt} = \upsilon \sum_{i=1}^{N_r} B_{ji}\, a_i(t) - \sum_{k=1}^{N_r}\sum_{i=1}^{N_r} C_{jki}\, a_k(t) a_i(t) \qquad j = 1, \dots, N_r \tag{3.9}$$

where

$$B_{ji} = \langle \nabla \boldsymbol{\varphi}_j, \nabla \boldsymbol{\varphi}_i \rangle_{L^2} \tag{3.10}$$

$$C_{jki} = \langle \boldsymbol{\varphi}_j, (\boldsymbol{\varphi}_k \cdot \nabla) \boldsymbol{\varphi}_i \rangle_{L^2} \tag{3.11}$$

$$a_j(0) = \langle \boldsymbol{\varphi}_j, \boldsymbol{u}_1(\boldsymbol{x}) \rangle_{L^2} \tag{3.12}$$

Equation (3.9) can be expressed as the following autonomous dynamical system in which the unknowns are the time-dependent coefficients $a_i(t)$:

$$\dot{\boldsymbol{a}} = \upsilon \boldsymbol{B}\boldsymbol{a} - \boldsymbol{a}^{\boldsymbol{T}} \boldsymbol{C}\boldsymbol{a} \tag{3.13}$$

In deriving the POD-G-ROM, two relevant assumptions are made:

a) The first one is the lack of a pressure term in Equation (3.9). This can be explained considering that the POD modes are linear combination of the snasphots, which are divergence-free since they satisfy the continuity equation. In this way, the POD modes preserve the divergence-free property (in discrete sense). The Galerkin projection of the pressure term reads:

$$\langle \boldsymbol{\varphi}_i, \nabla p \rangle_{L^2} = \int_{\Omega} \boldsymbol{\varphi}_i \cdot \nabla p \, d\boldsymbol{x} = -\int_{\Omega} p \cdot (\nabla \cdot \boldsymbol{\varphi}_i)\, d\boldsymbol{x} + \int_{\partial\Omega} p \cdot (\boldsymbol{\varphi}_i \cdot \boldsymbol{n})\, d\boldsymbol{x} \tag{3.14}$$

where the first term is null and the second one is also zero in case of enclosed flows (Lassila and Rozza, 2010). In general, the pressure term can be neglected if the computational domain is large enough (Wang et al., 2012), or proper boundary conditions are satisfied (Iliescu and Wang, 2014). On the other hand, in some cases it is not possible to eliminate this term and some additional terms (Noack et al., 2005), or the construction of a basis for the pressure are needed (Bergmann et al., 2009).

b) The second point is that the term B_{ij} (Equation (3.9)) representing the diffusive term is derived keeping into account that $\Delta u = \mathrm{div}(\nabla u)$ and applying the Green formula for the divergence operator. This procedure is typical of the weak formulation of differential problems in the FE approach and it is extended also to POD-G-ROM (Wang et al., 2012).

These two observations are relevant in the following application of POD-G-ROM to the FV discretization.

3.2.2 The Finite Volume method: issues for the reduced order modelling

The Finite Volume method is a discretization method based on a “balance” approach, well suited for the resolution of equations based on conservation laws. A local balance, obtained from the discretization of the integral form of the governing equations, is written on each discretization cell (i.e., control volume – see Figure 3.1).

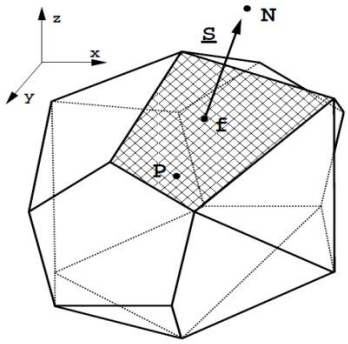

Figure 3.1. Example of a control volume (courtesy of Jasak, 1996).

This method is quite attractive for CFD since the quantities of interest (mass flow, momentum) are conserved at the discrete level (Jasak, 1996). Considering the momentum balance of Equation (3.1), the integral form on a generic control volume V_P reads

$$\int_t^{t+\Delta t}\left[\frac{\partial}{\partial t}\int_{V_P}\boldsymbol{u}_t dV+\int_{V_P}(\boldsymbol{u}\cdot\nabla)\boldsymbol{u}dV-\upsilon\int_{V_P}\Delta\boldsymbol{u}dV+\int_{V_P}\nabla p dV\right]dt=0 \tag{3.15}$$

In general, the variation of the velocity **u** around the centroid of the control volume (denoted as P in Figure 3.1) is taken as linear in order to have a second-order accurate method. In the following, this assumption is adopted.

In order to obtain a POD-FV-ROM, it is important to remind three relevant numeric issues characterizing the FV discretization of the Navier-Stokes equations:

a) the convective (non-linear) term, given the linear variation of **u** and applying the generalized form of the Gauss' theorem, is discretized as (Jasak, 1996)

$$\int_{V_P}(\boldsymbol{u}\cdot\nabla)\boldsymbol{u}=\int_{V_P}\boldsymbol{\nabla}\cdot(\boldsymbol{u}\boldsymbol{u})\approx\sum_f\boldsymbol{S}_f\cdot\boldsymbol{u}_f\boldsymbol{u}_f=\sum_f F\boldsymbol{u}_f \tag{3.16}$$

where $\mathbf{S}_f$ is the face area vector of the face (see Figure 3.1) and F is the face flux. This entails that the face flux field should be considered in the POD-FV-ROM procedure in order to be consistent with the full order modelling.

b) The continuity equation is discretised as follows

$$\int_{V_P}\nabla\cdot\boldsymbol{u}=\sum_f\boldsymbol{S}_f\cdot\boldsymbol{u}_f=\sum_f F=0 \tag{3.17}$$

i.e., the divergence-free constraint is applied not to the cell center value, but to the face flux. In this way, it is not possible anymore to neglect the pressure term, as seen for the POD-G-ROM, since the snapshots, calculated in the center cell value, are not divergence-free[14].

[14] Actually, the snapshots are "almost" divergence-free due to the relation between the center and the flux value. Notwithstanding, it is better not to consider the snapshot fields as solenoidal to avoid introducing error in the ROM due to the discretization process.

c) The diffusive term is discretised as

$$\upsilon \int_{V_P} \Delta \boldsymbol{u} = \upsilon \sum_f \boldsymbol{S}_f \cdot \nabla \boldsymbol{u}_f = \upsilon \sum_f |\Delta| \frac{\boldsymbol{u}_N - \boldsymbol{u}_P}{|\boldsymbol{d}|} + \boldsymbol{k} \cdot (\nabla \boldsymbol{u})_f \tag{3.18}$$

where the first term is the orthogonal contribution and the second one the non-orthogonal correction (Figure 3.2).

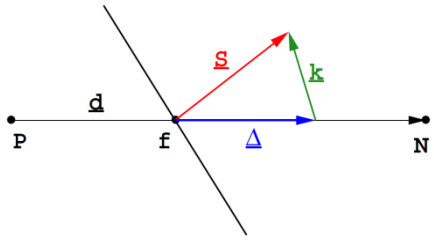

Figure 3.2. Non-orthogonality treatment of the diffusive term (courtesy of Jasak, 1996).

A second possible option for the discretization of the diffusive term can be undertaken. If we considered Δu=div(∇u) and if we applied the Green formula for the divergence operator, the following discretization would be obtained

$$\upsilon \int_{V_P} \nabla \cdot \nabla \boldsymbol{u} = \upsilon \sum_f \boldsymbol{S}_f \cdot \nabla \boldsymbol{u}_f = \upsilon \sum_f \boldsymbol{S}_f \cdot \left[f_x \left(\frac{1}{V} \sum_f \boldsymbol{S}_f \boldsymbol{u}_f \right)_P + (1 - f_x) \left(\frac{1}{V} \sum_f \boldsymbol{S}_f \boldsymbol{u}_f \right)_N \right] \tag{3.19}$$

It is clear that the Green formula leads to a different discretization of the diffusive term. The Equation (3.18) is usually preferred to Equation (3.19) since, although both are second-order accurate, the second one involves a larger computational molecule and the first term of the truncation error is four time larger than the first one (Jasak, 1996). Accordingly, the Green formula cannot be exploited in the POD-FV-ROM procedure since it would introduce discretization discrepancies between the Full Order Model and the Reduced Order one. As additional consequence, the boundary conditions cannot be explicitly incorporated in the reduced order model as in the POD-G-ROM case.

Finally, in the application of POD-G-ROM to the Finite Volume discretization, the three aforementioned issues typical of FV discretization should be carefully handled, considering the assumptions of the POD-G-ROM pointed out in the subsection 2.1. In the next section, the modifications needed in the light of the previous considerations are pointed out.

3.2.3 The POD-Galerkin Reduced Order Modelling for Finite Volume discretization

A POD-Galerkin Reduced Order Modelling for Finite Volume discretization should take into account the remarks outlined in the subsection 3.2.2, i.e., the need of calculating the face flux, the incorporation of the pressure term and the problem of considering the boundary conditions since the Green formula cannot be used. The procedure is intended to be the less “invasive” as possible to avoid modifying the Full Order Model, i.e., the code and solver usually adopted in industrial problems.

The first two issues can be solved expanding the face flux and the pressure as linear combination of some spatial modes:

$$F(\boldsymbol{x},t) \approx F_r(\boldsymbol{x},t) = \sum_{i=1}^{N_r} a_i(t)\psi_i(\boldsymbol{x}) \tag{3.20}$$

$$p(\boldsymbol{x},t) \approx p_r(\boldsymbol{x},t) = \sum_{i=1}^{N_r} a_i(t)\chi_i(\boldsymbol{x}) \tag{3.21}$$

where $\psi_i(\boldsymbol{x})$ and $\chi_i(\boldsymbol{x})$ are the functions of the spatial basis for the face flux and the pressure respectively. These spatial bases are constructed considering the eigenvectors of the correlation matrix of the velocity (Equation (3.7)) and the snapshots of the face flux/pressure ($F_n(\boldsymbol{x})$ and $p_n(\boldsymbol{x})$, obtained from the full order model) as follows:

$$\psi_i(\boldsymbol{x}) = \frac{1}{\sqrt{\lambda_i}} \sum_{n=1}^{N_s} \xi_{i,n} F_n(\boldsymbol{x}) \qquad i = 1, \dots, N_r \tag{3.22}$$

$$F_n(\boldsymbol{x}) \coloneqq F(\boldsymbol{x}, t_n) \qquad n = 1, \dots, N_s \tag{3.23}$$

$$\chi_i(\boldsymbol{x}) = \frac{1}{\sqrt{\lambda_i}} \sum_{n=1}^{N_s} \xi_{i,n} p_n(\boldsymbol{x}) \qquad i = 1, \dots, N_r \tag{3.24}$$

$$p_n(\boldsymbol{x}) \coloneqq p(\boldsymbol{x}, t_n) \qquad n = 1, \dots, N_s \tag{3.25}$$

Please note that the time coefficients for the approximated velocity, face flux and pressure are the same, therefore only the momentum equation is needed to solve them. Limited to the pressure, this approach was used in (Bergmann et al., 2009). On the other hand, in this work the weights employed to build the spatial basis are calculated from the eigenvectors of the correlation matrix of the velocity, and not a combination of velocity and pressure, as in the previous mentioned reference. In this way, the physical meaning of retaining the most energetic modes in the basis is conserved.

This approach can be interpreted as if the state vector of the variables of interest is expanded as linear combination of state vector spatial modes:

$$\begin{pmatrix} \boldsymbol{u}(\boldsymbol{x},t) \\ F(\boldsymbol{x},t) \\ p(\boldsymbol{x},t) \end{pmatrix} \approx \begin{pmatrix} \boldsymbol{u_r}(\boldsymbol{x},t) \\ F_r(\boldsymbol{x},t) \\ p_r(\boldsymbol{x},t) \end{pmatrix} = \sum_{i=1}^{N_r} a_i(t) \begin{pmatrix} \boldsymbol{\varphi}_i(\boldsymbol{x}) \\ \psi_i(\boldsymbol{x}) \\ \chi_i(\boldsymbol{x}) \end{pmatrix} \tag{3.26}$$

Replacing the velocity $\boldsymbol{u}$ with $\boldsymbol{u_r}$ and p with p_r in the Equation (3.1), employing the approximated face flux F_r in the convective term (Equation (3.16)), and applying the Galerkin projection, the following POD-Galerkin ROM for Finite Volume discretization (POD-FV-ROM) is obtained

$$\frac{da_j(t)}{dt} = \upsilon \sum_{i=1}^{N_r} B_{ji}\, a_i(t) - \sum_{k=1}^{N_r}\sum_{i=1}^{N_r} C_{jki}\, a_k(t) a_i(t) - \sum_{i=1}^{N_r} A_{ji}\, a_i(t) \tag{3.27}$$

where

$$B_{ji} = \langle \boldsymbol{\varphi}_j, \Delta \boldsymbol{\varphi}_i \rangle_{L^2} \tag{3.28}$$

$$C_{jki} = \langle \boldsymbol{\varphi}_j, \nabla \cdot (\psi_k, \boldsymbol{\varphi}_i) \rangle_{L^2} \tag{3.29}$$

$$A_{ji} = \langle \boldsymbol{\varphi}_j, \nabla \chi_i \rangle_{L^2} \tag{3.30}$$

The dynamical system of the time-dependent coefficient can be expressed as

$$\dot{\boldsymbol{a}} = \upsilon \boldsymbol{B}\boldsymbol{a} - \boldsymbol{a}^{\boldsymbol{T}}\boldsymbol{C}\boldsymbol{a} + \boldsymbol{A}\boldsymbol{a} \tag{3.31}$$

Please note that for the term B_{ji}, the Green formula has not been applied. Therefore, the Boundary Conditions (BCs) are "embedded" in the B_{ji} term and not explicit present in the ROM formulation.

This may be of concern if the control is the purpose of the reduce order modelling. In particular, in the fluid dynamics field, the classic control variable is the velocity at the boundary (Barbagallo et al., 2009) since it could be used to control the velocity field in the domain or an output variable of interest. In this view, if the reduced order model is directed to the synthesis of controllers, it should have the possibility to vary the velocity in order to test the several control action. Even if in this work the variation of the BCs is not considered in the numerical simulations, the possibility to parametrized the velocity at the BC in the reduced order model is taken into account. To this aim, a POD penalty method enforcing the BCs is considered (Sirisup and Karniadakis, 2005). As in the spectral methods (Gottlieb and Orszag, 1977), the Dirichlet BCs are directly incorporate in the Galerkin projection of the NSE as constraints

$$\langle \boldsymbol{\varphi}_j, \boldsymbol{u}_t + (\boldsymbol{u}\cdot\nabla)\boldsymbol{u} - \upsilon\Delta\boldsymbol{u} + \nabla p + \tau\Gamma(\boldsymbol{u} - \boldsymbol{u}_{\boldsymbol{BC}})\rangle_{L^2} = 0 \tag{3.32}$$

where $\mathbf{u}_{BC}$ is the Dirichlet boundary condition, τ the penalty factor and Γ is a null function except on the boundary where the condition is imposed (Sirisup and Karniadakis, 2005). The POD-penalty method allows not only incorporating and handling Dirichlet boundary conditions but it has two other significant advantages. The first one is that this procedure enforces the approximated velocity $\mathbf{u}_r$ to respect the B.C. of the problem. This should not be taken for granted since the approximated velocity is a linear combination of spatial functions, which in general do not respect the Dirichlet BC[15], except in the case of homogeneous one. The second advantage in using the POD penalty method lays in the fact that in this case the model is not autonomous anymore. In this way, wrong long-time integration behaviour and the initial condition issue are less troublesome (Sirisup and Karniadakis, 2005). As for the penalty factor, this number is usually tuned with a sensitivity analysis (Sirisup and Karniadakis, 2005; Bizon and Continillo, 2012). In general if τ tends to zero, the BCs are not enforced. On the other hand, if τ tends to infinity the reduced order model becomes ill-conditioned. (Sirisup and Karniadakis, 2005)

The POD-FV-ROM system is then modified accordingly:

$$\frac{da_i(t)}{dt} = \upsilon \sum_{i=1}^{N_r} B_{ji}\, a_i(t) - \sum_{k=1}^{N_r}\sum_{i=1}^{N_r} C_{jki}\, a_k(t) a_i(t) - \sum_{i=1}^{N_r} A_{ji}\, a_i(t) - \tau\left(\boldsymbol{u}_{\boldsymbol{BC}}\cdot\boldsymbol{D}_j - \sum_{i=1}^{N_r} E_{ji}\, a_i(t)\right) \tag{3.33}$$

where the additional terms with respect to Equation (3.27) are projected on the boundary considered as follows:

$$\boldsymbol{D}_j = \langle \boldsymbol{\varphi}_j \rangle_{L^2,\partial\Omega} \tag{3.34}$$

$$E_{ji} = \langle \boldsymbol{\varphi}_j, \boldsymbol{\varphi}_i \rangle_{L^2,\partial\Omega} \tag{3.35}$$

[15] The functions of the basis do not respect the Dirichlet BC since they are linear combination of snapshots (Equation (3.8)) which respect the BC in turn.

The POD-FV-ROM dynamical system for incompressible laminar NSE reads as

$$\dot{\boldsymbol{a}} = \upsilon \boldsymbol{B}\boldsymbol{a} - \boldsymbol{a}^{\boldsymbol{T}}\boldsymbol{C}\boldsymbol{a} - \boldsymbol{A}\boldsymbol{a} - \tau(\boldsymbol{u}_{\boldsymbol{BC}}\boldsymbol{D} - \boldsymbol{E}\boldsymbol{a}) \tag{3.36}$$

3.3. RANS turbulent POD-FV-ROM

The POD-FV-ROM presented in Section 3.2 is suitable for laminar flows since no turbulence treatment is considered in the Full Order Model (Equation (3.1)). Notwithstanding, the majority of the industrial applications deals with turbulent flows and the reduced order model should handle this aspect in order to become a powerful tool. To this end, the first choice to be made concerns the degree of detail in the modelling of turbulent flow. Even if in literature LES or DNS simulations are usually adopted for the FOM (i.e., for the snapshots as in Aubry et al., 1988; Bergmann and Bruneau, 2009; Wang et al., 2011; Balajewicz and Dowell, 2012; Wang et al., 2012; Balajewicz et al., 2013; Cordier et al., 2013; San and Iliescu, 2013; Iliescu and Wang, 2014; Osth et al., 2014; Protas et al., 2015), in this work the RANS approach is considered as in Rambo and Yoshi, 2005; Rambo, 2006; Rambo and Yoshi, 2007. This choice is due to the fact that in the modelling of industrial turbulent flows, this approach is preferred to the DNS or LES approaches since the latter are computationally too expensive for complex geometry (Versteeg and Malalasekera, 2007). Employing the RANS in the FOM and for the snapshot generation allows preserving the typical industrial modelling approach in the application of the reduced order modelling, as we will see in the following. Contrary to the work of Rambo et al., where a flux matching procedure is proposed, in this work the Galerkin projection is used. In this sense, this work constitutes first attempt in literature to use the POD-Galerkin approach to handle turbulence issues starting from RANS simulations.

The proposed procedure for incorporating the turbulence treatment in the POD-FV-ROM is different from the standard literature approach (Aubry et al., 1988; Zang et al., 2011). In the latter case, the POD-G-ROM is usually modified introducing a fictitious eddy viscosity, in order to prevent the occurrence of the blowup of the system. This undesired behaviour can be ascribed to the discard of the high order modes which contribute to the energy dissipation. The POD-G-ROM of Equation (3.9) is usually modified as follows:

$$\frac{da_j(t)}{dt} = \upsilon \sum_{i=1}^{N_r} B_{ji}\, a_i(t) - \sum_{i=1}^{N_r} H_{ji}\, a_i(t) - \sum_{k=1}^{N_r}\sum_{i=1}^{N_r} C_{jki}\, a_k(t) a_i(t) - \sum_{i=1}^{N_r} A_{ji}\, a_i(t) \tag{3.37}$$

where

$$H_{ji} = \langle \nabla \boldsymbol{\varphi}_j, \upsilon_{EV} \nabla \boldsymbol{\varphi}_i \rangle_{L^2} \tag{3.38}$$

There are several closure models for eddy viscosity υ_{EV} available in literature, the reader may refer to (San and Iliescu, 2013) for a general review. It should be noted that, differently from the literature cases that employ LES and DNS simulations for the snapshots creation, a term representing an eddy (turbulent) viscosity already exists if the RANS is adopted as FOM (Versteeg and Malalasekera, 2007). In particular, if we consider a general RANS eddy viscosity model, the equations of the FOM read:

$$\begin{cases} \boldsymbol{u}_t + (\boldsymbol{u}\cdot\nabla)\boldsymbol{u} = \nabla\cdot[-p\boldsymbol{I} + (\upsilon+\upsilon_t)(\nabla\boldsymbol{u} + (\nabla\boldsymbol{u})^{\boldsymbol{T}}) - 2/3k\boldsymbol{I}] \\ \nabla\cdot\boldsymbol{u} = 0 \end{cases} \tag{3.39}$$

The turbulent viscosity υ_t is usually function of one ($\tilde{\upsilon}$ in Spalart-Allmaras) or two variables (k and ε/ω in the respective models) (Versteeg and Malalasekera, 2007). The equations of these quantities are usually complicated, depending on several parameters and functions. In order to avoid the implementation of these complex relationships in the ROM, only the eddy viscosity is taken into account. The idea is once again to expand the eddy viscosity of Equation (3.39) as linear combination of spatial modes

$$\upsilon_t(\boldsymbol{x},t) \approx \upsilon_{t,r}(\boldsymbol{x},t) = \sum_{i=1}^{N_r} a_i(t)\phi_i(\boldsymbol{x}) \tag{3.40}$$

where $\phi_i(\boldsymbol{x})$ are the functios of the spatial basis for the eddy viscosity. As for the face flux and pressure, the spatial basis can be built starting from the snapshots of the viscosity ($\upsilon_{t,n}(\boldsymbol{x})$) and the eigenvectors of the correlation matrix of the velocity (Equation (3.7)).

$$\phi_i(\boldsymbol{x}) = \frac{1}{\sqrt{\lambda_i}}\sum_{n=1}^{N_s}\xi_{i,n}\upsilon_{t,n}(\boldsymbol{x}) \qquad i = 1,\dots,N_r \tag{3.41}$$

$$\upsilon_{t,n}(\boldsymbol{x}) \coloneqq \upsilon_t(\boldsymbol{x},t_n) \qquad n = 1,\dots,N_s \tag{3.42}$$

Also in this case, the time-coefficients are the same for velocity, face flux, pressure and turbulent viscosity, and only the momentum equation is needed to solve them. By adding the viscosity, the state vector of Equation (3.26) can be updated as:

$$\begin{pmatrix} \boldsymbol{u}(\boldsymbol{x},t) \\ F(\boldsymbol{x},t) \\ p(\boldsymbol{x},t) \\ \upsilon_t(\boldsymbol{x},t) \end{pmatrix} \approx \begin{pmatrix} \boldsymbol{u_r}(\boldsymbol{x},t) \\ F_r(\boldsymbol{x},t) \\ p_r(\boldsymbol{x},t) \\ \upsilon_{t,r}(\boldsymbol{x},t) \end{pmatrix} = \sum_{i=1}^{N_r} a_i(t)\begin{pmatrix} \boldsymbol{\varphi}_i(\boldsymbol{x}) \\ \psi_i(\boldsymbol{x}) \\ \chi_i(\boldsymbol{x}) \\ \phi_i(\boldsymbol{x}) \end{pmatrix} \tag{3.43}$$

The POD-FV-ROM for the RANS eddy viscosity model reads:

$$\begin{aligned} \frac{da_i(t)}{dt} = \upsilon\sum_{i=1}^{N_r} B_{ji}\,a_i(t) + \upsilon\sum_{i=1}^{N_r} BT_{ji}\,a_i(t) - \sum_{k=1}^{N_r}\sum_{i=1}^{N_r} C_{jki}\,a_k(t)a_i(t) + \sum_{k=1}^{N_r}\sum_{i=1}^{N_r} CT1_{jki}\,a_k(t)a_i(t) \\ + \sum_{k=1}^{N_r}\sum_{i=1}^{N_r} CT2_{jki}\,a_k(t)a_i(t) + \sum_{i=1}^{N_r} A_{ji}\,a_i(t) - \tau\left(\boldsymbol{u_{BC}}\cdot\boldsymbol{D}_j - \sum_{i=1}^{N_r} E_{ji}\,a_i(t)\right) \end{aligned} \tag{3.44}$$

where the additional terms with respect to Equation (3.33) are:

$$BT_{ji} = \langle\boldsymbol{\varphi}_j, \nabla\cdot\left(\nabla\boldsymbol{\varphi}_i{}^{\boldsymbol{T}}\right)\rangle_{L^2} \tag{3.45}$$

$$CT1_{jki} = \langle\boldsymbol{\varphi}_j, \phi_k\Delta\boldsymbol{\varphi}_i\rangle_{L^2} \tag{3.46}$$

$$CT2_{jki} = \langle\boldsymbol{\varphi}_j, \nabla\cdot\phi_k\left(\nabla\boldsymbol{\varphi}_i{}^{\boldsymbol{T}}\right)\rangle_{L^2} \tag{3.47}$$

Please note that the $2/3k\boldsymbol{I}$ term is neglected in the ROM since it can be incorporated in the pressure term (Pope, 2000). The dynamical system of the time-dependent coefficients for turbulence can be expressed as

$$\dot{\boldsymbol{a}} = \upsilon(\boldsymbol{B}+\boldsymbol{BT})\boldsymbol{a} - \boldsymbol{a}^{\boldsymbol{T}}(\boldsymbol{C}-\boldsymbol{CT1}-\boldsymbol{CT2})\boldsymbol{a} + \boldsymbol{Aa} - \tau(\boldsymbol{u_{BC}D} - \boldsymbol{Ea}) \tag{3.48}$$

The procedure proposed in this work has the advantage to be the more flexible possible and the less dependent to the turbulent modelling. In particular, the approach can be applied to any model that expresses the momentum equation as Equation (3.39), disregarding the specific modelling of the turbulent viscosity[16]. In addition, since in the POD-FV-ROM the diffusive term is not modified with the Green formula, the approach can be used also whether wall functions are applied. Indeed, problems may arise in the treatment of the wall functions if the BCs are directly incorporated in the ROM, since the wall functions of the turbulent quantities may be neither constant nor time-independent.

Even if the procedure proposed for the turbulent treatment is different from the classic one available in literature (Aubry et al., 1988; Zang et al., 2011), the Equation (3.48) is similar to the system obtained if we apply a modal eddy viscosity (Rempfer and Fasel, 1994; Noack et al., 2005; Osth et al., 2014). In these works, the eddy viscosity υ_{EV} is mode dependent and it is obtained by solution matching (Rempfer and Fasel, 1994) or power balance (Noack et al., 2005). In this work, υ_t is expanded in spatial modes calculated according RANS simulations.

3.4. Benchmark simulation tests

In this section, the POD-FV-ROM is tested in the classic benchmark of the numerical simulations for the 2D lid-driven cavity (Ghia et al., 1982; Botella and Peyret, 1998; Bruneau and Saad, 2006). It is worthwhile to remind that this is not a reduction from a 3D model to a 2D one and the 2D geometry is adopted for the sake of simplicity even if the approach can be easily extended to the 3D case. Two simulations at Re=1.000 and Re=100.000 are considered in order to assess both the laminar and turbulent flows. The lid-driven cavity is used as classical test problem for the evaluation of numerical techniques and validation of incompressible Navier-Stokes codes due to the simplicity of both the geometry and boundary conditions, despite the presence of unphysical singularities at its corners (Botella and Peyret, 1998). It is worthwhile to remind that we focus on the numerical aspects and aims of the benchmark, leaving out all the physical implications (Erturk, 2009). The geometry of the benchmark is depicted in Figure 3.3, i.e., a square cavity of unit length. The boundary conditions are **u**=(-1,0) on the side y=1 and **u**=(0,0) on the other three sides.

As figures of merit to evaluate the behaviour of the POD-FV-ROM, the kinetic energy, the velocity, the pressure and the respective L^2 error norm are considered. The results of the FOM are taken as reference to assess the ROM. In addition, for the laminar case, the comparison between the reduced order model steady-state solution and the data available in literature is presented.

[16] This is due to the choice to not project the equations that govern the eddy viscosity behaviour as the turbulent kinetic energy (k) and the specific rate dissipation (ω) in the k-ω modelling.

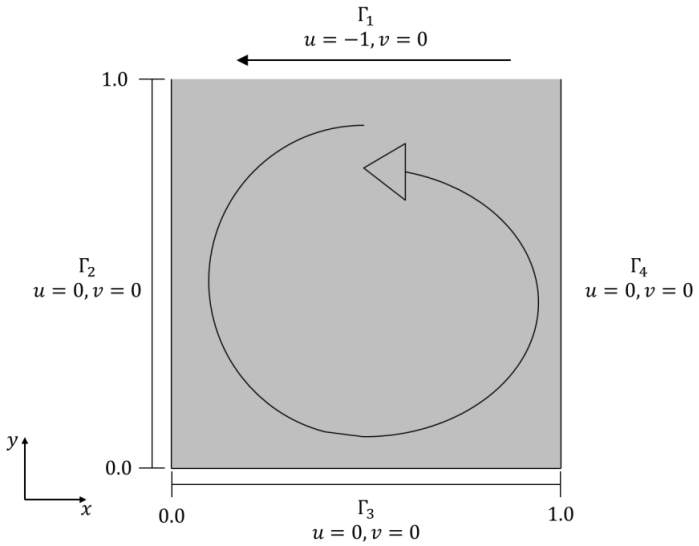

Figure 3.3. Geometry and BCs of the 2D lid-driven cavity test case.

3.4.1 Implementation aspects

The offline procedure, i.e., the calculation of the FOM solutions (i.e., the snapshots), the snapshots creation and the construction of the matrices of Equation (3.48), is performed in the OpenFOAM environment. OpenFOAM is an open source library for numerical simulation in continuum mechanics. The toolkit is very flexible thanks to the object-oriented programming, allowing users to customise, extend and implement complex physical model. Even if the POD creation is already present in the extended version of OpenFOAM (Jasak et al., 2007), some utilities have been updated or created in order to implement the offline phase of POD-FV-ROM in the library.

The online phase, i.e., the calculation of the ROM solutions and the implementation of the equation set of Equation (3.48), is performed with the Modelica language (Fritzson, 2004; The Modelica Association, 2014) in Dymola simulation environment (Elmqvist et al., 1993; DYMOLA, 2015). The component "cavity_laminar" with the Modelica code used to implement the cavity reduced order model for the laminar case is shown in Figure 3.4.

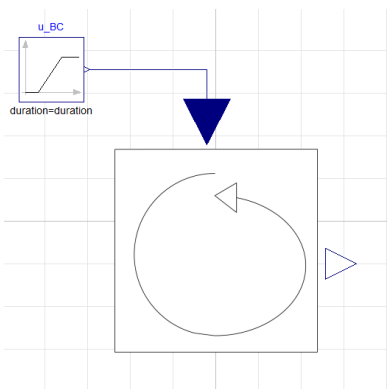


```
model cavity_laminar
import C_function;
parameter Integer N=53 "Number of functions in the basis";
parameter Real nu=1e-3 "Kinematic viscosity";
parameter Real A[:,:]=readMatrix("matrices.mat", "A", N,
N);
parameter Real B[:,:]=readMatrix("matrices.mat", "B", N,
N);
parameter Real E[:,:]=readMatrix("matrices.mat", "E", N,
N);
parameter Real D[:,1]=readMatrix("matrices.mat", "D", N,1
);
parameter Real ci[1,:]=readMatrix("ci.mat", "ci", 1,N);
parameter Real tau=1e-2;
equation
```

Figure 3.4. Cavity component and Modelica code for the laminar case.

For the sake of clarity, some numerical clarifications should be pointed out. As for the Full Order Model, a merged PISO-SIMPLE (PIMPLE) algorithm (Versteeg and Malalasekera, 2007; OpenFOAM, 2014) available in OpenFOAM is employed to solve the NSE and the RANS equations in order to obtain for each time step at least a convergence of 10^{-5} for the main variables (i.e., velocity, pressure, turbulent quantities, ….). The fourth-order numerical schemes for spatial discretization available in OpenFOAM are used, whereas a second order Backward Differentiation Formula (BDF) implicit scheme is adopted for the time discretization. A (1024 x 1024) structured equispaced mesh is employed to obtain an accurate solution without compromising the ROM performance since the ROM computational time does not depend on the degree of freedom of the FOM. The offline procedure was performed on the CINECA GALILEO cluster with 64 processors. As for the online phase, the integration algorithm DASSL (Petzold, 1982) is used to solve the ODE system with a 10^{-5} relative tolerance. The ROM simulation was carried out on a personal computer (single processor).

3.4.2 Laminar case

In the first simulation, an unsteady incompressible laminar flow at Re=1.000 (i.e., $\upsilon=10^{-3}$) in the 2D lid-driven cavity is considered. Let Ω = (0,1) X (0,1) and T > 0 the simulation time, the governing equations reads

$$\begin{cases} \boldsymbol{u}_t + (\boldsymbol{u}\cdot\nabla)\boldsymbol{u} - \upsilon\Delta\boldsymbol{u} + \nabla p = 0 & on\ [0,T]\ x\ \Omega \\ \nabla\cdot\boldsymbol{u} = 0 & on\ [0,T]\ x\ \Omega \\ \boldsymbol{u} = (-1,0) & on\ [0,T]\ x\ \Gamma_1 \\ \boldsymbol{u} = (0,0) & on\ [0,T]\ x\ \Gamma_{2,3,4} \\ \boldsymbol{u} = (0,0) & on\ [0]\ x\ \Omega \end{cases} \tag{3.49}$$

The full order simulation is performed until T=100 s with a constant time step of $5\cdot10^{-4}$. Figure 3.5a and Figure 3.6a present the velocity and the pressure of the full order simulation at different time. During the offline phase, the basis for the velocity, the face flux and the pressure are calculated following the procedure described in Section 3.2.2.

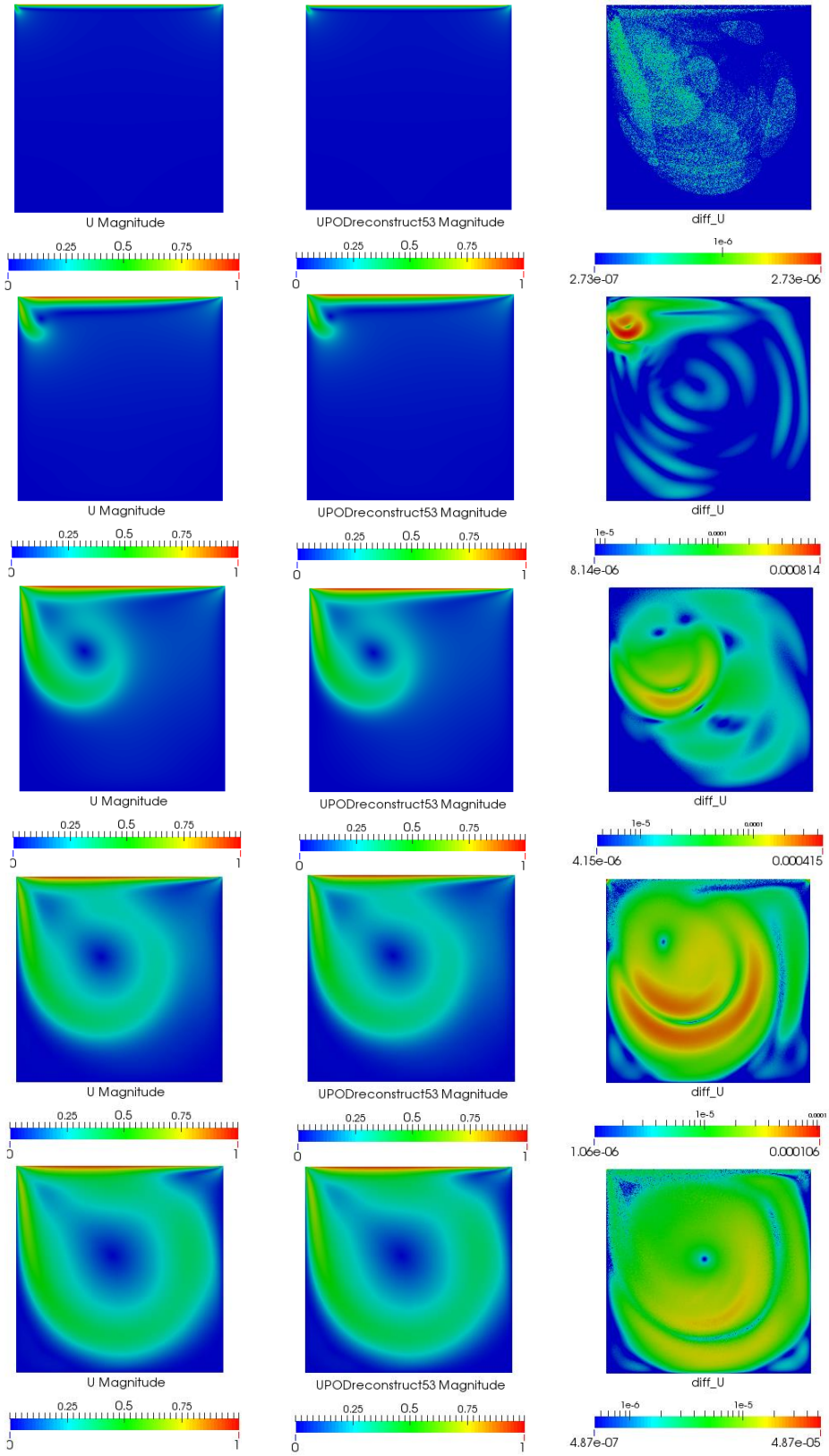

(a) FOM (b) ROM (c) difference

Figure 3.5. Laminar case (Re=1.000), contours of the velocity magnitude of the full order model (a), the reduced order model with Nr=53 (b) and relative difference (c) at different time. From top to bottom 0.1 s, 1 s, 5s, 10 s, 25 s.

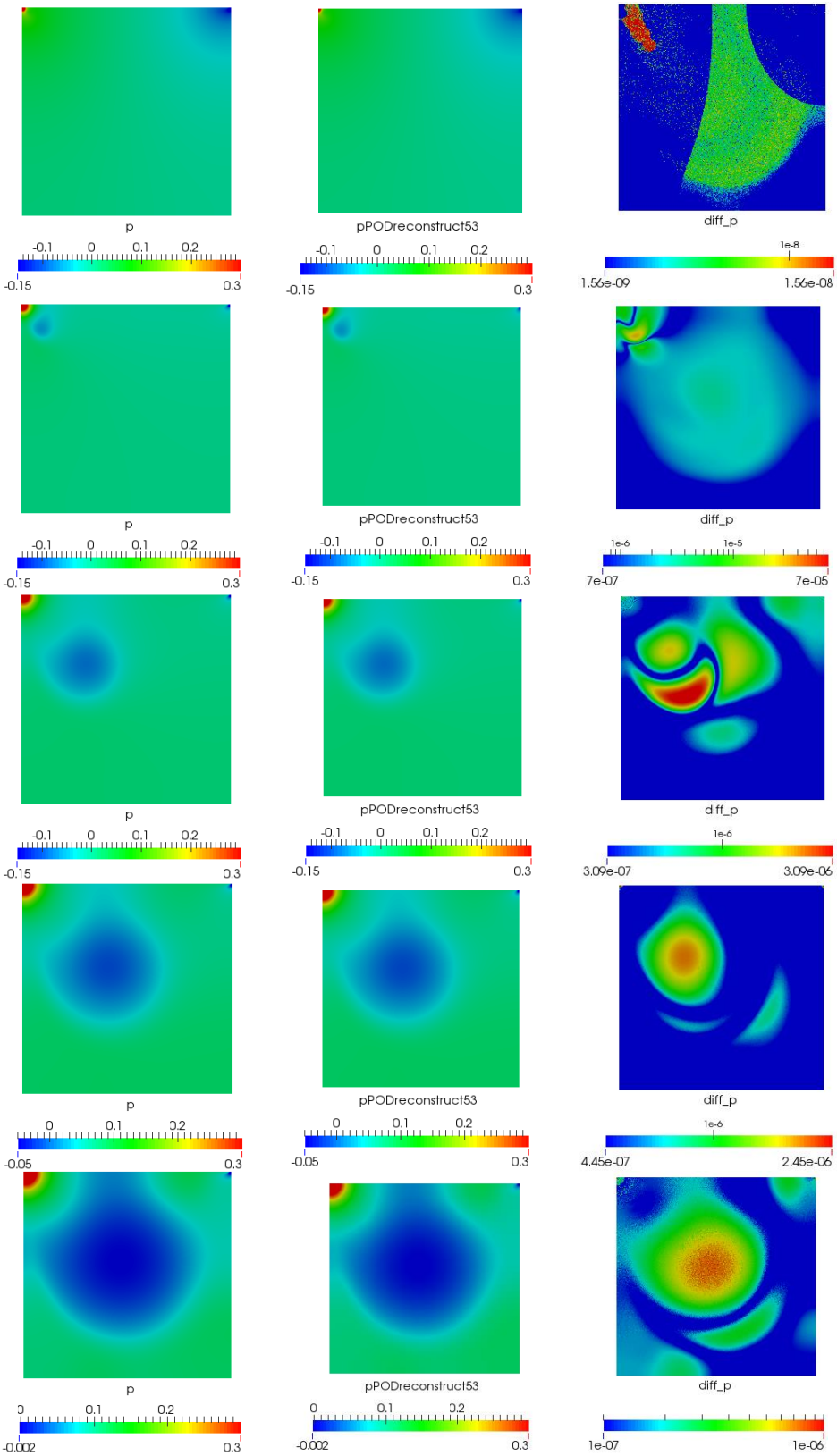

(a) FOM (b) ROM (c) difference

Figure 3.6. Laminar case (Re=1.000), contours of the pressure of the full order model (a), the reduced order model with N_r=53 (b) and relative difference (c) at different time. From top to bottom 0.1 s, 1 s, 5s, 10 s, 25 s.

As for the snapshots creation, the first three functions of the velocity and pressure bases are shown in Figure 3.7 and the decay of the normalized POD eigenvalues is given in Figure 3.8. From the latter figure, it is possible to establish the number of the functions in the basis given a "tolerance" on the normalized eigenvalues[17]. For the laminar case, 50-60 basis functions are sufficient to keep the normalized eigenvalue below 10^{-12}-10^{-14}. In particular, N_r=53 basis functions are used for the laminar case hereinafter in order to obtain a truncation error of 10^{-12} (Table 3.1). The truncation error of the POD procedure is defined as

$$e_{POD}(N) = 1 - \sum_{i=1}^{N} \lambda_i \tag{3.50}$$

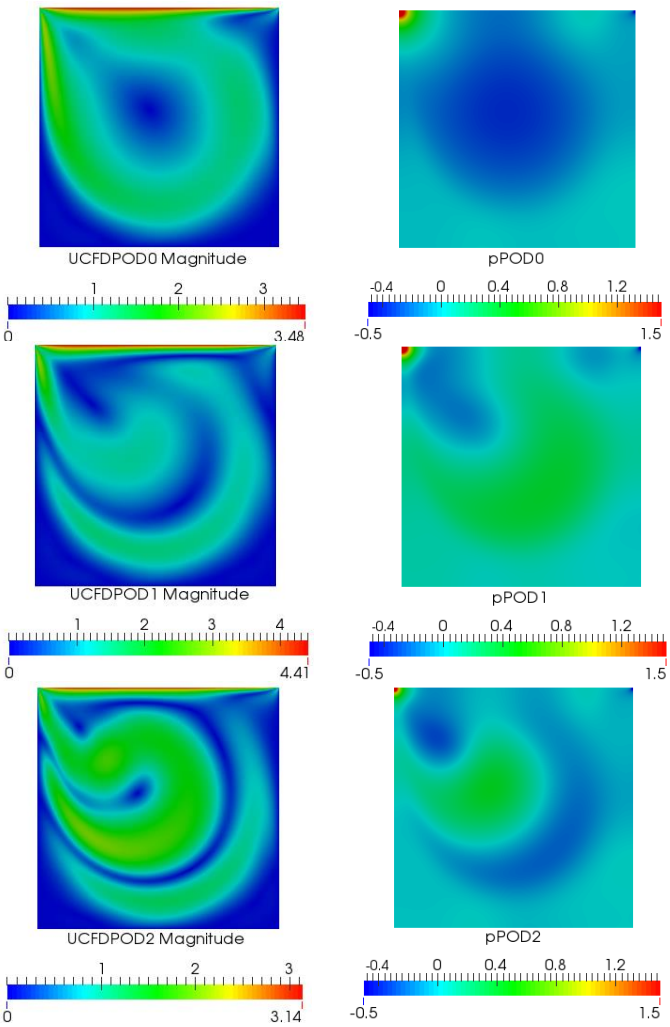

(a) velocity (b) pressure

Figure 3.7. Laminar case (Re=1.000), contours of the first three basis functions for (a) the velocity magnitude and (b) the pressure.

[17] It is important to remind that, even if the sum of the eigenvalues can be usually referred to the energy content in the snapshots, this number is not indicative of the relative error of the reduced order model.

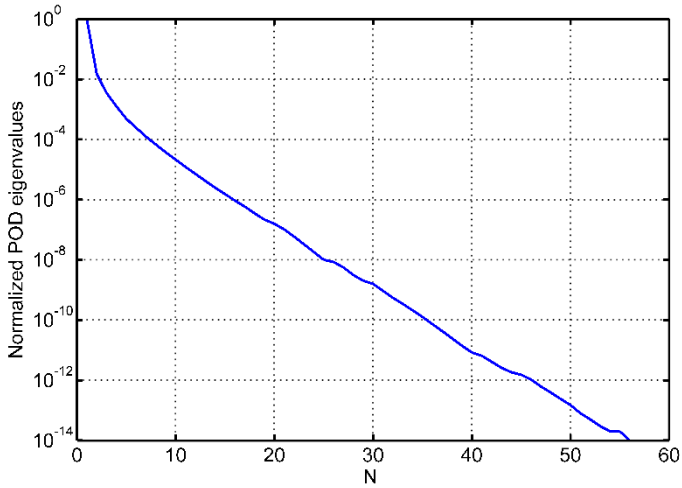

Figure 3.8. Laminar case (Re=1.000), normalized POD eigenvalues.

Table 3.1. Laminar case (Re=1.000). Number of basis functions versus truncation error.

N	e_{POD}
1	$2.1 \cdot 10^{-2}$
5	$5.2 \cdot 10^{-4}$
10	$3.0 \cdot 10^{-5}$
15	$2.5 \cdot 10^{-6}$
20	$2.5 \cdot 10^{-7}$
30	$2.3 \cdot 10^{-9}$
40	$2.0 \cdot 10^{-11}$
50	$1.2 \cdot 10^{-12}$
53	$1.0 \cdot 10^{-12}$

Once having calculated the matrices of the Equation (3.27), the set of the ODE is simulated in the Dymola environment. A sensitivity analysis was performed to establish a proper value of the penalizing factor τ between 10^{-5} and 100. A value of $\tau = 10^{-2}$ is found to be sufficient to enforce the BCs without afflicting the ODE system with ill-conditioning problems. A first check to assess the accuracy of the POD-FV-ROM is to calculate the relative error of the kinetic energy between FOM and ROM (Figure 3.9).

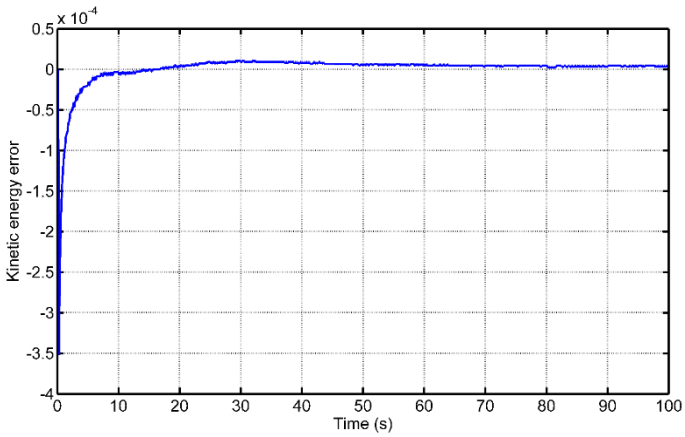

Figure 3.9. Laminar case (Re=1.000), kinetic energy difference between the FOM and ROM (N_r=53).

It is clear that the results are satisfactory being the error always lower than $4 \cdot 10^{-4}$. Moreover, in the second part of the transient, the error is positive indicating that the reduced order model is slightly underestimating the energy content. This means that the POD-FV-ROM is not affected by the energy blowup mentioned in the Section 3.1 (Osth et al., 2014; Couplet et al., 2003), even if this problem is more related to turbulent flows than laminar ones.

Figure 3.5b and Figure 3.6b present the velocity and the pressure fields reconstructed starting from the POD time coefficients whereas their relative difference with respect to the FOM results is depicted in Figure 3.5c and Figure 3.6c. In order to give a numerical estimation of the difference between the ROM and FOM, the L^2 error is introduced. For instance, for the velocity it reads:

$$\|e\|_{L^2} = \sqrt{\frac{\langle (\boldsymbol{u}_{FOM} - \boldsymbol{u}_r), (\boldsymbol{u}_{FOM} - \boldsymbol{u}_r) \rangle_{L^2}}{\langle \boldsymbol{u}_{FOM}, \boldsymbol{u}_{FOM} \rangle_{L^2}}} \tag{3.51}$$

In Figure 3.10, the L^2 error for the ROM velocity field is compared with the error of the velocity reconstructed from the Galerkin projection of the snapshots on the basis functions. The latter can be considered a "reference" value given a fixed number of basis functions. The error is always lower than 10^{-3}, being higher in the first part of the transient mainly because the flow starts at rest and the error is magnified by the small velocity magnitude. At the end of the transient, the error is set lower than 10^{-5}.

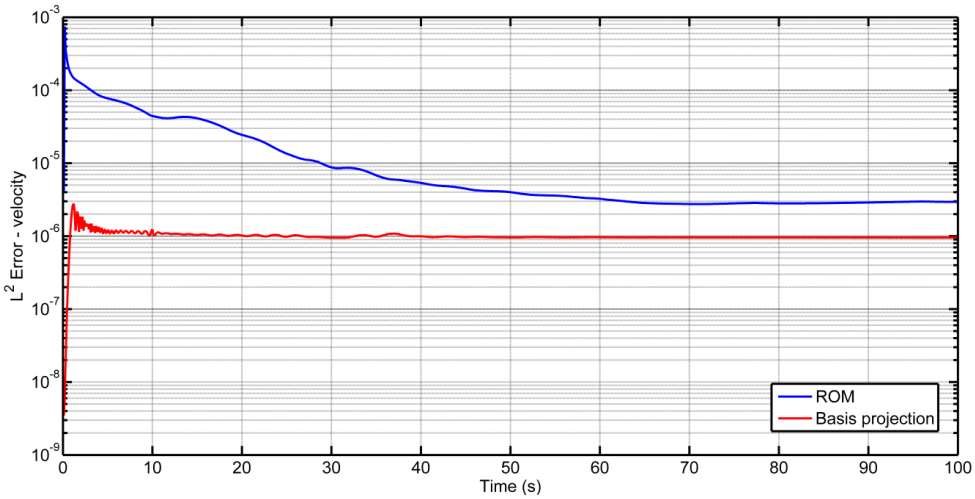

Figure 3.10. Laminar case (Re=1.000), L^2 error of the reconstructed velocity from ROM with Nr=53 (blue line) and basis projection (red line).

As for the pressure error (Figure 3.11), a good result is obtained since the error is between 10^{-3} and 10^{-6}. It is interesting to notice that in the second part of the transient, the ROM pressure error is lower than the basis projection ones. This is not surprising considering that the time coefficients for ROM pressure are the same with respect to the ROM velocity and the spatial basis for pressure are calculated from the eigenvectors of the correlation matrix of the velocity (see Equation (3.21) and Equation (3.24)).

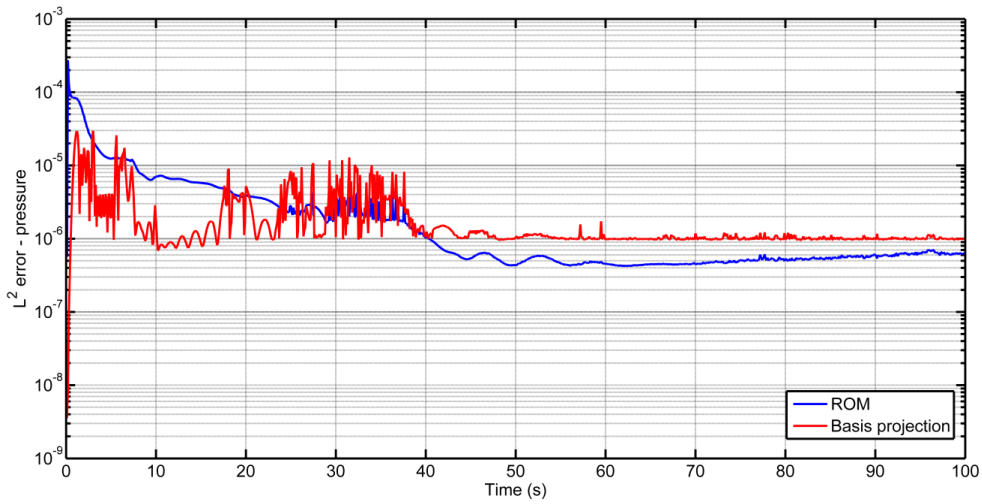

Figure 3.11. Laminar case (Re=1.000), L^2 error of the reconstructed pressure from ROM with N_r=53 (blue line) and basis projection (red line).

As last comparison, a benchmark with literature data (Ghia et al., 1982; Botella and Peyret, 1998) is also undertaken to prove the accuracy of the reduced order model. In particular, the ROM velocity at the end of the transient is compared with the steady-state solution of the lid-driven cavity at Re=1.000. Figure 3.12 presents the comparison through the horizontal and the vertical centreline of the cavity for the velocity, the pressure and the vorticity. As for the streamlines and the vorticity, the contours of these quantities are compared in Figure 3.13 and Figure 3.14, respectively (see Table 3.2 and Table 3.3 for the contour values). The almost perfect agreement between the literature data and the ROM results confirm the reliability of the POD-FV-ROM procedure for the laminar case.

Finally, for the full order model, a computational time of 2590 cpu-hours was required for the simulation of T=100 s. On the other hand, for the ROM, only a computational time of 5 s was needed to perform the same simulation. For the sake of completeness, for the POD generation and the ROM matrix calculation of the offline step, the procedure takes 150 and 180 minutes, respectively.

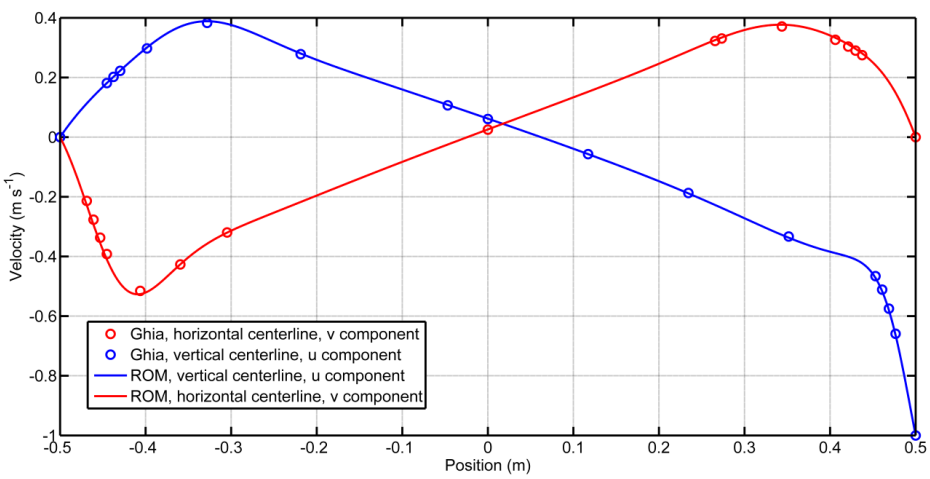

(a) velocity

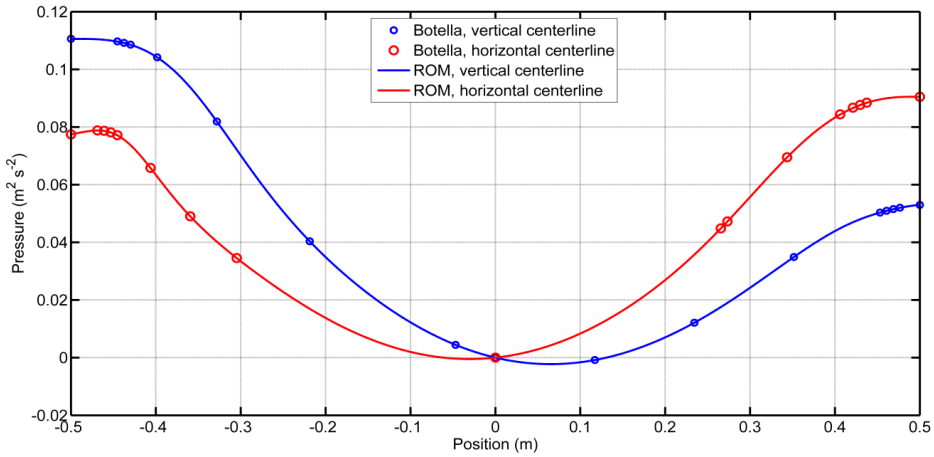

(b) pressure

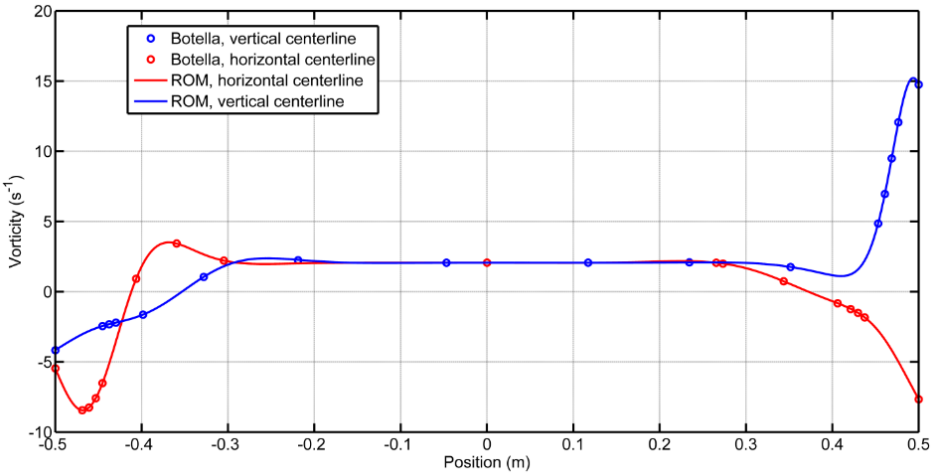

(c) vorticity

Figure 3.12. Laminar case (Re=1.000), comparison of velocity, pressure and vorticity between ROM results and literature data (Ghia et al., 1982; Botella and Peyret, 1998) along horizontal and vertical centerlines.

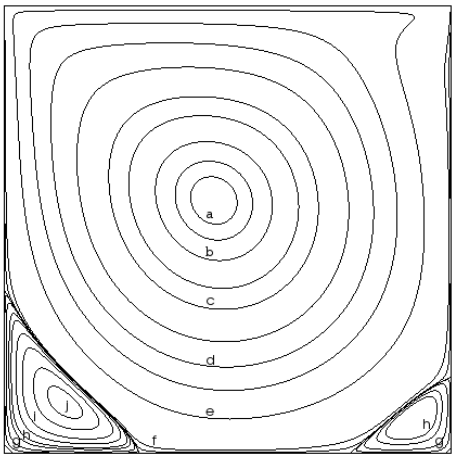

(a) present work

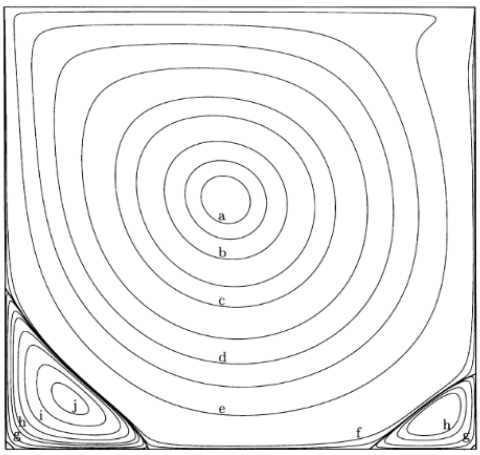

(b) work of Botella and Peyret (1998)

Figure 3.13. Laminar case (Re=1.000), streamline contours for the present work and the work of Botella and Peyret (1998).

Table 3.2. Streamfunction values shown in Figure 3.13 (Botella and Peyret, 1998).

Streamfunction							
Value	0.1175	0.115	0.11	0.1	$9\cdot10^{-2}$	$7\cdot10^{-2}$	$5\cdot10^{-2}$
label	a		b		c		d
Value	$3\cdot10^{-2}$	$1\cdot10^{-2}$	$1\cdot10^{-4}$	$1\cdot10^{-5}$	$1\cdot10^{-10}$	0	$-1\cdot10^{-6}$
label		e	f				
Value	$-1\cdot10^{-5}$	$-5\cdot10^{-5}$	$-1\cdot10^{-4}$	$-2.5\cdot10^{-4}$	$-5\cdot10^{-4}$	$-1\cdot10^{-3}$	$-1.5\cdot10^{-3}$
label	g		h		i		j

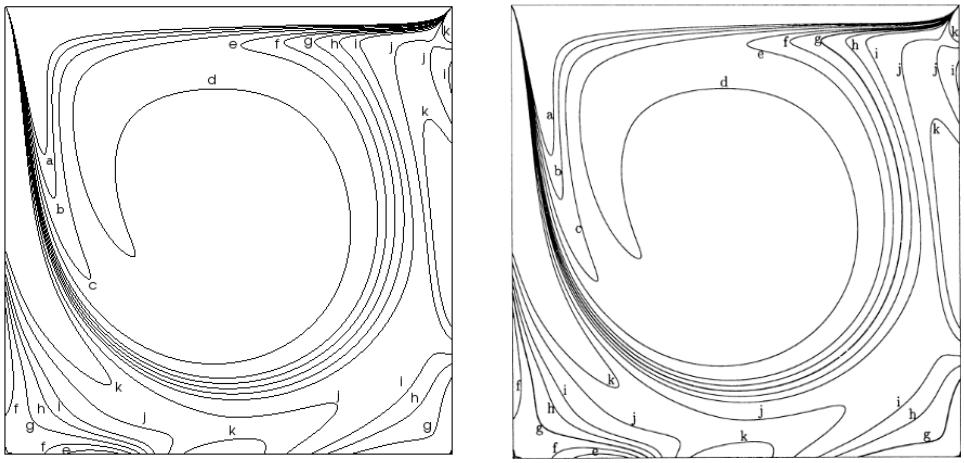

(a) present work (b) work of Botella and Peyret (1998)

Figure 3.14. Laminar case (Re=1.000), vorticity contours contours for the present work and the work of Botella and Peyret (1998).

Table 3.3. Vorticity contours shown in Figure 3.14 (Botella and Peyret, 1998).

Vorticity											
Value	5	4	3	2	1	0.5	0	-0.5	-1	-2	-3
label	a	b	c	d	e	f	g	h	i	j	k

3.4.3 Turbulent case

In the second simulation, an unsteady incompressible turbulent flow at Re=100.000 (i.e., $\upsilon=10^{-5}$) is considered. According to Section 3.3, any RANS approach with turbulent viscosity model can be applied to the POD-FV-ROM for turbulent flows. Nevertheless, for this simulation, the Shear Stress Transport (SST) formulation of the k-ω modelling (Menter, 1994; Menter et al., 2003) is selected for two main reasons.

$$\begin{cases} \boldsymbol{u}_t + (\boldsymbol{u}\cdot\nabla)\boldsymbol{u} = \nabla\cdot\left[-p\boldsymbol{I} + (\nu+\nu_t)(\nabla\boldsymbol{u} + (\nabla\boldsymbol{u})^T) - \frac{2}{3}k\boldsymbol{I}\right] & on\ [0,T]\ x\ \Omega \\ \nabla\cdot\boldsymbol{u} = 0 & on\ [0,T]\ x\ \Omega \\ \boldsymbol{u} = (-1,0) & on\ [0,T]\ x\ \Gamma_1 \\ \boldsymbol{u} = (0,0) & on\ [0,T]\ x\ \Gamma_{2,3,4} \\ \boldsymbol{u} = (0,0) & on\ [0]\ x\ \Omega \\ \frac{\partial k}{\partial t} + (\boldsymbol{u}\cdot\nabla)k = \nabla\cdot[(\nu+\nu_T\alpha_k)\nabla k] - \beta^* k\omega + P & on\ [0,T]\ x\ \Omega \\ \frac{\partial\omega}{\partial t} + (\boldsymbol{u}\cdot\nabla)\omega = \nabla\cdot[(\nu+\nu_T\alpha_\omega)\nabla\omega] - \beta\omega^2 + \frac{\gamma}{\nu_T}P + 2(F_1-1)\frac{\alpha_{\omega 2}}{\omega}\nabla k\cdot\nabla\omega & on\ [0,T]\ x\ \Omega \end{cases} \quad (3.52)$$

The first one is that SST k-ω is a low – Reynolds model and the mesh can be refined without compromising the solution stability. In this way, we provide the FOM, and in turn the ROM, with a fine mesh solution. The second reason to select SST k-ω relies on the fact that this model blends the k-ω features near the wall and the k-ε behaviour in the bulk flow. Let $\Omega = (0,1) \times (0,1)$ and $T > 0$ the simulation time, the governing equations reads (for further information about the model parameter, functions and the BC of the turbulent quantities, please refers to Menter, 1994; Menter et al., 2003; OpenFOAM, 2014).

The full order simulation is performed until T=100 s with a constant time step of $4 \cdot 10^{-4}$. Figure 3.15a, Figure 3.16a and Figure 3.17a present the velocity, the pressure and the eddy viscosity of the full order simulation at different time. During the offline phase, the basis for the velocity, the face flux, the pressure and the eddy viscosity are calculated following the procedure described in Section 3.3. As for the snapshots creation, the first three functions of the velocity, pressure and turbulent viscosity bases are shown in Figure 3.18 and the decay of the normalized POD eigenvalues is given in Figure 3.19. Considering the decay trend, N_r=85 basis functions are used for the turbulent case hereinafter in order to reach a good compromise between accuracy and computational requirements. The number of the basis functions is increased with respect to the laminar case as expected due to the increase of the Reynolds number and the flow complexity.

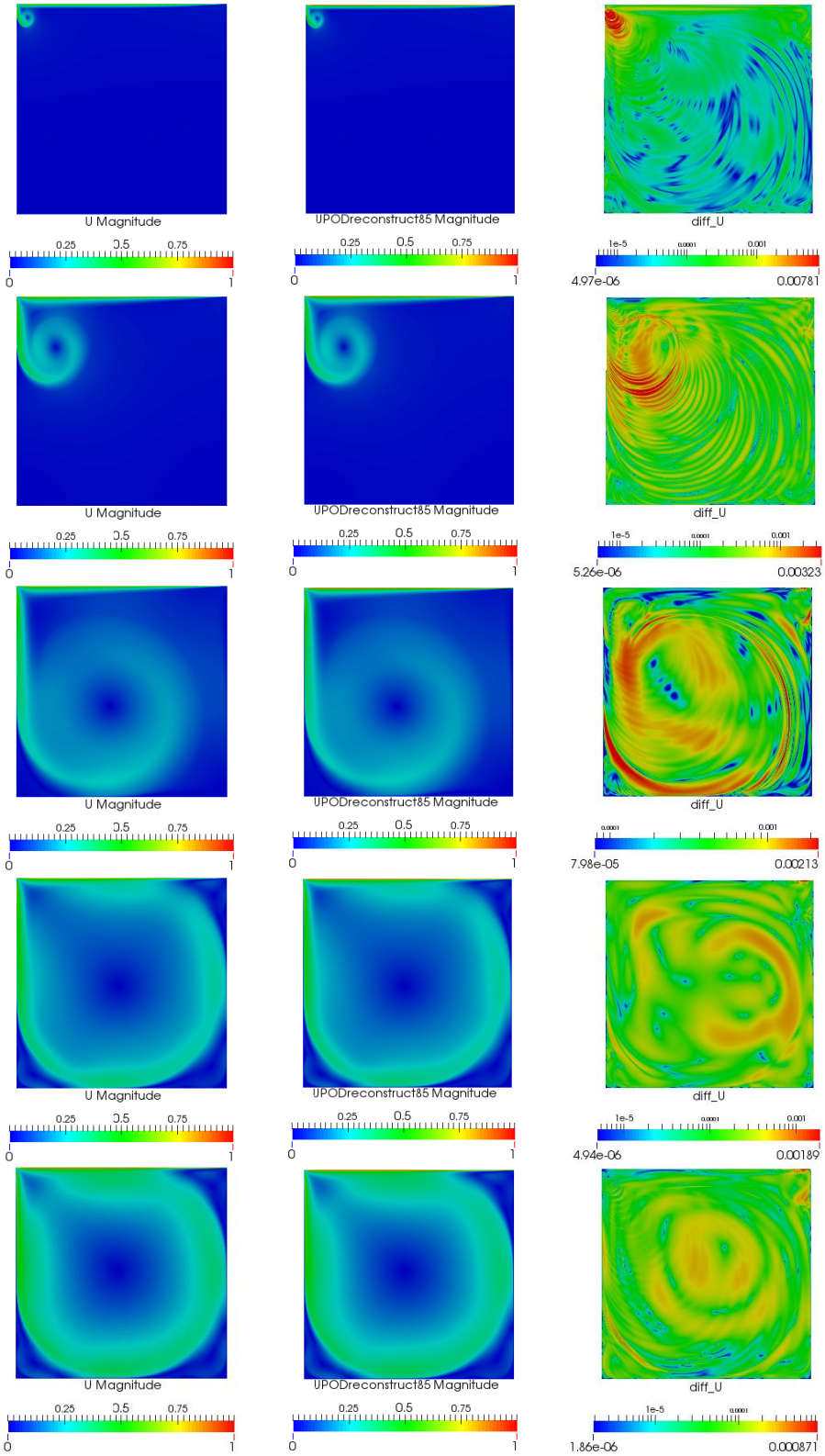

(a) FOM (b) ROM (c) difference

Figure 3.15. Turbulent case (Re=100.000), contours of the velocity magnitude of the full order model (a), the reduced order model with N_r=85 (b) and relative difference (c) at different time. From top to bottom 1 s, 5s, 20 s, 40 s, 100s.

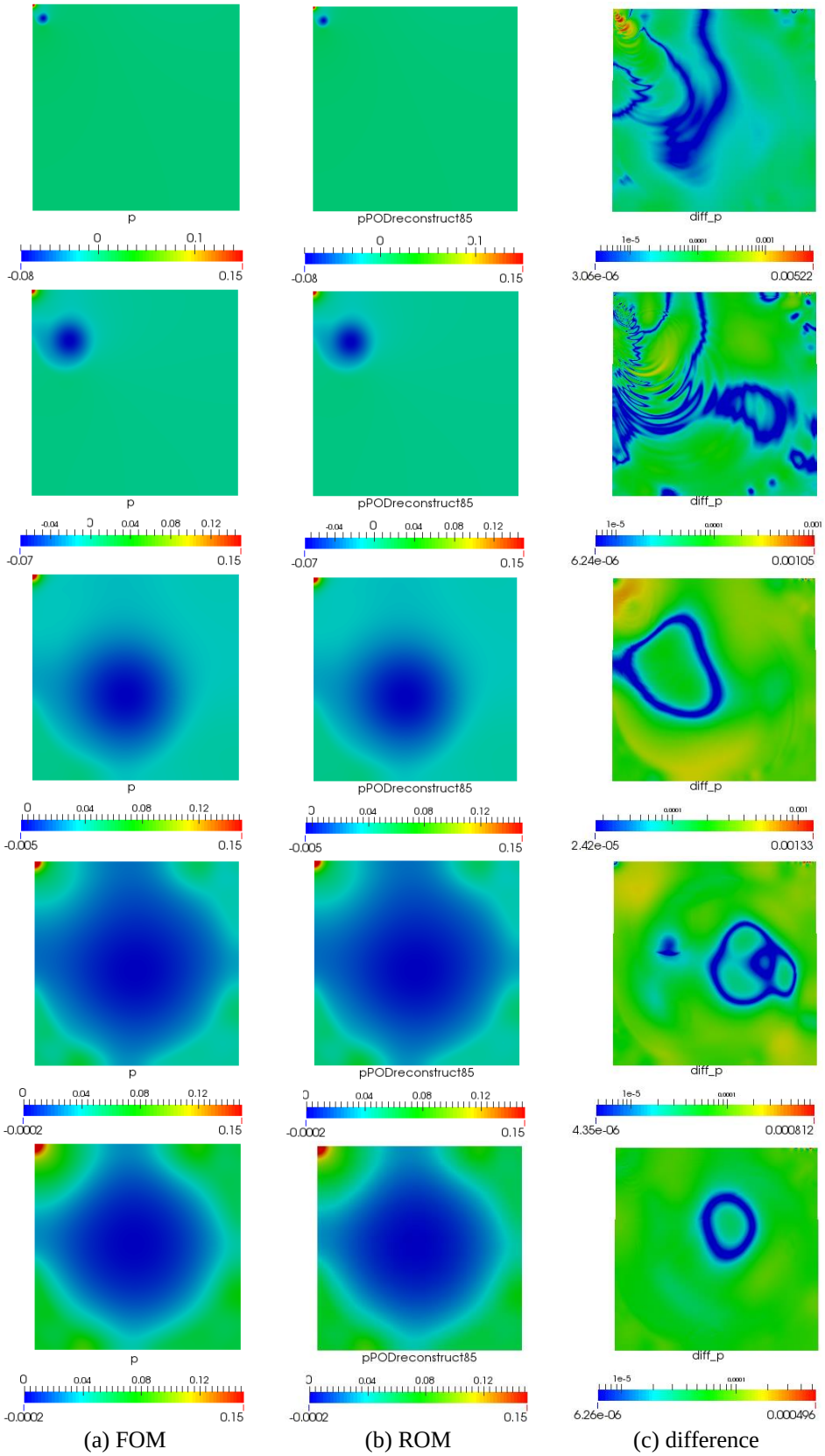

(a) FOM (b) ROM (c) difference

Figure 3.16. Turbulent case (Re=100.000), contours of the pressure of the full order model (a), the reduced order model with N_r=85 (b) and relative difference (c) at different time. From top to bottom 1 s, 5s, 20 s, 40 s, 100s.

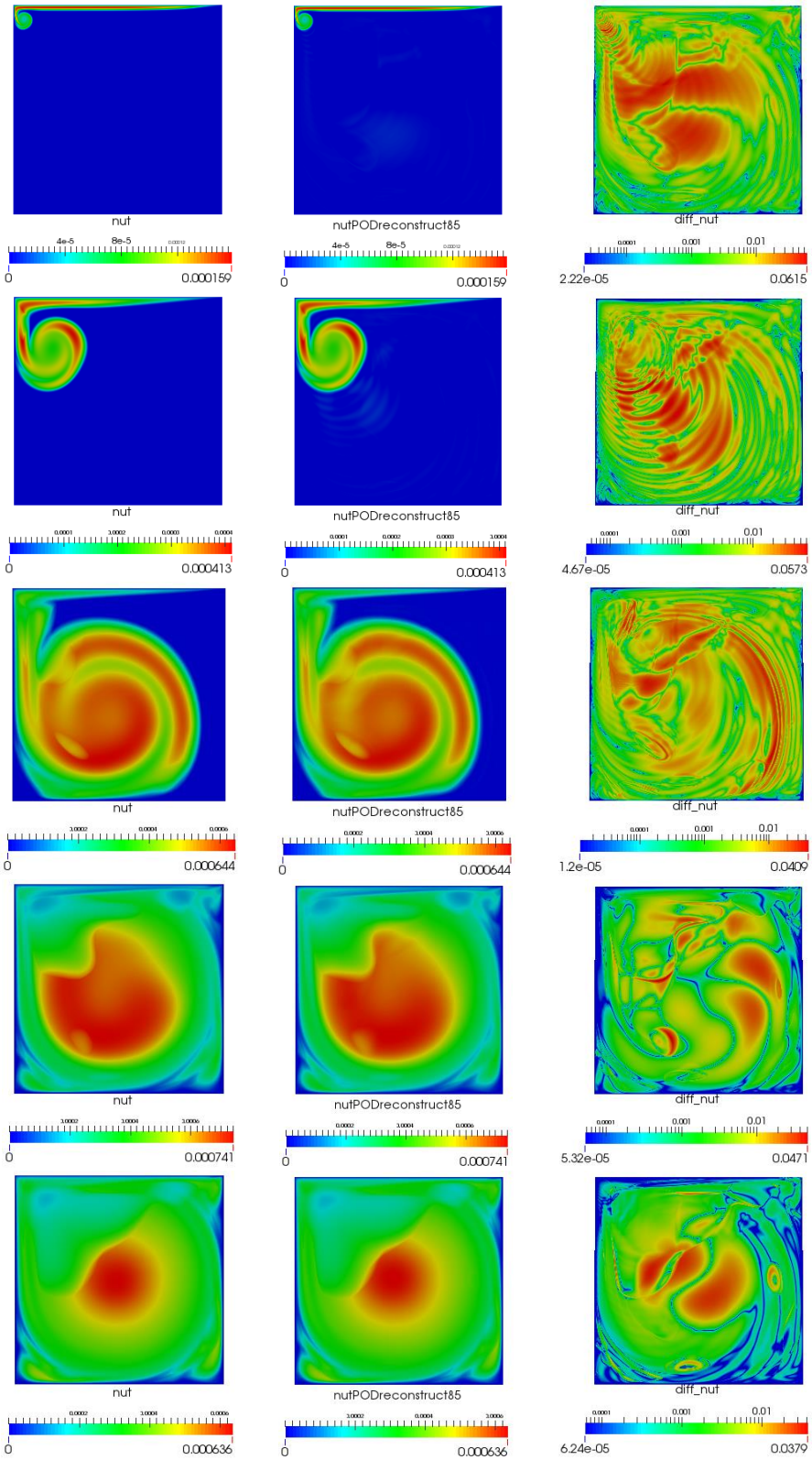

(a) FOM (b) ROM (c) difference

Figure 3.17. Turbulent case (Re=100.000), contours of the eddy viscosity of the full order model (a), the reduced order model with N_r=85 (b) and relative difference (c) at different time. From top to bottom 1 s, 5s, 20 s, 40 s, 100s.

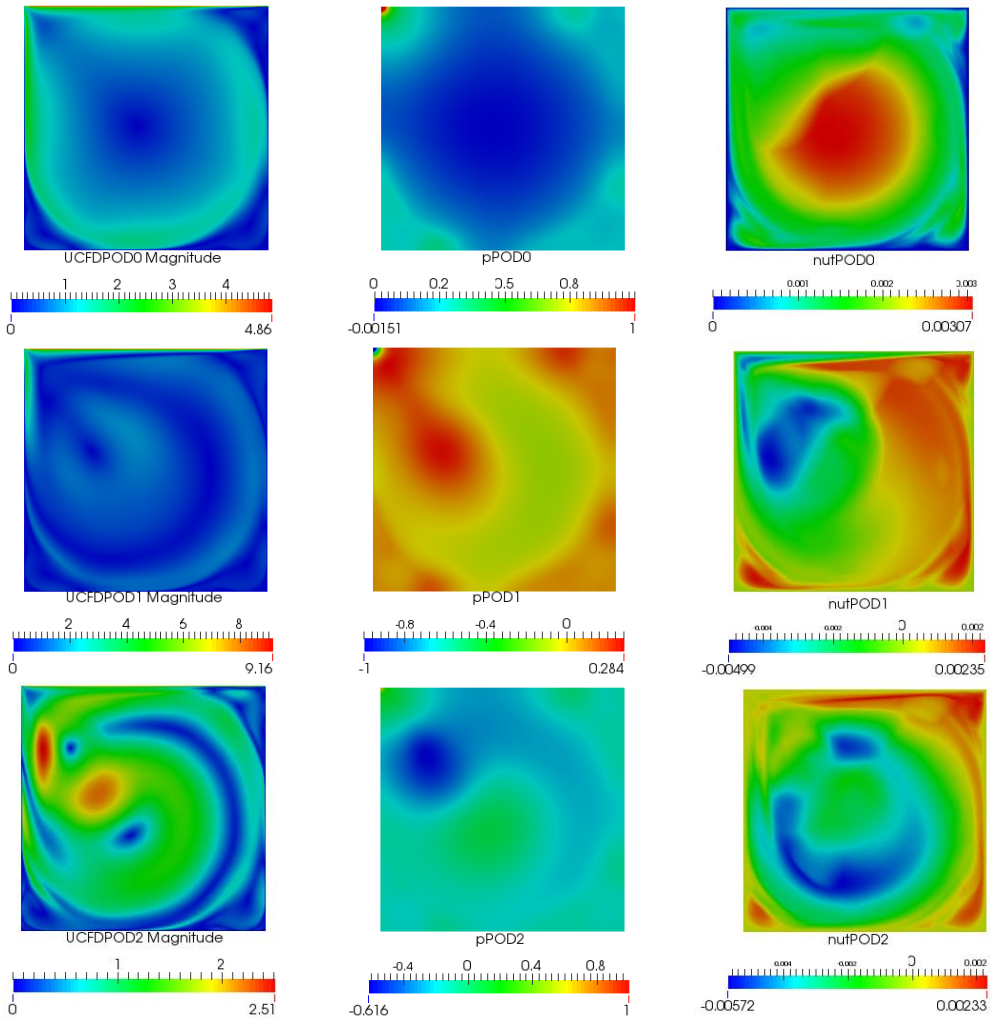

(a) velocity (b) pressure (c) turbulent viscosity

Figure 3.18. Turbulent case (Re=100.000), contours of the first three basis functions for the velocity (a), pressure (b) and turbulent viscosity (c).

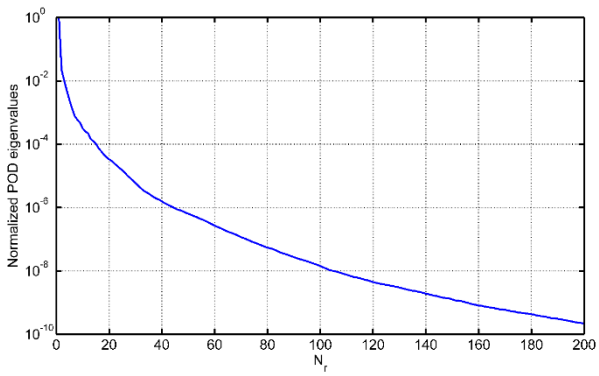

Figure 3.19. Turbulent case (Re=100.000), normalized POD eigenvalues.

Once having calculated the matrices of the Equation (3.27), the set of the ODE is simulated in the Dymola environment. The penalizing value τ is fixed at 10^{-2}. Due to the energy blow up afflicting the turbulent flows mentioned in the Section 3.1, the relative error of the kinetic energy between FOM and ROM could be significant (Figure 3.20). Except in the very initial moment of

the transient, the relative error is around 10^{-3}, indicating that the ROM is not affected by energy blow up. In particular, in the second part of the transient, even if the error is negative (i.e., the energy in ROM becomes slightly greater than the energy in FOM), the energy difference is reduced along the simulation time. Figure 3.15b, Figure 3.16b and Figure 3.17b present the velocity, the pressure and the turbulent viscosity field reconstructed starting from the POD time coefficients. The relative difference with respect to the FOM results is depicted in Figure 3.15c, Figure 3.16c and Figure 3.17c.

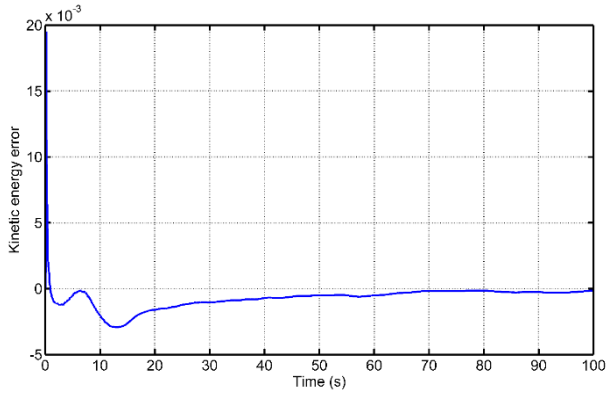

Figure 3.20. Turbulent case (Re = 100.000), kinetic energy difference between the FOM and ROM (N_r=85).

In Figure 3.21, the L^2 error for the ROM velocity is compared with the error of the velocity reconstructed from the Galerkin projection of the snapshots on the basis functions. Also in this case, the error is higher in the first part of the transient since the velocity magnitude starts at rest (see initial condition, Equation (3.52)) small. After 15 s, the error is lower than $6 \cdot 10^{-3}$ and at the end of the transient, it is set to $3.5 \cdot 10^{-4}$.

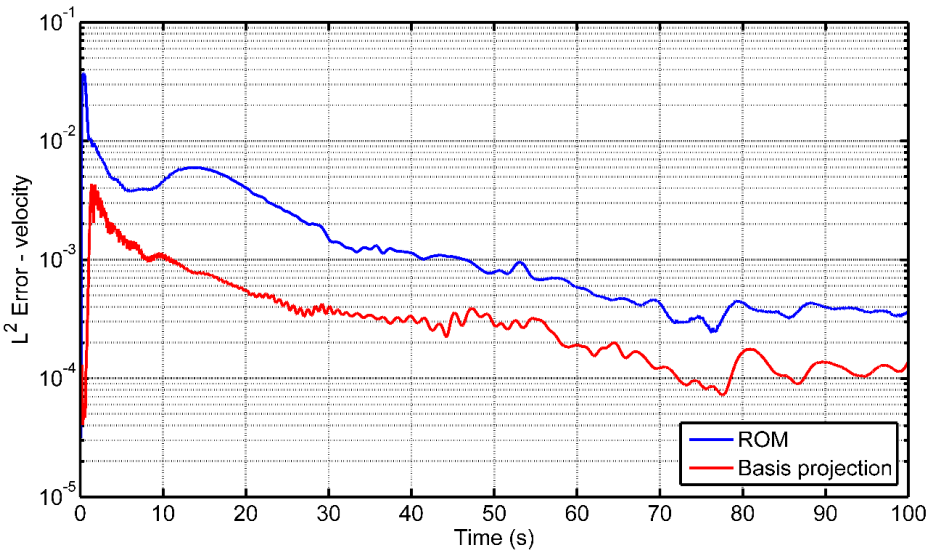

Figure 3.21. Turbulent case (Re=100.000), L^2 error of the reconstructed velocity from ROM with N_r=85 (blue line) and basis projection (red line).

Similar results are obtained for the pressure error (Figure 3.22). The error in the first instances is $4 \cdot 10^{-2}$, but just after some seconds is kept lower than $8 \cdot 10^{-3}$ for all the transient. The error for the turbulent viscosity is shown in Figure 3.23. The results seems to be less satisfactory with

respect to the velocity and pressure but it should consider that, in this work, as for the pressure, the spatial basis for the turbulent viscosity are calculated form the eigenvectors of the correlation matrix of the velocity and therefore they are not tailored for the turbulent viscosity. In this way, only the momentum equation is projected in the spatial basis, disregarding the complicated the equations for the turbulent quantities. Nevertheless, other options can be undertaken as the expansion of k and ω along with the projection of all the equation constituting the turbulence modelling. Notwithstanding, the maximum L^2 error is 10^{-1} at the beginning of the transient and after some seconds it sets to 10^{-2} for the rest of the transient.

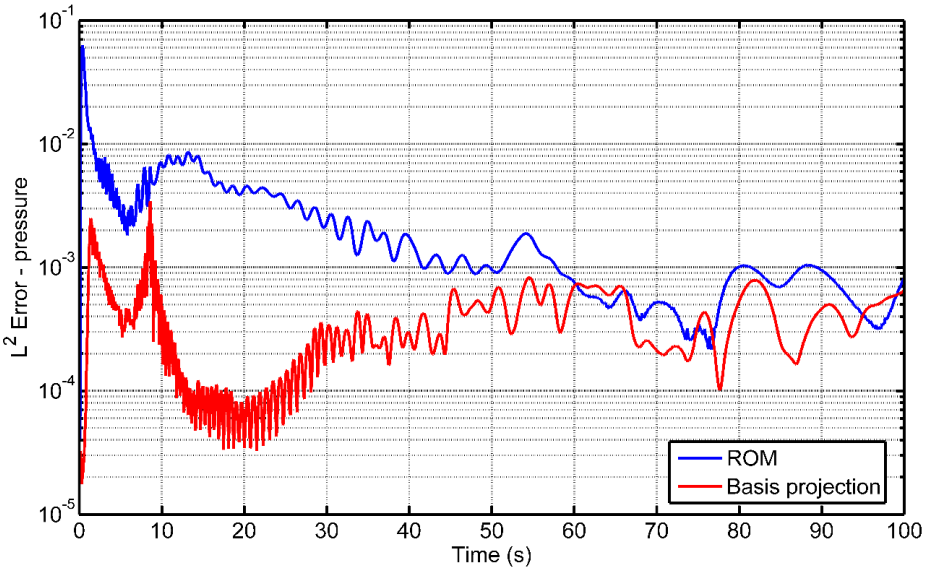

Figure 3.22. Turbulent case (Re=100.000), L^2 error of the reconstructed pressure from ROM with N_r=85 (blue line) and basis projection (red line).

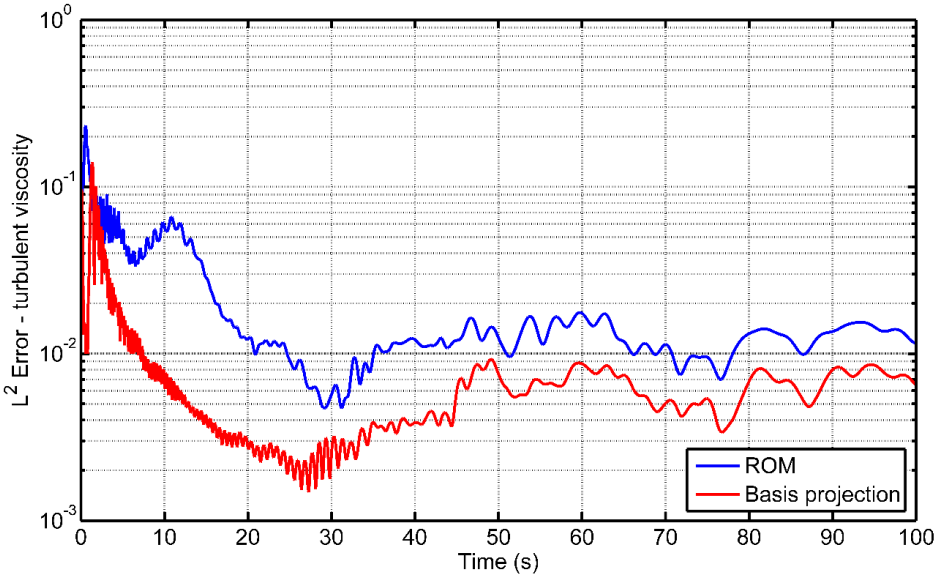

Figure 3.23. Turbulent case (Re = 100.000), L^2 error of the reconstructed turbulent viscosity from ROM with N_r=85 (blue line) and basis projection (red line).

Finally, for the full order model, a computational time of 4462 cpu-hours was required for the simulation of T=100 s. On the other hand, for the ROM, only a computational time of 45 s was

needed to perform the same simulation. For the sake of completeness, for the POD generation and the ROM matrix calculation of the offline step, the procedure takes 3 cpu-hours and 760 cpu-hours, respectively.

3.5. ALFRED pool model

A reduced order model of the ALFRED coolant pool (Figure 3.24a) has been set up according to the POD-FV-ROM procedure described in Sections 3.2 and 3.3. In particular, a 2D geometry (Figure 3.24b) is adopted for the sake of simplicity even if the approach can be easily extended to the 3D case. The reduced order model is aimed at being employed in the object-oriented plant simulator of the ALFRED reactor, substituting the zero-dimensional model of the cold pool. As already stated in Section 3.1, the spatial effects assume great relevance in a LFR pool especially whether the oxygen control is required. To this end, relying on a spatial model could provide additional information in the development of the control system design.

In order to demonstrate the possibility to employ ROM-based components in control-oriented simulator, the possibility to vary the input variables of the model should be undertaken. In this case, the latter are represented by the Steam Generator (SG) outlet ($\mathbf{u}_{SG1}$, $\mathbf{u}_{SG2}$) velocity. In particular, they could be a possible control variable employed to change the core inlet velocity profile[18] ($\mathbf{u}_{in}$). In addition, these variables are the connections between the cold pool component and the rest of the plant, the core inlet profile being an input parameter for the core component since it determines the mass flow rate for each FA, and the SG outlet velocity being an output parameter for the SG component. For this purpose, a *parametric* reduced order model of the ALFRED pool has been developed, focusing on the variation of the core inlet velocity profile following a SG outlet ($\mathbf{u}_{SG1}$, $\mathbf{u}_{SG2}$) velocity change. Considering the high density of the lead and the velocity in the pool, the turbulent approach described in Section 3.3 is applied to the ALFRED coolant pool case.

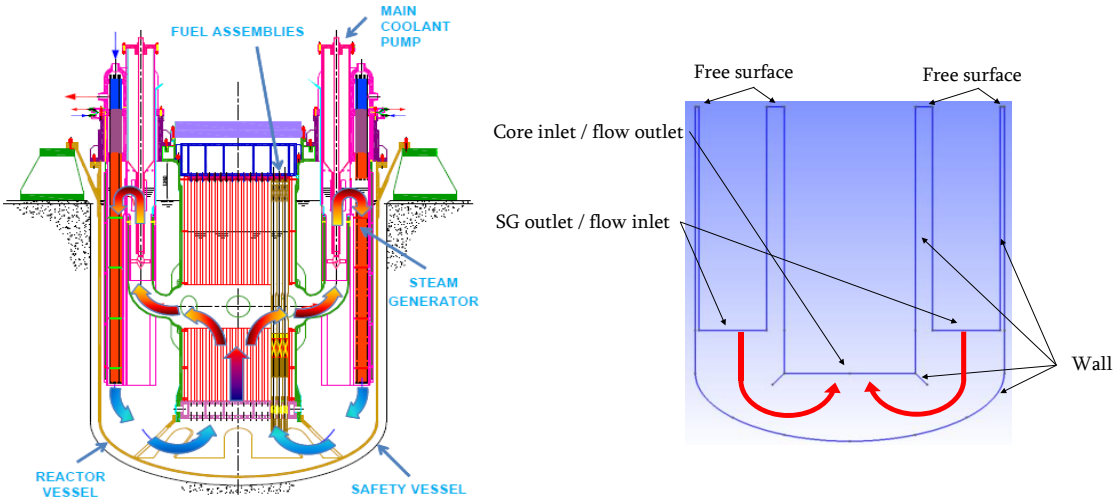

(a) (b)

Figure 3.24. (a) ALFRED pool configuration, (b) 2D geometry of the ALFRED pool model.

[18] The inlet temperature can be also changed whether the energy equation is considered.

3.5.1 The offline procedure

The offline procedure, i.e., the calculation of the FOM solutions, the snapshots creation and the construction of the matrix of Equation (3.48), is performed in the OpenFOAM environment (Weller et al., 1998; OpenFOAM, 2014) and exploiting the post-processing utilities developed for the cavity case (Section 3.4.1). The boundary conditions for pressure and velocity are shown in Figure 3.25. In particular, for the outlet SG velocity, a range between 0.17 m/s (nominal condition) and 0.085 m/s (50% reduction with respect to the nominal condition) is spanned.

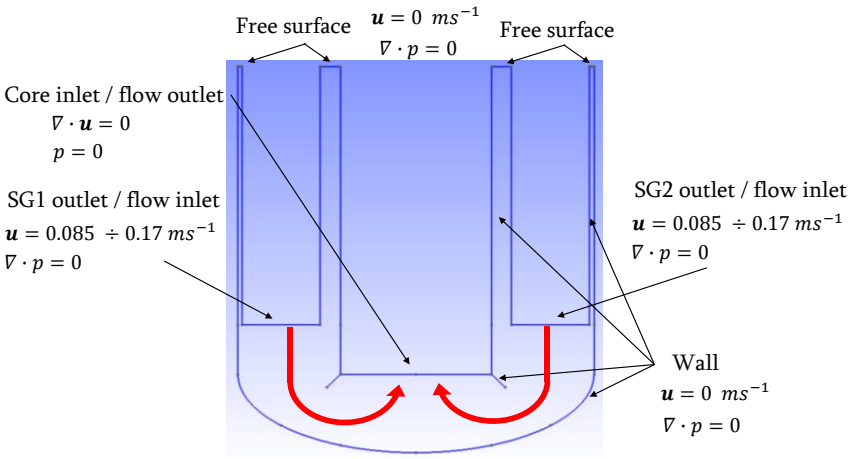

Figure 3.25. Boundary conditions for the ALFRED pool model.

As for the RANS turbulent modelling, the Shear Stress Transport (SST) formulation of the k-ω modelling (Menter, 1994; Menter et al., 2003; OpenFOAM, 2014) is selected because it is a low Reynolds model and it blends the k-ω features near the wall and the k-ε behaviour in the bulk flow. Notwithstanding, a steady-state comparison with respect to k-ε modelling with wall functions is performed in nominal condition stating a good agreement between the outcomes of the two modelling approaches (Figure 3.26 and Figure 3.27).

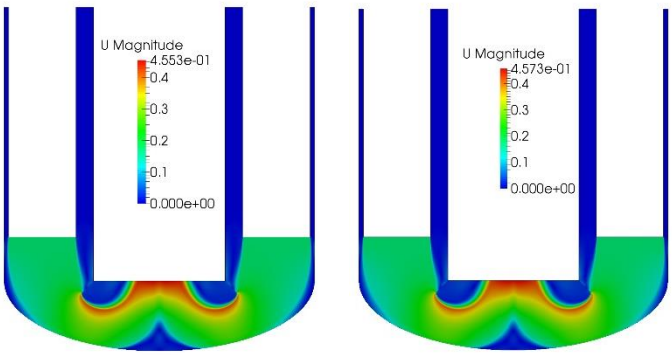

(a) (b)

Figure 3.26. ALFRED pool case. Contours of velocity magnitude in nominal condition calculated with (a) k-ω and (b) k-ε model.

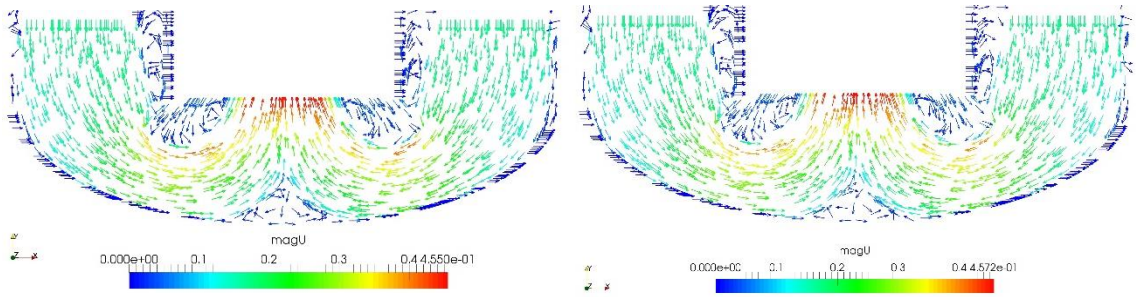

(a) (b)

Figure 3.27. ALFRED pool case. Vectors of velocity magnitude in nominal condition calculated with (a) k-ω and (b) k-ε model.

Sixteen transients are performed to span the range of the outlet velocity between 0.17 and 0.085 m/s (Table 3.4). After 0.5 s, a 5 s ramp decrease of the SG outlet velocity is carried out from the initial nominal value to the final value. Figure 3.28 represents the evolution of the contours of the velocity magnitude in Case 13, along with the profile of the velocity at the core inlet. Besides being a demanding transient both from a computational and operational point of view, it is interesting to point out the change in the velocity profile at the core inlet. After the decrease of the SG2 velocity, the profile at the core inlet is totally changed, moving from the center of the core to the periphery. This kind of information cannot be retrieved with a zero-dimensional/1D model where usually the core inlet velocity is decreased to the same amount of the SG decrease, with an unchanged profile. Even if the field of application is the control, it is clear that dealing with a model that is able to reproduce such behaviour can provide significant insight from a safety point of view. In particular, for the considered transient, the change in the core inlet profile results in the cooling modification of different core zones, especially for the left part of the core where the velocity of the coolant is close to zero and almost no cooling action is performed.

Table 3.4. ALFRED pool case. Transient cases performed for the construction of the parametric ROM.

Case #	$\mathbf{u}_{SG1}$ (m/s)		$\mathbf{u}_{SG2}$ (m/s)	
	initial	final	initial	final
1	0.170	0.085	0.170	0.085
2	0.170	0.085	0.170	0.119
3	0.170	0.085	0.170	0.153
4	0.170	0.085	0.170	0.170
5	0.170	0.119	0.170	0.085
6	0.170	0.119	0.170	0.119
7	0.170	0.119	0.170	0.153
8	0.170	0.119	0.170	0.170
9	0.170	0.153	0.170	0.085
10	0.170	0.153	0.170	0.119
11	0.170	0.153	0.170	0.153
12	0.170	0.153	0.170	0.170
13	0.170	0.170	0.170	0.085
14	0.170	0.170	0.170	0.119
15	0.170	0.170	0.170	0.153
16	0.170	0.170	0.170	0.170

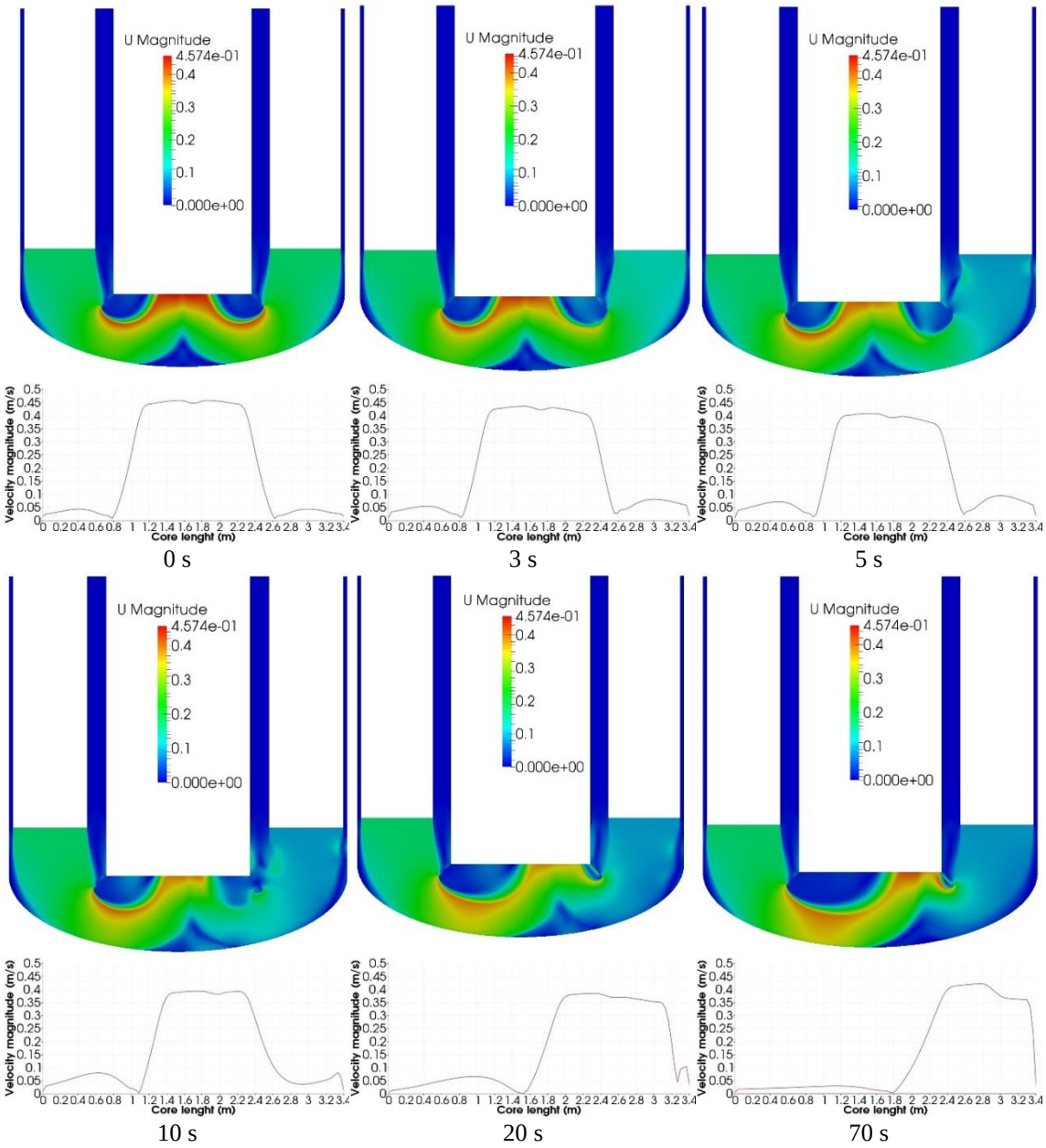

Figure 3.28. ALFRED pool case. Evolution of the contours of the velocity magnitude in Case 13, along with the profile of the velocity at the inlet core.

For the sake of clarity, some numerical clarifications should be pointed out. A PISO algorithm (Versteeg and Malalasekera, 2007; OpenFOAM, 2014) available in OpenFOAM is employed to solve the RANS since a fixed time step of $4 \cdot 10^{-4}$ s allows obtaining for each time step at least a convergence of 10^{-4} for the main variables (i.e., velocity, pressure, turbulent quantities, ….). The offline procedure was performed on the CINECA GALILEO cluster with 16 processors.

3.5.2. The object-oriented modelling

In the object-oriented simulator described in Chapter 1, the cold pool is modelled considering mass and energy balances (Figure 3.29). As pointed out in the Section 3.1, this kind of approach prevents the simulation tool from taking into account turbulence mixing and 3D effects, which

can have a remarkable impact both on control (i.e., the oxygen control in LFR) and safety (i.e., as in Case #13 of the previous section, see Figure 3.28) issues.

```
Model Cold_pool "Open tank with free surface"
    parameter Area A "Cross-sectional area";
    parameter Volume V0=0 "Volume at zero level";
    parameter Pressure pext=1.01325e5 "Surface pressure";
    parameter Boolean allowFlowReversal=system.allowFlowReversal "= true to allow flow reversal, false
    restricts to design direction";
    outer ThermoPower.System system "System wide properties";
    parameter Length ystart "Start level"
    parameter SpecificEnthalpy hstart=1e5
    Length y(start=ystart, stateSelect=StateSelect.prefer) "Level";
    Volume V "Liquid volume";
    Mass M "Liquid mass";
    Enthalpy H "Liquid (total) enthalpy";
    Medium.SpecificEnthalpy h(start=hstart, stateSelect=StateSelect.prefer)     "Liquid specific enthal
    py";
    Medium.SpecificEnthalpy hin "Inlet specific enthalpy";
    Medium.SpecificEnthalpy hout "Outlet specific enthalpy";
    Medium.AbsolutePressure p(start=pext) "Bottom pressure";
    constant Real g=Modelica.Constants.g_n;
    parameter Choices.Init.Options initOpt=Choices.Init.Options.noInit     "Initialisation option;

equation
    liquidState = Medium.setState_ph(pext, h);
    V = V0 + A*y "Liquid volume";
    M = V*Medium.density(liquidState) "Liquid mass";
    H = M*Medium.specificInternalEnergy(liquidState) "Liquid enthalpy";
    der(M) = inlet.m_flow + outlet.m_flow "Mass balance";
    der(H) = inlet.m_flow*hin + outlet.m_flow*hout "Energy balance";
    p - pext = Medium.density(liquidState)*g*y "Stevino's law";
end Cold_pool;
```

Figure 3.29. Modelica code of the *Cold_pool* component (Section 1.2.2).

The *Coolant Pool ROM* component of the ALFRED reactor (Figure 3.30) has been developed employing the turbulent POD-FV-ROM approach proposed in Sections 3.2 and 3.3, considering the velocity of the two SGs as parametrized boundary conditions. Accordingly, the Equation (3.48) is modified as follows

$$\dot{\boldsymbol{a}} = \upsilon(\boldsymbol{B} + \boldsymbol{BT})\boldsymbol{a} - \boldsymbol{a}^{\boldsymbol{T}}(\boldsymbol{C} - \boldsymbol{CT1} - \boldsymbol{CT2})\boldsymbol{a} + \boldsymbol{Aa} - \tau(\boldsymbol{u}_{\boldsymbol{SG1}}\boldsymbol{D}_{\boldsymbol{SG1}} + \boldsymbol{u}_{\boldsymbol{SG2}}\boldsymbol{D}_{\boldsymbol{SG2}} - \boldsymbol{Ea}) \tag{3.53}$$

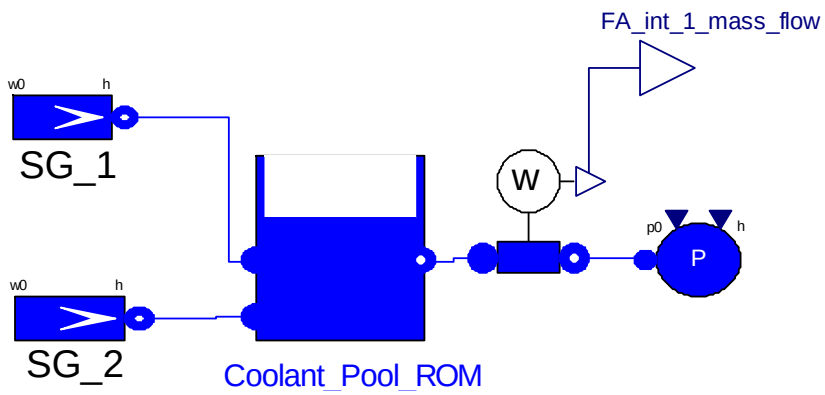

Figure 3.30. Object-oriented ROM-based component of the ALFRED pool.

The Equation (3.53) is implemented in the component (Figure 3.31) that calculates the mass flow rate of the central FA as possible output variable.

```
model pisoFoam_00
 extends ThermoPower.Icons.Water.Tank;
  import nonlinear_piso_bis;
  parameter Integer N=79 "Numer of basis";
   parameter Real B_b_1[:,1]=readMatrix("B_79.mat", "B_b_1", N,1);
   parameter Real B_b_2[:,1]=readMatrix("B_79.mat", "B_b_2", N,1);
   parameter Real Mat[:,:]=readMatrix("Mat_79.mat", "Mat", N, N);
   parameter Real FA_1_flow[1,:]=readMatrix("FA_in_1.mat", "FA_in_1_v", 1,N);
   parameter Real ci[1,:]=readMatrix("ci_79.mat", "ci_1", 1,N);
   parameter Real h1=1;
   parameter Real h2=1;
  parameter Real u_in_2=-0.17;
     Real a[N,1];

equation
  der(a)=Mat*a+B_b_1*inlet_SG_1.m_flow+B_b_2*inlet_SG_2.m_flow+nonlinear_piso_bis(a);
  FA_int_1.m_flow=-FA_1_flow[1,:]*a[:,1;

initial equation
   a=transpose(ci);
end pisoFoam_00;
```

Figure 3.31. Modelica code of the *Coolant pool ROM* component.

3.5.3. Simulation results

As for the simulation results, firstly, a reduced order model has been developed representing the time behaviour for fixed boundary conditions for each case. For the sake of brevity, only the results on the parametrized coolant pool ROM are presented in this Section. The following parametrized model has been developed starting from the snapshots of the cases involving only the velocity variation of the second steam generator (i.e., the Cases from 13 to 16, see Table 3.4).

In order to assess the accuracy of the ROM model, the difference between the ROM and FOM model is reported using the L^2 error (see Equation (3.51)). In Figure 3.32, the L^2 error of the ROM velocity is compared with 80 and 65 spatial basis functions following a velocity variation of the second SG of 10%, 30% and 50% with respect to the nominal value. For a velocity variation of 10% and 30% (i.e., $\mathbf{u}_{SG2}$ = 0.153 m/s and $\mathbf{u}_{SG2}$ = 0119 m/s, respectively), the error is almost always lower than $1\cdot10^{-2}$, whereas for a velocity variation of 50% (i.e., $\mathbf{u}_{SG2}$ = 0.085 m/s) the error is between $5\cdot10^{-2}$ and $8\cdot10^{-3}$. Even if a worse performance is obtained in the latter case, the results are very promising being the maximum relative error of 5%.

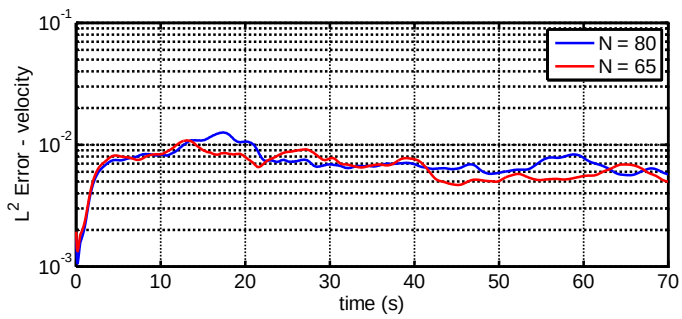

(a)

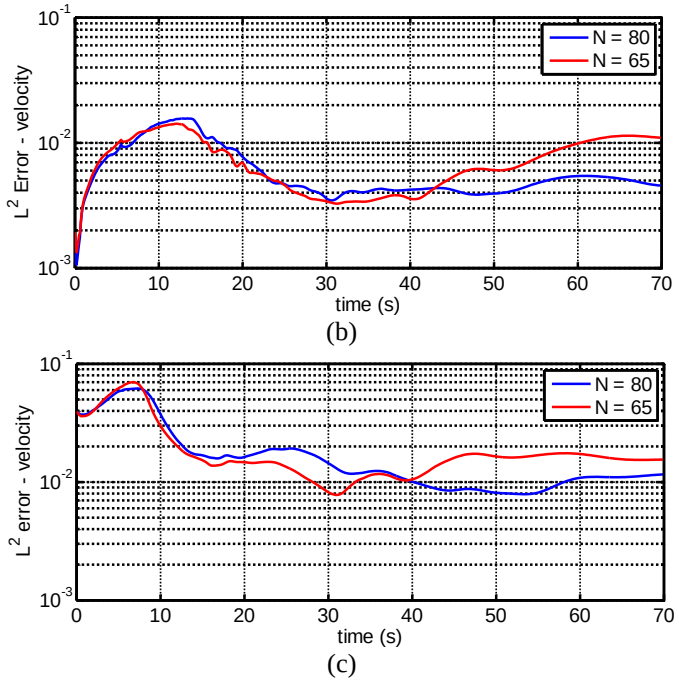

Figure 3.32. ALFRED pool case. L^2 error of the reconstructed velocity from ROM with N_r=80 (blue line) and N_r=65 (red line) following an SG variation of (a) 10% - u_{SG2}=0.153 m/s; (b) 30% - u_{SG2}=0.119 m/s; (c) 50% - u_{SG2}=0.085 m/s with respect to the nominal value.

The L^2 error of the velocity field is relevant for a general assessment of the accuracy of the reduced order model. On the other hand, since the purpose is the use of the ROM-based component in a control-oriented simulator, the evaluation of the discrepancies between the FOM and the ROM-based component in reproducing the output variables is relevant as well. In this sense, the output variables of the coolant pool model are the inlet mass flow rate of the FA since they represent the connection between the coolant pool ROM and the reactor core model. In Figure 3.33, the variation of the mass flow rate in the central FA is shown following a velocity variation of the second SG of 10%, 30% and 50% with respect to the nominal value.

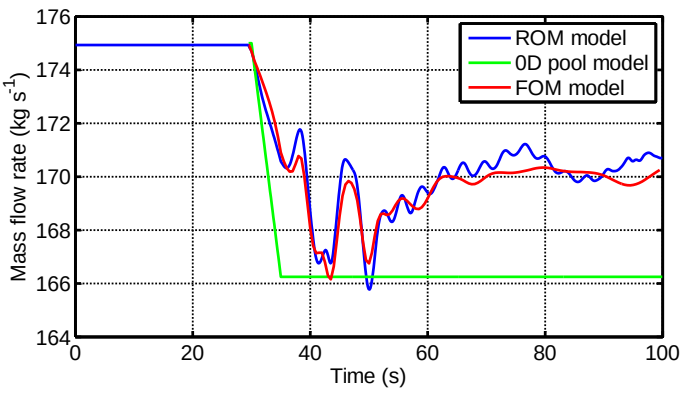

(a)

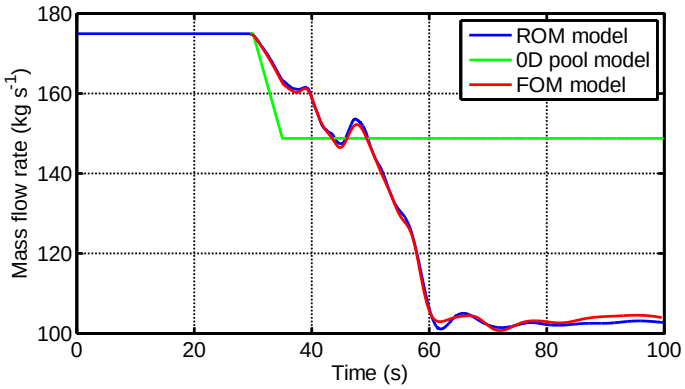

(b)

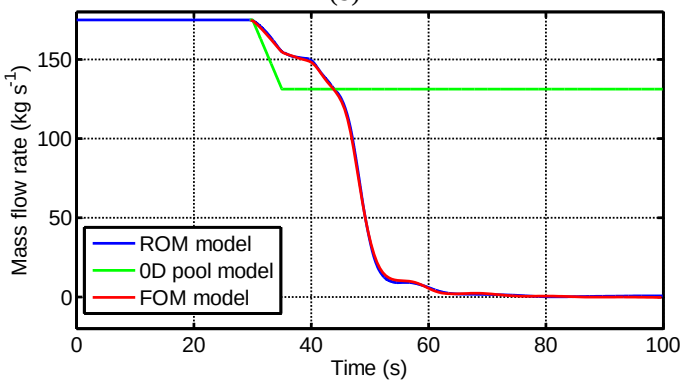

(c)

Figure 3.33. ALFRED pool case. .Evolution of the mass flow rate in the central FA following an SG variation of (a) 10% - uSG2 =0.153 m/s; (b) 30% - uSG2=0.119 m/s; (c) 50% - uSG2=0.085 m/s with respect to the nominal value. – FOM (red line), ROM (blue line) and zero dimensional (green line) model results.

In the different cases, there is a good agreement between the reduced order model and the full order model. It is worthwhile to underline that for all the three cases, the 0D model of the cold pool completely fails in reproducing the transient behaviour and the final mass flow rate value. This can be explained considering the Figure 3.28. In this asymmetric transient, the spatial information of the velocity is crucial since the inlet velocity profile moves to the periphery of the core. This effect is well represented in the full order model and in the derived reduced order model. On the other hand, the 0D model is not able to catch this spatial information and the outcome is an average mass flow rate along the entire core inlet.

As already done in Section 2.4.2 for the neutronics, the capability of the reduced order model to reproduce different situations from what included in the snapshots (Table 3.4) should be assessed. Even if the best option consists in calculating as much as possible snapshots related to the system behaviour in order to "train" the spatial basis, it is not possible to include every possible situation that may happen in the cold pool and therefore it is important to ensure acceptable results if the simulation is run outside the range delimited by the calculated snapshots. To this purpose, the variation of the second SG velocity of 20% and 40% with respect to the nominal value (i.e., $\mathbf{u}_{SG2}$ = 0.136 m/s and $\mathbf{u}_{SG2}$ = 0102 m/s, respectively) is considered with the full order model. The results are then compared with the ROM built starting from the snapshots calculated beforehand (i.e., the Cases from 13 to 16, see Table 3.4).

In Figure 3.34, the L^2 error of the ROM velocity with 80 spatial basis functions following a velocity variation of the second SG of 20%, and 40% with respect to the nominal value is shown.

Even if the error is around 10% at the end of the transient, the results should be read considering that these situations are not included in the snapshots set. In this case, there is no guarantee that the reduced order model can reproduce the correct behaviour. On the other hand, the coolant pool ROM turns out to give physical results without mathematical or numerical issues. This is mainly due to the fact that in this thesis the CRT approach has been selected rather than SRS (see Introduction), building the reduced order model upon a robust physical model.

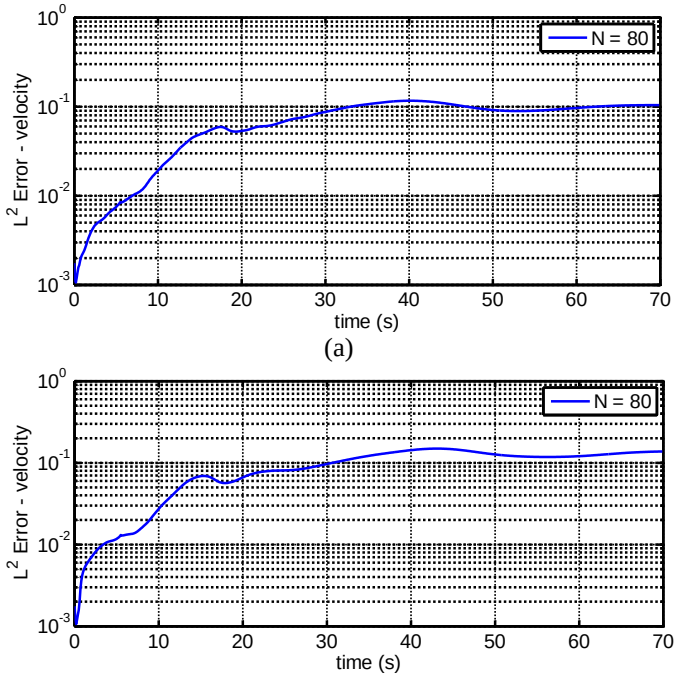

Figure 3.34. ALFRED pool case. L^2 error of the reconstructed velocity from ROM with Nr=80 following an SG variation of (a) 20% - u_{SG2} =0.136 m/s; (b) 40% - u_{SG2}=0.102 m/s with respect to the nominal value.

In addition, the assessment is performed also considering the output variable, i.e., the mass flow rate in the central FA (Figure 3.35). A good agreement is obtained in case of 20% variation (Figure 3.35a), whereas in the other case (Figure 3.35b) a bigger discrepancy is found. This can be explained considering the velocity inlet profile for FOM e ROM model (Figure 3.36). In particular, there is a shift in the profile between the two models, magnified by the fact that the mass flow rate behaviour in the central FA is considered. However, the result can be considered acceptable since the 0D model shows a bigger discrepancy than the ROM-based component with respect to the high fidelity model.

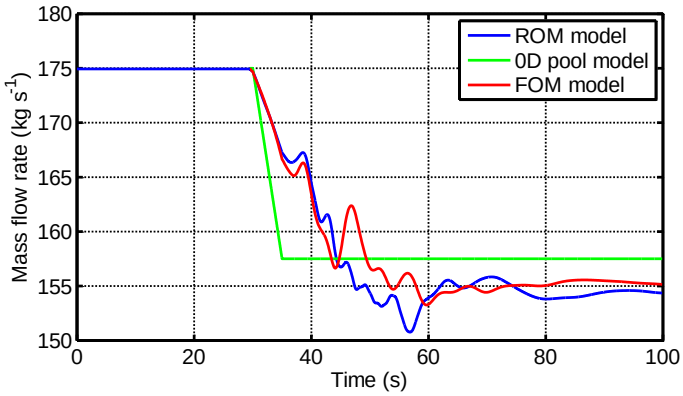

(a)

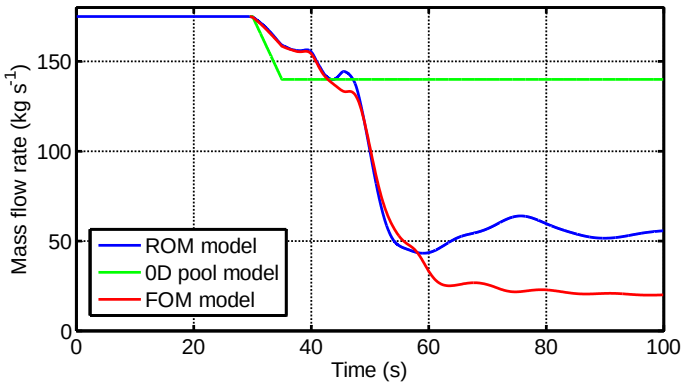

(b)

Figure 3.35. ALFRED pool case. Evolution of the mass flow rate in the central FA following an SG variation of (a) 20% - u_{SG2} =0.136 m/s; (b) 40% - u_{SG2}=0.102 m/s; with respect to the nominal value. – FOM (red line), ROM (blue line) and zero dimensional (green line) model results.

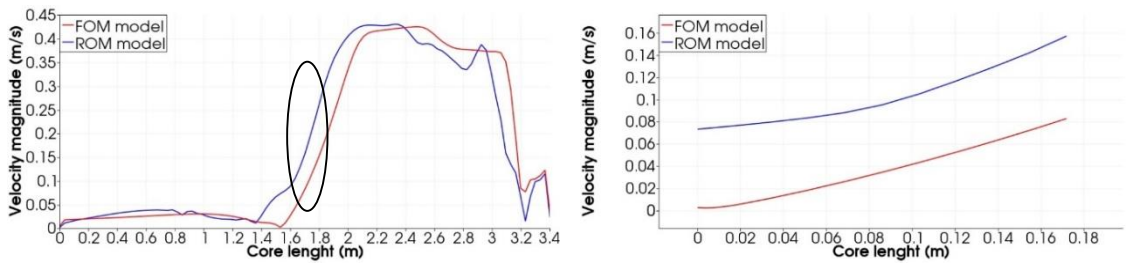

(a) (b)

Figure 3.36. ALFRED pool case. Inlet velocity profile following an SG variation of 40% - u_{SG2} =0.102 m/s with respect to the nominal value – FOM (red line), ROM (blue line) model results.

Finally, for the full order model, a computational time of 212 cpu-hours is required for a single simulation case of 70 s. On the other hand, for the ROM, only a computational time of 25 s (N_r=80) is needed to perform the same simulation. For the sake of completeness, for the POD generation and the ROM matrix calculation of the offline step, the procedure takes 0.3 cpu-hours and 40 cpu-hours, respectively.

3.6. Concluding remarks

In this Chapter, the development of a spatial model of the reactor pool is described. This approach is directed to overcome the 0D/1D modelling usually employed in control-oriented

models for the fluid dynamics. In particular, the 0D/1D approach prevents the simulation tool from taking into account the spatial features of the fluid flows, which can be relevant for certain reactor systems.

As first step to provide the object-oriented simulator with a ROM-based component representative of the ALFRED coolant pool, a POD-Galerkin Method for Finite Volume Approximation of Navier-Stokes and RANS equations has been developed. The aim of this new ROM approach is both to extend the classic POD-Galerkin-ROM method to the Finite Volume approximation of the Navier-Stokes equations and to build a reduced order model that is capable to handle turbulent flows modelled through the RANS equations. The reason behind this effort is to pursue the classic approach used in nuclear engineering for the turbulent flows based on the Finite Volume approach. Since for the control-related applications the RANS equations are sufficient to describe the main time-averaged properties of the flow (velocity, pressures stresses), the focus has been oriented to turbulence modelling such as the eddy viscosity models. The POD-FV-ROM procedure has been described starting from the modifications to the classic POD-G-ROM that should be adopted in a FV framework. A different approach from the literature cases that usually employ LES and DNS simulations for the snapshots creation has been adopted to treat the turbulence. The adoption of RANS with eddy viscosity models (necessary for the creation of the snapshots) allows avoiding the incorporation of the fictitious eddy viscosity since this quantity is already calculated in the Full Order Model. The eddy viscosity is expanded as a linear combination of spatial modes, but the time-coefficients are the same for velocity, face flux, pressure, and turbulent viscosity, and the spatial basis is calculated from the eigenvectors of the correlation matrix of the velocity. In this way, only the momentum equation is projected in order to obtain the set of ROM equations. Moreover, this procedure is not tailored to a specific turbulent model and can be applied to any eddy viscosity model, for all the different equations related to the turbulent quantities. The POD-FV-ROM has been tested in the classic benchmark of the numerical simulations for the 2D lid-driven cavity. In particular, two simulations at Re=1.000 and Re=100.000 have been considered in order to assess both laminar and turbulent flows. Some quantities have been compared with the FOM in order to assess the performance of the proposed ROM procedure i.e., the kinetic energy of the system, the reconstructed quantity of interest (velocity, pressure and turbulent viscosity), the L^2 error. In addition, for the laminar case, the comparison between the reduced order model steady-state solution and the data available in literature has been presented. The results have turned out to be very satisfactory. As for the laminar case, the ROM with 53 spatial modes reproduces very accurate results for both velocity and pressure, keeping the error well below 10^{-3} during all the transient and reaching $10^{-5}/10^{-6}$ at the end of the simulation (i.e., the steady-state). The time performance is also good with a simulation time of 5 s with respect to the 2590 cpu-hours of the FOM simulation. On the other hand, for the turbulent case, a higher number of spatial modes (N_r=85) is required, as expected, due to the higher Reynolds number. Considering the control-oriented purposes of the work, the outcomes are satisfactory being the error of the main variables of interest, i.e., velocity and pressure, is almost always below$\cdot 10^{-2}$ during the transient. Moreover, as the study of the kinetic energy has proved, the POD-FV-ROM is not affected by the energy blow up issue characteristic of the classic turbulent ROM (Wang et al., 2012). Even if a higher number of spatial modes is needed to obtain a fair reproduction of the transient with respect to the laminar case, the ROM

simulation time is 45 s against a FOM time of 4462 cpu-hours. This is very important considering the fast running requirement for a control-oriented simulator.

Starting from the proposed procedure, a parametric ROM-based component of the coolant pool of the ALFRED reactor has been developed. In order to demonstrate the possibility to employ a ROM-based component in a control-oriented simulator, the possibility to vary the input variables of the model has been undertaken. In particular, the SG outlet velocity has been considered as parametrized boundary condition since it can be a possible control variable. The variation of the SG oulet velocity has been shown to have an impact on the core inlet velocity profile and, in turn, on the distribution of the mass flow rate inside the core. The simulation results show a good agreement between the ROM and the FOM in reproducing the velocity field up to 50% variation of the SG velocity with respect to the nominal value, being the relative error of the velocity field always lower than 5%. As a major outcomes of the ROM, it has been proved that its behaviour is more accurate than 0D model without an excessive computational cost. In particular, in asymmetric transients where the spatial information of the velocity is crucial, the ROM well represents the inlet velocity profile movement from the centre to the periphery of the core. On the other hand, the 0D model is not able to catch this spatial information and the results is an average mass flow rate along the entire core inlet. Finally, the robustness of the model to reproduce different situations from what included in the snapshots has been assessed, giving acceptable results and, in any case, improving the accuracy with respect to the 0D modelling.

In conclusion, a spatial modelling approach of the coolant pool has been proposed aimed at being used in a control-oriented simulator. The adopted description allows for the spatial heterogeneity of the system, in particular as for the velocity field, i.e., the main variable of interest. On the other hand, it turns out to be employed in control-oriented applications, being accurate in both the velocity field and the output variable representation (e.g., mass flow rate) without an excessive computational cost. This modelling improvement may allow adopting innovative control strategies, whose feasibility in the nuclear field cannot be adequately studied with the 0D/1D approach.

List of symbols

Latin Symbols

a_i	time coefficient, -
$\boldsymbol{a}$	ROM time coefficient vector, -
$\boldsymbol{B}$	ROM matrix, -
$\boldsymbol{BT}$	ROM matrix, -
$\boldsymbol{C}$	ROM matrix, -
$\boldsymbol{CT1}$	ROM matrix, -
$\boldsymbol{CT2}$	ROM matrix, -
$\boldsymbol{D}$	ROM matrix, -
e	L^2 error of velocity, -
$\boldsymbol{E}$	ROM matrix, -
F	face flux, $m^3\ s^{-1}$
F_r	ROM face flux, $m^3\ s^{-1}$
k	turbulent kinetic energy, $m^2\ s^{-2}$
$\boldsymbol{n}$	normal vector, -
N_r	number of ROM functions, -
N_s	number of snapshots, -
p	normalized pressure, $m^2\ s^{-2}$
p_r	ROM normalized pressure, $m^2\ s^{-2}$
$\boldsymbol{u}$	velocity, $m\ s^{-1}$
$\boldsymbol{u}_r$	ROM velocity, $m\ s^{-1}$
$\boldsymbol{u}_n$	snapshots velocity, $m\ s^{-1}$
$\boldsymbol{u}_{BC}$	Dirichlet boundary condition of velocity, $m\ s^{-1}$
$\boldsymbol{u}_{FOM}$	FOM velocity, $m\ s^{-1}$

Greek Symbols

Γ	boundary function, -
υ	kinematic viscosity, $m^2\ s^{-1}$
υ_{EV}	eddy viscosity in POD-G-ROM, $m^2\ s^{-1}$
υ_t	turbulent viscosity, $m^2\ s^{-1}$
$\upsilon_{t,r}$	ROM turbulent viscosity, $m^2\ s^{-1}$
τ	penalty factor, -
$\boldsymbol{\varphi}_i$	velocity spatial modes, $m\ s^{-1}$
ψ_i	face flux spatial modes, $m^3\ s^{-1}$
ϕ_i	turbulent viscosity spatial modes, $m^2\ s^{-2}$
χ_i	pressure spatial modes, $m^2\ s^{-2}$
ω	specific dissipation, s^{-1}
Ω	spatial domain, m^3

(this page is intentionally left blank)

Conclusions

In this thesis, the control-oriented modelling of nuclear reactors is improved through the development of reduced order methods. Even if in the last years strong effort was spent in ROM techniques aimed at optimization and control, their implementation in simulation tools was never systematically studied in the nuclear field, especially as far as the control is concerned. This new methodology in the control-oriented modelling of the nuclear reactor is meant to overcome the classic approach based on 0D/1D modelling. The latter is in general appropriate for estimating integral quantities but it is of poor detail when the spatial dependence plays a relevant role in the respect of technological constraints or in general in the dynamics evolution, as in Lead-cooled Fast Reactor (LFR) systems. The thesis work is aimed at combining the high-detail modelling usually adopted for design purposes (e.g., 3D modelling) with the requirements demanded for a control-oriented tool, firstly the computational efficiency. Though the focus is kept more on the modelling aspects rather than control ones, this effort is a necessary step in the progress of the current approach employed in the control system design. The high accuracy guaranteed by the adoption of reduced order models allows solving some control issues related to modelling aspects, in particular the spatial ones, which otherwise could not be managed by means of the classic control-oriented approach.

The main outcomes of this Ph.D. thesis involve both methodological and applicative aspects with a special attention on the two main physics of the nuclear reactor, i.e., the neutronics and the thermal-hydraulics. In the following, the main achievements are summarized.

Methodological outcomes

The results of the work point out that it is possible to improve the control-oriented modelling of a nuclear reactor adopting efficient reduced order model techniques. In particular, this new methodology in the control-oriented modelling of the nuclear reactor ensures a higher level of detail without increasing the computational cost, and can be applied to any reactor concept.

As for the neutronics, the results are more relevant on the applicative side since a theoretical background is already present in literature (Stacey, 1969). Notwithstanding, some methodological conclusions on the neutronics can be drawn regarding the choice of the spatial basis and the test functions. As for the former topic, the Modal Method provides “a-priori” spatial basis, which does not allow insights into the simulation scenario. On the hand, the Proper Orthogonal Decomposition is able to provide “ad hoc” spatial basis tailored on the specific simulation case, thanks to its optimality property. As for the test functions, the use of adjoint flux allows a more efficient reduced order model since it is possible to employ less functions of the spatial basis, given a level of accuracy. These two outcomes led to the development of the *Adjoint Proper Orthogonal Decomposition*. This innovative ROM approach is proposed to merge the benefits of the POD spatial basis and the adjoint flux as test function.

As for the thermal-hydraulics, the results are more relevant from the methodological viewpoint since no previous theoretical background is present in literature on ROM procedures based on the Finite Volume approximation with a turbulence treatment that adopts RANS equations. In this sense, an innovative ROM procedure *(POD-FV-ROM)* is conceived, representing the first attempt in literature to use the POD-Galerkin approach to handle turbulence issues starting from RANS simulations (and in a parametrized context). Despite LES and DNS are more accurate than RANS equations, this method provides the control designer with a fast-running tool able to evaluate time-averaged flow properties (e.g., velocity, pressure and stress profiles) typical of CFD applications.

These two main innovative methodological achievements (i.e., the employment of adjoint flux as test function in POD-Galerkin approach and the development of a POD-Galerkin method for FV approximations based on RANS equations) can be exploited in several scientific and technological contexts different from the nuclear one.

Applicative outcomes

The application of this study is the improvement of a control-oriented simulator of a Lead-cooled Fast Reactor, i.e., substituting some components based on zero-dimensional approach with ROM-based models ensuring a high level of accuracy and a better physical description without increasing the computational burden. The simulator is based on the object-oriented modelling, is developed with Modelica language and implemented in the Dymola simulation environment. In the ROM framework, Modelica with its component approach turns out to be a powerful tool since it is possible to update or substitute a component with the respective ROM-based one without compromising the rest of the model.

The applicative results can be summarized as follows:

- **Neutronics.** The Modal Method (MM) has been assessed considering the adjoint flux as test function in a simple 3D case. The results show that the adoption of the adjoint flux improves the modelling accuracy with respect to the classic Point Kinetics, being the model capable to predict the reactivity evolution also in strong localized transients or relevant operational scenarios (e.g., shutdown).
- **Neutronics.** An object-oriented model of the 3D test case has been settled in order to prove the possibility to employ ROM-based components in control-oriented simulators. The developed model performs simulations in real time, being satisfactory from a computational point of view.
- **Neutronics.** A detailed model of the ALFRED reactor has been set up by means of the continuous energy MC neutron transport code SERPENT with a heterogeneous description of the active zone. The model represents 171 FAs, 107 dummy elements, 12 CRs and 4 safety rods, which constitute the core of ALFRED. The average cross-sections for each assembly, calculated by means of the MC model, have been used to solve the neutron diffusion PDEs exploiting the capabilities of the COMSOL software.
- **Neutronics.** The Adjoint Proper Orthogonal Decomposition has been tested in case of both thermal reactivity effects and CR movement, giving satisfactory results whereas the MM has proved not to be suitable for the latter case.

- **Thermal-hydraulics**. A benchmark on the numerical simulations for the 2D lid-driven cavity has been set up, both in laminar and turbulent conditions. Besides the comparison with reference results, as major outcomes, the POD-FV-ROM turns out not to be affected by the energy blow up issue characteristic of the classic turbulent POD-Galerkin methods.
- **Thermal-hydraulics**. The ROM-based component of the 2D ALFRED coolant pool, based on the developed method, has been settled in order to be employed in the object-oriented simulator, considering the SG outlet velocity as a parametrizable input. The model turns out to be both accurate and fast-running also in demanding transients. In particular, it has been stated that the ROM-based component behaviour is more accurate than 0D model without an excessive computational cost.

In addition, the high-fidelity simulations used to build the ROM-based components turn out to be useful also for the system design of the ALFRED reactor, assessing the spatial reactivity map of the lead density effect and the impact of an asymmetric transient in the reactor pool.

This thesis paves the way to several developments. Firstly, the use of reduced order modelling in the control-oriented simulation tools may allow adopting innovative control strategies, whose feasibility in the nuclear field cannot be adequately studied by means of a zero-dimensional model and providing, at the same time, some safety insights. For instance, with a spatial neutronics model, an optimal control of the Control Rods (CRs) movement that minimizes the perturbation on the neutron flux can be assessed, since the model allows for the flux distortion due to the CR insertion. Another possible application involves the oxygen control in the reactor pool due to the lead corrosion issues on structural materials. On the other hand, there is room for improvements in the selection of the optimal spatial basis and test function pairs. In this sense, the use of "adjoint velocity" as test function in the POD-FV-ROM can be envisaged. Moreover, some additional tests should be performed on the ROM components of the object-oriented simulator in order to definitively prove that no further issues arise in their employment. In particular, the coupling of different ROM components (e.g., spatial neutronics and coolant pool) and the behaviour in situations quite far from the snapshot ensemble are the main topics in this direction. Among the applicative developments, the inclusion of the energy equation in the POD-FV-ROM is of great interest in order to extend the approach also to multi-physics problems involving power production. Another possible perspective is the application of Uncertainty Quantification (UQ) techniques in the ROM framework for the considered problem. Finally, the reduced order methods developed in this thesis can be applied to different reactor concepts. In particular, it would be of interest to assess the capabilities of these methods in those reactors where the synergy between the several physics are particularly challenging, as in the Molten Salt Reactors (MSRs).

(this page is intentionally left blank)

Appendix A

In Section A.1 of this Appendix, the ALFRED reactor description is given, with the main core and SG parameters. The RGA method mentioned in Section 1.3 is briefly described in Section A.2. Some mathematical insights about the POD technique are presented in Section A.3, with particular attention to the POD calculation, to the optimality condition and to the relation with the Singular Value Decomposition. In the last part of the Appendix (Section A.4), the SERPENT input of the ALFRED reactor core is reported.

A.1 ALFRED reactor description

The reference reactor in this thesis is the Advanced Lead-cooled Fast Reactor European Demonstrator (ALFRED), developed within the European FP7 LEADER Project. The Project efforts were mainly focused on the resolution of the key issues emerged in the frame of the previous Euratom ELSY Project (Cinotti et al., 2008) to reach a new reference reactor configuration, which was used to design a fully representative scaled-down prototype. The demonstration ALFRED unit is foreseen to be built at ICN (Institute de Cercetari Nucleare) facility near Pitesti in southern Romania, where a fuel manufacturing plant is in operation for the two CANDU reactors operating in the country (Alemberti et al., 2013a).

ALFRED is a small-size (300 MWth) pool-type LFR. Its primary system current configuration (Alemberti et al., 2013b) is depicted in Figure A.1. All the major reactor primary system components, including core, primary pumps, and Steam Generators (SGs), are contained within the reactor vessel, being located in a large lead pool inside the reactor tank. The coolant flow coming from the cold pool enters the core and, once passed through the latter, is collected in a volume (hot collector) to be distributed to eight parallel pipes and delivered to as many SGs. After leaving the SGs, the coolant enters the cold pool through the cold leg and returns to the core.

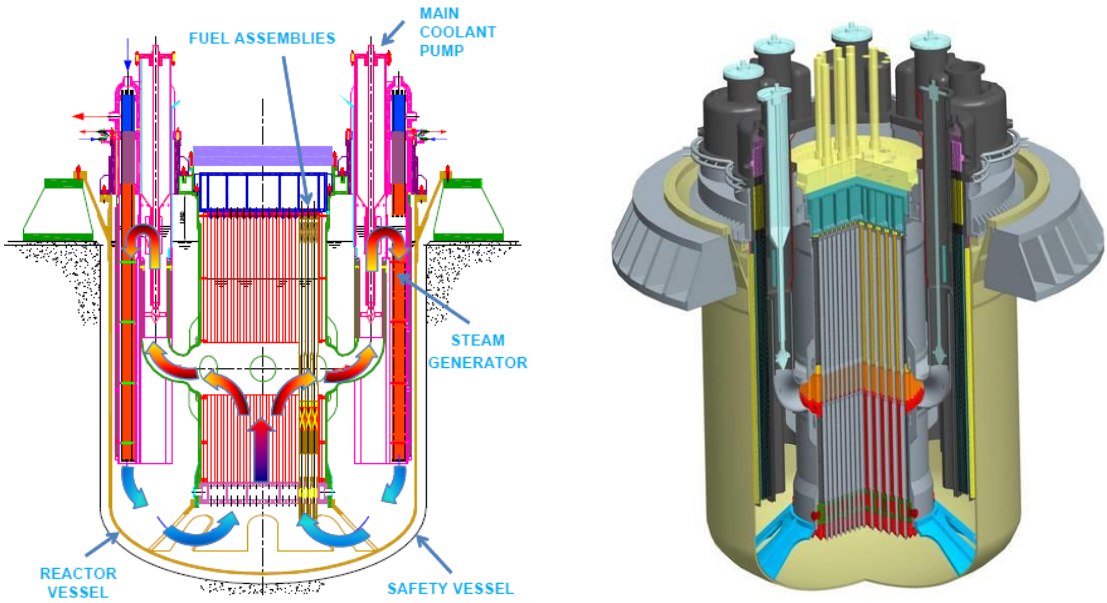

Figure A.1. ALFRED nuclear power plant layout.

The ALFRED core is composed by wrapped hexagonal Fuel Assemblies (FAs) with pins arranged on a triangular lattice (Figure A.2). The 171 FAs are subdivided into two radial zones with different plutonium fractions guaranteeing an effective power flattening, and surrounded by two rows of dummy elements (geometrically identical to the fuel assemblies but not producing thermal power) serving as reflector. Two different and independent control rods systems have been foreseen, namely, Control Rods (CRs) and Safety Rods (SRs). Power regulation and reactivity swing compensation during the cycle are performed by the former, while the simultaneous use of both is foreseen for scram purposes, assuring the required reliability for a

safe shutdown (Grasso et al., 2014). In Table A.1, the major preliminary nominal parameters employed as input data to implement the core model are presented.

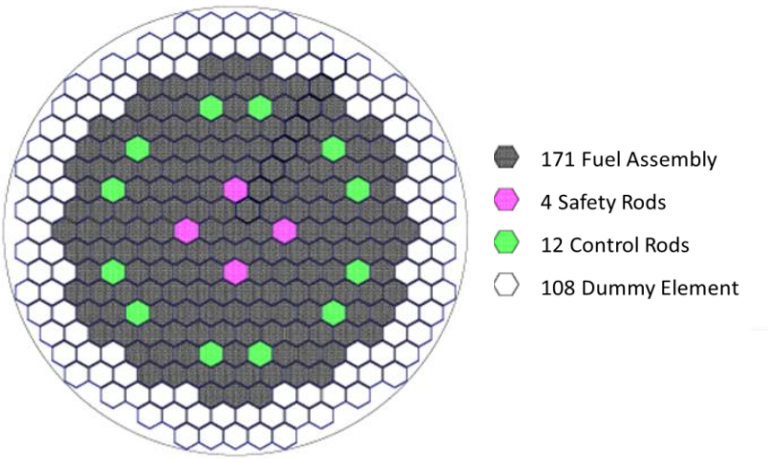

Figure A.2. ALFRED core configuration.

Table A.1. ALFRED core parameters (Grasso et al., 2014).

Parameter	Value		Unit
Core			
Thermal power	300		MW_{th}
Coolant mass flow rate	25984		kg s^{-1}
Total number of FAs	171		-
Pins per FA	127		-
Coolant inlet temperature, T_{in}	400		°C
Coolant outlet temperature, T_{out}	480		°C
Fuel pin			
Cladding material	15-15-Ti		-
Fuel material	MOX		-
Cladding outer radius	$5.25 \cdot 10^{-3}$		m
Cladding inner radius	$4.65 \cdot 10^{-3}$		m
Pellet outer radius	$4.50 \cdot 10^{-3}$		m
Pellet inner radius	$1.00 \cdot 10^{-3}$		m
Active height	0.6		m
Reactivity and kinetic coefficients	*BoC*	*EoC*	
Doppler constant, K_D	-555	-566	pcm
Lead expansion coefficient[19], α_L	-0.271	-0.268	pcm K^{-1}
Axial clad expansion, α_{CZ}	0.037	0.039	pcm K^{-1}
Axial wrapper tube expansion, α_{WZ}	0.022	0.023	pcm K^{-1}
Radial clad expansion, α_{CR}	0.008	0.011	pcm K^{-1}
Radial wrapper tube expansion, α_{WR}	0.002	0.003	pcm K^{-1}
Axial fuel expansion (free case), α_{FZ}	-0.148	-0.155	pcm K^{-1}
Axial fuel expansion (linked case), α_{FZ}	-0.232	-0.242	pcm K^{-1}
Diagrid expansion, α_{Diag}	-0.762	-0.789	pcm K^{-1}
Neutron generation time, Λ	$6.116 \cdot 10^{-7}$	$6.296 \cdot 10^{-7}$	s
Delayed neutron fraction, β	336	335	pcm

Each of the eight SGs incorporated in ALFRED (Figure A.3) consists of a bundle of vertical bayonet tubes. Each one of these tubes is constituted by an external safety tube and an internal

[19] Calculated for the whole height of the fissile sub-assemblies.

insulating layer (delimited by a slave tube), which is aimed at ensuring the production of superheated dry steam since the high temperature difference between the rising steam and the descending feedwater may promote steam condensation in the upper part of the SG without a proper insulation. The gap between the outermost and the outer bayonet tube provides mechanical decoupling between the components, and is filled with pressurized helium and high thermal conductivity particles to enhance the heat exchange capability (Damiani et al., 2013). The feedwater from dedicated headers flows in the slave tube and, after reversing the motion at the bottom, rises along the annulus between inner and outer tubes. On the primary side, lead flows downwards axially along the outermost tube. In Table A.2, the main SG parameters and specifications are listed.

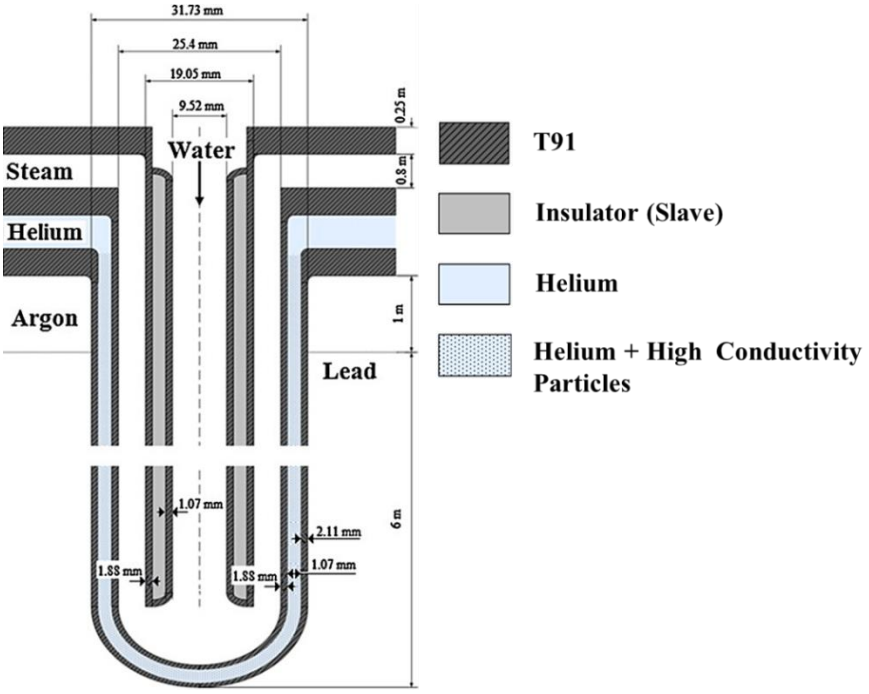

Figure A.3. ALFRED bayonet tube SG configuration.

Table A.2. ALFRED SG major nominal parameters (Damiani et al., 2013).

Parameter	Value		Unit
Single SG parameter			
Power	37.5		MW
Feedwater inlet temperature	335		°C
Steam outlet temperature	450		°C
Steam pressure	180		bar
Length of heat exchange	6		m
Number of tubes	510		-
	Outer diameter	*Thickness*	
Slave tube	$9.52 \cdot 10^{-3}$	$1.07 \cdot 10^{-3}$	m
Inner tube	$19.05 \cdot 10^{-3}$	$1.88 \cdot 10^{-3}$	m
Outer tube	$25.40 \cdot 10^{-3}$	$1.88 \cdot 10^{-3}$	m
Outermost tube	$31.75 \cdot 10^{-3}$	$2.11 \cdot 10^{-3}$	m

A.2 RGA method

In the definition of a suitable control strategy, once the system governing dynamics are defined, the next step to be taken into account is the choice of the pairings between input and output variables. The aim of this stage is to evaluate the influence performed by the control variables (the system inputs, u_i) on the candidate controlled variables (the system outputs, y_i) in order to select the most effective couplings.

Generally, most of the physical systems may be modelled as *Multiple Inputs* and *Multiple Outputs* (MIMO) systems. The different input/output variables present structural connections that strictly limit the direct application of the control techniques developed for *Single Input Single Output* (SISO) systems (Skogestad and Postlethwaite, 2005). A possible solution is represented by the centralized scheme shown in Figure A.4a, in which a dedicated block (indicated with Δ(s)) allows treating the MIMO system as if it were constituted by several uncoupled SISO systems, balancing the undesired cross influences between inputs and outputs. Nevertheless, such an option cannot be adopted if the system presents non-minimum phase behaviour and/or pure time delays as in the case of ALFRED reactor (Bortot et al., 2013). For this kind of systems, a specific decentralized control approach (Figure A.4b) has to be adopted, hence the undesired couplings between input and output cannot be compensated. Even if the performance of a decentralized scheme is poorer than the one of a centralized scheme, this configuration allows overcoming many limitations. In particular, the operation and maintenance of controllers are favoured by the simplicity of their implementation, and the resulting system is robust with respect to malfunctioning of the single control loops.

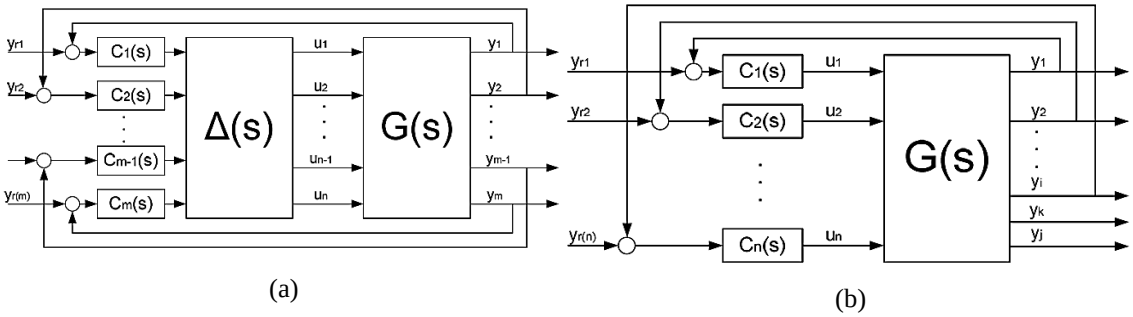

Figure A.4. Representation of a centralized control scheme (a), and of a decentralized control scheme (b). In particular, the physical process to be controlled (G(s)), the several implemented controllers (C_i(s)), the system output variables (y_i), the corresponding set-points (y_{ri}), and the system input variables (u_i) are shown.

In a *decentralized control scheme*, the first step is constituted by the selection of the most effective pairings between control and controlled variables. Accordingly, the input showing the most relevant interaction with a certain output, and at the same time not significantly affecting the behaviour of other variables of interest, represents the ideal candidate to achieve a feedback control loop. Interactions among variables constitute a physical feature of the system, and the best hints for the coupling can be derived by analysing the free dynamics response of the plant. These indications can be supported by some dedicated techniques, such as the RGA method. This procedure is a heuristic method that allows determining the most efficient input to control each

variable of interest, providing useful suggestions on how the model-based decentralized control system should be structured.

The effectiveness of a feedback control loop can be assessed by characterizing the MIMO system behaviour both in *open loop* and *closed loop* conditions. As far as the open loop gain is concerned, considering the system at equilibrium condition for fixed constant values of control variables, a step variation of amplitude δu_i on a certain input u_i is performed, causing a variation of the quantity δy_{jOL} of each output variable y_j (Figure A.5a). The open loop gain is defined as

$$g_{ji} = G_{ji}(0) = \frac{\delta y_{jOL}}{\delta u_i} \tag{A.1}$$

where $G_{ji}(0)$ is regarded as the gain of the transfer function between u_i and y_j. Instead, for the closed loop gain, it is assumed that, against the same variation of δu_i, an action is performed on all the other input variables in order to keep all the other outputs fixed, except for y_j, thanks to the action carried out by the other inputs (Figure A.5b). If the variation of y_j in closed loop configuration is indicated with δy_{jCL}, the closed loop gain between u_i and y_j can be defined as

$$h_{ji} = \frac{\delta y_{jCL}}{\delta u_i} \tag{A.2}$$

If the static gain for the open loop (g_{ji}) and for the closed loop (h_{ji}) are evaluated for all the input-output pairs, the RGA matrix Λ can be obtained. This matrix can be regarded as a quantitative measure of the input-output interaction at zero frequency for asymptotically stable processes. In particular, the elements λ_{ji} of this matrix, namely the relative gain of the pair (u_i, y_j), are defined as:

$$\lambda_{ji} = \frac{g_{ji}}{h_{ji}} \tag{A.3}$$

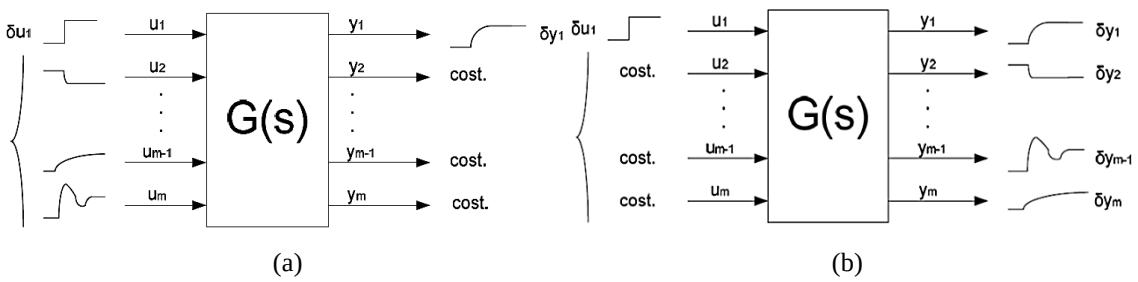

Figure A.5. Representation of an open loop response (a), and of a closed loop response (b). In particular, the physical process to be controlled (*G(s)*), the system output variables (y_j), the corresponding variation (δy_j), the system input variables (u_i), and the corresponding variation (δu_i) are shown.

In a control system development perspective, when the value of a λ_{ji} element approaches unity, there is a fair interaction that can be exploited, whereas if the value of a λ_{ji} element approaches zero the involved variables can be regarded as uncoupled. If the matrix element λ_{ji} is negative, it means that the control action may produce effects opposite to the desired ones on the controlled variable, depending on whether feedback control loops involve other output variables or not (Skogestad and Postlethwaite, 2005).

In common applications, the RGA matrix cannot always be applied since the physical system must have the same number of inputs and outputs. Most of the systems present a number of

outputs that is higher than the number of inputs, and thus it is necessary to redefine a formal procedure for the choice of input-output pairs. Such a procedure is offered by the NRG. In this case, the pairing process is performed in two phases: i) the less relevant outputs are disregarded in order to obtain a square input-output matrix; and ii) the choice of the input-output pairs. The first stage is performed by computing the sum of the elements on each row of the NRG matrix, which produces the Row Sum (RS) vector. The outputs associated to the largest figures of the RS vector are the most influenced ones by the inputs variation and thus the most relevant in a control perspective. At this point, the choice of the pairs can be made either through the RGA matrix of the reduced system or through the NRG matrix after having removed the rows concerning the outputs considered useless for the control, adopting the same selection criterion used in the RGA approach.

A.3 POD technique[20]

The proper orthogonal decomposition (POD) is a powerful and elegant method aimed at using low dimensional approximations of a high dimensional system according to an optimal criterion. The POD provides a basis for the modal decomposition of an ensemble of functions, such as data obtained in the course of experiments or, in the ROM framework, from the numerical solution of equations. It is considered the preferred basis in many contexts due to its optimality property. In particular, it provides the most efficient way of capturing the dominant components of an infinite-dimensional process with only finitely, and often surprisingly few, "modes." (Holmes et al., 1996).

The POD was introduced in the context of turbulence by Lumley (1967). In other disciplines the same procedure is called by other names, as Karhunen–Loève decomposition (Loève, 1955), principal components analysis (Jolliffe, 1986), singular systems analysis (Elsner and Tsonis, 1996), and singular value decomposition (Volkwein, 1999). The procedure has been used in various disciplines other than fluid mechanics, including random variables, image processing, signal analysis, data compression, process identification and control in chemical engineering, oceanography. The POD was initially used to analyse experimental data with a view to extracting dominant features and trends – in particular coherent structures (Berkooz et al., 1993). On the other hand, in the ROM framework, POD is used to provide a "relevant" set of basis functions that allows indentifying a low-dimensional subspace on which to construct a model by projection of the governing equations. The POD will produce the key spatial ingredients, from which the reduced order model will recreate the dynamics of the system as time-dependent mixtures of POD modes (Holmes et al., 1996).

A.3.1. POD calculation

Given an ensemble $\{u^k\}$ with members $u^k(\mathbf{x}) = u(\mathbf{x},t^k)$, we need to project each u onto candidate basis functions, assuming that the functions belong to an inner product space, e.g., an Hilbert space $\mathcal{H}$. In this sense, the optimal basis $\{\varphi_j(\mathbf{x})\}$ for the data set $\{u^k\}$ is the finite-dimensional representation

[20] This appendix is taken and partially re-elaborated from (Holmes et al., 1996).

$$u_N(\boldsymbol{x}, t^k) = \sum_{j=1}^{M} a_j(t^k)\varphi_j(\boldsymbol{x}) \tag{A.4}$$

$\{\varphi_j(\mathbf{x})\}$ is the optimal basis in the sense that it describes the members of the ensemble better than representations of the same dimension (i.e., same M) in any other basis.

The mathematical statement of optimality is that we should choose φ such that the average (squared) error between u and its projection onto φ is minimized

$$\min_{\varphi\in\mathcal{H}} \langle \left\| u - \frac{(u,\varphi)}{\|\varphi\|^2}\varphi \right\| \rangle \tag{A.5}$$

This is equivalent to maximizing the averaged projection of u onto φ, suitably normalized:

$$\max_{\varphi\in\mathcal{H}} \frac{\langle |(u,\varphi)|^2 \rangle}{\|\varphi\|^2} \tag{A.6}$$

The Equation (A.6) can be solved with the following eigenvalue problem (Holmes et al., 1996):

$$\mathcal{R}\varphi = \lambda\varphi \tag{A.7}$$

The optimal basis is given by the eigenfunctions φ_j of the operator $\mathcal{R}$ that is defined from the empirical data $\{u^k\}$. If we deal with finite dimensional space, i.e., $\mathcal{H} = \mathbb{R}^N$ with a data collection of M vectors $\boldsymbol{u}^k \in \mathbb{R}^N$, the operator $\mathcal{R}$ is a real and symmetric N × N correlation matrix defined as

$$\mathcal{R} = \frac{1}{M}\sum_{k=1}^{M} u^k (u^k)^T \qquad \mathcal{R}_{ij} = \frac{1}{M}\sum_{k=1}^{M} u_i^k u_j^k \tag{A.8}$$

The geometrical interpretation in this case is that the eigenvectors are simply the principal axes of the cloud of data points $\{u^k\}$ in the N-dimensional vector space (Holmes et al., 1996). If we deal with L^2 space, i.e., $\mathcal{H} = L^2$ with an ensemble of function u(x), the Equation (A.7) becomes

$$\mathcal{R}\varphi(x) = \int \langle u(x), u^*(x') \rangle \varphi(x') dx' = \lambda\varphi(x) \tag{A.9}$$

where the kernel of this integral equation is the averaged *autocorrelation function*

$$\mathcal{R}(x, x') = \langle u(x), u^*(x') \rangle \tag{A.10}$$

It is worthwhile to remind that if each observation u^k is a linear combination of eigenfunctions φ_j, it holds also the converse, i.e., each eigenfunctions φ_j can be expressed as a linear combination of observations u^k.

$$\varphi_j = \sum_{j=1}^{M} c_j u_j \tag{A.11}$$

A.3.2. Optimality condition

Let consider a decomposition of a time-dependent, statistically stationary signal *u(x,t)* with respect to *any* orthonormal basis $\{\psi_j(\mathbf{x})\}$

$$u(\boldsymbol{x},t) = \sum_j b_j(t)\psi_j(\boldsymbol{x}) \tag{A.12}$$

If $\psi_j(\mathbf{x})$ are orthonormal, it is possible to define a kind of energy of the signal as

$$\frac{1}{2}\langle \int u(x,t), u^*(x,t)\, dx\rangle = \frac{1}{2}\langle \sum_{ij} b_i(t) b_j^*(t) \int \psi_j(x,t), \psi_j^*(x,t)\, dx\rangle = \frac{1}{2}\sum_{ij}\langle b_i(t) b_j^*(t)\rangle \tag{A.13}$$

Considering the general decomposition of Equation (A.12) and the following POD decomposition

$$u(\boldsymbol{x},t) = \sum_i a_i(t)\varphi_i(\boldsymbol{x}) \tag{A.14}$$

the optimality for the POD is defined for every N as

$$\sum_{i=1}^{N}\langle a_i(t) a_i^*(t)\rangle = \sum_{i=1}^{N}\lambda_i \geq \sum_{i=1}^{N}\langle b_i(t) b_i^*(t)\rangle \tag{A.15}$$

i.e., the POD optimal can be interpreted as the first n POD basis functions capture more energy on average than the first n functions of any other basis.

Let $\{\psi_j(\mathbf{x})\}$ a set of n orthonormal vectors in L^2 forming an orthonormal basis. Let Q denote projection onto span$\{\psi_1, \dots, \psi_n\}$. We can express the kernel R in terms of $\{\psi_j(\mathbf{x})\}$ as

$$\mathcal{R}(x,x') = \langle u(x), u^*(x')\rangle = \langle \sum_i b_i(t)\psi_i(\boldsymbol{x}) \sum_j b_j^*(t)\psi_j^*(\boldsymbol{x}')\rangle = \sum_{ij}\langle b_i b_j^*\rangle \psi_i \psi_j^* \tag{A.16}$$

In operator matrix notation, $\mathcal{R}$ can be expressed as

$$\mathcal{R} = \begin{bmatrix} \langle b_1 b_1^*\rangle & \langle b_1 b_2^*\rangle & \cdots & \langle b_1 b_n^*\rangle \\ \langle b_2 b_1^*\rangle & \langle b_2 b_2^*\rangle & \cdots & \langle b_2 b_n^*\rangle \\ \vdots & \vdots & \ddots & \vdots \\ \langle b_n b_1^*\rangle & \langle b_n b_2^*\rangle & \cdots & \langle b_n b_n^*\rangle \end{bmatrix} \tag{A.17}$$

and the product $R \circ Q$ yields

$$\mathcal{R} \circ Q = \begin{bmatrix} \langle b_1 b_1^*\rangle & \langle b_1 b_2^*\rangle & \cdots & \langle b_1 b_n^*\rangle & 0 & \cdots & 0 \\ \langle b_2 b_1^*\rangle & \langle b_2 b_2^*\rangle & \cdots & \langle b_2 b_n^*\rangle & \vdots & \cdots & \vdots \\ \vdots & \vdots & \ddots & \vdots & \vdots & \cdots & \vdots \\ \langle b_n b_1^*\rangle & \langle b_n b_2^*\rangle & \cdots & \langle b_n b_n^*\rangle & \vdots & \cdots & \vdots \\ 0 & \cdots & \cdots & \cdots & 0 & \cdots & 0 \\ \vdots & \vdots & \vdots & \vdots & \vdots & \ddots & \ddots \\ 0 & \cdots & \cdots & \cdots & 0 & \cdots & 0 \end{bmatrix} \tag{A.18}$$

It is possible to state (Riesz and Nagy, 1955; Volkwein, 1999) that the sum of the first n eigenvalues of a self-adjoint operator is greater than or equal to the sum of the diagonal terms in any n-dimensional projection of it:

$$\sum_{i=1}^{N}\langle a_i(t) a_i^*(t)\rangle = \sum_{i=1}^{N}\lambda_i \geq tr(\mathcal{R} \circ Q) = \sum_{i=1}^{N}\langle b_i(t) b_i^*(t)\rangle \tag{A.19}$$

This characterization implies that, among all linear decompositions, the POD is the most efficient in the sense that for a given number of modes, *n*, the projection on the subspace spanned

by the leading *n* empirical eigenfunctions contains the greatest possible energy on average (Holmes et al., 1996).

A.3.3. Method of snapshots

Sirovich (1987) proposed the *method of snapshots* as a numerical procedure to save computational time for calculating the POD modes. In particular, this reduces the order of the eigenvalue computation (Equation (A.7)) from an N × N problem (where N is the number of point in the computational mesh) to an M × M problem, where M is the number of snapshots (Delville et al., 1999). Given $\{u_i\}$, which are the M members of the data set (i.e., *the snapshots*), and considering the discretized version of the inner product of the N-dimensional vector space, the eigenvector φ_j can be expressed as in Equation (A.11)

$$\varphi_j = \sum_{j=1}^{M} c_j u_j \tag{A.20}$$

where the coefficient c_j are unknown. Considering the Equation (A.8), the N-dimensional eigenfunction problem can be written as

$$\left(\frac{1}{M}\sum_{i=1}^{M} u_i (u_i)^T\right)\sum_{k=1}^{M} c_k u_k = \lambda \sum_{k=1}^{M} c_k u_k \tag{A.21}$$

$$\sum_{i=1}^{M}\left[\sum_{k=1}^{M}\frac{1}{M}(u_k, u_i)c_k\right]u_i = \lambda \sum_{k=1}^{M} c_k u_k \tag{A.22}$$

The sufficient condition for the solution of Equation (A.22) is to find the coefficients c_k such that

$$\sum_{k=1}^{M}\frac{1}{M}(u_k, u_i)c_k = \lambda c_i \qquad i = 1, \dots, M \tag{A.23}$$

representing an $M \times M$ eigenvalue problem.

A.3.4. SVD relationship

In the finite-dimensional case, the POD can be related to a singular decomposition of the given dataset. If the snapshots u_i are collected in an N × M matrix

$$X = [u_1, \dots, u_M] \tag{A.24}$$

the M × M eigenvalue problem of Equation (A.23) can be expressed as

$$\frac{1}{M}X^T X c = \lambda c \tag{A.25}$$

where $c=(c_1, \dots, c_M)$.

Considering a *singular value decomposition* of an N × M matrix

$$X = U\Sigma V^T = \sum_{j=1}^{r} \sigma_j \varphi_j v_j^T \tag{A.26}$$

where

$$U = [\varphi_1, \dots, \varphi_N] \qquad V = [v_1, \dots, v_M] \tag{A.27}$$

and r is the rank of X. The N × M matrix Σ is of the form

$$\Sigma = \begin{bmatrix} \Sigma_1 \\ 0 \end{bmatrix} \tag{A.28}$$

where Σ_1 is a diagonal matrix of real, non-negative singular values σ_j, arranged in descending order. Accordingly, the singular value decomposition of the data matrix X provides the POD modes as the columns of U.

A.4. SERPENT model of the ALFRED reactor

Serpent is a three dimensional continuous energy Monte Carlo (MC) neutron transport code, developed by the VTT Technical Research Centre in Finland. Its application is focused on lattice physics application ranging from the generation of homogenized few-group constants for reactor simulation code to fuel cycle analysis. The code is publicly distributed by the OECD/NEA Data Bank and RSICC since 2009, and has users in 35 organizations of 20 countries. The main advantage of using MC calculation instead of deterministic transport methods reactor physics calculations is the capability to model any fuel or reactor configuration using the same fundamental interaction data without major approximations. On the other hand, the drawback of using a Monte Carlo code in the burden calculation time due to the highly time consuming of the neutron history (a million of neutron histories have to be launched in order to have correct results). In this view, Serpent calculation methods can reduce the running time to acceptable level, making the Serpent code a viable alternative to deterministic transport codes.

A.4.1. SERPENT input

Similar to other Monte Carlo codes, such as MCNP and Keno-VI, Serpent uses a universe-based combinatorial solid geometry (CSG) model, which allows the description of practically any two- or three-dimensional fuel or reactor configuration. The geometry is divided in several levels, independently defined and gradually nested. The elementary element is the cell, i.e., a region of the space limited by surfaces. Each cell is filled with a homogenous material composition or with void or other elements (called universe) in order to build more and more complex configurations.

In the ALFRED reactor input, the elementary entity is the fuel pin (Figure A.6) defined by the pin geometry (Figure A.7) and filled with basic material (Figure A.8). The following level is the fuel assembly where the fuel pin universe is nested following the FA configuration (Figure A.9, Figure A.10). The same is done for the CR and the SR. Finally, the universes representing the FA, CR and SR are nested in the lattice representing the core which is surrounded by axial and radial reflectors, and the vessel (Figure A.11).

```
%Universe 50=active zone
%Universe 49=upper zone
%Universe 51=lower zone
%Active zone 1
cell     49       50       Void                -1  43 -42
cell     48       50       pin_inner         1 -2  43 -42
cell     47       50       Gap               2 -3  43 -42
cell     46       50       Cladding          3 -4  43 -42
cell     45       50       Lead_FA_inner     4     43 -42
%Active zone 2 Spacer
cell     50       50       Void                -1  44 -43
cell     51       50       pin_inner         1 -2  44 -43
cell     52       50       Gap               2 -3  44 -43
cell     53       50       Cladding          3 -4  44 -43
cell     54       50       Lead_FA_inner     4     44 -43
%Active zone 3
cell     55       50       Void                -1  45 -44
cell     56       50       pin_inner         1 -2  45 -44
cell     57       50       Gap               2 -3  45 -44
cell     58       50       Cladding          3 -4  45 -44
cell     59       50       Lead_FA_inner     4     45 -44
%Upper Insulator
cell     44       51       Insulator           -2  42 -41
cell     43       51       Gap               2 -3  42 -41
cell     42       51       Cladding          3 -4  42 -41
cell     41       51       Lead_out_FA_inner 4     42 -41
%Lower Insulator
cell     60       49       Insulator           -2  46 -45
cell     61       49       Gap               2 -3  46 -45
cell     62       49       Cladding          3 -4  46 -45
cell     63       49       Lead_in_FA_inner  4     46 -45
%Upper Plenum
cell     40       51       Plenum              -3  41 -40
cell     39       51       Cladding          3 -4  41 -40
cell     38       51       Lead_out_FA_inner 4     41 -40
%Upper Terminal part 1
cell     37       51       Insulator           -3  40 -39
cell     36       51       Cladding          3 -4  40 -39
cell     35       51       Lead_out_FA_inner 4     40 -39
%Upper Terminal - Spacer Grid
cell     34       51       Insulator           -4  39 -38
cell     33       51       Lead_out_FA_inner 4     39 -38
%Upper Terminal part 2
cell     32       51       Insulator           -4  38 -37
cell     31       51       Lead_out_FA_inner 4     38 -37
%Upper Empty
cell     732      51       Lead_out_FA_inner   -4  37 -36
cell     731      51       Lead_out_FA_inner 4     37 -36
%Upper Pappone
cell     733      51       Lead_out_FA_inner   -4  36 -35
cell     734      51       Lead_out_FA_inner 4     36 -35
%Lower Plenum 1
cell     64       49       Plenum              -6  47 -46
cell     65       49       Fuel_hold         6 -2  47 -46
cell     66       49       Plenum            2 -3  47 -46
cell     67       49       Cladding          3 -4  47 -46
cell     68       49       Lead_in_FA_inner  4     47 -46
%Lower Plenum - Space grid
cell     69       49       Plenum              -6  48 -47
cell     70       49       Fuel_hold         6 -2  48 -47
cell     71       49       Plenum            2 -3  48 -47
cell     72       49       Cladding          3 -4  48 -47
```

```
cell     73       49       Lead_in_FA_inner    4     48 -47
%Lower Plenum 2
cell     74       49       Plenum                -6  49 -48
cell     75       49       Fuel_hold           6 -2  49 -48
cell     76       49       Plenum              2 -3  49 -48
cell     77       49       Cladding            3 -4  49 -48
cell     78       49       Lead_in_FA_inner    4     49 -48
%Lower Terminal
cell     79       49       Insulator             -3  50 -49
cell     80       49       Cladding            3 -4  50 -49
cell     81       49       Lead_in_FA_inner    4     50 -49
%Pin grid support
cell     782      49       Spacer                -4  51 -50
cell     783      49       Spacer              4     51 -50
%Reflector
cell     30       51       Lead_out_FA_inner         35
cell     82       49       Lead_in_FA_inner             -51
```

Figure A.6. Fuel pin input.

```
surf     1        cyl        0.0 0.0 0.1      %Void radius
surf     6        cyl        0.0 0.0 0.4      %Gas lower plenum radius
surf     2        cyl        0.0 0.0 0.45     %Pellet radius
surf     3        cyl        0.0 0.0 0.465    %Inner radius of cladding
surf     4        cyl        0.0 0.0 0.525   %Outer radius of cladding
surf     5        hexxc  0.0 0.0 0.693       %1/2 pitch
surf     34       pz          225             %upper limit of the empty section (II)
surf     35       pz          182             %upper limit of pappone zone
surf     36       pz           99             %upper limit of the empty section
surf     37       pz           49             %upper limit of the pin
surf     38       pz           47             %upper limit of the 3°  grid spacer
surf     39       pz           45             %upper limit of the first part of upper terminal pin
surf     40       pz           43             %upper limit of the upper plenum
surf     41       pz           31             %upper limit of the upper insulator
surf     42       pz           30             %upper limit of the active zone
surf     43       pz            1             %upper limit of the 2°  grid spacer
surf     44       pz           -1             %lower limit of the 2°  grid spacer
surf     45       pz          -30             %lower limit of the active zone
surf     46       pz          -31             %lower limit of the lower insulator
surf     47       pz          -46             %lower limit of the 1°  part of the lower plenum
surf     48       pz          -48             %lower limit of the 1°  grid spacer
surf     49       pz          -86             %lower limit of the lower plenum
surf     50       pz          -88             %lower limit of the pin
surf     51       pz          -93             %lower limit of Pin support grid
surf    111       inf
```

Figure A.7. Fuel geometry input.

```
% Fuel in inner
mat pin_inner  -10.443 rgb 250 0 0
U-234.15c          7.9091E-06
U-235.15c          1.0783E-03
U-236.15c          2.6364E-05
U-238.15c          2.6252E-01
Pu-238.15c         1.6935E-03
Pu-239.15c         4.1123E-02
Pu-240.15c         1.9439E-02
Pu-241.15c         4.3773E-03
Pu-242.15c         5.4931E-03
Am-241.15c         9.3764E-04
O-16.15c           66.33E-02
```

```
%Fuel in outer
mat pin_outer  -10.47 rgb 0 250 0
U-234.12c          7.2929E-06
U-235.12c          9.9427E-04
U-236.12c          2.4310E-05
U-238.12c          2.4207E-01
Pu-238.12c         2.1696E-03
Pu-239.12c         5.2683E-02
Pu-240.12c         2.4903E-02
Pu-241.12c         5.6078E-03
Pu-242.12c         7.0373E-03
Am-241.12c         1.2012E-03
O-16.12c           66.33E-02
```

```
% --- Coolant (Lead) active zone @440° C
mat Lead -10.515 rgb 0 102 204
Pb-204.06c        -1.4e-2
Pb-206.06c        -24.1e-2
Pb-207.06c        -22.1e-2
Pb-208.06c        -52.4e-2
% --- Coolant (Lead) active zone @440° C FA_inner
mat Lead_FA_inner -10.515 rgb 0 102 204
Pb-204.06c        -1.4e-2
Pb-206.06c        -24.1e-2
Pb-207.06c        -22.1e-2
Pb-208.06c        -52.4e-2
% --- Coolant (Lead) active zone @440° C FA_outer
mat Lead_FA_outer -10.515 rgb 0 102 204
Pb-204.06c        -1.4e-2
Pb-206.06c        -24.1e-2
Pb-207.06c        -22.1e-2
Pb-208.06c        -52.4e-2
% --- Coolant (Lead) active zone @440° C dummy
mat Lead_dummy -10.515 rgb 0 102 204
Pb-204.06c        -1.4e-2
Pb-206.06c        -24.1e-2
Pb-207.06c        -22.1e-2
Pb-208.06c        -52.4e-2
% Inlet Coolant @400° C
mat Lead_in -10.563 rgb 0 0 255
Pb-204.06c        -1.4e-2
Pb-206.06c        -24.1e-2
Pb-207.06c        -22.1e-2
Pb-208.06c        -52.4e-2
% Inlet Coolant @400° C
mat Lead_in_1 -10.563 rgb 0 0 255
Pb-204.06c        -1.4e-2
Pb-206.06c        -24.1e-2
Pb-207.06c        -22.1e-2
Pb-208.06c        -52.4e-2
% Inlet Coolant @400° C
mat Lead_in_2 -10.563 rgb 0 255 0
Pb-204.06c        -1.4e-2
Pb-206.06c        -24.1e-2
Pb-207.06c        -22.1e-2
Pb-208.06c        -52.4e-2
% Inlet Coolant @400° C
mat Lead_in_3 -10.563 rgb 255 0 0
Pb-204.06c        -1.4e-2
Pb-206.06c        -24.1e-2
Pb-207.06c        -22.1e-2
Pb-208.06c        -52.4e-2
% Inlet Coolant @400° C FA_inner
mat Lead_in_FA_inner -10.563 rgb 0 0 255
Pb-204.06c        -1.4e-2
Pb-206.06c        -24.1e-2
Pb-207.06c        -22.1e-2
Pb-208.06c        -52.4e-2
% Inlet Coolant @400° C FA_outer
mat Lead_in_FA_outer -10.563 rgb 0 0 255
Pb-204.06c        -1.4e-2
Pb-206.06c        -24.1e-2
Pb-207.06c        -22.1e-2
Pb-208.06c        -52.4e-2
% Inlet Coolant @400° C FA_outer
mat Lead_in_dummy -10.563 rgb 0 0 255
Pb-204.06c        -1.4e-2
Pb-206.06c        -24.1e-2
Pb-207.06c        -22.1e-2
Pb-208.06c        -52.4e-2
% Outer Coolant @480° C
mat Lead_out -10.467 rgb 51 204 255
Pb-204.06c        -1.4e-2
Pb-206.06c        -24.1e-2
Pb-207.06c        -22.1e-2
Pb-208.06c        -52.4e-2
% Outer Coolant @480° C FA_inner
mat Lead_out_FA_inner -10.467 rgb 51 204 255
Pb-204.06c        -1.4e-2
Pb-206.06c        -24.1e-2
Pb-207.06c        -22.1e-2
Pb-208.06c        -52.4e-2
% Outer Coolant @480° C FA_inner
mat Lead_out_FA_outer -10.467 rgb 51 204 255
Pb-204.06c        -1.4e-2
Pb-206.06c        -24.1e-2
Pb-207.06c        -22.1e-2
Pb-208.06c        -52.4e-2
% Outer Coolant @480° C dummy
mat Lead_out_dummy -10.467 rgb 51 204 255
Pb-204.06c        -1.4e-2
Pb-206.06c        -24.1e-2
Pb-207.06c        -22.1e-2
Pb-208.06c        -52.4e-2
% --- Void (He) @20° C
mat Void -1.64E-04 rgb 255 255 0
He-4.12c          -1
% --- Gap in active zone @20° C
mat Gap -1.64E-04 rgb 255 255 0
He-4.09c          -1
% --- Lower/Upper penum (He)
mat Plenum -1.64E-04 rgb 255 255 0
He-4.06c          -1
%Vessel @20° C
mat AISI316LN  -7.9 rgb 221 221 221
C-nat.06c         -0.024E-02
Cr-nat.06c        -16.89E-02
Ni-nat.06c        -10.07E-02
Mn-55.06c         -1.51E-02
Mo-nat.06c        -2.16E-02
Ti-nat.06c        -0.02E-02
Si-nat.06c        -0.42E-02
B-11.06c -0.00067E-02
P-31.06c -0.026E-02
N-14.06c -0.0597E-02
S-nat.06c         -0.0016E-02
Al-27.06c         -0.0143E-02
V-nat.06c         -0.03E-02
W-nat.06c         -0.03E-02
Nb-93.06c         -0.025E-02
Ta-181.06c        -0.03E-02
Cu-nat.06c        -0.35E-02
Co-59.06c         -0.03E-02
Ca-nat.06c        -0.2E-02
Fe-nat.06c        -68.35E-02
```

```
% --- Cladding delle fuel pin (Ti 15-15) @20° C
(Fuelholder, Wrapper)
mat Cladding -7.95 rgb 164 144 119
C-12.06c          -0.09E-02
Cr-50.06c         -0.63E-02
Cr-52.06c         -12.1E-02
Cr-53.06c         -1.38E-02
Cr-54.06c         -0.343E-02
Ni-58.06c         -10.6E-02
Ni-60.06c         -4.07E-02
Ni-61.06c         -0.177E-02
Ni-62.06c         -0.563E-02
Ni-64.06c         -0.144E-02
Mn-55.06c         -1.5E-02
Mo-92.06c         -0.223E-02
Mo-94.06c         -0.139E-02
Mo-95.06c         -0.239E-02
Mo-96.06c         -0.25E-02
Mo-97.06c         -0.143E-02
Mo-98.06c         -0.362E-02
Mo-100.06c        -0.144E-02
Ti-46.06c         -3.2E-04
Ti-47.06c         -2.92E-04
Ti-48.06c         -2.95E-03
Ti-49.06c         -2.20E-04
Ti-50.06c         -2.16E-04
Si-28.06c         -0.784E-02
Si-29.06c         -3.97E-04
Si-30.06c         -2.64E-04
B-10.06c          -1.19E-05
B-11.06c          -4.81E-05
P-31.06c          -0.045E-02
N-14.06c          -0.015E-02
S-32.06c          -1.43E-04
S-33.06c          -1.13E-06
S-34.06c          -6.32E-06
S-36.06c          -3.0E-07
Al-27.06c         -0.015E-02
Zr-90.06c         -1.54E-04
Zr-91.06c         -3.37E-05
Zr-92.06c         -5.15E-05
Zr-94.06c         -5.21E-05
Zr-96.06c         -8.40E-06
V-51.06c          -0.03E-02
W-182.06c         -7.95E-05
W-183.06c         -4.29E-06
W-184.06c         -9.19E-05
W-186.06c         -8.53E-05
Nb-93.06c         -0.015E-02
Ta-181.06c        -0.015E-02
Cu-63.06c         -2.08E-04
Cu-65.06c         -9.25E-05
Co-59.06c         -0.03E-02
Ca-40.06c         -2.91E-04
Ca-42.06c         -2.35E-06
Ca-44.06c         -6.90E-06
Fe-54.06c         -3.79E-02
Fe-56.06c         -59.9E-02
Fe-57.06c         -1.44E-02
Fe-58.06c         -0.183E-02
```

```
% mix lead @400 (86% vol) and Ti-15-15 (14% vol)
@400° C (average)
mat Spacer -10.18 rgb 1 1 1
C-nat.06c         -1.00E-04
Cr-nat.06c        -1.61E-02
Ni-nat.06c        -1.72E-02
Mn-55.06c         -1.67E-03
Mo-nat.06c        -1.67E-03
Ti-nat.06c        -4.45E-04
Si-nat.06c        -9.45E-04
B-10.06c -6.67E-06
P-31.06c -5.00E-05
N-14.06c -1.67E-05
S-nat.06c         -1.67E-05
Al-27.06c         -1.67E-05
Zr-nat.06c        -3.34E-05
V-nat.06c         -3.34E-05
W-nat.06c         -3.34E-05
Nb-93.06c         -1.67E-05
Ta-181.06c        -1.67E-05
Cu-nat.06c        -3.34E-05
Co-59.06c         -3.34E-05
Ca-nat.06c        -3.34E-05
Fe-nat.06c        -7.27E-02
Pb-204.06c        -1.24E-02
Pb-206.06c        -2.14E-01
Pb-207.06c        -1.96E-01
Pb-208.06c        -4.66E-01

%control and Safety rod (ref D7)
mat CRSR   -2.2 rgb 0 250 0
B-10.06c  0.72
B-11.06c  0.08
C-nat.06c          0.20

%Upper and lower insulator
mat Insulator     -6 rgb 0 0 0
O-16.06c           66.33E-02
Y-89.06c  2.00E-02
Zr-nat.06c         31.67E-02
```

Figure A.8. Material input.

```
include "Pin_level/Alfred_cell_pin_inner"
%Lower FA
pin 59
Lead_in_FA_inner
lat 100 3 0.0 0.0 15 15 1.386
59 59 59 59 59 59 59 59 59 59 59 59 59 59 59
 59 59 59 59 59 59 59 49 49 49 49 49 49 49 59
  59 59 59 59 59 59 49 49 49 49 49 49 49 49 59
   59 59 59 59 59 49 49 49 49 49 49 49 49 49 59
    59 59 59 59 49 49 49 49 49 49 49 49 49 49 59
     59 59 59 49 49 49 49 49 49 49 49 49 49 49 59
      59 59 49 49 49 49 49 49 49 49 49 49 49 49 59
       59 49 49 49 49 49 49 49 49 49 49 49 49 49 59
        59 49 49 49 49 49 49 49 49 49 49 49 49 59 59
         59 49 49 49 49 49 49 49 49 49 49 49 59 59 59
          59 49 49 49 49 49 49 49 49 49 49 59 59 59 59
           59 49 49 49 49 49 49 49 49 49 59 59 59 59 59
            59 49 49 49 49 49 49 49 49 59 59 59 59 59 59
             59 49 49 49 49 49 49 49 59 59 59 59 59 59 59
              59 59 59 59 59 59 59 59 59 59 59 59 59 59 59
 %Active FA
 pin 60
 Lead_FA_inner
lat 101 3 0.0 0.0 15 15 1.386
60 60 60 60 60 60 60 60 60 60 60 60 60 60 60
 60 60 60 60 60 60 60 50 50 50 50 50 50 50 60
  60 60 60 60 60 60 50 50 50 50 50 50 50 50 60
   60 60 60 60 60 50 50 50 50 50 50 50 50 50 60
    60 60 60 60 50 50 50 50 50 50 50 50 50 50 60
     60 60 60 50 50 50 50 50 50 50 50 50 50 50 60
      60 60 50 50 50 50 50 50 50 50 50 50 50 50 60
       60 50 50 50 50 50 50 50 50 50 50 50 50 50 60
        60 50 50 50 50 50 50 50 50 50 50 50 50 60 60
         60 50 50 50 50 50 50 50 50 50 50 50 60 60 60
          60 50 50 50 50 50 50 50 50 50 50 60 60 60 60
           60 50 50 50 50 50 50 50 50 50 60 60 60 60 60
            60 50 50 50 50 50 50 50 50 60 60 60 60 60 60
             60 50 50 50 50 50 50 50 60 60 60 60 60 60 60
              60 60 60 60 60 60 60 60 60 60 60 60 60 60 60
%Upper FA
pin 61
Lead_out_FA_inner
lat 102 3 0.0 0.0 15 15 1.386
61 61 61 61 61 61 61 61 61 61 61 61 61 61 61
 61 61 61 61 61 61 61 51 51 51 51 51 51 51 61
  61 61 61 61 61 61 51 51 51 51 51 51 51 51 61
   61 61 61 61 61 51 51 51 51 51 51 51 51 51 61
    61 61 61 61 51 51 51 51 51 51 51 51 51 51 61
     61 61 61 51 51 51 51 51 51 51 51 51 51 51 61
      61 61 51 51 51 51 51 51 51 51 51 51 51 51 61
       61 51 51 51 51 51 51 51 51 51 51 51 51 51 61
        61 51 51 51 51 51 51 51 51 51 51 51 51 61 61
         61 51 51 51 51 51 51 51 51 51 51 51 61 61 61
          61 51 51 51 51 51 51 51 51 51 51 61 61 61 61
           61 51 51 51 51 51 51 51 51 51 61 61 61 61 61
            61 51 51 51 51 51 51 51 51 61 61 61 61 61 61
             61 51 51 51 51 51 51 51 61 61 61 61 61 61 61
              61 61 61 61 61 61 61 61 61 61 61 61 61 61 61
include "FA_level/FA_inner/FA_inner_1"
...
include "FA_level/FA_inner/FA_inner_57"
```

Figure A.9. General FA input.

```
cell   1004   1011  fill 100                    -100
cell   1005   1011  Wrapper                 100 -101
cell   1006   1011  Lead_in_FA_inner         101
cell   1007   1012  fill 101                    -100
cell   1008   1012  Wrapper                 100 -101
cell   1009   1012  Lead_FA_inner           101
cell   1010   1013  fill 102                    -100
cell   1011   1013  Wrapper                 100 -101
cell   1012   1013  Lead_out_FA_inner       101
cell   1013   1010  fill 1011                   -102      -45
cell   1014   1010  fill 1012                   -102  45  -42
cell   1015   1010  fill 1013                   -102  42
```

Figure A.10. Central FA input.

```
include "FA_level/Alfred_cell_FA_inner"
include "FA_level/Alfred_cell_FA_outer"
include "FA_level/Alfred_cell_CR"
include "FA_level/Alfred_cell_SR"
include "FA_level/Alfred_cell_FA_dummy"
include "FA_level/Rod_mov"

%Universe 106= FA inner
%Universe 307 = CR
%Universe 205= FA outer
%Universe 407 = SR
%Universe 506 = Dummy element

pin 99
Lead_in

lat 1000 2 0.0 0.0 23 23 17.1
99  99  99  99  99  99  99  99  99  99  99  99  99  99  99  99  99  99  99  99  99  99  99
99  99  99  99  99  99  99  99  99  99  99  99  99  99 506 506 506 506 506  99  99  99  99
99  99  99  99  99  99  99  99  99  99  99  99 506 506 506 506 506 506 506 506  99  99  99
99  99  99  99  99  99  99  99  99  99 506 506 506 506 3020 3010 3000 506 506 506 506  99  99
99  99  99  99  99  99  99  99 506 506 506 2690 2680 2670 2660 2650 2640 2630 2620 506 506 506  99
99  99  99  99  99  99  99 506 506 506 2700 2400 2390 7040 2380 7030 2370 2360 2610 506 506 506  99
99  99  99  99  99  99 506 506 3030 2710 2410 2110 2100 2090 2080 2070 2060 2350 2600 2990 506 506  99
99  99  99  99  99 506 506 3040 2720 7050 2120 1420 1410 1400 1390 1380 2050 7020 2590 2980 506 506 99
99  99  99  99 506 506 3050 2730 2420 2130 1430 1220 1210 1200 1190 1370 2040 2340 2580 2970 506 506 99
99  99  99  99 506 506 2740 7060 2140 1440 1230 1100 8020 1090 1180 1360 2030 7010 2570 506 506  99 99
99  99  99 506 506 2750 2430 2150 1450 1240 1110 1040 1030 1080 1170 1350 2020 2330 2560 506 506  99 99
99  99 506 506 2760 2440 2160 1460 1250 8030 1050 1010 1020 8010 1160 1340 2010 2320 2550 506 506 99 99
99  99 506 506 2770 2450 2170 1470 1260 1120 1060 1070 1150 1330 1570 2300 2310 2960 506 506  99  99 99
99  99 506 506 2780 7070 2180 1480 1270 1130 8040 1140 1320 1560 2290 7120 2950 506 506  99  99  99  99
99 506 506 3060 2790 2460 2190 1490 1280 1290 1300 1310 1550 2280 2540 2940 3140 506 506  99  99  99 99
99 506 506 3070 2800 7080 2200 1500 1510 1520 1530 1540 2270 7110 2930 3130 506 506  99  99  99  99  99
99 506 506 3080 2810 2470 2210 2220 2230 2240 2250 2260 2530 2920 3120 506 506  99  99  99  99  99  99
99 506 506 506 2820 2480 2490 7090 2500 7100 2510 2520 2910 506 506 506  99  99  99  99  99  99  99
99 506 506 506 2830 2840 2850 2860 2870 2880 2890 2900 506 506 506  99  99  99  99  99  99  99  99
99  99 506 506 506 506 3090 3100 3110 506 506 506 506  99  99  99  99  99  99  99  99  99  99
99  99  99 506 506 506 506 506 506 506 506  99  99  99  99  99  99  99  99  99  99  99  99
99  99  99  99 506 506 506 506 506  99  99  99  99  99  99  99  99  99  99  99  99  99  99
99  99  99  99  99  99  99  99  99  99  99  99  99  99  99  99  99  99  99  99  99  99  99
cell     110   0  fill 1000              -1000 -999 998
cell     111   0  AISI316LN          1000 -1001 -999 998
cell     112   0  Lead_in   1001 -1002 -999 998
cell     113   0  outside   1002
cell     114   0  outside    999  -1002
cell     115   0  outside   -998  -1002
set bc 1                  %periodic
```

Figure A.11. Core input.

(this page is intentionally left blank)

List of Figures

(this page is intentionally left blank)

List of Tables

References

Alemberti, A., De Bruyn, D., Grasso, G., Mansani, L., Mattioli, D., Roelofs, F., 2013a. The European Lead Fast Reactor Strategy and the Roadmap for the Demonstrator ALFRED. In *Proceedings of the International Conference on Fast Reactors and related Fuel Cycles*: Safe Technologies and Sustainable Scenarios, Paris, France, March 4–7, 2013.

Alemberti, A., Frogheri, M., Mansani, L., 2013b. The Lead fast reactor Demonstrator (ALFRED) and ELFR design. In *Proceedings of the International Conference on Fast Reactors and related Fuel Cycles*: Safe Technologies and Sustainable Scenarios, Paris, France, March 4–7, 2013.

Amsallem, D., Farhat, C., 2012. Stabilization of Projection-Based Reduced-Order Models. International Journal for Numerical Methods in Engineering, **91**, 358–377.

Antoulas, T., 2010. Model reduction of large-scale systems. Presentation for YY Fest, Kyoto University, March, 29–31, 2010.

Åström, K.J., Hägglund, T., 1995. *PID Controllers: Theory, Design and Tuning*. The International Society of Automation, Research Triangle Park, NC, USA.

Aubry, N., Holmes, P., Lumley, J., Stone, E., 1988. The dynamics of coherent structures in the wall region of a turbulent boundary layer. *Journal of Fluid Mechanics*, **192**, 115–173.

Aufiero, M., Cammi, A., Geoffroy, O., Losa, M., Luzzi, L., Ricotti, M. E., Rouch, H., 2014. Development of an OpenFOAM model for the Molten Salt Fast Reactor transient analysis. *Chemical Engineering Science*, **111**, 390–401

Balajewicz, M., Dowell, E. H., 2012. Stabilization of projection-based reduced order models of the Navier–Stokes. *Nonlinear Dynamics*, **70**, 1619–1632

Balajewicz, M. J., Dowell, E. H., Noack, B. R., 2013. Low-dimensional modelling of high-Reynolds-number shear flows incorporating constraints from the Navier–Stokes equation. *Journal of Fluid Mechanics*, **729**, 285–308.

Barbagallo, A., Sipp, D., Schmid, P. J., 2009. Closed-loop control of an open cavity flow using reduced-order models. *Journal of Fluid Mechanics*, **641**, 1–50.

Bergmann, M., Bruneau, C. H., Iollo, A., 2009. Enablers for robust POD models. *Journal of Computational Physics*, **228**, 516–538.

Bergmann, M., Cordier, L., Brancher, J. P., 2005. Optimal rotary control of the cylinder wake using proper orthogonal decomposition reduced-order model. *Physics of Fluids*, **17**, 097101.

Berkooz, G., Holmes, P., Lumley, J. L., 1993. The Proper Orthogonal Decomposition in the analysis of turbulent flows. Annual Review of Fluid Mechanics, **25**, 539–575.

Bizon, K., Continillo, G., 2012. Reduced order modelling of chemical reactors with recycle by means of POD-penalty method. *Computers and Chemical Engineering*, **39**, 22–32.

Bortot, S., Cammi, A., Lorenzi, S., Ponciroli, R., Della Bona, A., Juarez, N.B., 2013. Stability analyses for the European LFR Demonstrator. *Nuclear Engineering and Design*, **265**, 1238–1245.

Botella, O., Peyret, R., 1998. Benchmark Spectral Results on the Lid-driven Cavity Flow. *Computers & Fluids*, **27**(4), 421–433.

Brenan, K.E., Campbell, S.L., Petzold, L.R., 1989. *Numerical solution of initial-value problems in differential algebraic equations*. North-Holland Ed., New York.

Bristol, E. H., 1966. On a new measure of interaction of multivariable process control. *IEEE Transactions on Automatic Control*, **11**, 133–134.

Bruneau, C.H., Saad, M., 2006. The 2D lid-driven cavity problem revisited. Computers & Fluids, **35**, 326–348.

Cai, J., Watanabe, T., 2011. Numerical Simulation of Thermal Stratification in Cold Legs by Using OpenFOAM. *Progress in Nuclear Science and Technology*, **2**, 107–113.

Cammi, A., Casella, F., Ricotti, M.E., Schiavo, F., 2005. Object-Oriented Modelling, Simulation and Control of IRIS Nuclear Power Plant with Modelica. In *Proceedings of the 4th International Modelica Conference*, Hamburg, Germany, March 7–8, 2005.

Carlberg, K., Farhat, C., 2008. A Compact Proper Orthogonal Decomposition Basis for Optimization-Oriented Reduced-Order Models. In *Proceedings of the 12th AIAA/ISSMO Multidisciplinary Analysis and optimization Conference*, Victoria, Canada, September 10–12, 2008.

Casella, F., Leva, A., 2006. Modeling of thermo-hydraulic power generation processes using Modelica. *Mathematical and Computer Modeling of Dynamical Systems*, **12**(1), 19–33.

Cazemier, W. Verstappen, R.W.C.P., Veldman, A.E.P., 1998. Proper orthogonal decomposition and low-dimensional models for driven cavity flows. *Physics of Fluids*, **10**, 1685–1699.

Chang, J.W., Yu, C.C., 1990. The Relative Gain for Non-Square Multivariable Systems. *Chemical Engineering Science*, **45**, 1309–1323.

Cheng, X., Tak, N.I., 2006. Investigation on Turbulent Heat Transfer to Lead-Bismuth Eutectic Flows in Circular Tubes for Nuclear Applications. *Nuclear Engineering and Design*, **236**, 385–393.

Chinesta, F., Huerta, A., Rozza, G., Wilcox, K., 2015. Model Order Reduction. Preprint SISSA 55/2015/MATE. For Encyclopedia of Computational Mechanics 2016 Edition.

Cinotti, L., Locatelli, G., Aït Abderrahim, H., Monti, S., Benamati, G., Tucek, K., Struwe, D., Orden, A., Corsini, G., Le Carpentier, D., 2008. The ELSY Project. In *Proceedings of the International Conference on the Physics of Reactors Nuclear Power*: A Sustainable Resource, Interlaken, Switzerland, September 14-19, 2008

Clifford, I., Ivanov K., Avramova, M., 2013. A multi-scale homogenization and reconstruction approach for solid material temperature calculations in prismatic high temperature reactor cores. *Nuclear Engineering and Design*, **256**, 1–13.

COMSOL, 2011. COMSOL Multiphysics® 4.2a, User's Guide. COMSOL Inc.

Cordier, L., Noack, B. R., Tissot, G., Lehnasch, G., Delville, J., Balajewicz, M., Daviller, G., Niven, R. K., 2013. Identification strategies for model-based control. Experiments in Fluids, **54**:1580.

Couplet M., Sagaut, P., Basdevant, C., 2003. Intermodal energy transfers in a proper orthogonal decomposition – Galerkin representation of a turbulent separated flow. *Journal of Fluid Mechanics*, **491**, 275–284.

Damiani, L., Montecucco, M., Pini Prato, A., 2013. Conceptual design of a bayonet tube steam generator for the ALFRED lead-cooled reactor. *Nuclear Engineering and Design*, **265**, 154–163.

Delville, J., Ukeiley, L., Cordier, L., Bonnet, J. P., Glauser, M., 1999. Examination of large-scale structures in a turbulent plane mixing layer. Part 1. Proper orthogonal decomposition. *Journal of Fluid Mechanics*, **391**, 91–122.

Dolezal, R., Varcop, L., 1970. *Process Dynamics: Automatic Control of Steam Generation Plant*. Elsevier Science.

Drohmann, M., Haasdonk, B., Ohlberger, M., 2009. Reduced basis method for finite volume approximation of evolution equations on parametrized geometries. In Proceedings of ALGORITMY, 1–10.

Duderstadt J.J., Hamilton L. J., 1976. *Nuclear Reactor Analysis*. John Wiley and Sons, New York.

Dulla, S., Picca P., Ravetto P., 2009. Variational Methods in the Kinetic Modeling of Nuclear Reactors: Recent Advances. In *Proceedings of International Conference on Mathematics, Computational Methods & Reactor Physics*, Saratoga Springs, NY, May 3–9, 2009.

DYMOLA, 2015. Version, 2015. Dassault Systèmes, France. http://www.3ds.com/products-services/catia/products/dymola

El-Farra, N. H., Christofides, P. D., 2002. Hybrid Control of Parabolic PDE Systems. In *Proceedings of the 41st IEEE Conference on Decision and Control*, Las Vegas, USA, December 10–13, 2002.

Elmqvist, H., Cellier, F.E., Otter, M., 1993. Object-Oriented Modeling of Hybrid Systems. In *Proceedings of the European Simulation Symposium*, Delft, Netherlands, October 25–28, 1993.

Elsner, J.B., Tsonis, A.A., 1996. *Singular Spectrum Analysis. A New Tool in Time Series Analysis*. Plenum Press.

Erturk, E., 2009. Discussions On Driven Cavity Flow. *International Journal for Numerical Methods in Fluids*, **60**, 275–294.

Eymard, R., Gallouët, T., Herbin, R., 2000. The finite volume method. In *Handbook for Numerical Analysis*, P.G. Ciarlet, J.L. Lions eds., **7**, 713–1020.

Fiorina, C., Clifford, I., Aufiero, M., Mikityuk, K., 2015. GeN-Foam: a novel OpenFOAM® based multi-physics solver for 2D/3D transient analysis of nuclear reactors. *Nuclear Engineering and Design Volume*, **294**, 24–37.

Fletcher, C. A. J., 1996. *Computational Techniques for Fluid Dynamics, Vol. 1: Fundamental and General Techniques*. Springer.

Fritzson, P., 2004. *Principles of Object-Oriented Modeling and Simulation with Modelica 2.1*. Wiley-IEEE Press.

Fritzson, P., 2011. A cyber-physical modeling language and the OpenModelica environment. In *Proceedings of the 7th International Wireless Communications and Mobile Computing Conference*, Istanbul, Turkey, July 4–8, 2011.

Gandhir, A., Hassan, Y., 2011. RANS modeling for flow in nuclear fuel bundle in pressurized water reactors (PWR). *Nuclear Engineering and Design*, **241**, 4404–4408.

Gavoille, P., Courcelle, A., Seran, J.L., Averty, X., Bourdiliau, B., Provitina, O., Garat, V., Verwaerde, D., 2013. Mechanical Properties of Cladding and Wrapper Materials for the ASTRID Fast-Reactor Project. In *Proceedings of the International Conference on Fast Reactors and related Fuel Cycles*: Safe Technologies and Sustainable Scenarios, Paris, France, March 4–7, 2013.

Gen IV International Forum, 2013. Annual Report, available at https://www.gen-4.org/gif/upload/docs/application/pdf/2014-06/gif_2013_annual_report-final.pdf.

Ghia, U., Ghia, K. N., Shin, C. T., 1982. High-Re Solutions for Incompressible Flow Using the Navier-Stokes Equations and a Multigrid Method. *Journal of Computational Physics*, **48**, 387–411.

Gottlieb, D., Orszag, S.A., 1977. *Numerical Analysis of Spectral Methods: Theory and Applications*. CBMS-NSF Regional Conference Series in Applied Mathematics. Society for Industrial and Applied Mathematics, Philadelphia.

Grasso, G., Petrovich, C., Mattioli, D., Artioli, C., Sciora, P., Gugiu, D., Bandini, G., Bubelis, E., and Mikityuk, K., 2014. The Core Design of ALFRED, a Demonstrator for the European Lead-Cooled Reactors. *Nuclear Engineering and Design*, **278**, 287–301.

Guerrieri, C., Cammi, A., Luzzi, L., 2014. A preliminary approach to the MSFR control issues. *Annals of Nuclear Energy*, **64**, 472–484.

Gunzburger, M.D., 2003. *Perspectives in Flow Control and Optimization in Advances in Design and Control*. Society for Industrial and Applied Mathematics, Philadelphia.

Haasdonk, B., Ohlberger, M., 2008a. Adaptive basis enrichment for the reduced basis method applied to finite volume schemes. In *Proceedings of 5th Internatonal Symposum on Finite Volumes for Complex Applications*, Aussois, France, June 8–13, 2008.

Haasdonk, B., Ohlberger, M., 2008b. Reduced basis method for finite volume approximations of parametrized linear evolution equations. *Mathematical Modelling and Numerical Analysis*, **42**, 277–302.

Haasdonk, B., Ohlberger, M., Rozza, G., 2008. A reduced basis method for evolution schemes with parameter-dependent explicit operators. Electronic Transactions on Numerical Analysis, **32**, 145–161.

Haasdonk, B., Ohlberger, M., 2009. Reduced basis method for explicit finite volume approximations of nonlinear conservation laws. In Proceedings of Symposia in Applied Mathematics, **67**(2).

Henry, A.F., 1975. Nuclear reactor analysis. The MIT Press, Cambridge, MA, USA.

Hesthaven, J. S., Rozza, G., Stamm, B., 2016. *Certified Reduced Basis Methods for Parametrized Partial Differential Equations*. SpringerBriefs in Mathematics. Spinger International Publishing.

Hetrick, D.L., 1993. *Dynamics of Nuclear Reactors*. American Nuclear Society, La Grange Park, IL, USA.

Holmes, P., Lumley, J. L., Berkooz, G., 1996. *Turbulence, Coherent Structures, Dynamical Systems and Symmetry*. Cambridge Monographs on Mechanics, Cambridge University Press, Cambridge, UK.

http://www.leader-fp7.eu/ (accessed 15.10.2015).

Iaccarino, G., 2001. Predictions of a Turbulent Separated Flow Using Commercial CFD Codes, *Journal of Fluids Engineering*, **123**, 819–828.

IAEA, 1999. Modern Instrumentation and Control for Nuclear Power Plants: A Guidebook. Technical Reports Series No. 387. International Atomic Energy Agency, Vienna.

IAEA, 2009. Implementing Digital Instrumentation and Control Systems in the Modernization of Nuclear Power Plants. IAEA Nuclear Energy Series NP-T-1.4. International Atomic Energy Agency, Vienna.

Iliescu, T., Wang, Z., 2014. Variational multiscale proper orthogonal decomposition: Navier-stokes equations. *Numerical Methods for Partial Differential Equations*, **30**, 641–663.

Jasak, H., 1996. Error analysis and estimation in the Finite Volume method with applications to fluid flows. PhD thesis, Imperial College, University of London.

Jasak, H., Jemcov, A., Tukovic, Z., 2007. OpenFOAM: A C++ Library for Complex Physics Simulations. In *Proceedings of International Workshop on Coupled Methods in Numerical Dynamics*, Dubrovnik, Croatia, September 19–21, 2007.

Kolmogorov, A. N., 1941. The local structure of turbulence in incompressible viscous fluid for very large Reynolds numbers. In *Proceedings of the USSR Academy of Sciences* (in Russian), **32**, 16–18. Reprinted in English: *Proceedings of the Royal Society A*, **434**, 9–13.

Koning A., Forrest, R., Kellet, M., Mills, R., Henriksson, H., Rugama, Y., 2006. The JEFF-3.1 Nuclear Data Library. Technical Report. JEFF Report 21. NEA–OECD.

Kozlowski, T., Downar, T.J., 2007. PWR MOX/UO2 Core Transient Benchmark. Technical report, Working Party on Scientific Issues of Reactor Systems, OECD/NEA.

Kunisch, K., Volkwein, S., 2003. Galerkin Proper Orthogonal Decomposition Methods for a General Equation in Fluid Dynamics. *SIAM Journal on Numerical Analysis*, **40**, 492–515.

Jareteg, K., Vinai, P., Sasic, S., Demazière, C., 2015. Coupled fine-mesh neutronics and thermal-hydraulics – Modeling and implementation for PWR fuel assemblies. *Annals of Nuclear Energy*, **84**, 244-257.

Jolliffe, L. T., 1986. *Principle Component Analysis*. Springer-Verlag, New York.

Lassila, T., Manzoni, A., Quarteroni, A., Rozza, G., 2013. Model order reduction in fluid dynamics: challenges and perspectives in *Reduced Order Methods for Modeling and Computational Reduction*, MS&A Series, **9**, 235–274, Springer Milano.

Lassila, T., Rozza, G., 2010. Parametric free-form shape design with PDE models and reduced basis method. *Computer Methods in Applied Mechanics and Engineering*, **199**(23–24), 1583–1592

Laub, A.J., Heath, M.T., Paige, C.C., Ward, R.C., 1987. Computation of System Balancing Transformations and Other Applications of Simultaneous Diagonalization Algorithms. *IEEE Transactions on Automatic Control*, **32**(2), 115–122.

Levine, W. S., 1996. *The Control Handbook*. IEEE Press.

Loéve, M., 1955. *Probability theory*. Van Nostrand, Princeton, NJ.

Lorenzi, S., Bortot, S., Cammi, A., Ponciroli, R., 2012. Evaluation of the coolant reactivity coefficient influence on the dynamic response of a small LFR system. In *Proceedings of International Topical Meeting on Advances in Reactor Physics*, Knoxville, USA, April 15–20, 2012.

Lumley, J. L., 1967. The structure of inhomogeneous turbulent flows. In *Atmospheric Turbulence and RadioWave Propagation*, 166–178.

Luzzi, L., Cammi, A., Di Marcello, V., Lorenzi, S., Pizzocri, D., Van Uffelen, P., 2014. Application of the TRANSURANUS code for the fuel pin design process of the ALFRED reactor. *Nuclear Engineering and Design*, **277**, 173–187.

Manzoni, A., Quarteroni, A., Rozza, G., 2012. Computational Reduction for Parametrized PDEs: Strategies and Applications, Milan Journal of Mathematics, **80**(2), 283–309.

Menter, F. R. 1994. Two-Equation Eddy-Viscosity Turbulence Models for Engineering Applications. *American Institute of Aeronautics and Astronautics Journal*, **32**(8), 1598–1605.

Menter, F. R., Kuntz, M., Langtry, R., 2003. Ten Years of Industrial Experience with the SST Turbulence Model. *Turbulence, Heat and Mass Transfer*, **4**, 2003, 625–632.

Moore, B.C., 1981. Principal component analysis in linear systems: controllability, observability, and model reduction. *IEEE Transactions on Automatic Control*, **26**(1), 17–32.

NIST (National Institute of Standards and Technology), http://physics.nist.gov/cgi-bin/Compositions/stand_alone.pl

Noack, B., Papas, P., Monkewitz, P., 2005. The need for a pressure-term representation in empirical Galerkin models of incompressible shear flows. *Journal of Fluid Mechanics*, **523**(1), 339–365

OECD-NEA, 2007. *Handbook on Lead-bismuth Eutectic Alloy and Lead Properties, Materials Compatibility*. Thermal Hydraulics and Technologies, No. 6195.

Ogata, K., 2009. *Modern Control Engineering*. Prentice Hall.

Oliveira, I., Patera, A., 2007. Reduced-basis techniques for rapid reliable optimization of systems described by affinely parametrized coercive elliptic partial differential equations. *Optimization and Engineering*, **8**(1), 43–65.

OpenFOAM, 2014. Version 2.3, www.openfoam.org.

Östh, J., Noack, B. R., Krajnovi¢, S., Barros, D. Borée, J., 2014. On the need for a nonlinear subscale turbulence term in POD models as exemplified for a high-Reynolds-number flow over an Ahmed body. *Journal of Fluid Mechanics*, **747**, 515–544.

Papadourakis, A., Doherty, M.F., Douglas, J.M., 1987. Relative gain array for units in plants with recycle. *Industrial & Engineering Chemistry Research*, **26**(6), 1259–1262.

Petzold, L. R., 1982. A Description of DASSL: A Differential/Algebraic System Solver. In Proceedings of 10th IMACS World Congress, Montréal, Canada, August 8–12, 1982.

Ponciroli, R., 2014. Development of a Model-based approach for studying the system dynamics and control of Gen-IV Lead-cooled Fast Reactors. PhD thesis, Politecnico di Milano.

Ponciroli, R., Bigoni, A., Cammi, A., Lorenzi, S., Luzzi, L., 2014a. Object-oriented modelling and simulation for the ALFRED dynamics. *Progress in Nuclear Energy*, **71**, 15–29.

Ponciroli, R., Cammi, A., Lorenzi, S., Luzzi, L., 2014b. A preliminary approach to the ALFRED reactor control strategy. *Progress in Nuclear Energy*, **73**, 113–128.

Ponciroli, R., Cammi, A., Della Bona, A., Lorenzi, S., Luzzi, L., 2015a. Development of the ALFRED reactor full power mode control system. *Progress in Nuclear Energy*, **85**, 428–440.

Ponciroli, R., Cammi, A., Lorenzi, S., Luzzi, L. 2015c. Petri-net based modelling approach for ALFRED reactor operation and control system design. Submitted to *Progress in Nuclear Energy*.

Ponciroli, R., Cammi, A., Lorenzi, S., Luzzi, L., 2015b. Control approach to the load frequency regulation of a Generation IV Lead-cooled Fast Reactor. *Energy Conversion and Management*, **103**, 43–56.

Pope, S. B., 2000. *Turbulent Flows*. Cambridge University Press.

Protas, B., Noack, B. R., Östh, J., 2015. Optimal nonlinear eddy viscosity in Galerkin models of turbulent flows. *Journal of Fluid Mechanics*, **766**, 337–367.

Quarteroni, A., Manzoni, A., Negri, F., 2016. *Reduced Basis Methods for Partial Differential Equations. An Introduction*. Springer International Publishing, Switzerland.

Quarteroni, A., Rozza, G., Manzoni, A., 2011. Certified reduced basis approximation for parametrized partial differential equations and applications. *Journal of Mathematics in Industry*, **1**:3.

Rambo, J., 2006. Reduced-order modeling of multiscale turbulent convection: application to data center thermal management. PhD thesis, Georgia Institute of Technology.

Rambo, J., Joshi, Y., 2005. Reduced order modeling of steady turbulent flows using the POD. In *Proceedings of the ASME Summer Heat Transfer Conference*, **3**, 837–846.

Rambo, J., Joshi, Y., 2007. Reduced-order modeling of turbulent forced convection with parametric conditions. *International Journal of Heat and Mass Transfer*, **50**, 539–551.

Rempfer, D., Fasel, F. H., 1994. Evolution of three-dimensional coherent structures in a flat-plate boundary-layer. *Journal of Fluid Mechanics*, **260**, 351–375.

Richardson, L. F., 1922. *Weather Prediction by Numerical Process*. Cambridge University Press.

Riesz, F., Nagy, B. S., 1955. *Functional Analysis*. Ungar, New York.

Rozza, G., Huynh, D. B. T., Patera, A. T., 2008. Reduced Basis Approximation and a Posteriori Error Estimation for Affinely Parametrized Elliptic Coercive Partial Differential Equations, *Archives of Computational Methods in Engineering*, **15**, 229–275.

Rozza, G., Huynh, D. B. T., Nguyen, N. C., Patera, A. T., 2008. Real-time reliable simulation of heat transfer phenomena. In *Proceedings of the HT2009 ASME Summer Heat Transfer Conference*, San Francisco, California, USA, July 19–23, 2009.

San, O., Iliescu, T., 2013. Proper Orthogonal Decomposition Closure Models For Fluid Flows: Burgers Equation. *International Journal Of Numerical Analysis And Modeling, Series B Computing and Information*, **1**, 1–18.

Sartori, A., Baroli, D., Cammi, A., Chiesa, D., Luzzi, L., Ponciroli, R., Previtali, E., Ricotti, M.E., Rozza, G., Sisti, M., 2013. Comparison of a Modal Method and a Proper Orthogonal Decomposition approach for multi-group time-dependent reactor spatial kinetics. *Annals of Nuclear Energy*, **71**, 217–229.

Schultz, M. A., 1961. *Control of Nuclear Reactors and Power Plants*, McGraw Hill, New York.

SERPENT, 2011. PSG2/Serpent Monte Carlo Reactor Physics Burnup Calculation Code. URL http://montecarlo.vtt.fi.

Shapiro, B., 2003. Creating Compact Models for Electronic Systems: An Overview and Suggested Use of Existing Model Reduction and Experimental System Identification Tools. *IEEE Transactions on Components, Packaging, and Manufacturing Technology – Part A*, **26**(1), 65–172.

Sirisup, S., Karniadakis, G.E., 2005. Stability and accuracy of periodic flow solutions obtained by a POD-penalty method. *Physica D*, **202**, 218–237.

Sirovich, L., 1996. Turbulence and the dynamics of coherent structures, Part I–III. *Quarterly of Applied Mathematics*, **45**, 561–590.

Skogestad, S., Postlethwaite, I., 2005. *Multivariable Feedback Control: Analysis and Design*, John Wiley and Sons, New York, USA.

Sobolev, V., Malambu, E., Aït Abderrahim, H., 2009. Design of a Fuel Element for a Lead-cooled Fast Reactor. *Journal of Nuclear Materials*, **385**, 392–399.

Souyri, A., Bouskela, D., Pentori, B., Kerkar, N., 2006. Pressurized Water Reactor Modelling with Modelica. In *Proceedings of the 5th International Modelica Conference*, Vienna, Austria, September 4–5, 2006.

Stacey, W. M., 1969. *Space-Time Nuclear Reactor Kinetics*. Academic Press.

The MathWorks, Inc. 2015.

The Modelica Association, 2014. Modelica 3.2.2 Language Specification. Available online at: http://www.modelica.org/

Todreas, N., Kazimi, M.S., 2012. *Nuclear Systems – Thermal Hydraulic Fundamentals. vol. 1*, CRC Press, 2nd edition.

Tucek, K., Carlsson, J., Wider, H., 2006. Comparison of sodium and lead-cooled fast reactors regarding reactor physics aspects, severe safety and economical issues. *Nuclear Engineering and Design*, **236**, 1589–1598.

Van Dooren, P., 2000. Gramian Based Model Reduction of Large-Scale Dynamical Systems, in: Watson, G.A, Griffiths, D.F. (Eds.), Numerical Analysis 1999. Chapman & Hall/CRC Research Notes in Mathematics Series, London, pp. 231–247.

Versteeg, H. K., Malalasekera, W., 2007. *An Introduction to Computational Fluid Dynamics, the Finite Volume Method*. Pearson Education Limited.

Volkwein, S., 1999. Proper Orthogonal Decomposition and Singular Value Decomposition. Karl-Franzens-Universität Graz & Technische Universität Graz.

Waltar, A.E., Todd, D.R., and Tsvetkon, P.V., Editors, 2012. *Fast Spectrum Reactors*. Springer, New York.

Wang, Z., Akhtar, I., Borggaard, J., Iliescu, T., 2011. Two-level discretizations of nonlinear closure models for proper orthogonal decomposition. *Journal of Computational Physics*, **230**, 126–146.

Wang, Z., Akhtar, I., Borggaard, J., Iliescu, T., 2012. Proper orthogonal decomposition closure models for turbulent flows: a numerical comparison. *Computer Methods in Applied Mechanics and Engineering*, **237–240**, 10–26.

Weller, H. G., Tabor, G., Jasak, H., Fureby, C., 1998. A tensorial approach to computational continuum mechanics using object-oriented techniques. *Computer in Physics*, **12**, 620–631.

Weller, J., Lombardi, E., Bergmann, M., Iollo, A., 2010. Numerical methods for low-order modeling of fluid flows based on POD. *International Journal for Numerical Methods in Fluids*, **63**(2), 249–268.